Chong Di

MODELING AND ANALYSIS OF A HIGH-SPEED SOLID-ROTOR INDUCTION MACHINE

ACTA UNIVERSITATIS LAPPEENRANTAENSIS 902

Chong Di

MODELING AND ANALYSIS OF A HIGH-SPEED SOLID-ROTOR INDUCTION MACHINE

Dissertation for the degree of Doctor of Science (Technology) to be presented with due permission for public examination and criticism in Room 1316 at Lappeenranta–Lahti University of Technology LUT, Lappeenranta, Finland on the 28th of April, 2020, at noon.

Acta Universitatis
Lappeenrantaensis 902

Supervisors Professor Juha Pyrhönen
LUT School of Energy Systems
Lappeenranta–Lahti University of Technology LUT
Finland

Dr. Ilya Petrov
LUT School of Energy Systems
Lappeenranta–Lahti University of Technology LUT
Finland

Reviewers Professor Yujing Liu
Department of Electric Power Engineering
Chalmers University of Technology
Sweden

Professor Anouar Belachen
Department of Electrical Engineering and Automation
Aalto University
Finland

Opponents Professor Yujing Liu
Department of Electric Power Engineering
Chalmers University of Technology
Sweden

Professor Anouar Belachen
Department of Electrical Engineering and Automation
Aalto University
Finland

ISBN 978-952-335-506-4
ISBN 978-952-335-507-1 (PDF)
ISSN-L 1456-4491
ISSN 1456-4491

Lappeenranta–Lahti University of Technology LUT
LUT University Press 2020

Abstract

Chong Di
Modeling and Analysis of a High-Speed Solid-Rotor Induction Machine
Lappeenranta 2020
72 pages
Acta Universitatis Lappeenrantaensis 902
Diss. Lappeenranta–Lahti University of Technology LUT
ISBN 978-952-335-506-4, ISBN 978-952-335-507-1 (PDF), ISSN-L 1456-4491, ISSN 1456-4491

Over the last few decades, high-speed electrical machines have become more popular than ever before because of the rapid development of power electronics, magnetic materials, and control engineering. Among all the machine types, the solid-rotor induction machine (IM) has the greatest potential to rotate with the highest rotor peripheral speed. Therefore, this doctoral dissertation focuses on the high-speed solid-rotor IM, contributing to modeling of the solid-rotor IM, extraction of solid-rotor eddy-current harmonic losses, and mitigation of current unbalance caused by the asymmetric winding arrangement.

Because of its high accuracy, the Finite Element Analysis (FEA) is well appreciated in the electrical machine design. Nevertheless, the FEA transient magnetic (TM) solution is sometimes too time consuming, especially for the IM analysis. The situation is even worse when it comes to the solid-rotor IM. The doctoral dissertation introduces a potential approach to accelerate the TM analysis of IMs, implemented by reducing the stator and rotor electromagnetic time constants and shown to be more efficient than the traditional direct transient method.

The rotor eddy-current losses are a significant factor in the solid-rotor IM design. To efficiently mitigate the losses, it is of paramount importance to first fully understand the generation of losses and extract the harmonic losses from the total rotor losses. In this doctoral dissertation, the 2D fast Fourier transform was employed to extract the harmonics of the air-gap flux density. Then, all the important harmonics were rebuilt by a special setting in the air gap with the FEA to excite the solid rotor alone, which finally extracted the solid-rotor eddy-current harmonic losses successfully.

To achieve the stator winding installation with prefabricated coils, it was decided to apply an asymmetric winding arrangement in the electromagnetic design stage. Nevertheless, this solution produced some inherent stator leakage inductance unbalance. A novel winding coil arrangement was introduced to mitigate the current unbalance. The stator inductance was adjusted by placing coils in a different position in each slot. The final coil arrangement yielded a much more balanced three-phase stator current after the optimization.

Keywords: High-speed solid-rotor induction machine (IM), finite element analysis (FEA), electromagnetic time constant, eddy-current losses, asymmetric winding

Acknowledgments

The research work linked to this doctoral dissertation was conducted at the Department of Electrical Engineering, School of Energy Systems, Lappeenranta–Lahti University of Technology LUT, Finland, between 2017 and 2020. The research was funded by a China Scholarship Council (CSC) scholarship and from a project to develop multimegawatt (MMW) range high-speed machines funded by the Regional Council of South Karelia.

I would like to express my gratitude to my first supervisor Professor Juha Pyrhönen for his patient guidance. His great research experience, smart ideas, and interesting tasks made my research work much easier. His intelligence in the field of electrical machine design helps me to improve my knowledge to a higher level. I would also like to thank my second supervisor Dr. Ilya Petrov for his continuous support for the research. With his rigorous attitude toward research, he is a very good example for me to follow. First and foremost, in addition to theoretical knowledge, the daily academic discussions with him have taught me practical knowledge of electrical machine design. I would also like to show my respect for both of my supervisors again for not only providing knowledge, ideas, and suggestions, but also for their attitude toward both life and science, which will benefit me a lot in the future.

Special thanks are reserved to Associate Professor Pia Lindh for her efforts to arrange my doctoral studies at LUT. The academic research cooperation with her also strengthens my experience in the field of electrical machine design. I would also like to thank Associate Professor Janne Nerg for the guidance in numerical analysis.

I express my gratitude to Associate Professor Hanna Niemelä for the English language review of my publications and this doctoral dissertation. My English has improved significantly by following her professional comments and advice.

I am grateful to all my colleagues Valerii Abramenko, Dmitry Egorov, Hannu Kärkkäinen, Minhaj Zaheer, and Alvaro Hoffer for academic discussions and sharing ideas with me.

I would like to extend my thanks to all my friends from Lappeenrannan Skruuvi Kerho. The weekly training has helped me a lot to relax and release my mind from the study.

I would also like to thank Professor Xiaohua Bao at Hefei University of Technology, China, for his support for my doctoral studies.

Finally, I would like to express my deepest gratitude to my parents and grandmother for their continuous support and encouragement.

Chong Di
April 2020
Lappeenranta, Finland

Contents

List of publications

Publication I

Di, C., Petrov, I., Pyrhönen, J., and Chen, J., "Accelerating the Time-Stepping Finite-Element Analysis of Induction Machines in Transient-Magnetic Solutions," *IEEE Access*, vol. 7, pp. 122251–122260, 2019.

Publication II

Di, C., Petrov, I., and Pyrhönen, J., "Extraction of Rotor Eddy-Current Harmonic Losses in High-Speed Solid-Rotor Induction Machines by an Improved Virtual Permanent Magnet Harmonic Machine Model," *IEEE Access*, vol. 7, pp. 27746–27755, 2019.

Publication III

Di, C., Petrov, I., and Pyrhönen, J., "Modeling and Mitigation of Rotor Eddy-Current Losses in High-Speed Solid-Rotor Induction Machines by a Virtual Permanent Magnet Harmonic Machine," *IEEE Transactions on Magnetics*, vol. 54, no. 12, pp. 1–12, Dec. 2018.

Publication IV

Di, C., Petrov, I., and Pyrhönen, J., "Design of a High-Speed Solid-Rotor Induction Machine with an Asymmetric Winding and Suppression of the Current Unbalance by Special Coil Arrangements," *IEEE Access*, vol. 7, pp. 83175–83186, 2019.

Publication V

Di, C., Petrov, I., Pyrhönen, J., and Bao, X., "Unbalanced Magnetic Pull Compensation With Active Magnetic Bearings in a 2 MW High-Speed Induction Machine by FEM," *IEEE Transactions on Magnetics*, vol. 54, no. 8, pp. 1–13, Aug. 2018.

Publication VI

Kurvinen, E., Di, C., Petrov, I., Jastrzebski, R. P., Kepsu, D., and Pyrhönen, J., "Comparison of the Performance of Different Asynchronous Solid-Rotor Constructions in a Megawatt-Range High-Speed Induction Motor," *in 2019 IEEE International Electric Machines & Drives Conference, IEMDC 2019*, pp. 820–825, May 2019.

Author's contribution

In **Publication I**, the author of this doctoral dissertation proposed the simulation model in the FEA to accelerate the time-stepping finite-element analysis of induction machines

and conducted the simulations based on the coauthors' ideas and suggestions. He wrote the first draft and was also the corresponding author of the publication.

In **Publications II and III**, the author of this doctoral dissertation proposed the original idea of extracting the harmonic losses from the total solid-rotor eddy-current losses, and the idea was further improved based on the coauthors' suggestions. He wrote the first draft and was also the corresponding author of the publications.

In **Publication IV**, the author of this doctoral dissertation conducted the modeling and simulations of the high-speed machine based on the coauthors' original idea. In the course of the simulations, the author of this doctoral dissertation further improved the original idea, thereby enhancing the electromagnetic performance of the model. He wrote the first draft and was also the corresponding author of the publication.

In **Publication V**, the author of this doctoral dissertation analyzed the model of the machine in eccentricity conditions and found the detailed approach to compensate the unbalanced magnetic pull caused by the rotor eccentricity fault, based on the original idea proposed by the coauthors. He wrote the first draft and was also the corresponding author of the publication.

In **Publication VI**, the original idea of comparing the machine performance with different solid-rotor structures was proposed by Dr. Emil Kurvinen. The author of this doctoral dissertation was responsible for the electromagnetic simulations of the induction machines.

Nomenclature

Latin alphabet

a	Number of parallel branches	–
$\underline{a}$	Phasor operator ($1\angle 120°$)	–
B	Flux density	T
$\widehat{B}$	Amplitude of the flux density	T
B_{eq}	Equivalent flux density	T
$\widehat{B}_n$	Amplitude of the n^{th} air-gap flux density in the stator core	T
$\widehat{B}_\nu$	Amplitude of the ν^{th} air-gap flux density	T
b_{02}	Rotor slit width	m
D_{s}	Stator inner diameter	m
D_{se}	Stator outer diameter	m
D_{r}	Rotor outer diameter	m
E_2	Rotor-induced voltage	V
f	Supply frequency	Hz
f_{N}	Rated supply frequency	Hz
f_n	Frequency of the n^{th} alternating flux in the stator core	Hz
f_ν	Stator current frequency induced by the ν^{th} air-gap flux density	Hz
H	Magnetic strength	A/m
$\widehat{H}$	Amplitude of the magnetic strength	A/m
H	Heaviside step function	–
H_{eq}	Equivalent magnetic strength	A/m
h_{22}	Rotor slit depth	m
I	Stator phase or line current	A
$\underline{I}$	Stator phase or line current phasor	A
$\underline{I}_{\mathrm{PS}}$	Positive-sequence current	A
I_{N}	Rated current	A
$\underline{I}_{\mathrm{NS}}$	Negative-sequence current	A
I'_{r}	Rotor current referred to the stator coordinates	A
$\underline{I}_{\mathrm{ZS}}$	Zero-sequence current	A
J_{Z}	The rotor eddy-current density in the z direction	$\mathrm{A/m^2}$
k	Positive integer	–
k_{ec}	Coefficient of classic eddy-current losses	$\mathrm{W/(T/s)^2/m^3}$
k_{exc}	Coefficient of excess losses	$\mathrm{W/(T/s)^{1.5}/m^3}$
k_{hys}	Coefficient of hysteresis losses	$\mathrm{Ws/T^2/m^3}$
L_{m}	Magnetizing inductance	H
$L'_{\mathrm{r}\sigma}$	Rotor leakage inductance referred to the stator coordinates	H
$L_{\mathrm{s}\sigma}$	Stator leakage inductance	H
l	Stack physical iron length	m
l_{ef}	Stack active iron length	m
N_{s}	Number of turns in series per phase	–
n_{r}	Rotor rotational speed	r/min

n_{syn}	Synchronous speed	r/min
P_1	Solid-rotor eddy-current losses of Model 1	W
P_2	Solid-rotor eddy-current losses of Model 2	W
P_{ec}	Classic eddy-current losses	W
P_{eddy}	Rotor eddy-current losses	W
P_{exc}	Excess losses	W
P_{Fe}	Stator core losses	W
P_{fit}	Fitted stator core losses	W
P_{hys}	Hysteresis losses	W
P_N	Rated power	W
P_{test}	Tested stator core losses	W
P_ν	Solid-rotor eddy-current losses caused by the ν^{th} air-gap flux density	W
p	Number of pole pairs	–
Q_s	Number of stator slots	–
Q_r	Number of rotor slots	–
R_{Fe}	Stator iron losses equivalent resistance	Ω
R'_r	Rotor resistance referred to the stator coordinates	Ω
R_{ring}	Rotor end ring resistance	Ω
R_s	Stator winding resistance	Ω
s	Per-unit slip	–
s_N	Rated per-unit slip	–
T_N	Rated torque	Nm
t	Time	s
t_s	Excitation switching time	s
U_C	Voltage drop of the current source	V
U_N	Rated voltage	V
U_s	Stator supply voltage	V
U_V	Voltage drop of the voltage source	V
$\widehat{U}_V$	Voltage amplitude of the voltage source	V
W	Short pitching measured by the number of stator slots	–
$Z_{r,linear}$	Rotor impedance calculated based on the linear material theory	–
$Z_{r,nonlinear}$	Rotor impedance calculated based on the nonlinear material theory	–

Greek alphabet

Γ	Stator core area in the 2D domain FEM	–
Δt	Time step in the FEM	s
δ_ν	Penetration depth caused by the ν^{th} air-gap flux density	mm
θ	Stator mechanical position	°
μ_0	Permeability of vacuum	H/m
μ_r	Relative permeability	–
ν	Harmonic order	–
Σ	Rotor core area in the 2D domain FEM	–
σ	Conductivity of the material	S/m
τ_p	Pole pitch measured by the number of stator slots	–

τ_r	Rotor electromagnetic time constant	s
$\tau_{r,m}$	Modified rotor electromagnetic time constant	s
τ_s	Stator electromagnetic time constant	s
φ_0	Initial phase of the voltage source	rad
φ_v	Initial phase of the the v^{th} air-gap flux density	rad
Ω_r	Rotor angular speed	rad/s
Ω_v	Angular speed of the v^{th} air-gap flux density	rad/s
ω	Electrical angular frequency	rad/s
ω_r	Rotor electrical angular frequency	rad/s

Abbreviations

2D	Two-dimensional
3D	Three-dimensional
CUF	Current unbalance factor
CUR	Current unbalance ratio
DC	Direct current
IM	Induction machine
IPM	Interior permanent magnet
FEA	Finite element analysis
FEM	Finite element method
LS	Loss surface
MS	Magneto static
NS	Negative-sequence
OEM	Original equipment manufacturer
PMSM	Permanent magnet synchronous machine
PS	Positive-sequence
SM	Synchronous machine
SPM	Surface-mounted permanent magnet
SRM	Switched reluctance machines
SynRM	Synchronous reluctance machines
TDM	Time decomposition method
TM	Transient magnetic
TH	Time harmonic
ZS	Zero-sequence

1 Introduction

The electromagnetic effect and electromagnetic induction were first discovered by a Danish physicist Hans Christian Ørsted and an English scientist Michael Faraday in 1820 and 1831 respectively. Ørsted's discovery was formulated into a law today known as Ampère's circuital law, and Faraday's experimental observations were developed into Faraday's law of induction [1], [2]. These two laws together with the Lorentz force are the basic principles for energy conversion in all electrical machines. Later in the 1860s, the classical electromagnetism was governed by the four partial differential equations formulated by James Clerk Maxwell [3]. These four equations are collectively known as Maxwell's equations, and they comprise Gauss's law, Gauss's law for magnetism, Faraday's law (Faraday's law of induction), and Ampère's law (Ampère's circuital law). However, Oliver Heaviside (1850–1925) further formulated the equations in the form we use nowadays. These laws along with the Lorentz force law gradually became the fundamentals of the design of an electrical machine, and the engineers have to follow them throughout the stages of machine design, including for instance magnetic circuit design, insulation design, and torque production [4]. Simultaneously with the development of the theory of electromagnetism, after the mid-19th century, DC machines, synchronous machines (SMs), permanent magnetic synchronous machines (PMSMs), induction machines (IMs), and synchronous reluctance machines (SynRMs) were invented. All these machine types accelerated and strengthened the development of electrical power industries. During that time, electric appliances started to replace steam engines, which opened the age of electricity. Finally, the Second Industrial Revolution started in the 1870s, followed by a significant improvement in the scale of production.

Since the Second Industrial Revolution, electrical generators have provided virtually all the electricity on Earth, and electrical machines have consumed a major share of electricity. Nowadays, electrical machines as the main power and drive sources have successfully penetrated into all human activities, such as industrial applications, agricultural processes, national defense, and daily life. Currently, electrical motors in different forms account for approximately 70% of the whole industrial energy consumption and 45% of the global electricity consumption [5].

In the 20th and 21st centuries, because of the rapid growth of modern industrial production and the resulting high demand for electricity, emissions into the atmosphere have become a serious problem. The main reason for this is that so far, the majority of electricity has been produced in fossil coal power plants. To reduce emissions, carbon-free electricity generation must be increased and the generated electricity must be used efficiently.

The efficiency improvement of electrical machines is of high significance, and there are many ways to increase the efficiency of electrical machines. Introduction of new materials, promotion of modern machine design technologies, and advancement of high efficiency standards are crucial steps towards this goal [6]–[8].

One of the promising design technologies that has been under research over the recent decades is the high-speed machines. Their increased popularity in industry can be explained by their high power density and high efficiency, especially in processes that inherently require high rotational speeds. High-speed machines also require less materials (e.g. copper, electromagnetic steel sheets, cast iron, molded steel) compared with traditional machines. Consequently, the design and manufacturing of high-speed electrical machines is highly appreciated in cases where designers can take advantage of high-speed technologies. High-speed machines are already widely used in different original equipment manufacturer (OEM) applications, such as electric vehicles, flywheel energy storages, gas compressors, and turbomolecular pumps [9]–[12]. Thus, the design of high-speed electrical machines is still a highly relevant topic of academic research, typically involving multidiscipline and multiphysics analysis.

1.1 Review of high-speed electrical machines

Generally, there is no common definition of "high-speed" electrical machines, because the definition of high speed may vary depending on the power and size of the machine [13]. According to [14] and [15], electrical machines with a rotational speed higher than 10000 r/min and r/min$\sqrt{\text{kW}}$ higher than 1×10^5 fall into the "high speed" category.

In the last few decades, mainly three types of electrical machines were considered suitable for high-speed applications: IMs, PMSMs, and switched reluctance machines (SRMs). All of them have already been intensively studied and used in industrial applications [16]–[18]. Recently, SynRMs have become yet another suitable alternative in some special high-speed applications [19]–[20]. However, the former three electrical machine types have already been shown to work efficiently in high-speed systems and have a longer background of usage in high-speed industrial applications. Therefore, only the former three are discussed hereafter.

Typically, different rotor structures, which are primarily determined by the rotor material, peripheral speed, and power of the machine, are applied in different types of high-speed electrical machines. For IMs, the rotor core can be made of laminated electromagnetic steel (with cage winding) or solid structural steel (with or without cage winding and end rings). For PMSMs, the only choices available are the surface-mounted permanent magnet (SPM) rotor and the interior permanent magnet (IPM) rotor. Because of the strong centrifugal force during rotation, retaining sleeves with different materials are usually used to keep the magnets in place and maintain rotor robustness. For SRMs, the laminated salient pole rotor made from a vanadium-iron-cobalt material having high yield strength is highly appreciated [14].

Fig. 1.1 shows the rotor maximum peripheral speed achieved by different machine types and rotor structures, reported in [11] and [21]–[26]. It can be seen that the SRM has the lowest maximum rotor peripheral speed, about 200 m/s. This speed is roughly estimated because the rotor diameter is not given in the original document [14], [21]. The rotor in the SRM has the simplest structure with a relatively simple manufacturing process.

However, the drawback of the SRM is its special control topology, which should be developed individually for each machine design. Of different machine types, the SRM is considered to be among the most difficult ones to control. Moreover, the SRM has a higher noise and vibration level compared with other types of electrical machines, making it less suitable for certain applications.

Fig. 1.1 also shows that the rotor maximum peripheral speeds found in the literature for IPM-PMSMs and SPM-PMSMs are 233 m/s and 294 m/s respectively. In order to withstand the high rotational speeds, SiFe and titanium sleeves are employed for these two cases. The PMSM is capable of providing a very high rotational speed with almost the highest power (torque) density among all machine types (having the same rotational speed). A relatively simple control algorithm, high efficiency, and a high power factor are the other advantages of this machine type. However, the high cost of the permanent magnet material is one of the disadvantages of the PMSM. The risk of irreversible demagnetization of the magnet may also pose additional challenges for the PMSM design.

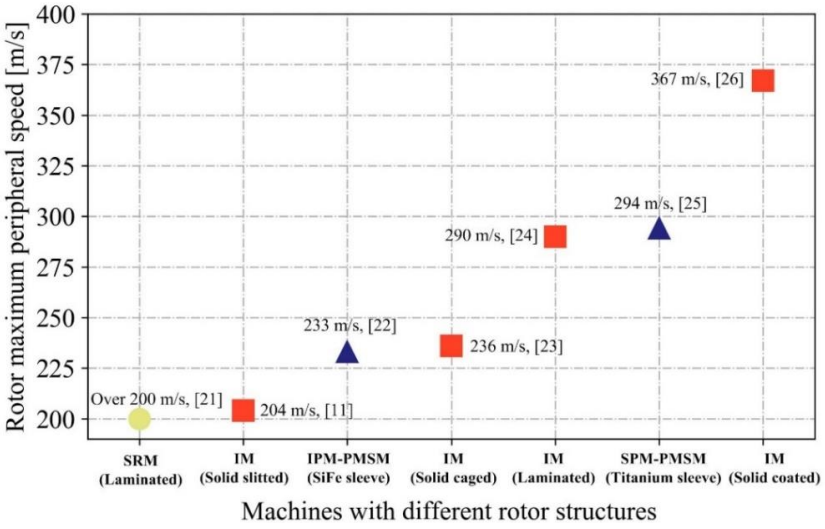

Fig. 1.1 Rotor maximum peripheral speed achieved by different machine types and rotor structures (data were originally collected and presented in [11] and [21]–[26]).

The rotor maximum peripheral speed for the IM varies in a large range depending on the rotor structure. The maximum speeds found are 204 m/s, 236 m/s, 290 m/s, and 367 m/s for a solid slitted rotor, a solid caged rotor, a laminated rotor, and a smooth solid coated rotor respectively. The smooth solid coated rotor IM can reach, in principle, the maximum possible rotor peripheral speed, yet the laminated rotor can also reach a very high peripheral speed of 290 m/s. It is still recommended in [16] and [23] that it is safer to use a solid rotor structure for the IM design at a higher peripheral speed. This means that when the highest rotor peripheral speed has to be achieved, a solid coated rotor IM is

required. However, the electromagnetic performance of this machine type is inferior to other types, which is due to the low power factor.

Table 1.1 provides a brief comparison of different machines in high-speed applications. The highest possible rotor peripheral speed, relatively simple manufacture, low cost, high reliability, and convenient maintenance properties are the main reasons for the popularity of IMs and their wide use in high-speed applications. This justifies the importance of research on the high-speed IM equipped with a solid rotor.

TABLE 1.1 COMPARISON OF DIFFERENT MACHINES IN HIGH-SPEED APPLICATIONS

Machine type	Rotor peripheral speed	Cost	Control	Noise	Manufacture
IM	High	Average	Complex	Average	Average
PMSM	Average	High	Average	Average	Difficult
SRM	Low	Low	Difficult	High	Easy

1.2 Overview of the main design of the high-speed solid-rotor IM

The high-speed IM studied in this dissertation is a 2-pole, 660 V, 2 MW, 12000 r/min high-speed IM, which has been reported in detail in **Publications III–V**. The main machine parameters are listed in Table 1.2. The solid slitted rotor is chosen as the rotor structure in this design because of the more robust rotor compared with the laminated rotor. The rotor peripheral speed at the nominal load is about 167 m/s. The machine is, however, also expected to be able to run at a slightly higher speed, as a result of which the maximum rotor peripheral speed may approach approx. 200 m/s. Consequently, the solid rotor is employed in the final version.

Slits are applied in the solid rotor because they strongly increase the torque-producing capability of the rotor and dampen the effects of higher-harmonic eddy currents on the rotor surface area, which could generate high losses on smooth surfaces. The mutual flux at the nominal load can hardly penetrate deep into the rotor yoke area if the smooth solid rotor is applied, which means that the rotor inner area cannot produce torque. To take full use of the rotor active material to generate torque, rotor slits are recommended in the literature found on practical applications [27]–[29]. The rotor slit dimensions should be optimized to allow the flux to penetrate deep into the rotor core. As a result, a smaller rated per-unit slip s can be obtained. Thus, slip-related rotor losses are reduced and the power factor becomes higher. In Table 1.2, the rotor slit width and slit depth are 4 mm and 50 mm respectively. The slit depth is about 38% of the solid-rotor radius, which is close to the recommendation of 40%–60% of the rotor radius to achieve the highest rotor efficiency [30], [31]. It is further suggested in [11] that the rotor slit depth should not exceed 50% of the rotor radius to guarantee the electromagnetically and mechanically reasonable performance of the machine.

TABLE 1.2 MAIN PARAMETERS OF THE HIGH-SPEED SOLID-ROTOR IM

Parameter	Value
Rated power P_N, [kW]	2000
Rated voltage U_N, [Vrms]	660
Number of pole pairs, p	1
Rated supply frequency f_N, [Hz]	200
Synchronous speed n_{syn}, [r/min]	12000
Stack physical iron length l, [mm]	563
Stack active length l_{ef}, [mm]	538
Stator inner diameter D_s, [mm]	280
Stator outer diameter D_{se}, [mm]	700
Rotor outer diameter D_r, [mm]	266
Rotor slit width b_{02}, [mm]	4
Rotor slit depth h_{22}, [mm]	50
Number of stator slots Q_s	36
Number of rotor slits Q_r	44
Number of turns in series per phase N_s	6
Number of parallel branches a	2
Winding connection	Delta
Winding type	Double layer
Short pitching W/τ_p	5/6
Stator lamination material	M270-35A
Solid rotor material	S355 (Fe52)

It is very important to understand the generation of rotor losses in the high-speed solid-rotor IM as it is not only related to the machine efficiency but also to the cooling system. There are many technologies available to cool the stator or the stator frame, such as forced air cooling, water jacket, and direct liquid cooling [32], [33]. Meanwhile, the approaches to cool the rotor are limited. Therefore, significant attention is paid to the mitigation of the rotor losses by all means. For a solid-rotor IM, an efficient way to reduce the rotor losses is to choose a correct rotor material to reduce the slip-related losses, which are directly associated with the fundamental of the air-gap flux density. Table 1.2 shows that the selected rotor material is S355 (Fe52), which is a compromise between the rotor losses and rotor robustness.

Fig. 1.2 illustrates the resistivity and tensile strength for several possible rotor materials; the corresponding data were originally collected and presented in [34]. To get lower solid rotor slip-related losses, a lower resistivity is always recommended. In Fig. 1.2(a), Fe52, C15, Fe-Cu, and Fe-Si (consumet) are qualified as suitable materials in terms of rotor losses. It is further shown in [34] that machines with these four materials can achieve a higher machine efficiency than the machines with other material types. Considering the tensile strength in Fig. 1.2(b), Fe52 is the most promising one among these rotor materials in terms of both electromagnetic and mechanical properties. Therefore, S355 (Fe52) is finally selected as the rotor material.

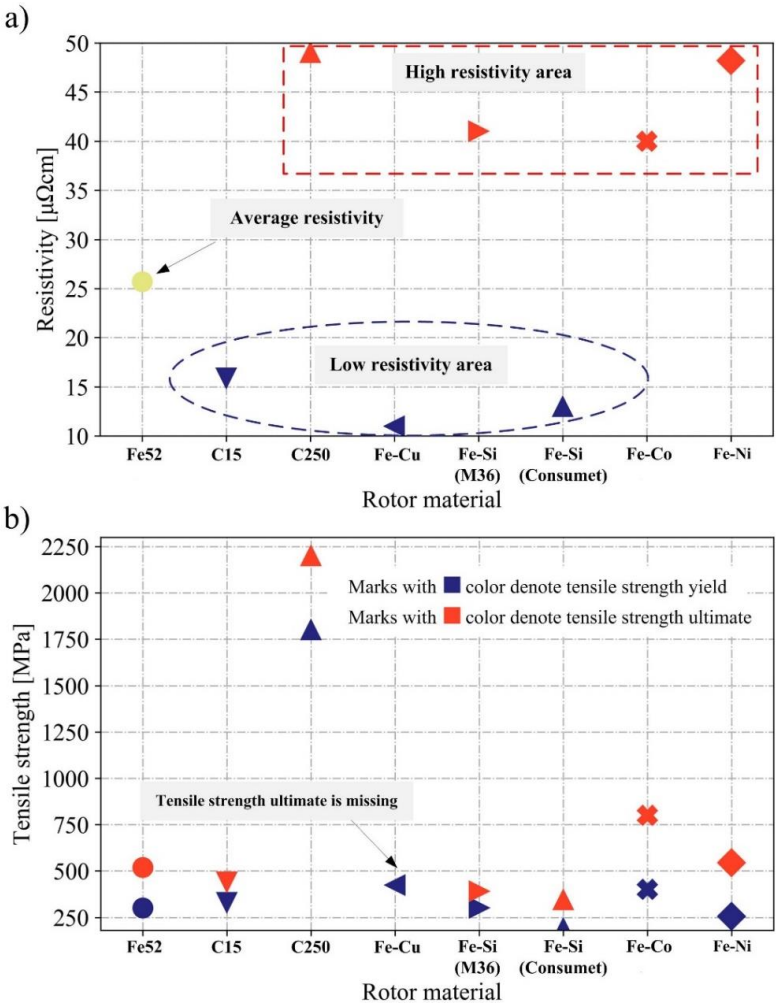

Fig. 1.2 Resistivity and tensile strength for some solid rotor materials at room temperature. (a) Resistivity varying with rotor materials. (b) Tensile strength varying with rotor materials (data were originally collected and presented in [34]).

Fig. 1.3 shows the finite element analysis (FEA) model in Altair Flux (2D) for the high-speed solid-rotor IM. The stator is designed and optimized to have a relatively large outer diameter (with a significant proportion of stator yoke) to achieve smaller stator core losses. The stator winding with a short pitching of 5/6 is aimed to eliminate the rotor eddy-current losses, which are generated by the $+5^{th}$ and -7^{th} stator winding harmonics. The purpose of the semimagnetic wedge is to mitigate the stator slot harmonics. Concurrently, to create the same amount of air-gap flux density as the machine without semimagnetic wedges, a smaller magnetizing current is needed, which means that by using semimagnetic wedges it is possible to achieve a higher efficiency (lower stator winding copper losses, lower rotor eddy-current harmonic losses). A more detailed discussion about the effects of semimagnetic wedges on the fundamental and harmonic rotor losses are presented in **Publication III**.

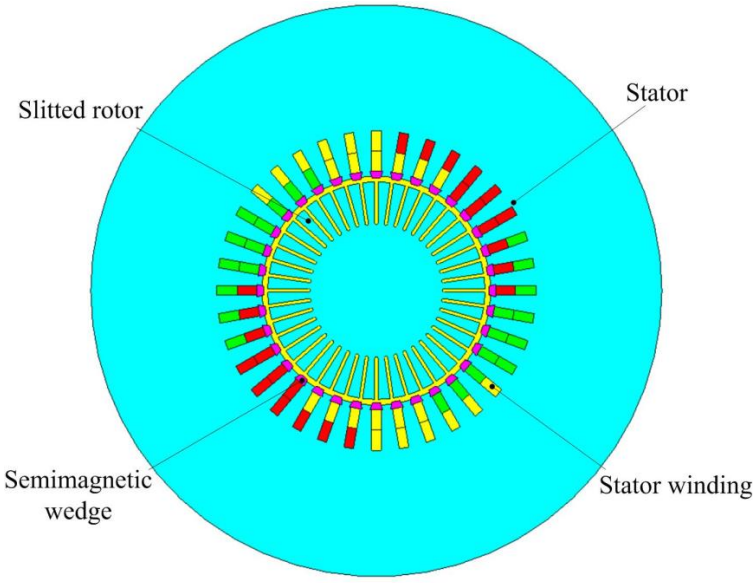

Fig. 1.3 High-speed solid-rotor IM model in Altair Flux (2D).

It is critical to correctly estimate the rotor end effect by the finite element method (FEM) in the electromagnetic analysis of the solid rotor. The rotor end effect not only affects the rotor resistance (described by the equivalent circuit), but also the rotor power factor [35]. In other words, a strong rotor end effect causes changes in the rotor impedance. There are two main approaches to modify the rotor impedance for a solid rotor in the design stage (using the FEM environment). One is to model the machine with the 3D FEM and the other one is to use some coefficients (estimated analytically) to correct the rotor impedance in the 2D FEM [11], [36]. However, both of these methods have their disadvantages. The 3D FEM model consumes too much computational resources, and because of the denser mesh and the smaller time step, it is even worse if the high-order harmonic effects have to be considered. The main drawback of the analytical method is

that it is difficult to consider the nonlinear rotor material property and impedance variation as function of rotor frequency.

Therefore, because of the too time-consuming 3D FEM simulation process and the inaccuracy of the analytical method, only the 2D FEM model is studied in this doctoral dissertation, yet the 3D trend in the optimization can still show useful results in the electromagnetic design stage. If the rotor end effect has to be considered, the results simulated in 2D can also be corrected by postprocessing based on the analytical method. For example, the rotor losses can be corrected by multiplying the end effect factor at the nominal load. Typically, the high-speed solid-rotor IM has a small per-unit slip at the nominal load, which means that the machine is most probably operating in the linear range on the torque–slip curve. Therefore, once the rotor resistivity is increased by the end effect factor, the per-unit slip will also be increased by the same ratio. This further indicates that the fundamental (slip) related solid rotor losses should also be corrected by the same means.

Fig. 1.4 shows the mesh setting in the solid rotor area. To take into account the induced rotor eddy currents generated by the harmonics of the air-gap flux density, a special rectangular mesh setting (6×18 elements, second-order mesh elements) is used in the rotor surface area (this mesh is a compromise between accuracy and speed). The depth of the mesh in the rotor surface area is estimated by the depth of penetration, which will be discussed further in Chapter 3. This kind of mesh setting is highly recommended in the Altair Flux official tutorial document, and at least two layers of elements should be applied within this depth.

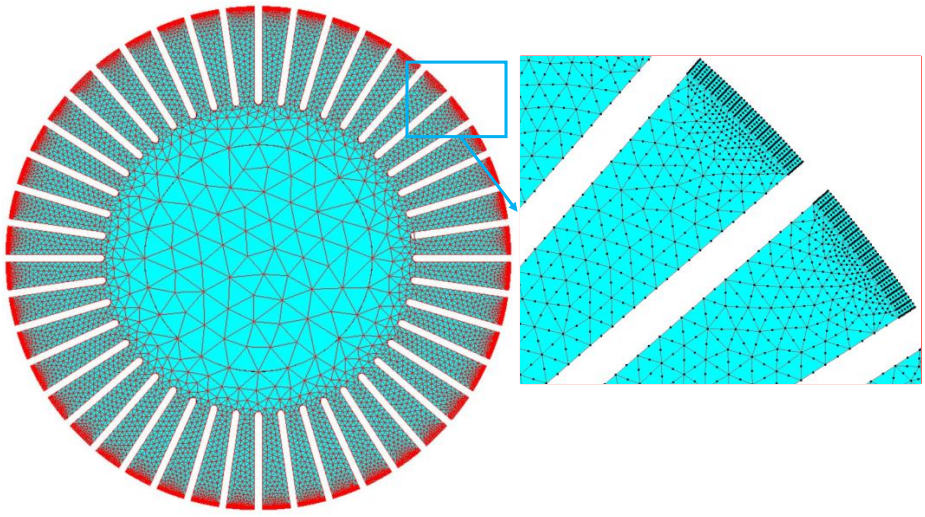

Fig. 1.4 Solid rotor mesh of the high-speed IM model in Altair Flux (2D).

Table 1.3 lists the main performance characteristics of the high-speed solid-rotor IM at the nominal load. The simulation is conducted by the Altair Flux 2D transient solver with

an imposed speed. The time step in the simulation is 5×10^{-5} s (100 points per electrical period). All the data in Table 1.3 are obtained at the simulation time of 0.4 s, which is close to the steady state. The full steady-state performance will be discussed in Chapter 2.

TABLE 1.3 MAIN PERFORMANCE CHARACTERISTICS OF THE HIGH-SPEED SOLID-ROTOR IM AT THE NOMINAL LOAD

Parameter	Value	Comment
Per-unit slip s_N at the nominal load	0.0046	Imposed speed
Output torque T_N, [Nm]	1598	1600 Nm is required
Stator line current I_N, [Arms]	2572	Three-phase average value
Power factor cosφ	0.69	Corrected based on **Publication IV**
Stator winding losses, [kW]	4.86	100°C, analytical method
Stator iron losses, [kW]	14.15	Bertotti model with harmonics
Solid rotor eddy-current losses, [kW]	22.97	Corrected, see Section 3.3
Mechanical losses (friction and windage), [kW]	10	0.5% of the nominal load power
Extra losses, [kW]	10	0.5% of the nominal load power
Total losses, [kW]	61.98	
Efficiency, [%]	96.90	

In Table 1.3, the stator winding Joule losses are calculated by the analytical method and the stator core losses are estimated during postprocessing by the modified Bertotti's loss model in considering harmonics, which can be expressed in the stator area Γ in the 2D domain as [37], [38]:

$$\begin{aligned} P_{\mathrm{Fe}} &= \int_{\Gamma} (P_{\mathrm{hys}} + P_{\mathrm{ec}} + P_{\mathrm{exc}}) \mathrm{d}\Gamma \cdot l_{\mathrm{ef}} \\ &= \int_{\Gamma} \sum_{n=1}^{N} \left[k_{\mathrm{hys}} f_n \hat{B}_n^2 + k_{\mathrm{ec}} \left(f_n \hat{B}_n \right)^2 + k_{\mathrm{exc}} \left(f_n \hat{B}_n \right)^{1.5} \right] \mathrm{d}\Gamma \cdot l_{\mathrm{ef}} \end{aligned}, \quad (1)$$

where P_{hys}, P_{ec}, and P_{exc} denote the hysteresis losses, classical eddy-current losses, and excess losses respectively, k_{hys}, k_{ec}, and k_{exc} are the corresponding loss coefficients, f_n is the frequency of the n^{th} alternating flux, and $\hat{B}_n$ is the peak value of the n^{th} flux density (B_n) in the stator core.

The core loss coefficients are estimated by fitting the tested multi-frequency *B-P* curves of the stator material (M270-35) with the analytical equation. Multi-frequency *B-P* curves are used instead of the single-frequency *B-P* curve because the fitted coefficients are also suitable for the harmonic loss calculation. The coefficients are optimum results, when the minimum square of the difference between the fitted curves and the tested curves is achieved. The criterion is written as follows [39]:

$$err(k_{\mathrm{hyst}},\ k_{\mathrm{ec}},\ k_{\mathrm{exc}}) = \sum_i (P_{\mathrm{fit},i} - P_{\mathrm{test},i})^2 = min\ , \tag{2}$$

where $P_{\mathrm{fit},i}$ and $P_{\mathrm{test},i}$ are the i^{th} points on the fitted and tested *B-P* curves. The measured and fitted *B-P* curves are shown in Fig. 1.5. It can be seen that the fitted curves stay very close to the measured curves at 100 Hz, 200 Hz, and 400 Hz. As a result, the coefficients k_{hyst}, k_{ec}, and k_{exc} are 213.95, 0.33, and 0.

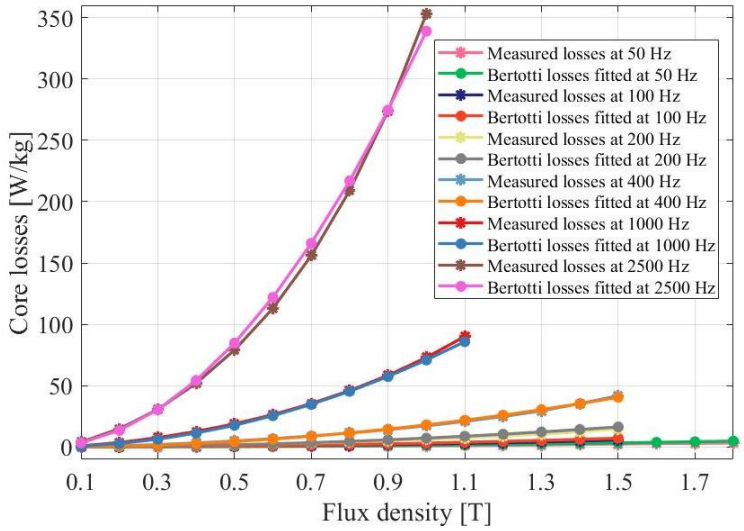

Fig. 1.5 Comparison of the measured and Bertotti losses (curve fitted) as a function of flux density at different frequencies.

According to Equation (1), to estimate the core losses, it is important to calculate the peak value $\widehat{B}_n$ of the n^{th} flux density B_n in the stator core. To solve this problem, the flux density B at each node of the finite element model is decomposed into B_x and B_y in the x-y Cartesian coordinate system. After that, $\widehat{B}_n$ can be obtained by the harmonic components from B_x and B_y calculated by the Fourier transform.

Fig. 1.6 shows the total core loss density distribution in each element in the stator region at the nominal load. The flux density harmonics up to 2500 Hz are considered because the original measured *B-P* curves are available up to 2500 Hz (theoretically, the harmonics up to 10000 Hz can be considered with a 20000 Hz sampling frequency). It

can be seen in the figure that the stator tooth region suffers a higher core loss density compared with the stator yoke region. This is explained by the fact that there is a clearly higher flux density in the stator tooth region than in the stator yoke. The teeth flux density is also modulated by the rotor slitting. The stator yoke is designed with large dimensions, and as a result, the stator yoke is operating at a moderate flux density.

Consequently, core losses estimated by Equation (1) are about 14.15 kW when considering harmonics as discussed above. For comparison, core losses are also estimated by the loss surface (LS) model. The LS model is a dynamic hysteresis model, which requires a well-defined magnetic behavior obtained by experiments. The embedded solution of the LS model in Altair Flux is applied; the solution is discussed in more detail in [37]. The losses estimated by the LS model are about 13.84 kW. The difference is only about 2%, which means that Bertotti's loss model for harmonics is acceptable.

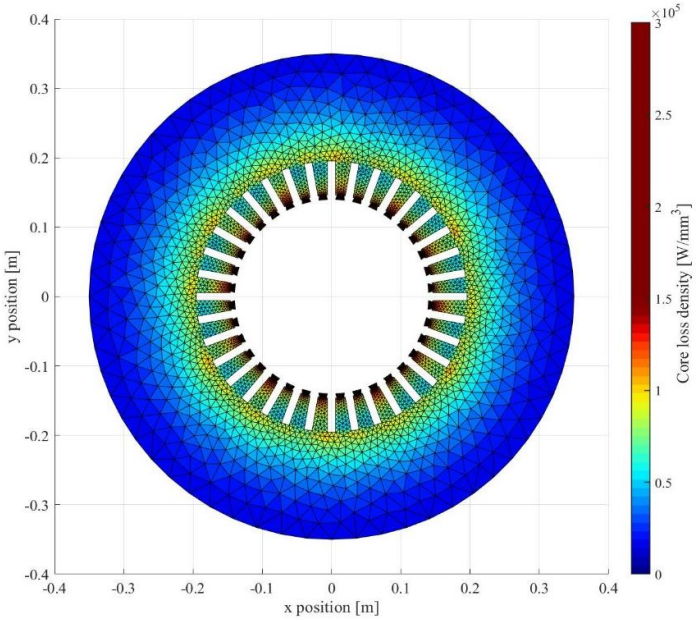

Fig. 1.6 Core loss density distribution at the nominal load taking flux density harmonics up to 2500 Hz into consideration.

The solid rotor eddy-current losses in Table 1.3 considering all the harmonic effects are calculated in the rotor area Σ in the 2D domain as presented in **Publication III** and [40]:

$$P_{\text{eddy}} = \int_{\Sigma} \frac{J_{\text{Z}}^2}{\sigma} \mathrm{d}\Sigma \cdot l_{\text{ef}}, \tag{3}$$

where J_{Z} is the induced eddy-current density in the solid-rotor area, and σ is the conductivity of the solid-rotor material.

The mechanical losses are about 5.4 kW (0.27% of the nominal load power) calculated by the analytical equations reported in [4] and [30]. Finally, however, 10 kW of mechanical losses were predicted because of the safety reserve during the design stage.

Fig. 1.7 shows both the flux line and flux density distributions at the nominal load. The stator is not very saturated because of the large stator outer diameter (the stator yoke occupies a significant region). Therefore, the stator iron losses are moderate. It can be also seen in the figure that almost the whole rotor is highly saturated and the flux penetrates deep into the rotor. This is partially due to the correct optimization of the rotor slit width and depth.

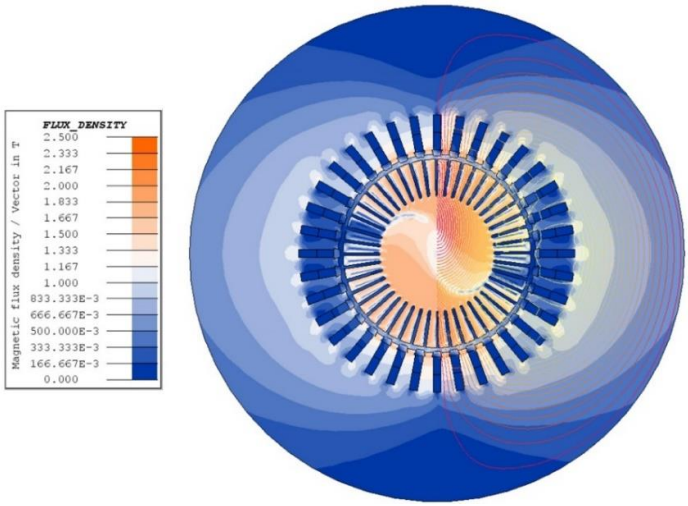

Fig. 1.7 Flux line and flux density distributions at the nominal load. The flux penetrates well into the rotor core at per-unit slip s = 0.005, which means that the rotor is well designed.

In addition, the solid rotor is highly saturated, as it is shown in Fig. 1.7. This results in a higher rotor power factor. According to the theoretical analysis, the rotor impedance angle varies in the range from 26.6° to 45° (the rotor impedances are proportional to 1+j and 2+j respectively) depending on the rotor saturation, as a result of which the rotor power factor varies between 0.707 and 0.894 [11], [30]. These two analytical rotor impedances are calculated based on the linear material theory (pure linear *B*-*H* curve) and Agarwal's limiting nonlinear theory (rectangular *B*-*H* curve) respectively. They are expressed as follows:

$$\begin{cases} Z_{\mathrm{r,linear}} = (1+j)\sqrt{\dfrac{\omega_{\mathrm{r}}\mu}{2\sigma}} \\ Z_{\mathrm{r,nonlinear}} = (2+j)\dfrac{8}{3\pi\sigma\delta} \end{cases}, \tag{4}$$

where ω_r is the rotor electrical angular frequency, μ is the permeability of the rotor material, and δ is the penetration depth.

Fig. 1.8 shows the air-gap flux density curve at the nominal load and its spectrum analysis results. It can be seen in Fig. 1.8(a) that the waveform is similar to a pure sinusoidal curve. Some strong ripple, which is mainly caused by the slotting effect, is also shown in the waveform. Fig. 1.8(b) shows the spatial spectrum by a traditional fast Fourier transform. A more accurate time and spatial spectrum will be presented in Chapter 3. This figure shows that the winding harmonics, especially the $+5^{th}$ and -7^{th} harmonics, are successfully suppressed by the short pitch winding. The first-order stator slot harmonics, the $+35^{th}$ (0.0151 T) and -37^{th} (0.0128 T), are mitigated by semimagnetic wedges. The first-order rotor slot harmonics, the $+43^{rd}$ (0.0348 T) and -45^{th} (0.0458 T), have higher amplitudes compared with other harmonics because of the 4 mm rotor slit opening. Although these rotor-related harmonics may cause extra losses in the stator lamination, they do not generate any extra losses on the rotor side. However, the main attention is paid to mitigate the rotor losses, as it is easier to cool the stator lamination and the stator frame.

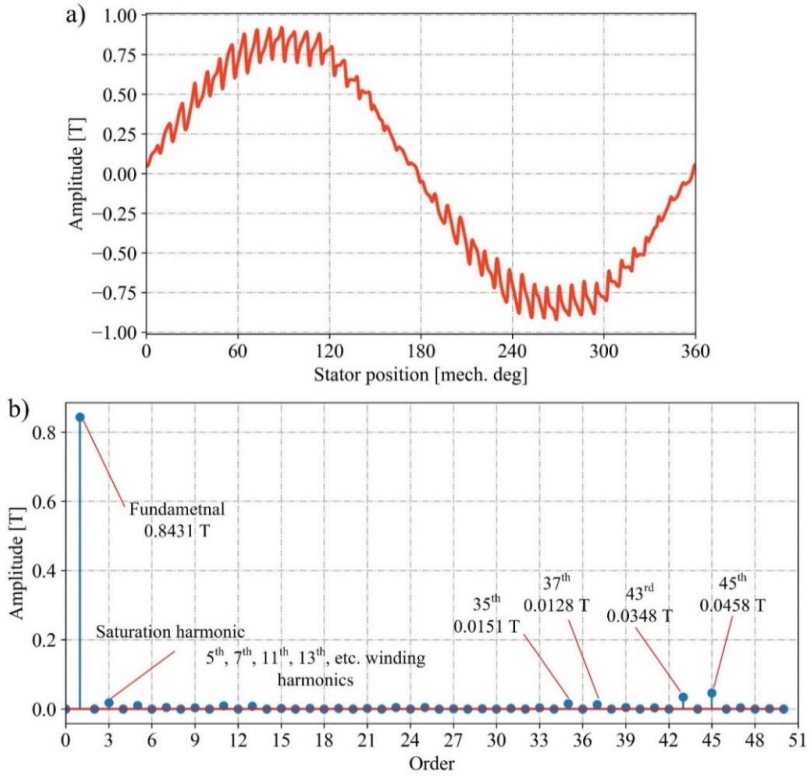

Fig. 1.8 Air-gap flux density curve and its spatial spectrum of the high-speed IM at the nominal load. (a) Air-gap flux density waveform. (b) Spatial spectrum by a traditional fast Fourier transform (adapted from **Publication III**).

1.3 Outline and scientific contribution

The doctoral dissertation focuses on the modeling and analysis of the high-speed solid-rotor IM. The study covers three main topics; modeling with the fast transient simulation by the FEM, extraction of solid-rotor eddy-current harmonic losses, and suppression of the unbalanced current. The introductory section of the dissertation consists of five chapters related to six publications, the main content and contributions of which are as follows:

- Chapter 1 provides a literature review of the research topic and presents the main design of the high-speed solid-rotor IM. The chapter starts with the history and development of the classical electromagnetism. Significant research into the design of a high-speed solid-rotor IM is also reviewed, with the focus on the following aspects: rotor material, rotor slits, end effect, and modeling. Further, the high-speed solid-rotor IM design is discussed with the main parameters and operation data. This chapter is linked with **Publications V** and **VI**.

- Chapter 2 studies the opportunity of accelerating the transient simulation with a voltage supply by the FEM. The proposed method is based on reducing the stator and rotor electromagnetic time constants, which are the main reasons for the relatively long electromagnetic transient in IMs. The method is implemented by a locked rotor model (to reduce the rotor electromagnetic time constant) and an adjustable supply source (to reduce the stator electromagnetic time constant). This chapter is linked with **Publication I**.

- Chapter 3 concentrates on the extraction of the solid-rotor eddy-current harmonics by the FEM. First, the air-gap flux density harmonics are analyzed by a 2D fast Fourier transform. In that way, both the time and spatial properties can be analyzed more accurately compared with the traditional fast Fourier transform. Then, the rotor harmonic losses are extracted by producing the same harmonic in the air gap. The rotor saturation is also modeled by fundamental excitation in the air gap. The proposed method is capable of extracting not only the harmonic losses, but also other electromagnetic phenomena. This chapter is linked with **Publications II** and **III**.

- Chapter 4 investigates the option to suppress the unbalanced current in the high-speed solid-rotor IM. The current unbalance is caused by the asymmetric winding, which is made of prefabricated coils. The unbalance can cause some adverse effects for the machine performance, such as extra losses, unbalanced magnetic pull, and extra electromagnetic noise. A special winding arrangement is proposed in this study to balance the currents as precisely as possible. The coils in different slots are placed in different slot positions to adjust the inductances for different phases. Consequently, the current unbalance situation is mitigated. This chapter is linked with **Publication IV**.

- Chapter 5 concludes the doctoral dissertation and presents the research results. In addition, the chapter also suggests some directions for further work on the modeling and design of the high-speed solid-rotor IM.

The contributions of this doctoral dissertation are as follows:

- A new approach is proposed to expedite the solid-rotor IM simulation in the FEM compared with the traditional solution. The method is capable of taking into account the nonlinear material properties (as in the traditional FEM simulation approaches), and the model is specifically designed for voltage-driven cases.

- A novel method is proposed to extract the electromagnetic performance caused by the harmonics from the total performance of the electrical machine. Investigation of the solid-rotor harmonic losses is chosen as an example for introducing the proposed method. This method has the potential to be further developed and employed in other applications where harmonic phenomena are involved.

- Without any extra investments in the power electronic devices, the dissertation puts forward a different solution to mitigate the current unbalance resulting from the inherent inductance unbalance of the asymmetric winding. The three-phase stator winding inductance is corrected by placing the conductors in a different position in the stator slots.

2 Accelerating the numerical transient in IM simulations

Finite element analysis (FEA) is widely applied in many disciplines, especially in different fields of engineering. In the past few decades, the FEA has become an important and viable tool in the electrical machine design. Applications using FEA tools in the electrical machine design have been reported in [41]–[44], where most of the machine types are mentioned.

Typically, there are three types of solvers for the electromagnetic FEA: the magneto static (MS) solver, the time harmonic (TH) solver, and the transient magnetic (TM) solver. They are suitable for different applications; a comparison of these three solvers for electrical machine modeling in the FEA is provided in Table 2.1. The MS and TH solvers are very fast, but both have limitations of their own. The MS solver cannot model the induced eddy currents, which means that it is not suitable for IM modeling, excluding simple evaluation of no-load operation. In the TH solver, only linear material (or linearized material) can be used, which means that the solver is not able to consider the high-order harmonic behavior in full detail. The TM solvers are the most expensive ones and suitable for all machine types. However, the use of the TM solver may take a significant computation time before reaching the steady state for IM modeling. Therefore, a feasible method should be applied to reduce the computation time while performing the analysis of an IM using a numerical solution.

TABLE 2.1 COMPARISON OF MS, TH, AND TM SOLVERS FOR ELECTRICAL MACHINE MODELING IN THE FEA

Solver type	Speed	Usage range	Comment
Magneto static	Fast	PMSM, SynRM	Induced eddy currents are ignored.
Time harmonic	Fast	IM	Linear material properties; Motion, and harmonics are ignored.
Transient magnetic	Low	All machine types	The most expensive one; Requires a significant time and computational resources.

2.1 Overview of approaches to accelerate the numerical transient

The simulation time with a TM solver for a high-speed solid-rotor IM is even longer than with the traditional squirrel-cage IM, because the solid-rotor can be regarded as a strong damper (similar to a large-inductance load in an electrical circuit). There are some methods available to accelerate the numerical transient for IM simulation. Some of them are based on applying a full computational resource available, such as parallel and distributed computation, or the time decomposition method (TDM), which are reported in [45]–[47]. These solutions are universal and suitable for all kinds of FEA. However, the drawback of the approach for reducing the computational time is also obvious, as the simulation speed highly depends on the computer performance.

There are some other methods to accelerate the numerical transient by adjusting the physical properties of the machine. To be more specific, for an IM analysis with the TM solution, a fast simulation can be implemented by reducing or eliminating the electromagnetic time constants, which are, in principle, the main source of the electromagnetic transient condition in the FEA. Some possible approaches to accelerate the numerical transient in the case of IM simulation are listed and compared in Table 2.2. It can be seen in the table that both the alternating flux linkage model and the phase balancing method aim at mitigating the transient by suppressing the electromagnetic behavior caused by a slowly attenuating DC component. They are not suitable for solving the problems when eddy-current effects are involved.

TABLE 2.2 COMPARISON OF THREE APPROACHES TO ACCELERATE THE NUMERICAL TRANSIENT IN IM SIMULATIONS

Approach	Main principle	Limitation	Reference
Alternating flux linkage model	Eliminate the DC flux linkage	Eddy-current effects are ignored	[48]
Phase balancing method	Eliminate the DC current at each step	Eddy-current effects are ignored	[49]
TM solution initialized with proper initial values	Create a proper initial condition	The speed is affected by the material.	[50]

The TM solution initialized with proper initial values (e.g. initial values provided by the TH solution) is suitable for the solid-rotor IM simulation. However, the transient condition of this method is sometimes still quite long, and it is affected by the material properties. The reason for this is that the TH solution can use only a linear (or equivalent) material property for creating the initial condition for the TM simulation. Therefore, there may be significant differences between the initial electromagnetic condition (derived by the TH) and the final steady-state electromagnetic condition after completing the TM simulation. Fig. 2.1 shows the flux density distributions by TM and TH solvers. These differences can cause subtransients in the TM solution.

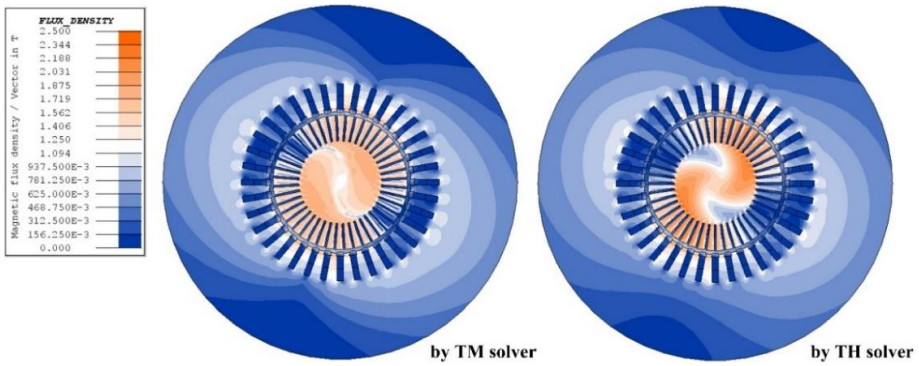

Fig. 2.1 Comparison of the flux density distributions in the steady state by TM and TH solvers (adapted from **Publication I**).

Fig. 2.2 shows the three-phase line current and torque curves during the transient as a function of time at the nominal load by the traditional direct TM method. It can be seen in Fig. 2.2(a) that the stator line current has a high amplitude before 0.1 s, after which the current attenuates. The current reaches a steady state quickly because the stator winding resistance and the stator leakage inductance are modified to achieve a smaller stator electromagnetic time constant, which enables the simulation to reach the steady state faster. In the simulation shown in Fig. 2.2, the stator winding resistance is 0.01 Ω (7.35×10^{-4} Ω in **Publication IV**) and the stator leakage inductance is 1×10^{-7} H (3.5×10^{-5} H in **Publication IV**) per phase, which means that the stator electromagnetic time constant has already been modified to a small value. Therefore, the power factor is actually slightly higher (0.72) than expected, and it is further corrected based on the calculation in **Publication IV** with slightly different mesh settings, which are listed in Table 1.3.

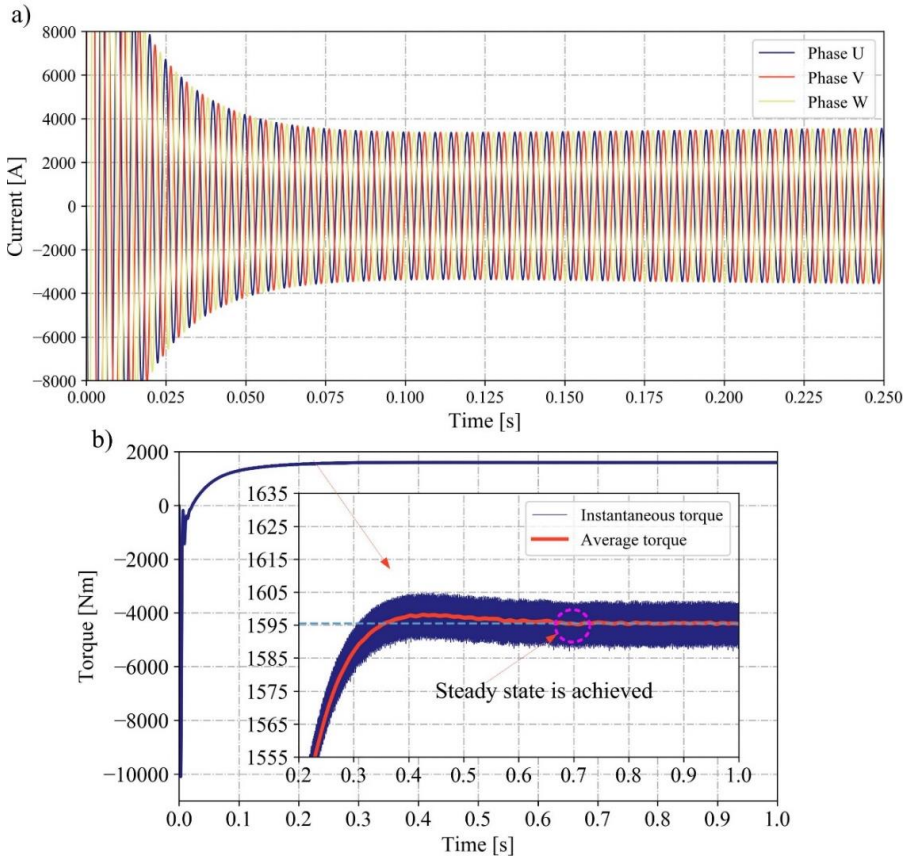

Fig. 2.2 Three-phase line currents and torque as a function of time during an initial transient to the nominal load by the traditional direct TM method (0.01 Ω stator winding resistance and 1×10^{-7} H stator leakage inductance). (a) Three-phase line current curves. (b) Instantaneous and average torque curves (adapted from **Publication I**).

Although some efforts have been made by changing the stator circuit parameter to reduce the transient period, it still takes considerable time to reach the steady-state condition as can be seen in Fig. 2.2(b). In the figure, the average torque is used to estimate the steady-state region, because the instantaneous torque curve contains some torque ripple. The average torque at each time step is defined as the average value of the original torque curve over the last electrical period. The average torque reaches the steady state at about 0.7 s with 1595.5 Nm in Fig. 2.2(b). It takes about 14000 calculation steps with a time step of 5×10^{-5} s (100 steps per electrical time period), and it takes more than 30 h of computer CPU time. Such a long simulation time causes some problems for the design and optimization of the IM. Therefore, a new approach should be proposed to accelerate the simulation process with the TM solution.

2.2 Method to accelerate the numerical transient

Theoretically, from the mechanical and electromagnetic points of view, there are two types of time constant (the mechanical time constant and the electromagnetic time constant), which result in mechanical and electromagnetic transients in the FEA. The mechanical time constant depends for instance on the electromagnetic torque, the rotor rotational speed, and rotor inertia. It can be completely eliminated by setting the rotor with a constant rotational speed, and this has already been done in this doctoral dissertation. Therefore, only the electromagnetic transient is included in the simulation.

The electromagnetic transient can be further divided into two parts: the stator electromagnetic time constant and the rotor electromagnetic time constant. To further explain these two concepts, a classical equivalent circuit presented for the IM characterization is shown in Fig. 2.3. It can be seen in the equivalent circuit that the circuit can actually be divided into two subcircuits including the stator circuit and the rotor circuit. Theoretically, they are galvanically isolated from each other, which is quite similar to a transformer. The energy conversion is performed through the air gap. These two electrical circuits both contain inductance and resistance components connected in series, which means that these electrical circuits are inherently prone to electrical transients when there are deviations in the applied voltage value (which have electrical time constant values of their own).

According to the previous discussion, it can be concluded that to accelerate the TM simulation, the task can be decomposed into two parts related to the reduction of the stator and rotor electromagnetic time constants. The stator electromagnetic time constant can be completely eliminated by using a current source excitation for the stator winding (instead of a voltage source excitation). To solve the rotor electromagnetic transient, a locked rotor model is presented in [48]. The method proposed in this doctoral dissertation is a further modification of the locked rotor model, which allows fast convergence even if a stator voltage supply must be used. The necessity of using a voltage supply in the simulation can be justified by the actual operating condition of the IM supplied by a

typical frequency converter (e.g. in the scalar mode). Therefore, the analysis of an IM with a voltage supply is investigated in this doctoral dissertation.

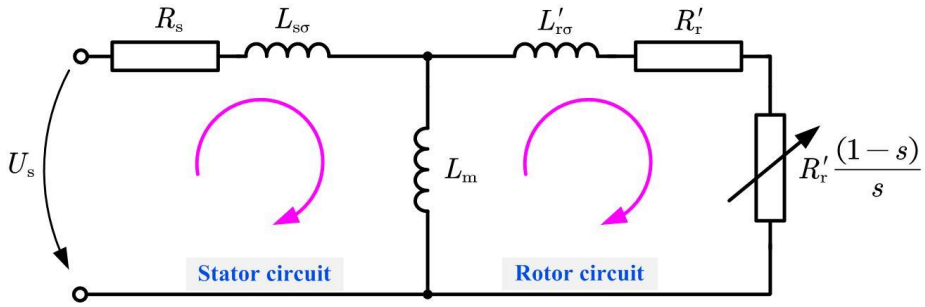

Fig. 2.3 Classical equivalent circuit described for the IM characterization (valid for the fundamental behavior), where U_s is the stator supply phase voltage, R_s is the stator winding resistance per phase, $L_{s\sigma}$ is the stator leakage inductance, L_m is the magnetizing inductance, $L'_{r\sigma}$ is the rotor leakage inductance referred to the stator coordinates, and R'_r is the rotor resistance referred to the stator coordinates.

The rotor current referred to the stator coordinates for a normal rotating rotor model with a per-unit slip s can be derived from the equivalent circuit in Fig. 2.3 as:

$$I'_r = \frac{sE_2}{R'_r + j s\omega (L_m + L'_{r\sigma})} , \tag{5}$$

where ω is the supply electrical angular frequency (equal to $2\pi f$), and E_2 is the rotor-induced voltage. The corresponding rotor electromagnetic time constant can be expressed as:

$$\tau_r = \frac{L_m + L'_{r\sigma}}{R'_r} , \tag{6}$$

According to Equation (6), it can be concluded that in a normal rotating rotor model with a per-unit slip s, the rotor electromagnetic time constant is quite long because L_m has a high value while R'_r is low. Equations (5) and (6) can be rewritten and the rotor current will not be changed. Nevertheless, the rotor circuit frequency is changed from $s\omega$ to ω, and the rotor electromagnetic time constant is modified from τ_r to $\tau_{r,m}$ as:

$$\begin{cases} I'_r = \dfrac{E_2}{R'_r/s + j\omega (L_m + L'_{r\sigma})} \\ \tau_{r,m} = \dfrac{L_m + L'_{r\sigma}}{R'_r/s} \end{cases} , \tag{7}$$

In Equation (7), the rotor electromagnetic time constant is significantly reduced ($\tau_{r,m}=s\tau_r$). The modified IM model must have a nonrotating rotor with further modifications of rotor characteristics as listed in Table 2.3. The simulation process with the locked rotor can achieve the convergence within a much shorter time period, especially if the stator time constant is eliminated (e.g. by using a current source supply). The stator time constant is defined in a similar way as the rotor time constant from the equivalent circuit as:

$$\tau_s = \frac{L_m + L_{s\sigma}}{R_s} \quad , \tag{8}$$

However, the locked rotor approach cannot correctly analyze the high-order eddy-current harmonics generated in the rotor. There are mainly two reasons for this. First, the locked rotor model setting is only modified based on the fundamental behavior using the slip-related approach (it can be explained by the equivalent circuit in Fig. 2.3). Second, the rotor is locked and not rotating, and thus, the slotting effects cannot be considered.

TABLE 2.3 PHYSICAL SETTINGS FOR THE MODIFIED IM MODEL

Parameter	Setting
Rotor speed n_r, [r/min]	0
Rotor conductivity σ, [S/m]	$s_N\sigma$
End ring resistance R_{ring}, [Ω]	R_{ring}/s_N

A more detailed description of the implementation of the proposed method is shown in Fig. 2.4. The proposed simulation process is driven with a voltage supply at the final stage, and the rotor is running at the nominal speed considering all the harmonics induced in the rotor. The two earlier phases of the model can be regarded as initialization stages to enable a fast convergence of the last phase. It can be seen in the figure that there are three main stages in the simulation. Before the simulation starts, it is necessary to get the initial rated current and per-unit slip values to initialize the TM simulation. These parameters can be accurately predicted by a TH solution or even by an analytical method. In this doctoral dissertation, the stator line current is 2571 Arms provided by the TH solution, and it is 2576 Arms after it has fully reached its steady state at 1 s (in Table 1.3 it is 2572 Arms because it is calculated at 0.4 s).

The locked rotor model with the current excitation in stage 1 in Fig. 2.4 is capable of creating an initial electromagnetic condition of the IM within a relatively short time period, which is fairly close to the final steady state. Then, in stage 2, the current excitation is switched to the corresponding voltage excitation. The process of switching the supply source will be further explained in the following paragraphs. Once the current source is switched to the voltage source, the stator circuit in Fig. 2.3 is disengaged, which can react to any disturbances in the circuit. After that in stage 3, the locked rotor is switched to a rotating rotor, and simultaneously, the rotor conductivity is also adjusted to

its normal value. At that stage, an additional electromagnetic transient may appear, the strength of which depends on the voltage or flux linkage disturbances during the transition process. After stage 3 the model becomes exactly the same as in the traditional simulation process with the voltage source.

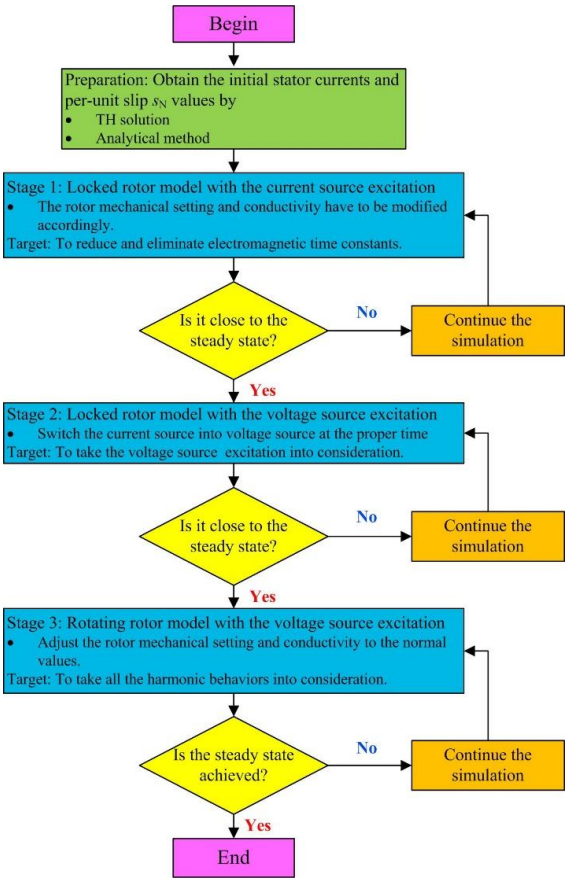

Fig. 2.4 Implementation of the proposed method to reach a fast convergence in the TM numerical simulation of a solid-rotor IM (adapted from **Publication I**).

Fig. 2.5 shows a potential circuit for the automatic switching from the current supply source to the voltage supply source during stage 2. In the circuit, the voltage and current source blocks are positioned in parallel, but they are not connected to the machine at the same time. Initially, the current supply source block (having the current values from the TH or preliminary analytical computations) is connected to the machine until the switching time t_s, whereas the voltage excitation block is not connected to the stator winding before that time. After the current excitation block is switched off (at the switching time t_s), the voltage excitation is switched on. Therefore, the sum of the three-phase supply voltages can be expressed as:

$$\begin{cases} U_{\mathrm{S,U}} = U_{\mathrm{C,U}}(t)H(t_\mathrm{s}-t) + U_{\mathrm{V,U}}(t)H[t-(t_\mathrm{s}+\Delta t)] \\ U_{\mathrm{S,V}} = U_{\mathrm{C,V}}(t)H(t_\mathrm{s}-t) + U_{\mathrm{V,V}}(t)H[t-(t_\mathrm{s}+\Delta t)] \\ U_{\mathrm{S,W}} = U_{\mathrm{C,W}}(t)H(t_\mathrm{s}-t) + U_{\mathrm{V,W}}(t)H[t-(t_\mathrm{s}+\Delta t)] \end{cases}, \tag{9}$$

where $U_{\mathrm{C,U}}$, $U_{\mathrm{C,V}}$, and $U_{\mathrm{C,W}}$ are the three-phase voltage drops of the current sources, which are obtained directly from the FEM, H denotes the Heaviside step function (H(x)=1 if $x \geq 0$), Δt is the time step in the FEM, and $U_{\mathrm{V,U}}$, $U_{\mathrm{V,V}}$, and $U_{\mathrm{V,W}}$ are the three-phase voltages, which can be written as:

$$\begin{cases} U_{\mathrm{V,U}}(t) = \hat{U}_{\mathrm{V,U}}\cos[2\pi f(t-t_\mathrm{s}) - \varphi_0] \\ U_{\mathrm{V,V}}(t) = \hat{U}_{\mathrm{V,V}}\cos[2\pi f(t-t_\mathrm{s}) - 2/3\pi - \varphi_0] \\ U_{\mathrm{V,W}}(t) = \hat{U}_{\mathrm{V,W}}\cos[2\pi f(t-t_\mathrm{s}) + 2/3\pi - \varphi_0] \end{cases}, \tag{10}$$

where $\hat{U}_{\mathrm{V,U}}$, $\hat{U}_{\mathrm{V,V}}$, and $\hat{U}_{\mathrm{V,W}}$ are amplitudes ($380 \times \sqrt{2} = 537.4$ V) and φ_0 is the initial phase. It is difficult to estimate the initial phase of the voltage at a random switching time. However, once the voltage (e.g. phase U) reaches the positive or negative peak values at t_s, the initial phase can be regarded as 0 or π ($\cos 0 = 1$ or $\cos\pi = -1$). Therefore, it is recommended to switch the current supply source to the voltage supply source at these particular time points; this has been done in this dissertation.

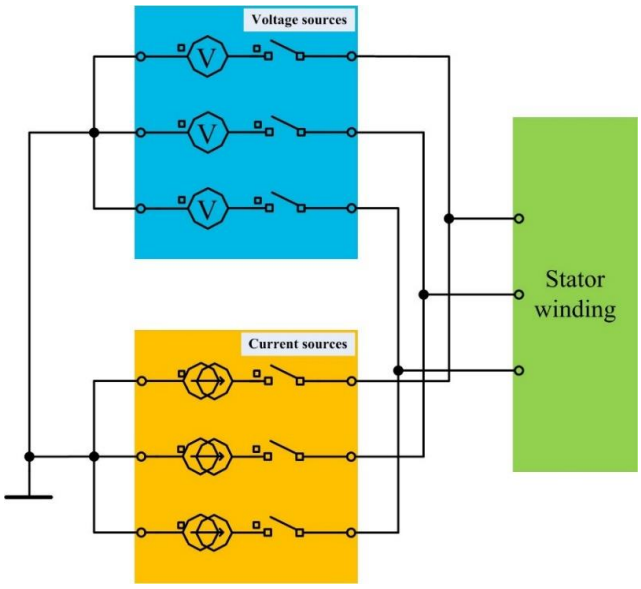

Fig. 2.5 Circuit of the proposed approach in the FEA for the automatic switching of the stator winding supply source (e.g. switching from the current source to the voltage source).

The switching sequences can be generated automatically, and the practical implementation of these sequences can vary depending on the software solution applied. It is also possible to implement different stages (shown in Fig. 2.5) manually. The model can be initialized with the current supply source until it reaches the steady state, after which the voltage waveforms over the current source can be obtained. Then, based on Equation (9), the voltage waveforms of the current source can be connected to the voltage source manually.

2.3 Simulated results of the proposed method

Fig. 2.6 shows the supply voltage (both the current source voltage drop and the voltage source voltage) waveforms starting from the very beginning of the simulation in stage 1. In Fig. 2.6(a) there are strong pulses right after the simulation starts. They are caused by

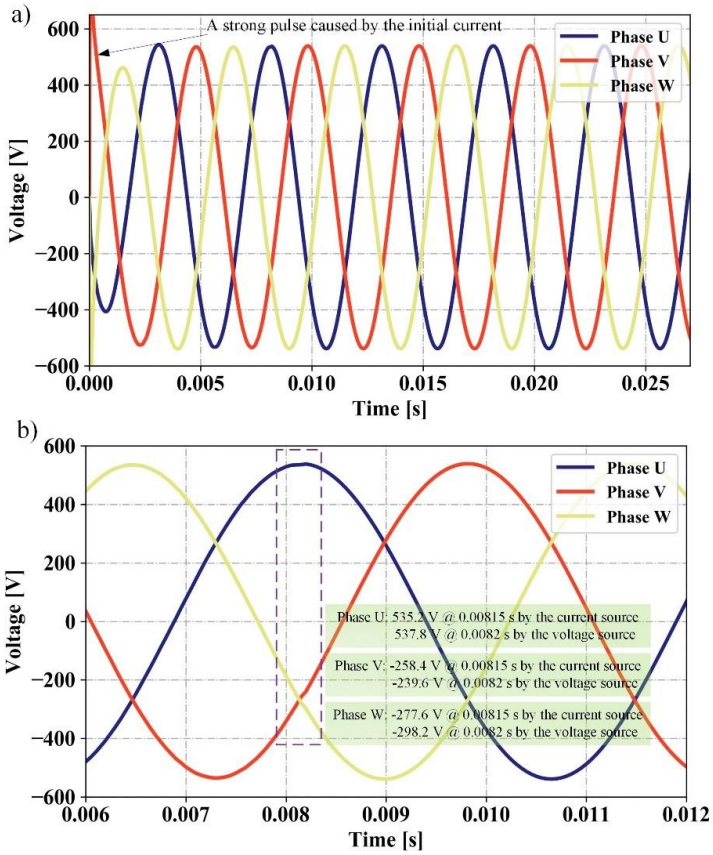

Fig. 2.6 Three-phase supply voltage waveforms as a function of time. (a) Three-phase supply voltage waveforms at the very beginning of the simulation during the initial current source supply. (b) Three-phase supply voltage waveforms in the neighborhood where the current supply is changed to a corresponding voltage supply.

the interaction of the current sources in the stator windings and the electromagnetic condition of the locked rotor. The locked rotor model reaches the steady state within one or two electrical time periods (e.g. after 0.005 s; this aspect is discussed in more detail in **Publication I**). This is quite a short time period for reaching the steady-state condition even if the locked rotor is applied, because the current supply source eliminates the stator winding electromagnetic transient. In addition, Fig. 2.6 shows that from 0 to 0.00815 s, the machine is supplied by the current source, and after that, the voltage source is applied to the stator winding. Switching of the supply source occurs at the time point when the voltage waveform in the current source (and consequently, in the voltage source, as they have the same phase shift) reaches its peak value, as suggested by Equation (10). Finally, the curves in Fig. 2.6(b) indicate that the switching process of the excitations is successful.

Despite the very small oscillation during the switching process as shown in Fig. 2.6(b), the locked rotor model with the current excitation at stage 1 still meets the desired target. The flux density distribution of the IM plotted at 0.01 s in Fig. 2.7 shows a similar pattern as the steady-state pattern shown in Fig. 2.1, which means that an initial condition close to the steady state has already been achieved by the proposed method. As a result of the high rotor resistivity, the flux has already penetrated deep into the solid rotor, which also indicates that the locked rotor approach is prone to a significant reduction in the rotor electromagnetic time.

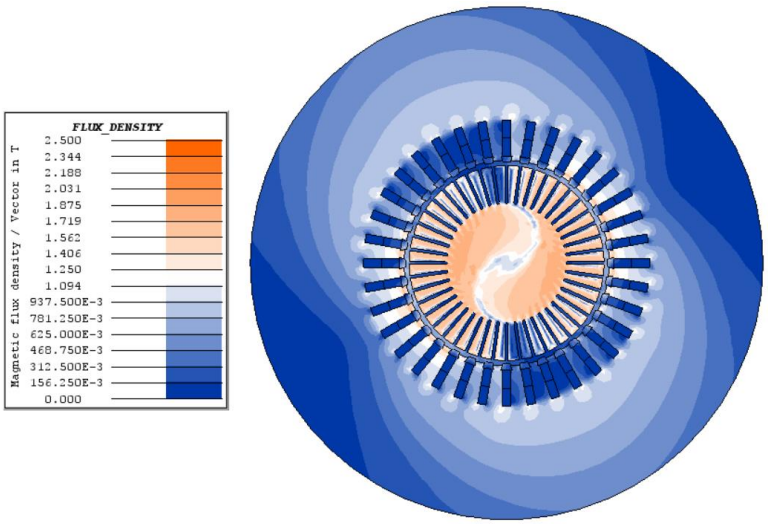

Fig. 2.7 Flux density distribution of the IM with the locked rotor model at 0.01 s.

Fig. 2.8 shows three-phase supply current waveforms during the excitation switch. It can be seen in the figure that the three-phase current does not suffer any significant oscillation after the current source has been switched to the voltage source. This is due to the relatively small voltage deviations before and after the switching period, and the machine itself is capable of filtering small deviations. It is better to switch the current source to the

voltage source while the locked rotor principle is applied, because the rotor has a smaller electromagnetic time constant at this stage (a much higher equivalent rotor resistance). This helps to reduce some current transient in the stator winding after the supply source switching process (at 0.0082 s).

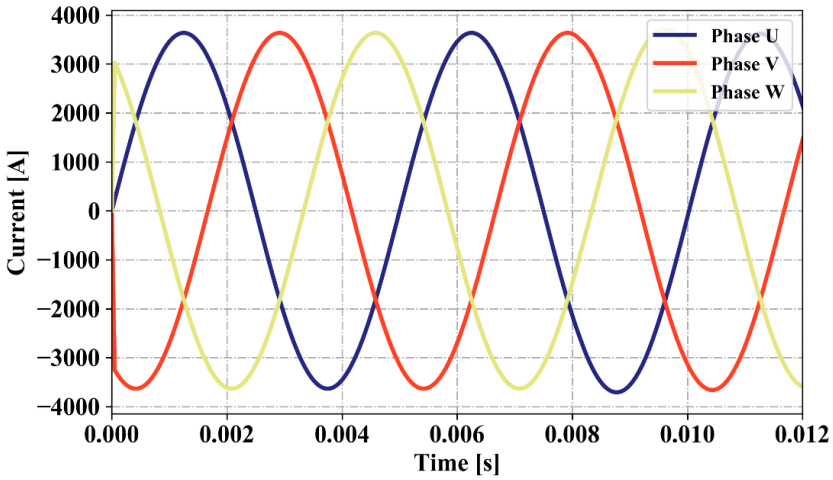

Fig. 2.8 Three-phase supply current waveforms as a function of time in the neighborhood where the current supply is changed to a corresponding voltage supply.

After switching the supply source, the three-phase voltage applied to the stator winding always has a sinusoidal pattern with a particular peak value and phase shift, which can be presented directly by the analytical equation. Thus, there is no need to plot the waveforms any more after that time period. However, the current in the stator winding can vary at different transients or load conditions. Therefore, it is necessary to check the current waveform, especially when switching from the locked rotor state to the rotating rotor state at the nominal speed (stage 3) at 0.02 s.

The current waveforms are presented in Fig. 2.9. It can be seen in the figure that there is an obvious oscillation in the current waveforms right after 0.02 s. It might be caused by the stator slotting effect on the rotor side, which could not be taken into account at the locked rotor. Nevertheless, the current oscillations are suppressed in a relatively short time period, and the current waveforms become smooth after two or three electrical periods. In addition, the current peak values in the figure are gradually increasing after 0.02 s. Therefore, it takes considerable extra time before the complete steady state is reached. The reason for the relatively long transient period is that the final rotor electromagnetic time constant becomes the same as in the original rotor because of the same final rotor conductivity. Consequently, the rest of the simulation time starting from 0.02 s (at stage 3) can be regarded as the adjusting time period (stage 3).

Fig. 2.10(a) shows the torque curve as a function of time at the beginning of the simulation up to 0.05 s. The three stages are shown clearly in the figure. Some torque ripple appears

in stage 2 because of the somewhat imperfect excitation switch. A strong subtransient is also shown after the rotor starts to rotate, and it disappears in a relatively short time period. After that, the torque is gradually decreasing until reaching the steady-state value.

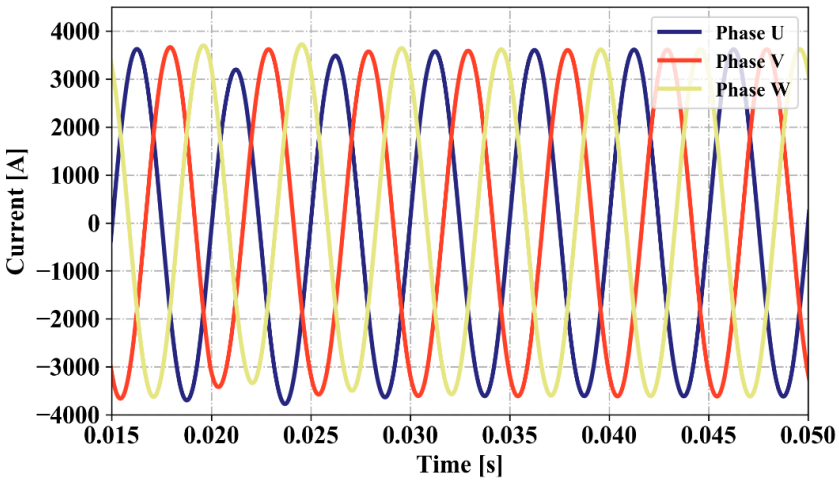

Fig. 2.9 Three-phase supply current waveforms as a function of time when the rotor is switched from the nonrotating state to the rotating state.

It can be seen in Fig. 2.10(b) that the torque produced by the proposed method reaches the steady state faster than by the traditional direct TM method, and by the proposed method, the simulation time to reach the steady state is about half of the original solution. There can be two reasons for this phenomenon. First, a good initial condition close to the final steady state has been created at the very beginning of the simulation before stage 3 by using the proposed method. Second, there is almost no overshoot in the torque curve, which helps to achieve the convergence within a short time.

Fig. 2.10 indicates that it still takes several electrical time periods to fully reach the steady state even when the proposed method is used. A simplified equivalent circuit for the IM considering harmonics is shown in Fig. 2.11 [4]. According to this figure, it can be concluded that the proposed method is only capable of reducing the electromagnetic transient for the fundamental circuit. The stator winding harmonic effects are also partly mitigated in stage 2 when the current excitation is switched to the voltage excitation. Therefore, in theory, it is better to change the excitation before changing the rotor movement, because the rotor is still locked in stage 2 and the rotor electromagnetic time constant is still relatively small. In stage 3, other harmonics appear, especially the stator slot harmonic, which will also cause a transient, because the rotor resistivity is reset to the normal value at that time. The harmonic transient itself is not very long, but it is coupled with the fundamental circuit, and the fundamental-related transient in this time period is long.

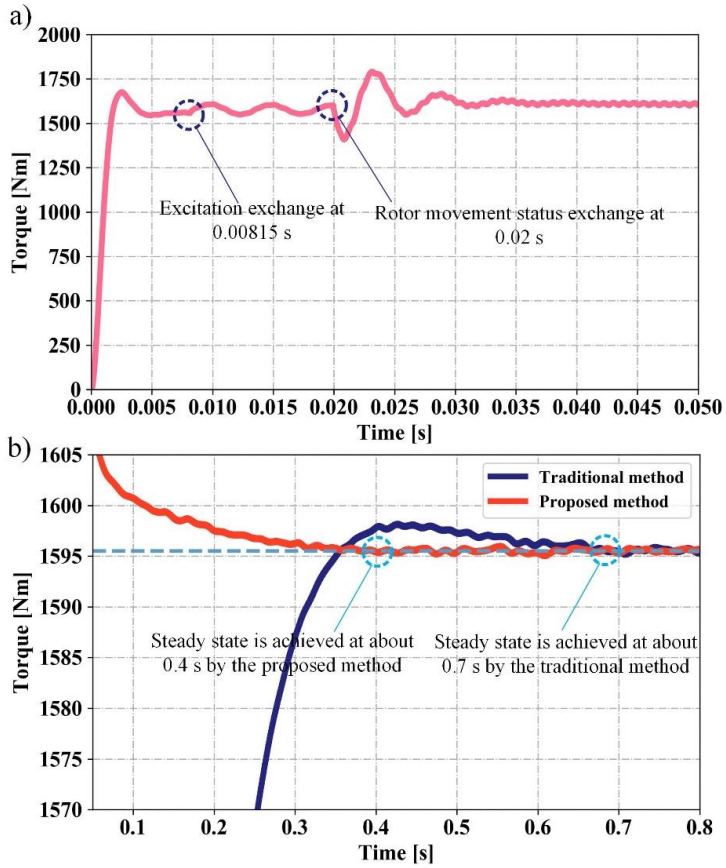

Fig. 2.10 Torque as a function of time by both the traditional direct TM method and the proposed method. (a) Instantaneous torque as a function of time by the proposed method. (b) Comparison of the average torque as function of time by both methods.

It is possible to reduce the simulation time even more if there is no oscillation in the torque curve during the excitation switch stage. An example of such a case is reported in **Publication I**. Fig. 6 in **Publication I** shows that there is no obvious torque oscillation when the excitation is switched at 0.00815 s. Therefore, the machine reaches the steady state much faster, and it only takes about 34% of the simulation time compared with the traditional direct TM solution.

Nevertheless, most probably, the subtransient and overall simulation times are highly affected by the initial currents, matching of the voltage values in the current supply source and the voltage supply source when the switching of the supply sources takes place, and additional phenomena (e.g. slotting effect) after switching from the locked rotor to the running rotor. The usage of the proposed method for the squirrel-cage IM simulation and initial current error effects on the simulation time are discussed in more detail in **Publication I**.

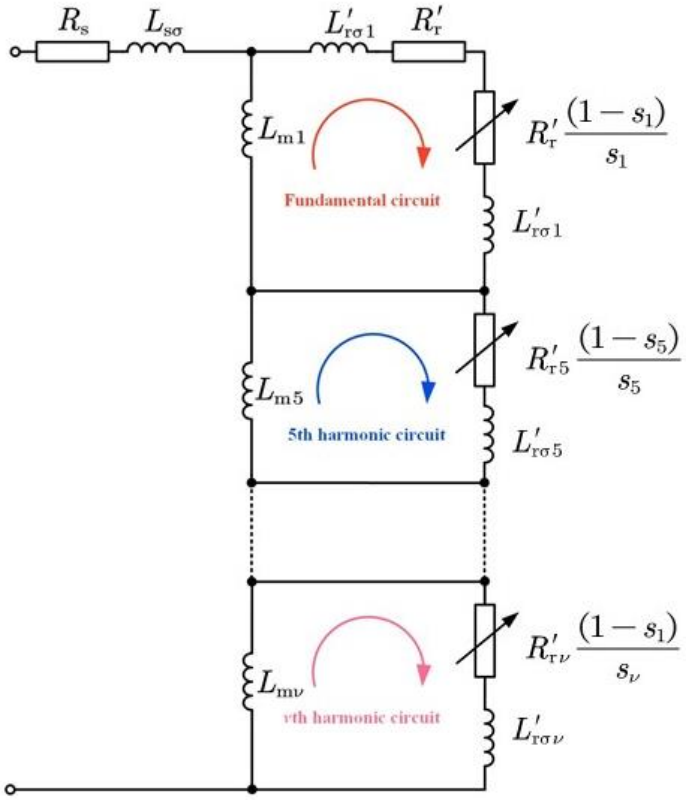

Fig. 2.11 Simplified equivalent circuit for the IM considering harmonics.

2.4 Comparison of the proposed method with commercial solutions

As described at the beginning of this chapter, it is possible to initialize the TM solver with the results calculated by the TH solver included in some commercial packages. However, the TH solver cannot directly consider the nonlinear *B*-*H* curve of the material. To be more specific, in TH solutions, all the excitations (inputs) are assumed to be sinusoidal, and the corresponding responses (outputs) should also be sinusoidal. To solve this problem, there are some approaches available to create an equivalent *B*-*H* curve based on the original nonlinear *B*-*H* curve. Therefore, it is necessary to first briefly introduce the principles of calculating the equivalent *B*-*H* curve.

Generally, based on the different inputs and outputs, there are two main methods to create an equivalent *B*-*H* curve: The one assumes that the value *B* provided by the original *B*-*H* curve is changing sinusoidally, and the equivalent *H* is the output. The other assumes that the initial *H* provided by the initial *B*-*H* curve is changing sinusoidally, and the equivalent *B* is the output. Packages applying different principles are listed in Table 2.4. It can be seen in the table that not all the packages have both the solutions, which means that the

simulation speed of the commercial approach of initializing the TM solver with TH calculation may be limited by the equivalent material models.

TABLE 2.4 PRINCIPLES IN DIFFERENT PACKAGES TO ESTIMATE THE EQUIVALENT *B*-*H* CURVE OF THE MATERIAL

Package	Principle	Comment
Altair Flux	sin. *B*–eq. *H* and sin. *H*–eq. *B*	Collected from the official tutorial/help documents
ANSYS Maxwell	sin. *B*–eq. *H*	
COMSOL	sin. *H*–eq. *B*	
FEMM	sin. *H*–eq. *B*	
JMAG	sin. *H*–eq. *B*	

As mentioned previously, Altair Flux is used for the computation in this doctoral dissertation. Therefore, both the cases 'sinusoidal *B*–equivalent *H*' and 'sinusoidal *H*–equivalent *B*' are discussed here. The equivalent *H* or *B* in Altair Flux is estimated by the average electromagnetic energy approach. The corresponding equations are written as follows [51], [52]:

$$\begin{cases} B \text{ varies sinusoidally: } H_{\mathrm{eq}} = \dfrac{1}{\pi f \widehat{B}} \displaystyle\int_0^{2\pi f} \int_0^{B} H \,\mathrm{d}B \,\mathrm{d}t \\ H \text{ varies sinusoidally: } B_{\mathrm{eq}} = \dfrac{1}{\pi f \widehat{H}} \displaystyle\int_0^{2\pi f} \int_0^{B} H \,\mathrm{d}B \,\mathrm{d}t \end{cases}, \tag{11}$$

where B and H are the real magnetic field density and magnetic field strength values extracted from the original *B*-*H* curve, and $\widehat{B}$ and $\widehat{H}$ are the amplitudes of the assumed sinusoidal variables.

Fig. 2.12 shows the real and equivalent *B*-*H* curves of the stator material estimated by Equation (11). It can be seen in the figure that the 'equivalent *H*–sinusoidal *B*' has a narrow range of the magnetic strength *H*. This is explained by the fact that in that case the sinusoidal *B* is the input, and the algorithm is capable of estimating the equivalent *H* up to B = 1.7 T from the original nonlinear *B*-*H* curve.

After obtaining the equivalent *B*-*H* curves, TH simulations can be conducted to set up the initial conditions for the following TM simulation. After that, the initial conditions created by different materials can be compared; a comparison is shown in Fig. 2.13. The initial flux density distributions obtained by the TH solutions are both plotted at t = 0 followed by the full transient simulation initialized from the TH solution. The initial flux

density distribution created by the proposed TM harmonic is plotted at t = 0.02 s because after 0.02 s the machine starts to run, and all the other settings are exactly the same with the other two transient models initialized from the TH solutions.

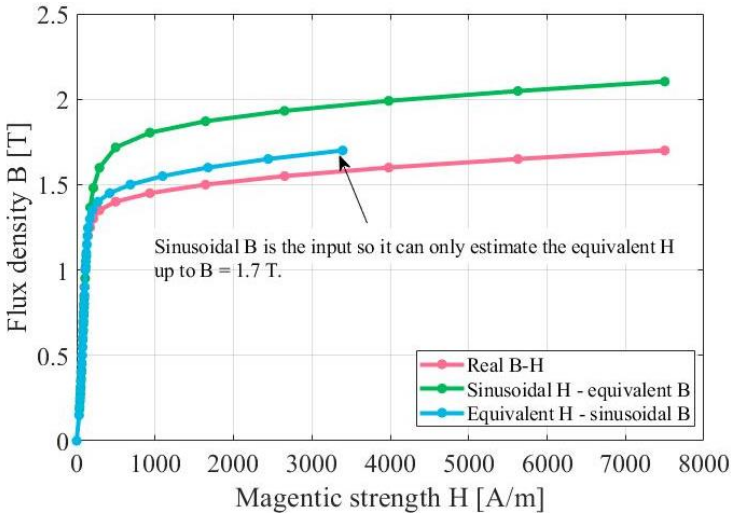

Fig. 2.12 Equivalent *B*-*H* curves of the stator material based on different principles.

It can be seen in Fig. 2.13 that the two models simulated by the TH solver have a similar flux density distribution. Nevertheless, the model with sinusoidal *H*–equivalent *B* materials has a stronger flux density distribution in the rotor area compared with the other one. This can be explained by the *B*-*H* curves shown in Fig. 2.12. In a certain range, with the same magnetic strength, a higher flux density will be obtained from the sinusoidal *H*–equivalent *B* curve.

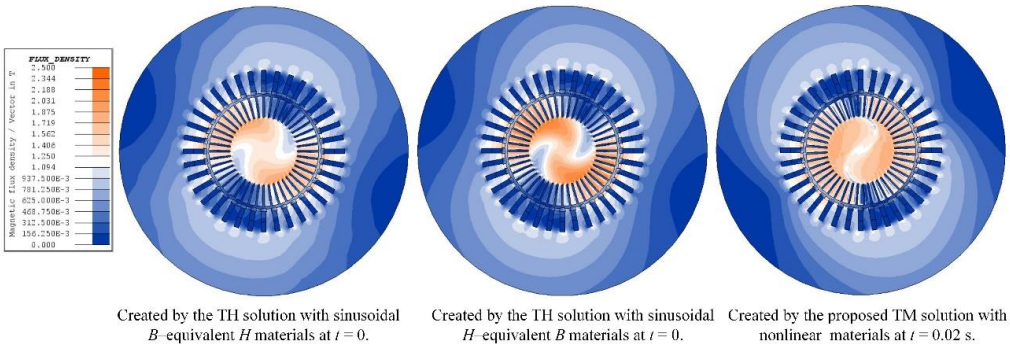

Fig. 2.13 Comparison of the initial flux density distributions based on different principles (note that the initial flux density distribution obtained by the TH solution in this figure has a 90° phase shift compared with the pattern shown in Fig. 2.1. It is caused by the default setting of the software, according to which there is a 90° phase shift after importing the initial condition in the TM solver from the TH solver).

Fig. 2.14 shows the average torque curves calculated by the TM solutions with different approaches. According to Fig. 2.14(a), it can be roughly estimated that the steady state is achieved at 0.3 s (actually, it has an overshoot below 1595.5 Nm, and it is too difficult to exactly define the steady state), 0.4 s, and 0.5 s by these three different methods, and all these methods are faster than the traditional direct transient solution. The simulation speed of the proposed method is faster than the TH to the TM method with equivalent *H*–sinusoidal *B* materials when considering the accurate steady state (0.4 s and 0.5 s). On the other hand, the proposed method is slower than the TH to the TM method with sinusoidal *H*–equivalent *B* materials when considering the accurate steady state (0.4 s and 0.3 s).

Nevertheless, 0.3 s (6000 steps) or 0.4 s (8000 steps) in the time-step FEM still takes a long time to accomplish the simulation. In practice, some minor error is always acceptable, especially in industrial applications. The advantage of the proposed method is thus significant if some minor error is acceptable. It can be seen in Fig. 2.14 that the proposed method is faster than the TH to the TM method with sinusoidal *H*–equivalent *B* materials before 0.22 s. Both methods reach 1597 Nm at 0.22 s, and after that time the speed of the

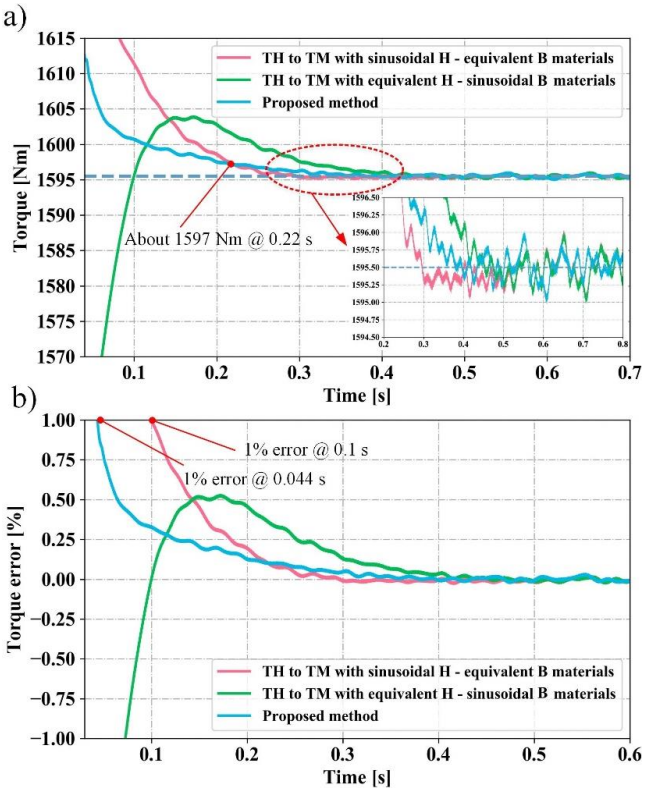

Fig. 2.14 Average torque and its corresponding error as a function of time obtained by the TM initialized with the TH methods and the proposed method. (a) Comparison of the average torque as a function of time obtained by different methods. (b) Comparison of the average torque error as a function of time obtained by different methods.

proposed method decreases. If 1% of the torque error is acceptable, it takes only 0.044 s (880 steps) for the proposed method and 0.1 s (2000 steps) for the other methods to reach that amount of error.

Based on the previous analysis, it seems that the proposed method is a good alternative in commercial solutions (the TM initialized with the TH calculation). Some of the possible advantages of the proposed method can be listed as follows:

- The proposed approach is easy to implement compared with commercial solutions, because not all the packages, especially some open source packages (e.g. GetDP), have the function of running the TM initialized with the TH calculation.

- The proposed approach is capable of considering the nonlinear *B*-*H* curve of the materials at the very beginning of the simulation, which means that a better initial condition can be established compared with the commercial solution. Although commercial packages are able to give the equivalent *B*-*H* curve of the materials, the algorithm to estimate the equivalent *B*-*H* curve will significantly affect the following TM simulation, as shown in Fig. 2.14. On the other hand, not all the packages can provide both of the equivalent materials as listed in Table 2.4.

- The proposed approach is capable of providing results in the shortest simulation time with a minor error compared with the other methods, which is acceptable in practice in most cases.

It has to be emphasized, however, that the simulation speed of the proposed approach may vary depending on many aspects (e.g. nonlinear *B*-*H* curves, machine parameters, algorithms of evaluating equivalent *B*-*H* curves, the time of excitation switch, the time of rotating the rotor, FEM packages), and it is not possible to consider all these factors in detail in a single doctoral dissertation.

3 Extraction of solid-rotor eddy-current harmonic losses

The solid-rotor IM typically suffers from higher eddy-current losses, which is not always a serious problem for a squirrel-cage IM, because the solid rotor provides a clear conducting path in the axial direction for the eddy currents generated by a large number of high-order air-gap flux density harmonics. Typically, in the electrical machine design, some measures can be taken to mitigate these air-gap flux density harmonics so that the corresponding rotor eddy-current losses decrease. For example, short pitching is used to suppress the winding harmonics. Further, semimagnetic wedges are capable of mitigating the slotting effects, and the skew angle can be adjusted accordingly to reduce the effects of certain air-gap flux density harmonics on the induced eddy currents in the solid rotor. Nevertheless, in the preliminary design, it is necessary to determine how much eddy-current losses would be generated in the solid rotor by a certain harmonic. After that, the harmonics that generate the highest losses could be mitigated by some special means. This is the main target of this chapter.

3.1 Harmonic analysis with 2D fast Fourier transform

Before analyzing the solid-rotor eddy-current harmonic losses, it is necessary to first correctly extract the air-gap flux density harmonics. The ν^{th} air-gap flux density harmonic can be expressed by the analytical method as follows [53]:

$$B_\nu(\theta,t) = \hat{B}_\nu \cos(\nu\theta - \Omega_\nu t - \varphi_\nu) \ , \tag{12}$$

where θ is the stator mechanical position measured by mechanical degree, and $\hat{B}_\nu$, Ω_ν, and φ_ν are the amplitude, mechanical angular velocity (note that spatial harmonics of the same order may have different rotational speeds and should be corrected based on Fig. 3.1), and initial phase of the ν^{th} harmonic respectively. From the mathematics point of view, Equation (12) can be regarded as a function with two variables.

According to the exhaustive theoretical analysis in [54], the most important air-gap flux density harmonics can be listed in Table 3.1. Saturation harmonics are not given in the table because of their special properties, which will be explained later in the following paragraphs. The table shows that some of the harmonics have the same stator or rotor current frequency (stator and rotor current frequencies mean that the frequencies of the induced currents in the stator and rotor are caused by the air-gap flux density harmonics). This means that it is impossible to analyze the air-gap flux density harmonics using the fast Fourier transform in the spatial or time domain alone, because in this case some of the harmonics would be merged in one harmonic without the possibility of splitting them. This is a clear drawback of the traditional fast Fourier transform (applied in the time domain or the spatial domain only) in the air-gap flux density harmonic analysis. Therefore, a more accurate algorithm should be applied to replace the traditional solution. One potential solution is to use a 2D fast Fourier transform, which is capable of performing the Fourier analysis in both the time and spatial domains simultaneously. This

algorithm has already been used in many academic studies in different fields, especially in the field of electromagnetic noise analysis of the electrical machine, as reported in [55], [56].

TABLE 3.1 MAIN AIR-GAP FLUX DENSITY HARMONICS

Order (ν)	**Velocity,** [r/m]	**Stator current frequency,** [Hz]	**Rotor current frequency,** [Hz]	**Comment**
p	n_{syn}	f	sf	Fundamental
$6k\pm1$	$\pm n_{syn}/\nu$	f	$\pm f[1-\nu(1-s)]$	Winding harmonic
$k\,Q_s\pm p$	$\pm n_{syn}/\nu$	f	$\pm f[1-\nu(1-s)]$	Stator slot harmonic
$k\,Q_r\pm p$	$n_{syn}[\nu(1-s)\pm s]/\nu$	$f[\nu(1-s)\pm s]$	$\pm sf$	Rotor slot harmonic

k is a positive integer

Fig. 3.1 shows the time and spatial harmonic analysis of the air-gap flux density at the nominal load by the 2D fast Fourier transform. It is emphasized that the sampling frequency is 20000 Hz (100 sampling points per electrical period) in the time domain, and 100 sampling points are used for the spectrum analysis. It means that based on the Shannon sampling theorem, the FEM simulation is only capable of modeling frequencies up to 10000 Hz. The rotor-related harmonics do not cause losses in the rotor itself, and therefore, the rotor-related harmonics are not shown in Fig. 3.1 and will not be studied in detail here.

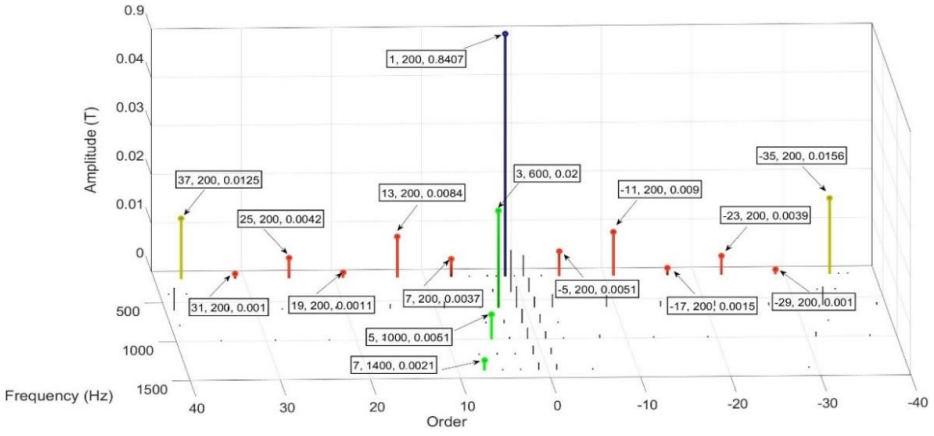

Fig. 3.1 Time and spatial harmonic analysis of the air-gap flux density at the nominal load (s_N = 0.0046) by the 2D fast Fourier transform. The figures in the boxes are the ordinal of the harmonic, the related frequency, and amplitude. Blue: fundamental, red: stator winding harmonics, green: saturation harmonics, and yellow: stator slot harmonics. The negative sign in the Order axis means that this harmonic travels in the opposite direction with respect to positive harmonics. The causes for the rest of the harmonics are complex, and they are most likely due to the interaction of the two types of different harmonics (adapted from **Publication II**).

In this figure, the blue bar indicates the fundamental, and the red bars are the stator winding harmonics (-5^{th}, $+7^{th}$, -11^{th}, etc.). The yellow bars are the stator slot harmonics (-35^{th} and $+37^{th}$), and they can generate a 7200 Hz eddy-current harmonic on the rotor surface. The green bars are the saturation harmonics traveling fixed to the fundamental. They are caused by the stator and rotor material properties together, and there is no effective method to separate them and distinguish what part of these harmonics is generated by the stator side or the rotor side, because both the stator and rotor saturation harmonics have the same order and frequencies. In addition, it can be seen that the $+5^{th}$ saturation harmonic and the -5^{th} stator winding harmonic have the same order in the spatial domain. It reveals that there is also some overlapping in the spectrum if the traditional fast Fourier transform is applied in the spatial domain. However, this overlapping in both the time and spatial domains can be avoided by using the 2D fast Fourier transform.

3.2 Method to extract solid-rotor harmonic losses

The main idea of the proposed method is to create exactly the same harmonics obtained by the 2D fast Fourier transform in the air gap of the actual IM model and then use these harmonics directly to excite the solid rotor. A proposed simulation model for the FEM calculation of rotor losses by the air-gap flux density harmonics is presented in Fig. 3.2. It can be seen in the figure that the model contains only three parts: a rotating rotor, air gaps (including a rotating air gap and a nonrotating air gap), and a rotating source of flux density (implemented by a magnet layer) with the adjustable magnetization (it can also be replaced by an appropriate boundary condition). The magnet layer should be relatively thin (about 2 mm in the model) with a very low permeability of 10^{-30} to avoid any practical deviations in the preset flux density in the magnet and the actual flux density in the air gap. The validation of this model is confirmed in **Publication II**.

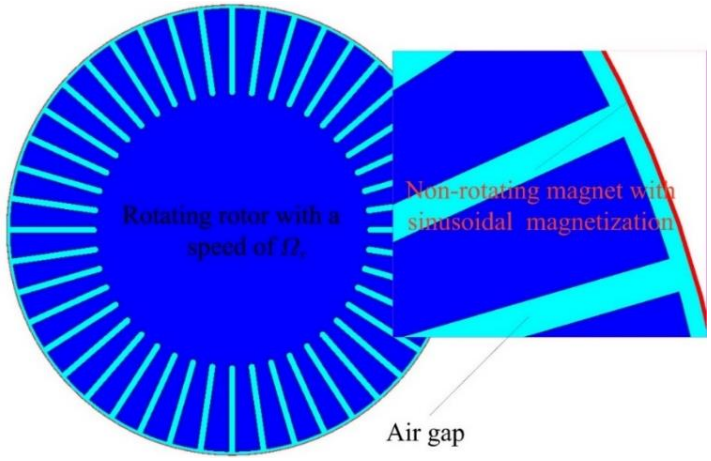

Fig. 3.2 Method proposed for the extraction of solid-rotor eddy-current harmonics (adapted from **Publication II**).

Although the magnet in Fig. 3.2 is fixed, it is still capable of generating rotating air-gap flux density harmonics by the variation in the preset remanent flux density in the magnet. According to Equation (12), neglecting the initial phase angle, the magnetization in the x-y coordinate system (Cartesian coordinate system) can be expressed as:

$$\begin{cases} B_{\mathrm{x}}(\theta,t) = \hat{B}_{\nu}\cos\left(\nu\theta - \dfrac{2\pi f_{\nu}}{\nu}t\right)\cos\left(\arctan\dfrac{y}{x}\right) \\ B_{\mathrm{y}}(\theta,t) = \hat{B}_{\nu}\cos\left(\nu\theta - \dfrac{2\pi f_{\nu}}{\nu}t\right)\sin\left(\arctan\dfrac{y}{x}\right) \end{cases}, \tag{13}$$

where f_{ν} is the stator current frequency of the harmonic defined in Table 3.1. Using Equation (13) as the preset remanent flux density in the magnet (for a certain harmonic or several harmonics simultaneously), it is possible to induce the required air-gap flux density harmonics (with the required amplitude, order in the spatial domain, and frequency in the time domain) in the air gap.

The next critical step is to consider the saturation in the rotor, because the saturation significantly affects the overall permeability in the rotor region and, consequently, affects the eddy-current penetration depth on the rotor surface caused by the air-gap flux density harmonics. The eddy-current penetration depth caused by the ν^{th} harmonic can be expressed as **Publication II**:

$$\delta_{\nu} = \frac{1}{\sqrt{\pi\mu_0\mu_{\mathrm{r}}\sigma f|1-\nu(1-s)|}}, \tag{14}$$

where μ_0 and μ_{r} are the vacuum permeability and the relative permeability in the rotor region. This equitation indicates that the rotor relative permeability is capable of affecting the penetration depth, and the air-gap flux density harmonics would penetrate deeper if the rotor permeability were smaller. In addition, the air-gap flux density harmonic is a distributed parameter, which means that the penetration depth also varies on the rotor surface depending on the flux density distribution. The saturation is distributed across the rotor region, which means that the penetration depth also varies on the rotor surface depending on the saturation distribution. Therefore, accurate modeling of the rotor surface permeability is a critical aspect for precise evaluation of the rotor losses.

To accurately model the rotor permeability, a specially designed procedure is presented in Fig. 3.3. It can be seen in the flowchart that the harmonic losses are calculated by the loss difference from the two models (Model 1 and Model 2). The structure of these two models is described in Fig. 3.2. However, the magnets in these models are excited with different excitation patterns. The magnet in Model 1 is excited with a hybrid excitation, which contains the fundamental and an additional high-order harmonic. The fundamental in this hybrid excitation is used to create a similar rotor permeability distribution as in the actual IM model. Once the fundamental harmonic is applied to the rotor, the permeability

distribution in the rotor region is positioned similarly as in the actual IM model (having the same *B-H* curve of the material in the rotor). This means that the correct rotor permeability distribution in the rotor area is achieved automatically by applying the fundamental. This allows to investigate the losses generated in the rotor by some other high-order harmonics considering the correct permeability distribution in the rotor region. Model 2 is excited only with the fundamental, which provides rotor losses generated only by the fundamental. After that, the loss difference in these two models can be regarded as the losses in the rotor induced by the investigated high-order harmonic.

The proposed method can be used not only for the harmonic loss analysis in the rotor, but it is also valid for extracting other electromagnetic harmonic behaviors. The main novelty of the method is that it is capable of accurately taking the distributed parameters into consideration, for instance the harmonic flux density distribution and the rotor permeability distribution. In the simulation, this is achieved by applying the fundamental, which has a much higher amplitude than the other harmonics, and which contributes most to the permeability distribution in the rotor region.

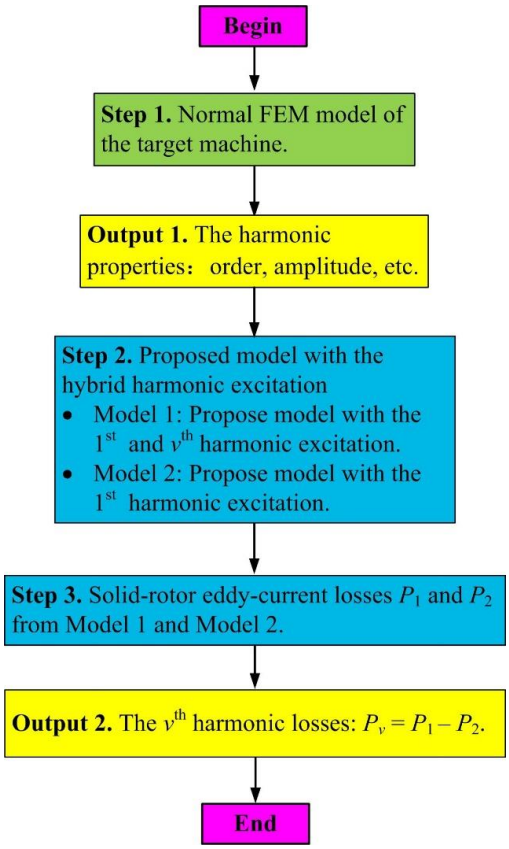

Fig. 3.3 Flowchart of the extraction of solid-rotor eddy-current harmonic losses caused by a particular air-gap flux density harmonic by the proposed method (adapted from **Publication II**).

3.3 Loss analysis by the proposed method

First, it is noted that the total solid-rotor eddy-current losses in the IM are 11.48 kW (11483 W) including all the harmonic effects at the nominal load (s_N = 0.0046) calculated directly by the FEM (Altair Flux 2D). However, in Table 1.3, the solid-rotor eddy-current losses are 22.97 kW. The losses are doubled because the solid rotor end effect is considered in the postprocessing. Theoretically, to take the end effect into account, the rotor resistivity can be modified by multiplying the end effect factor, which is close to 2 in low slip ranges [57]. For the sake of simplicity, all the losses discussed in this chapter refer to those obtained directly from the FEM (without multiplication by 2).

The solid-rotor eddy-current harmonic losses computed by the proposed method are shown in Fig. 3.4. The sum of the losses (11104 W) in the figure is close to the total losses (11483 W) obtained by the normal computation. There is a 379 W (3.3% of the total losses) difference between the total rotor losses estimated by the proposed method and the total rotor losses estimated by the traditional method (using the standard IM model). This error might be caused by the difference in the permeability distribution (as the permeability distribution in the proposed method is considered only for the fundamental), the mesh difference, or the fact that not all the harmonics are taken into consideration in the proposed method.

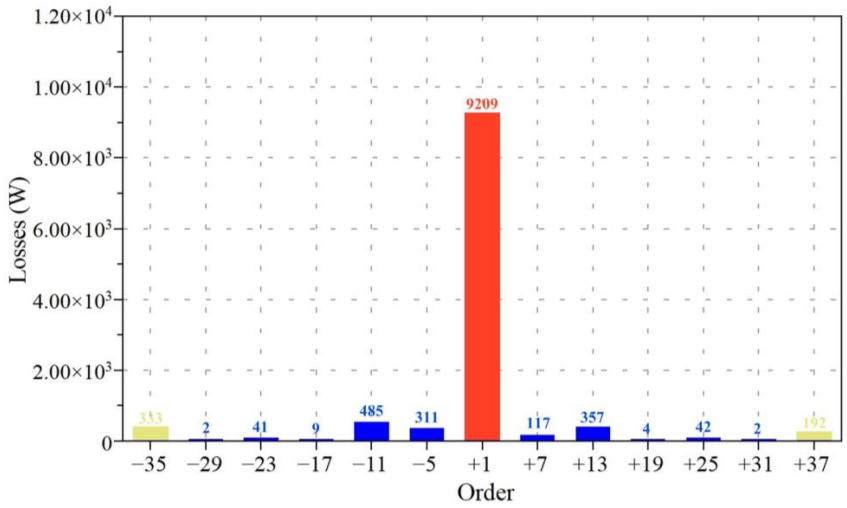

Fig. 3.4 Solid-rotor eddy-current losses generated by different air-gap flux density harmonics at the nominal load (s = 0.046) estimated by the proposed method (adapted from **Publication II**).

It can be seen in the figure that the losses in the rotor caused by the fundamental are the highest among all losses. The rotor losses caused by the fundamental are directly related to the per-unit slip, which can be hardly reduced further as it varies according to the generated torque (having certain rotor material properties and rotor geometry). The -5^{th} and $+7^{th}$ stator winding harmonic losses are 311 W and 117 W, which have already been

minimized by the short pitching. The -11^{th} and $+13^{th}$ harmonics belong to the 2^{nd}-order stator winding harmonics, and they produce the highest harmonic losses (485 W and 387 W). The rest of the winding harmonics produce only small losses in the solid rotor. The -35^{th} and $+37^{th}$ are the stator slot harmonics, and they produce 353 W and 192 W of solid rotor losses, although the stator slot harmonics have already been mitigated by applying semimagnetic wedges. The data in Fig. 3.4 indicate that if some extra measure (e.g. skewing) were taken to mitigate the rotor losses, it should focus on the −11th and $+13^{th}$ or -35^{th} and $+37^{th}$ harmonics.

The results presented in Fig. 3.1 and Fig. 3.4 also show that the amplitudes of the -35^{th} and $+37^{th}$ harmonics are higher than the -11^{th} and $+13^{th}$ harmonics, but they generate less losses on the rotor surface. This is due to the deeper penetration depth of the -11^{th} and $+13^{th}$ harmonics, because the eddy-current frequency caused by the -11^{th} and $+13^{th}$ harmonics is lower than the eddy-current frequency induced by the -35^{th} and $+37^{th}$ harmonics. Based on the proposed method demonstrated in Fig. 3.3, it is possible to extract the distribution of the eddy currents induced by a particular harmonic. It is arranged by using a similar flowchart as in the loss calculation, and the harmonic eddy-current distribution is calculated by the difference between Model 1 and Model 2. Detailed harmonic eddy-current distributions in the rotor region caused by two different air-gap flux density harmonics are shown in Fig. 3.5.

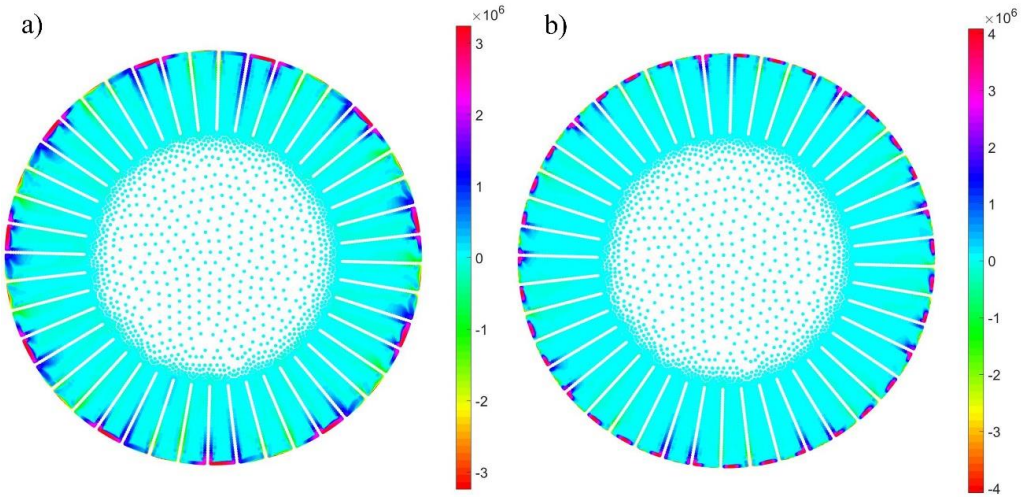

Fig. 3.5 Harmonic eddy-current distributions at the nominal load (s_N = 0.0046) in the steady state. (a) -11^{th} harmonic eddy-current distribution. (b) -35^{th} harmonic eddy-current distribution (adapted from **Publication II**).

The maximum current density value generated by the -35^{th} harmonic is higher than the maximum current density value generated by the -11^{th} harmonic, as shown in Fig. 3.5(b) because of the higher induced eddy-current frequency. However, the -11^{th} harmonic, as shown in Fig. 3.5(a), causes a deeper penetration depth. It means that the solid-rotor eddy-

current losses are determined by multiple factors rather than one single factor. Another possible reason for the higher losses is that the wavelength of the -11^{th} harmonic is longer and would thus create a larger induced eddy-current area on the rotor surface.

4 Mitigation of asymmetric winding current unbalance

Asymmetric windings are gaining popularity in the electrical machine design, as reported in [58], [59]. They can bring some benefits for the electrical machine such as an easy assembly of the winding for the manufacturer or achieving a special control algorithm. Nevertheless, it also causes problems for the machine. Typically, an asymmetric winding creates some current unbalance, if no special measures are taken to mitigate it. The current unbalance will further cause an asymmetric air-gap flux density distribution and generate all kinds of side effects in the machine electromagnetic performance, such as torque ripple, noise, vibration, and unbalanced magnetic pull [60], [61]. Therefore, it is essential to improve the machine performance by mitigating the current unbalance resulting from an asymmetric winding arrangement.

There are some effective ways to suppress the current unbalance (or asymmetric impedance) [60], [62]. However, most of them treat the unbalance system by means of electrical drive control principles or power electronics, which means that some more investments in power electronics devices are needed or a special design control algorithm has to be developed in some cases. These measures are more suitable for the strong asymmetry condition. In the asymmetric winding, the current unbalance is most frequently caused by the inherent unbalanced impedance (where resistance can be neglected and only the magnetizing and leakage inductances can be considered). In cases where only the leakage inductance causes the unbalanced impedance, the unbalance level is usually not very significant. Consequently, in these cases, it is not necessary to suppress the inherent unbalanced impedance by means of power electronics, while it is possible to balance the impedance (or current supply unbalance) by further adjusting the winding arrangement inside the stator at the design stage.

A special coil arrangement is employed to mitigate the current unbalance resulting from the inherently asymmetric winding arrangement. It is implemented by placing the coils of different phases in different depths in slots. The FEA results verify that this method is capable of significantly reducing the current unbalance.

4.1 Asymmetric winding arrangement

It is determined in the design stage of the 2 MW machine that the prefabricated coil with a liquid cooling duct embedded inside the coil will be used in the stator winding arrangement. This brings the advantage of an efficient cooling condition for the stator winding. The target is to build a winding providing a similar electromagnetic performance as a normal two-layer short-pitched winding. Building such a traditional winding using a conductor material with a cooling duct embedded would be very challenging, and therefore, a new solution offering easy manufacturing is proposed.

In this chapter, an asymmetric winding is developed and discussed, which is capable of guaranteeing satisfactory electromagnetic performance, simultaneously facilitating the

installation of the winding. The asymmetric winding arrangement is illustrated in Fig. 4.1. The special assembly sequence is also shown in the same figure. The main idea of the new assembly is to build one phase winding completely ready before proceeding to the second and third phase windings. In a traditional double-layer winding, all bottom coil sides must be installed before the topmost coil sides. Such an approach would be almost impossible with this winding material.

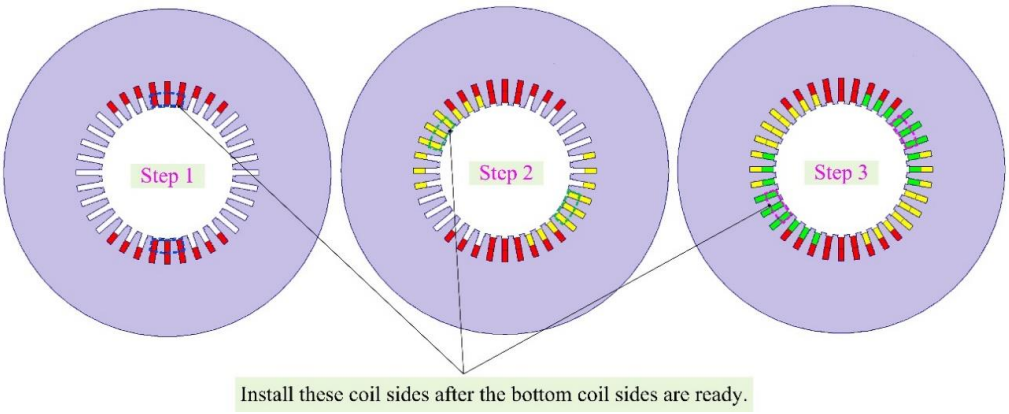

Fig. 4.1 Asymmetric winding arrangement and its assembly sequence (adapted from **Publication IV**).

It can be seen in the figure that every phase winding is built of two similar coil sets, which can be connected in parallel. This enables low-voltage operation of the 2 MW high-speed machine. It could be assumed that the magnetizing inductance is fully symmetric with such an arrangement. However, it does not provide fully symmetrical total inductances in all three phases, because the three-phase stator slot leakage inductance is not symmetric. As shown in Fig. 4.1, there are different numbers of winding turns (18, 6, and 12) for phases U, V, and W placed in the slot bottom. This winding arrangement will cause asymmetric stator leakage inductances, and they will be $L_{s\sigma,U} > L_{s\sigma,W} > L_{s\sigma,V}$. These asymmetric leakage inductances will not cause very strong asymmetry in the stator impedance. However, they will slightly affect the magnetizing inductance in some cases. If the machine is driven with a voltage source, the overall flux input from the supply terminal is always constant. Once the leakage inductance is asymmetric, a different proportion of leakage flux leads to a different proportion of the flux that penetrates the air gap (magnetizing flux). This causes a different amount of magnetizing flux produced by different phases, which also leads to a different influence of the magnetizing flux on the permeability distribution, whereas a different permeability distribution affects the magnetizing inductance. It means that the magnetizing inductance in all three phases is not asymmetric with this winding arrangement either.

The phase currents (the total of two branches in parallel) at the nominal load (per-unit slip $s_N = 0.0046$) for the machine equipped with the proposed asymmetric winding in the steady state (1 s in the FEM) are about 1315 Arms (phase U), 1418 Arms (phase V), and

1368 Arms (phase W). To maintain the option of low-voltage operation, the winding is in the delta connection, and therefore, these unbalance currents along with the third harmonic currents will finally cause circulating currents within the delta connection. The corresponding line currents are 2332 Arms, 2363 Arms, and 2409 A rms. These data indicate that the line current unbalance is slightly smaller than the phase current unbalance. One of the reasons is that the circulating current can only travel inside the delta connection.

Some indices are proposed here to describe the current unbalance. The first index is the current unbalance ratio (CUR). It is also defined in **Publication IV**, and it is originally taken from the voltage unbalance ratio, which is defined in the IEEE standard [63]. It can be expressed by:

$$\mathrm{CUR} = \frac{\mathrm{Max}\left(|I_\mathrm{U} - I_\mathrm{V}|, |I_\mathrm{U} - I_\mathrm{W}|, |I_\mathrm{V} - I_\mathrm{W}|\right)}{\mathrm{Avg}\left(I_\mathrm{U}, I_\mathrm{V}, I_\mathrm{W}\right)} \times 100\% \ , \tag{15}$$

where I_U, I_V, and I_W are the fundamentals of the three-phase current. In fact, this equation describes the degree of the maximum current deviation with respect to the average current value.

Some other indices are proposed to describe the current unbalance. The current can also be decomposed into the positive-sequence (PS) current ($\underline{I}_\mathrm{PS}$), the negative-sequence (NS) current ($\underline{I}_\mathrm{NS}$), and the zero-sequence (ZS) current ($\underline{I}_\mathrm{ZS}$). Current unbalance factors (CUFs) for the NS current and the ZS current are proposed in **Publication IV** as:

$$\begin{cases} \mathrm{CUF}_\mathrm{NS} = \dfrac{\underline{I}_\mathrm{NS}}{\underline{I}_\mathrm{PS}} \times 100\% \\ \mathrm{CUF}_\mathrm{ZS} = \dfrac{\underline{I}_\mathrm{ZS}}{\underline{I}_\mathrm{PS}} \times 100\% \end{cases} , \tag{16}$$

where $\underline{I}_\mathrm{PS}$, $\underline{I}_\mathrm{NS}$, and $\underline{I}_\mathrm{ZS}$ can be expressed by the three-phase phase or line current as:

$$\begin{cases} \underline{I}_\mathrm{ZS} = \dfrac{\underline{I}_\mathrm{U} + \underline{I}_\mathrm{V} + \underline{I}_\mathrm{W}}{3} \\ \underline{I}_\mathrm{PS} = \dfrac{\underline{I}_\mathrm{U} + \underline{a}\,\underline{I}_\mathrm{V} + \underline{a}^{\,2}\,\underline{I}_\mathrm{W}}{3} \\ \underline{I}_\mathrm{NS} = \dfrac{\underline{I}_\mathrm{U} + \underline{a}^{\,2}\,\underline{I}_\mathrm{V} + \underline{a}\,\underline{I}_\mathrm{W}}{3} \end{cases} , \tag{17}$$

where $\underline{I}_U$, $\underline{I}_V$, and $\underline{I}_W$ are the current phasors, and $\underline{a}$ is the operator ($1\angle 120°$).

Based on Equations (15) and (16), CURs and CUFs can be calculated for both the three-phase phase and line currents at the nominal load, and the indices are listed in Table 4.1. The table shows that the line CUR is almost half of the phase CUR. It is caused by the circulating current in the delta connection. It can be seen in the table that there is no ZS current in the line current. This is explained by the fact that the ZS current belongs to the circulating current, and it cannot flow into the line current. In addition, the phase CUF_{NS} and the line CUF_{NS} are almost the same because the NS current is capable of traveling out of the delta connection.

TABLE 4.1 CURRENT UNBALANCE INDICES AT THE NOMINAL LOAD WITH THE ASYMMETRIC WINDING

Index	**Value**
CUR (phase current), [%]	7.52
CUR (line current), [%]	3.26
CUF_{NS} (phase current), [%]	1.90
CUF_{ZS} (phase current), [%]	2.46
3rd harmonic circulating current, [Arms]	37.93
CUF_{NS} (line current), [%]	1.91

In addition, the current balance results in a 71.5 Nm torque ripple (peak-peak value, about 4.5% of the rated torque). The analysis above indicates that the asymmetric winding does not cause a very strong current unbalance. However, this minor current unbalance produces some circulating currents, torque ripple, and even extra losses. Still, it is possible to mitigate the inherent current unbalance by a further modification of the coil arrangement, as the inherent current unbalance is not very strong.

4.2 Method to mitigate the current unbalance

It was mentioned in the previous section that the current unbalance is mainly caused by the unbalanced stator inductance (mainly because of the leakage flux inductance $L_{s\sigma,U} > L_{s\sigma,W} > L_{s\sigma,V}$). Therefore, one possible way to mitigate the current unbalance is to reduce the phase U inductance, and simultaneously increase the phase W and phase V inductances. In addition, it is more efficient to adjust the slot leakage flux inductance, and therefore, the proposed method to mitigate the current unbalance is implemented by adjusting the winding coil position in the slot. It is possible that some air-gap main flux is lost, as a result of which the slip may increase. This happens because some more stator leakage is produced as the stator slot depth has to be increased to perform the leakage inductance adjustment. In order not to sacrifice the efficiency as a result of the increased slip, the terminal voltage of the machine can, in theory, be adjusted. In practice, the main

dimensions of the machine can be slightly modified, or the slots could be made somewhat wider to compensate for the extra depth.

Fig. 4.2(a) shows a schematic diagram of the idea to adjust the slot leakage. The slot leakage can be changed when the height of the slot is adjusted. In the figure, it is shown that when the slot height is increased, some empty slot areas appear. These areas can be filled with a nonconducting nonmagnetic material (e.g. fiberglass material). The position of these empty areas within the slot will affect the slot leakage. If the extra slot area is located at the top of the slot, it provides an extra path for the flux, as shown in Fig. 4.2(a). The extra path for the flux can be considered as an extra magnetic reluctance (which does not cross the air gap) in parallel with the main magnetic circuit (which crosses the air gap). Therefore, the total magnetic reluctance will be increased, and thus, the current (to induce the same magnetic flux) will decrease, which is suitable for phase W and phase V, as they have a lower flux leakage compared with phase U.

However, the extra slot area will not significantly affect the magnetic circuit if it is located at the bottom of the slot. If the empty space is at the bottom of the slot, there is no current linkage to drive the slot leakage flux in that area. This is because an extra parallel path for the flux at the bottom of the slot does not significantly change the total magnetic reluctance of the magnetic circuit as the stator yoke (which is located just below the slot) already has a very high permeability, where the flux travels freely. Thus, this extra reluctance can almost be neglected, while the flux is more likely to travel in the yoke compared with the extra slot area with a high magnetic reluctance. Therefore, the extra area at the bottom of the slot can hardly affect the overall leakage magnetic flux. However, it might affect the main magnetic circuit by changing the yoke width, because with the increased slot height (keeping the same outer stator diameter), the yoke width is reduced. Therefore, the overall magnetic reluctance increases in all phases, which can be used for reducing the inductance in phase U. Naturally, the inductance is reduced also in phases W and V, which is later increased to a certain extent by the correct positioning of the windings within the slot, applying the phenomenon described above.

According to the idea of adjusting the slot leakage described in the previous section, the specific implementation is shown in Fig. 4.2(b). There are two steps; the first step is to introduce some extra slot areas in all the slots equally (to keep the stator lamination geometry symmetrical), keeping an empty slot area at the top of the slot for phases V and W so that the currents in these phases will be reduced (because of the higher overall inductance). Simultaneously, an empty slot area is positioned at the bottom of the slot for phase U to increase the supply current (because of the lower overall inductance). After the first step, as shown in Figure 4 in **Publication IV**, the extra slot height reaches 10 mm (keeping an empty slot area at the top of the slot for phases W and V, and at the bottom of the slot for phase U). At this point, the currents in phases U and V are almost the same, but the current in phase W is slightly smaller than in the other two phases. However, already at this step all the current unbalance indices are significantly reduced.

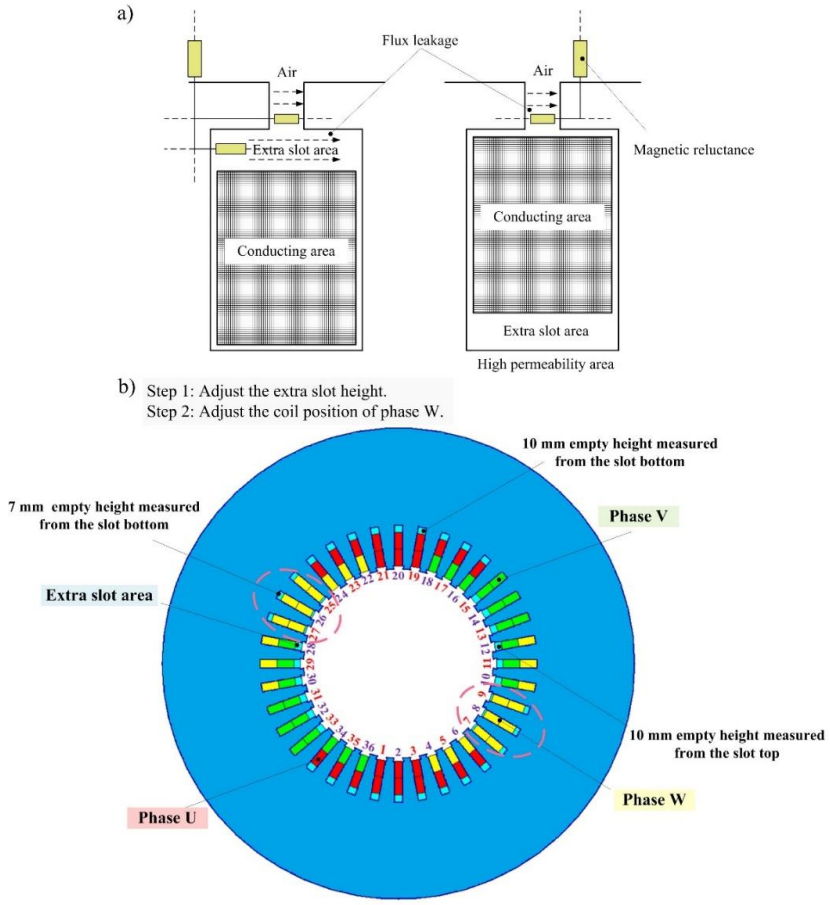

Fig. 4.2 Coil arrangement for mitigation of the current unbalance. (a) Stator slot leakage flux paths with the different coil positions in the stator slot (the slot leakage flux permeance is increased on the left side). (b) Steps to mitigate the current unbalance with a modified coil arrangement (adapted from **Publication IV**).

After the extra slot height has been optimized, the next step is to further adjust the phase W current, and the current should be increased. Because the current in phase W is smaller than in the other two phases after step 1, it should be increased by reducing the leakage inductance in this phase. Therefore, the position of coil sides Nos. 25, 26, 27, 7, 8, and 9 defined in Fig. 4.2(b) can be adjusted accordingly. After step 1, the windings of phase W (Nos. 25, 26, 27, 7, 8, and 9) are located at the bottom of the slot (an empty slot area at the top of the slot), and thus, the leakage inductance is the highest. Now, the position of the winding can be adjusted so that the empty slot area at the top of the slot is reduced while an extra empty slot area appears at the bottom of the slot. Once the height of the empty slot at the bottom of the slot reaches 7 mm, the three-phase current is, in practice, balanced. The corresponding detailed analysis is shown in **Publication IV**; please note, however, that the simulations in **Publication IV** are conducted at per-unit slip $s = 0.005$.

The final coil arrangement, especially positioning of the coils within the stator slots, is shown in Fig. 4.2(b).

4.3 Current unbalance analysis with the modified coil arrangement

The simulated current waveforms in the steady state of the modified coil arrangement are show in Fig.4.3. Fig. 4.3(a) shows that the phase currents are almost balanced. The peak values are about 1977 A, 1969 A, and 1975 A, and the fundamentals are about 1362 Arms, 1356 Arms, and 1361 Arms. These values seem quite acceptable for a 2 MW machine. Because the machine is in the delta connection, the circulating current can hardly be avoided even though the phase current is almost balanced. In this case, the strongest circulating current is about 36 Arms among all harmonics, and it belongs to the 3rd-order harmonic current. The fundamental circulating current is very small, about 8.6 Arms (fundamental ZS current).

In Fig. 4.3(b), the line current peak values are about 3344 A, 3342 A, and 3305 A, and the fundamentals are about 2363 Arms, 2365 Arms, and 2336 Arms. All the corresponding current unbalance indices are listed in Table 4.2. It can be seen that most of the unbalance indices are significantly reduced by the proposed coil, which increases the acceptance of the present current unbalance in practice. However, the 3rd harmonic circulating current almost does not change, because the 3rd harmonic current is not directly related to the unbalance problem. On the other hand, the 3rd harmonic circulating current is more related to the saturation harmonic, which is affected by the stator and rotor saturation, and it can hardly be mitigated without significant changes in the machine structure and geometry. Further, as it was mentioned in Chapter 1, in the solid-rotor IM, the rotor should run at high saturation to obtain a higher rotor power factor. Finally, applying the proposed method to balance the currents in the originally unbalanced windings, the torque ripple is reduced from 71.5 Nm (peak-peak value, 4.5% of the rated torque) to 29.9 Nm (peak-peak value, 1.9% of the rated torque). It is reduced by more than 50% of the original value.

In this section, a special coil arrangement is proposed to mitigate the current unbalance (winding inductance unbalance) caused by the asymmetric winding arrangement. Its main advantages are that it does not need any extra investments in power electronics devices, and it promotes a simple installation of the stator winding. The simulated results show that all the current unbalance indices are kept within a low range if the proposed arrangement is used. However, the drawback of the method is that it somewhat degrades the efficiency of the machine if the machine is not further modified (e.g. by increasing the stator outer diameter).

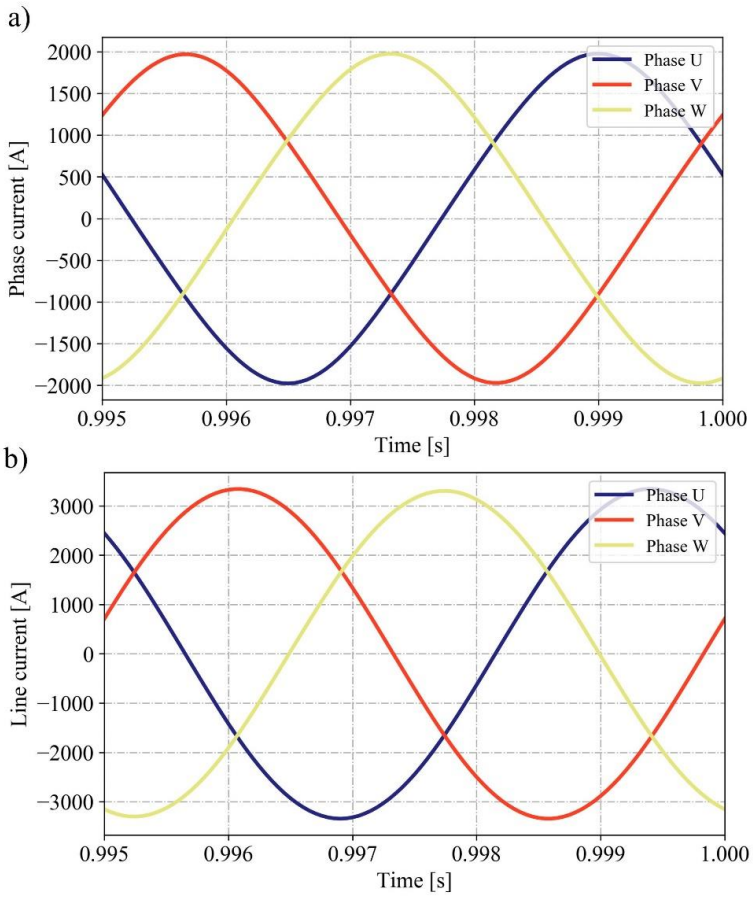

Fig. 4.3 Phase and line current waveforms at the nominal load (per-unit $s_N = 0.0046$) in the steady state with the modified coil arrangement. (a) Three-phase phase current waveforms. (b) Three-phase line current waveforms.

TABLE 4.2 CURRENT UNBALANCE INDICES AT THE NOMINAL LOAD WITH THE MODIFIED ASYMMETRIC WINDING

Index	Value	Reduction, [%]
CUR (phase current), [%]	0.39	94.8
CUR (line current), [%]	1.19	63.5
CUF_{NS} (phase current), [%]	0.77	59.5
CUF_{ZS} (phase current), [%]	0.63	74.4
3^{rd} harmonic circulating current, [Arms]	36	5.0
CUF_{NS} (line current), [%]	0.77	59.7

5 Conclusions

5.1 Summary

The research documented in this doctoral dissertation focused on the modeling and analysis of a high-speed solid-rotor IM. The research was divided into three topics, which were addressed in detail in the accompanying publications and the introductory part of this dissertation. The initial design of the solid-rotor IM was reported in **Publication V**, and it was modified and improved in **Publication IV**.

The first topic concerned acceleration of the numerical transient of the transient magnetic (TM) finite element solution for the solid rotor in the 2D FEA. The reasons for the electromagnetic transient were first explained, and it was decomposed into two elements including the stator electromagnetic time constant and the rotor electromagnetic time constant. A special method was proposed based on reducing these two time constants for a voltage-driven solid-rotor IM. The proposed method was implemented by using a modified locked rotor model and a switchable excitation. The simulation time varied depending on the accuracy of the initial current. If the initial solution current value is not correct when the current excitation is switched to the voltage transient, a subtransient will be seen, prolonging the attenuation of the solution to the final values. The simulation time was about 57% of the original full transient solution to achieve the accurate defined steady state, and in **Publication I**, the simulation time was about 37% of the original full transient solution. A detailed error analysis of the initial current was presented in **Publication I**. The proposed method was also compared with commercial solutions, and the results showed that it is a potential alternative to the commercial solutions available.

The second topic dealt with the extraction of the solid-rotor eddy-current harmonic losses. It is important to know which harmonic creates the highest rotor-surface losses. To be able to mitigate the effect, the air-gap flux density harmonics were investigated before computing the harmonic losses. An analytical method was used to determine the properties of the harmonics including the order, rotational speed, and induced current. The 2D fast Fourier transform was employed to extract the air-gap flux density harmonics. After that, the solid-rotor eddy-current harmonic losses were modeled by setting the specific air-gap flux density harmonic in the air gap using the actual local permeability of the rotor. The main contribution of this method is that it is capable of taking the rotor saturation into consideration, which is achieved by a hybrid excitation. Finally, the solid-rotor eddy-current harmonic losses (by each individual harmonic) could be computed in the FEM. In addition, the method described here is also capable of extracting other electromagnetic factors caused by harmonics, such as penetration depth and permeability distribution. All the corresponding materials were reported in detail in **Publications II** and **III**.

The last topic was associated with the mitigation of the current unbalance resulting from an asymmetric stator winding arrangement. First, the asymmetric winding arrangement

was presented, and it was found that there is an inherent unbalanced phase inductance that causes some current unbalance. The unbalance was not very significant, and therefore, there was potential to mitigate it by changing the winding coil positions in the stator slot. The coil arrangement was further optimized, and finally, most of the current unbalance factors stayed within 1% except for the current unbalance ratio (line current). The torque ripple resulting from the negative-sequence current was also significantly suppressed. A more detailed analysis was reported in **Publication IV**.

5.2 Suggestions for further work

Some further work can be done in terms of the topics presented in this doctoral dissertation as follows:

To the author's knowledge, full 3D finite element analyses of different solid rotors have not been thoroughly reported yet. The 3D simulation of a solid-rotor IM is always very time consuming, and therefore, the approach presented in Chapter 2 has the potential to be developed and improved for 3D applications. In addition, if eddy-current effects of the permanent magnets in PMSMs caused by harmonics are analyzed, it also takes several electrical time periods to reach the steady state in the TM solution. Thus, it is also recommended to use the proposed method for PMSMs when strong eddy currents are involved. Besides, some further aspects that will affect the transient performance of the proposed approach could also be studied, especially the algorithm of changing the rotor resistivity and the rotor speed accordingly, when the locked rotor starts to rotate.

In Chapter 3, the solid-rotor eddy-current losses were analyzed by the proposed approach. The same means can be employed to further study the stator iron losses caused by the harmonics. In addition, it was mentioned in Chapter 3 that the saturation harmonics will also cause some rotor losses, and this phenomenon calls for more investigation. The rotor was designed to operate at a high flux density, and the stator winding was in the delta connection to be able to design a low-voltage machine. However, saturation causes a circulating current in that condition. Therefore, mitigating the circulating current is also highly significant. In addition, it is important to further reduce the rotor losses by applying skewing; the skew angle can be adjusted based on the harmonic losses provided by the proposed approach. Skewing seems to be an effective method for reducing rotor harmonic losses in the case of a slitted solid rotor.

The current unbalance caused by the asymmetric winding arrangement was significantly mitigated by the proposed special coil arrangement reported in Chapter 4. It provides an opportunity to design a machine winding in a more flexible way. Some other asymmetric windings can be used for special purposes, and the inherent asymmetric inductance can be mitigated by the method described in Chapter 4.

References

[1] P. T. Pappas, L. P. Pappas, and T. P. Pappas, “Ampère Cardinal Forces-Electrodynamics—Proof and Prediction of Empirical Faraday Induction,” *Physics Essays*, vol. 27, no. 4, pp. 570–579, Dec. 2014.

[2] F. T. Ulaby, *Fundamentals of Applied Electromagnetics (5th Edition)*, Prentice Hall, 2006.

[3] K. Yee, “Numerical Solution of Initial Boundary Value Problems Involving Maxwell's Equations in Isotropic Media,” *IEEE Transactions on Antennas and Propagation*, vol. 14, no. 3, pp. 302–307, May 1966.

[4] J. Pyrhönen, T. Jokinen, and V. Hrabovcova, *Design of Rotating Electrical Machines*, John Wiley & Sons, 2013.

[5] J. Pyrhönen, V. Hrabovcova, and R. S. Semken, *Electrical Machine Drives Control: An Introduction*, John Wiley & Sons, 2016.

[6] H. Aalto, K. Lyytikäinen, K. Murashko, L. Laurila, T. Koiranen, K. Koiranen, and J. Pyrhönen, “Carbon Nanotube Supercellulose Supercapacitor,” in *2014 16th European Conference on Power Electronics and Applications*, pp. 1–10, Aug. 2014.

[7] K. Fonteyn, A. Belahcen, R. Kouhia, P. Rasilo, and A. Arkkio, “FEM for Directly Coupled Magneto-Mechanical Phenomena in Electrical Machines,” *IEEE Transactions on Magnetics*, vol. 46, no. 8, pp. 2923–2923, Aug. 2010.

[8] M. Enokizono, “Vector Magnetic Characteristic Technology for Development of Super Premium Efficiency (IE4 Level) Motor,” *IEEE Transactions on Magnetics*, vol. 48, no. 11, pp. 3054–3059, Nov. 2012.

[9] M. A. Rahman, A. Chiba, and T. Fukao, “Super High Speed Electrical Machines-Summary,” in *IEEE Power Engineering Society General Meeting, 2004*, pp. 1272–1275, June 2004.

[10] R. Pena-Alzola, R. Sebastián, J. Quesada, and A. Colmenar, “Review of Flywheel Based Energy Storage Systems,” in *2011 International Conference on Power Engineering, Energy and Electrical Drives*, pp. 1–6, May 2011.

[11] J. Pyrhönen, J. Nerg, P. Kurronen, and U. Lauber, “High-Speed High-Output Solid-Rotor Induction-Motor Technology for Gas Compression,” *IEEE Transactions on Industrial Electronics*, vol. 57, no. 1, pp. 272–280, Jan. 2010.

[12] Z. Huang, B. Han, and Y. Le, “Multidisciplinary Design Strategies for Turbomolecular Pumps with Ultrahigh Vacuum Performance,” *IEEE Transactions on Industrial Electronics*, vol. 66, no. 12, pp. 9549–9558, Dec. 2019.

[13] A. Maeda and H. Tomita, “Power and Speed Limitations in High Speed Electrical Machines,” in *Proceedings of the International Power Electronics Conference (IPEC)-Yokohama*, pp. 1321–1326, 1995.

[14] D. Gerada, A. Mebarki, N. L. Brown, K. J. Bradley, C. Gerada, A. Cavagnino, and A. Boglietti, "High-Speed Electrical Machines: Technologies, Trends, and Developments," *IEEE Transactions on Industrial Electronics*, vol. 61, no. 6, pp. 2946–2959, June. 2014.

[15] R. D. van Millingen, and J. D. van Millingen. "Phase Shift Torquemeters for Gas Turbine Development and Monitoring," in *ASME 1991 International Gas Turbine and Aeroengine Congress and Exposition*, pp. 1–10, June 1991.

[16] D. Gerada, A. Mebarki, N. L. Brown, K. J. Bradley, and C. Gerada, "Design Aspects of High-Speed High-Power-Density Laminated-Rotor Induction Machines," *IEEE Transactions on Industrial Electronics*, vol. 58, no. 9, pp. 4039–4047, Sept. 2011.

[17] Z. Huang, J. Fang, X. Liu, and B. Han, "Loss Calculation and Thermal Analysis of Rotors Supported by Active Magnetic Bearings for High-Speed Permanent-Magnet Electrical Machines," *IEEE Transactions on Industrial Electronics*, vol. 63, no. 4, pp. 2027–2035, Apr. 2016.

[18] S. M. Castano, B. Bilgin, E. Fairall, and A. Emadi, "Acoustic Noise Analysis of a High-Speed High-Power Switched Reluctance Machine: Frame Effects," *IEEE Transactions on Energy Conversion*, vol. 31, no. 1, pp. 69–77, Mar. 2016.

[19] M-I. Lamghari-Jamal, J. Fouladgar, E-H. Zaim, and D. Trichet, "A Magneto-Thermal Study of a High-Speed Synchronous Reluctance Machine," *IEEE Transactions on Magnetics*, vol. 42, no. 4, pp. 1271–1274, Apr. 2006.

[20] H. Hofmann and S. R. Sanders, "High-Speed Synchronous Reluctance Machine with Minimized Rotor Losses," *IEEE Transactions on Industry Applications*, vol. 36, no. 2, pp. 531–539, Mar. 2000.

[21] E. Richter and C. Ferreira, "Performance Evaluation of a 250 kW Switched Reluctance Starter Generator," in *IAS'95. Conference Record of the 1995 IEEE Industry Applications Conference Thirtieth IAS Annual Meeting*, vol. 1, pp. 434–440, Oct. 1995.

[22] Y. Honda, S. Yokote, T. Higaki, and Y. Takeda, "Using the Halbach Magnet Array to Develop an Ultrahigh-Speed Spindle Motor for Machine Tools," *IAS '97. Conference Record of the 1997 IEEE Industry Applications Conference Thirty-Second IAS Annual Meeting*, vol. 1, pp. 56–60, Oct. 1997.

[23] J. Lahteenmaki, "Design and Voltage Supply of High-Speed Induction Machines," Doctoral dissertation, Helsinki University of Technology, Espoo, Finland, 2002.

[24] M. Caprio, V. Lelos, J. Herbst, and J. Upshaw, "Advanced Induction Motor Endring Design Features for High Speed Applications," in *IEEE International Conference on Electric Machines and Drives*, pp. 993–998, May 2005.

[25] K. Wang, M. J. Jin, J. X. Shen, and H. Hao, "Study on Rotor Structure With Different Magnet Assembly in High-Speed Sensorless Brushless DC Motors," *IET Electric Power Applications*, vol. 4, no. 4, pp. 241–248, Sept. 2010.

[26] J. Saari and A. Arkkio, "Losses in High Speed Asynchronous Motors," in *International Conference on Electrical Machines*, vol. 3, pp. 704–708, Sept. 1994.

[27] S. L. Ho, S. Niu, and W. N. Fu, "A Novel Solid-Rotor Induction Motor With Skewed Slits in Radial and Axial Directions and Its Performance Analysis Using Finite Element Method," *IEEE Transactions on Applied Superconductivity*, vol. 20, no. 3, pp. 1089–1092, Jun. 2010.

[28] M. O. Gulbahce, D. T. Mcguiness, and D. A. Kocabas, "Shielded Axially Slitted Solid Rotor Design for High-Speed Solid Rotor Induction Motors," *IET Electric Power Applications*, vol. 12, no. 9, pp. 1371–1377, 2018.

[29] A. H. Oguz, M. O. Gülbahce, and D. A. Kocabas, "Design and Optimization of an Axially-Slitted High-Speed Solid Rotor Induction Motor," in *2015 9th International Conference on Electrical and Electronics Engineering (ELECO)*, pp. 568–573, Nov. 2015.

[30] T. Aho, "Electromagnetic Design of a Solid Steel Rotor Motor for Demanding Operation Environments," Doctoral dissertation, Lappeenranta University of Technology, Lappeenranta, Finland, 2007.

[31] T. Aho, J. Nerg, J. Sopanen, J. Huppunen, and J. Pyrhönen, "Analyzing the Effect of the Rotor Slit Depth on the Electric and Mechanical Performance of a Solid-Rotor Induction Motor," *International Review of Electrical Engineering*, vol. 1, no. 4, pp. 516–524, Sept./Oct. 2006.

[32] B. Zhang, R. Qu, X. Fan, and J. Wang, "Thermal and Mechanical Optimization of Water Jacket of Permanent Magnet Synchronous Machines for EV Application," in *2015 IEEE International Electric Machines Drives Conference (IEMDC)*, pp. 1329–1335, May 2015.

[33] P. Lindh, I. Petrov, P. Immonen, J. Pyrhönen, M. Niemelä, J. Anttila, M. Paakkinen, and E. Scherman, "Performance of a Direct-Liquid-Cooled Motor in an Electric Bus Under Different Load Cycles," *IEEE Access*, vol. 7, pp. 86897–86905, 2019.

[34] T. Aho, V. Sihvo, J. Nerg, and J. Pyrhonen, "Rotor Materials for Medium-Speed Solid-Rotor Induction Motors," in *2007 IEEE International Electric Machines Drives Conference*, pp. 525–530, May 2007.

[35] J. Huppunen, "High-speed Solid-Rotor Induction Machine–Electromagnetic Calculation and Design," Doctoral dissertation, Lappeenranta University of Technology, Lappeenranta, Finland, 2004.

[36] T. Aho, J. Nerg, and J. Pyrhonen, “Experimental and Finite Element Analysis of Solid Rotor End Effects,” in *2007 IEEE International Symposium on Industrial Electronics*, pp. 1242–1247, June 2007.

[37] A. Krings and J. Soulard, “Overview and Comparison of Iron Loss Models for Electrical Machines,” *Journal of Electrical Engineering*, vol. 10, no. 3, pp. 162–169, 2010.

[38] A. Belahcen and A. Arkkio, “Comprehensive Dynamic Loss Model of Electrical Steel Applied to FE Simulation of Electrical Machines,” *IEEE Transactions on Magnetics*, vol. 44, no. 6, pp. 886–889, June 2008.

[39] İ. Tarımer, S. Arslan, and M. E. Güven, “Investigation for Losses of M19 and Amorphous Core Materials Asynchronous Motor by Finite Elements Methods,” *Elektronika ir Elektrotechnika*, vol. 18, no. 9, pp. 15–18, May 2012.

[40] Y. H. Hu, S. S. Zhu, and C. Liu, “Magnet Eddy-Current Loss Analysis of Interior PM Machines for Electric Vehicle Application,” *IEEE Transactions on Magnetics*, vol. 53, no. 11, pp. 1–4, Nov. 2017.

[41] C. Di, X. Bao, F. Wang, Q. Lv, and Y. He, “Modeling and Analysis of Unbalanced Magnetic Pull in Cage Induction Motors with Curved Dynamic Eccentricity,” *IEEE Transactions on Magnetics*, vol. 51, no. 8, pp. 1–7, Aug. 2015.

[42] I. Petrov, P. Lindh, and J. Pyrhönen, “Importance of Accurate Iron Permeability in Saturated Condition on Performance Evaluation of Flux-Switching Permanent Magnet Synchronous Machines,” *IEEE Transactions on Magnetics*, vol. 54, no. 6, pp. 1–7, June 2018.

[43] Y. Wang, D. Lonel, D. G. Dorrell, and S. Stretz, “Establishing the Power Factor Limitations for Synchronous Reluctance Machines,” *IEEE Transactions on Magnetics*, vol. 51, no. 11, pp. 1–4, Nov. 2015.

[44] G. J. Li, K. Zhang, Z. Q. Zhu, and G. W. Jewell, “Comparative Studies of Torque Performance Improvement for Different Doubly Salient Synchronous Reluctance Machines by Current Harmonic Injection,” *IEEE Transactions on Energy Conversion*, vol. 34, no. 2, pp. 1094–1104, June 2019.

[45] J. Keränen, P. Ponomarev, J. Pippuri, P. Raback, M. Lyly, and J. Westerlund,“Parallel Performance of Multi-Slice Finite-Element Modeling of Skewed Electrical Machines,” *IEEE Transactions on Magnetics*, vol. 53, no. 6, pp. 1–4, June 2017.

[46] W. Jiang, T. M. Jahns, T. A. Lipo, W. Taylor, and Y. Suzuki, “Machine Design Optimization Based on Finite Element Analysis in a High-Throughput Computing Environment,” in *2012 IEEE Energy Conversion Congress and Exposition (ECCE)*, pp. 869–876, Sept. 2012.

[47] O. Biro and K. Preis, “An Efficient Time Domain Method for Nonlinear Periodic Eddy Current Problems,” *IEEE Transactions on Magnetics*, vol. 42, no. 4, pp. 695–698, Apr. 2006.

[48] D. Lin, P. Zhou, N. Chen, C. Lu, and M. Christini, “Fast Methods for Reaching AC Steady State in FE Transient Analysis,” in *2017 IEEE International Electric Machines and Drives Conference (IEMDC)*, pp. 1–6, May 2017.

[49] D. N. Dyck and P. J. Weicker, “Periodic Steady-State Solution of Voltage-Driven Magnetic Devices,” *IEEE Transactions on Magnetics*, vol. 43, no. 4, pp. 1533–1536, Apr. 2007.

[50] M. Rosu, P. Zhou, D. Lin, D. M. Ionel, M. Popescu, F. Blaabjerg, V. Rallabandi, and D. Staton, *Multiphysics Simulation by Design for Electrical Machines, Power Electronics and Drives*, John Wiley & Sons, 2017.

[51] E. Vassent, G. Meunier, and J. C. Sabonnadier, “Simulation of Induction Machine Operation Using Complex Magnetodynamic Finite Elements,” *IEEE Transactions on Magnetics*, vol. 25, no. 4, pp. 3064–3066, July 1989.

[52] A. Stermecki, O. Bíró, K. Preis, S. Rainer, and G. Ofner, “Numerical Analysis of Steady-State Operation of Three-Phase Induction Machines by an Approximate Frequency Domain Technique,” *e & i Elektrotechnik und Informationstechnik*, vol. 128, no. 3, pp. 81–85, Mar. 2011.

[53] A. H. Amor, P. L. Timar, and M. Poloujadoff, “Induction Squirrel Cage Machine Design with Minimization of Electromagnetic Noise,” *IEEE Transactions on Magnetics*, vol. 10, no. 4, pp. 681–687, Dec. 1995.

[54] Q. Gu, L. Yuan, Z. Zhao, F. Lu, and J. Sun, “An Accurate Stray Loss Calculation Method of Squirrel-Cage Induction Motors for Efficiency Optimization,” in *2015 18th International Conference on Electrical Machines and Systems (ICEMS)*, pp. 143–149, Oct. 2015.

[55] D. Kim, H. Kim, J. Hong, and C. Park, “Estimation of Acoustic Noise and Vibration in an Induction Machine Considering Rotor Eccentricity,” *IEEE Transactions on Magnetics*, vol. 50, no. 2, pp. 857–860, Feb. 2014.

[56] C. Wang, X. Bao, S. Xu, Y. Zhou, W. Xu, and Y. Chen, “Analysis of Vibration and Noise for Different Skewed Slot-type Squirrel-Cage Induction Motors,” *IEEE Transactions on Magnetics*, vol. 53, no. 11, pp. 1–6, Nov. 2017.

[57] M. Jagiela and T. Garbiec, “Evaluation of Rotor-End Factors in Solid-Rotor Induction Motors,” *IEEE Transactions on Magnetics*, vol. 48, no. 1, pp. 137–142, Jan. 2012.

[58] Y. Demir and M. Aydin, “A Novel Asymmetric and Unconventional Stator Winding Configuration and Placement for a Dual Three-Phase Surface PM Motor,” *IEEE Transactions on Magnetics*, vol. 53, no. 11, pp. 1–5, Nov. 2017.

[59] E. Yolacan, M. K. Guven, and M. Aydin, “A Novel Torque Quality Improvement of an Asymmetric Windings Permanent-Magnet Synchronous Motor,” *IEEE Transactions on Magnetics*, vol. 53, no. 11, pp. 1–6, Nov. 2017.

[60] Y. Hu, Z. Q. Zhu, and M. Odavic, “Compensation of Unbalanced Impedance of Asymmetric Wind Power PMSG Compensated by External Circuits in Series,” *CES Transactions on Electrical Machines and Systems*, vol. 1, no. 2, pp. 180–188, July 2017.

[61] Z. Q. Zhu, M. L. Mohd Jamil, and L. J. Wu, “Influence of Slot and Pole Number Combinations on Unbalanced Magnetic Force in PM Machines with Diametrically Asymmetric Windings,” *IEEE Transactions on Industry Applications*, vol. 49, no. 1, pp. 19–30, Jan. 2013.

[62] P. Verdelho and G. D. Marques, “An Active Power Filter and Unbalanced Current Compensator,” *IEEE Transactions on Industrial Electronics*, vol. 44, no. 3, pp. 321–328, June 1997.

[63] “IEEE Guide for Self-Commutated Converters, ” *ANSI/IEEE Std 936-1987*, pp. 1–42, 1987.

Publication I

Di, C., Petrov, I., Pyrhönen, J., and Chen, J.
Accelerating the Time-Stepping Finite-Element Analysis of Induction Machines in Transient-Magnetic Solutions

Reprinted with permission from
IEEE Access
Vol. 7, pp. 122251-122260, 2019

IEEE Access
Multidisciplinary ⋮ Rapid Review ⋮ Open Access Journal

Received August 20, 2019, accepted August 26, 2019, date of publication August 29, 2019, date of current version September 11, 2019.

Digital Object Identifier 10.1109/ACCESS.2019.2938269

Accelerating the Time-Stepping Finite-Element Analysis of Induction Machines in Transient-Magnetic Solutions

CHONG DI[1], ILYA PETROV[1], JUHA J. PYRHÖNEN[1], (Senior Member, IEEE), AND JIAHAO CHEN[2], (Student Member, IEEE)

[1]Department of Electrical Engineering, Lappeenranta University of Technology, 53851 Lappeenranta, Finland
[2]Department of Electrical and Computer Engineering, University of Wisconsin–Madison, Madison, WI 53706, USA

Corresponding author: Chong Di (chong.di@lut.fi)

This work was supported in part by a scholarship from the China Scholarship Council (CSC) under Grant 201706690032.

ABSTRACT Finite-element analysis (FEA) is one of the most significant tools in the designing and analyzing of electrical machines, which mainly includes the transient-magnetic (TM), magnet-static (MS) and time-harmonic (TH) solutions. The transient-magnetic (TM) solution in FEA is capable of considering both the harmonic effects and eddy-current effects accurately, which makes it suitable for the induction machine (IM) simulation. However, the drawback of the TM FEA for the IM modelling is that it takes some time before reaching the steady state because of the longer numerical transient, which is affected by the inherent electromagnetic time constants of the IM directly. In this paper, a new approach is proposed to reduce the duration of the numerical transient of the IM in the time-stepping FEA so that the steady state can be achieved in a short time. The proposed approach is capable of creating an initial condition close to the final steady state for the simulation by eliminating or reducing the stator and rotor electromagnetic time constants separately. The stator electromagnetic time constant is eliminated by an initial current excitation (obtained by the TH solution or the analytical method) and the rotor electromagnetic time constant is reduced by a locked rotor model at the beginning of the simulation. Then the initial current excitation is switched to a voltage excitation and the locked rotor is turned to the rotating state at proper time. Finally, the proposed approach is tested and proved efficient to reduce the transients by two typical cases (a solid-rotor IM and a squirrel-cage IM) with 2D FEA.

INDEX TERMS Numerical transient, finite-element analysis (FEA), induction machine (IM), electromagnetic time constant, transient-magnetic (TM) solution.

I. INTRODUCTION

Finite-element analysis (FEA) has become very helpful and popular in the modelling of electrical machines in both academia and industry, owing to the rapid development of the modelling technologies and computational abilities, which makes the design and optimization of different types of electrical machines much more convenient than ever before [1]–[7]. Typically, there are mainly three types of solutions available for the electrical machine analysis in FEA: the magnet-static (MS) solution, time-harmonic (TH) solution and transient-magnetic (TM) solution [8]–[10]. Different solutions are suitable for different kinds of problems. MS solution is valid for applications where the eddy-current effects (e.g. rotor induced eddy currents or permanent magnet induced eddy currents) are ignored, which can be used to analyze permanent magnet synchronous machines (PMSMs) related problems without considering eddy-current losses in the permanent magnets. The TH solution is very efficient and capable of taking the eddy-current effects into account, which makes it suitable for the induction machine (IM) simulation. But the drawback for the TH solution is that neither the space nor time harmonics (e.g. winding harmonics or supply harmonics) can be modelled accurately. The TM solution is the most precise one and is suitable for all types of machines. However, sometimes it

The associate editor coordinating the review of this article and approving it for publication was Xiaodong Sun.

takes several supply periods to reach the steady state. This numerical transient in some cases, e.g. in IM simulations, is very long because of the strong rotor eddy-current effects and very high rotor electromagnetic time constants. The strong induced eddy currents do not frequently appear in other types of machines, and therefore, the focus of this paper is on IMs only. In most cases, the steady-state performance of the machine is the topic of primary interest. Therefore, reducing the numerical transient or simulation time for IMs is an important issue, especially in 3D simulations, parametric optimization and similar processes.

Basically, there are mainly two approaches available to reduce the physical simulation time. One approach is to take full advantage of the computational sources of the computers, such as the parallel computation and distributed computation. These functions are available for most of the well-known commercial packages for the electrical machine design e.g. Altair Flux, ANSYS Maxwell, JMAG and even some open source packages e.g. Elmer, GetDDM [11]–[15]. The time decomposition method (TDM) is another effective option for parallel computation realized by simulating several time steps in parallel and this function is already available in ANSYS Maxwell [16]. The key benefit of these approaches is that they are universal methods and valid for all the solutions instead of the a specific solution. The advantage is that the numerical transient remains the same as the traditional solution and only the simulation time is significantly reduced. The drawback of this approach is that it highly depends on the computer performance, it is sometimes efficient only when a workstation or a supercomputer is employed (e.g. 3D IM TM solutions), which means that this method calls for considerable hardware investments.

The other approach aims at shortening the numerical transient, which is actually based on the machine time constants and achieved by modifying the model in the simulation. The alternating flux (AF) linkage model is one of the effective approaches to reduce the transient [17]. The idea of this method is to eliminate the DC flux linkage during the transient by exciting the machine with an extra voltage. This has proved to be efficient for the simulation of transformers and synchronous generators [18]. The phase balancing (PB) method is yet another option to quickly reach a steady state by mitigating the DC currents in each step during the transient, which is very suitable for the brushless DC machine and synchronous machine [19], [20]. However, these two methods are not valid for cases, in which induced eddy currents are involved. The model order reduction (MOR) technique is capable of considering the eddy-current effects with the advantage of a low computing capacity and a quick transient [21]–[23]. The main drawback is, however, that the MOR is not suitable for applications where a high precision is required especially for the magnetic field distribution.

The use of appropriate initial values (for initialization of the TM solution) is one of the possible methods to shorten the numerical transient emersed in the TM solution during the IM simulation [24], [25]. This approach is suitable for eddy-current issues in IMs and the computing speed is highly depended on the initial conditions including currents, voltages, and even magnetic field distributions. Therefore, it is always recommended to use the TH solution to achieve the initial conditions for the TM solution. However, according to the classical theory, only the linear material with constant permeability can typically be used in a TH solution, because both the excitation and the response have to be sinusoidal in that case. The permeability has to be linearized to the operating point on the *B-H* curve, and a compromise has to be made because different parts of the machine operate at different flux densities. Thus, saturation cannot be considered accurately, and the field distributions are not precise enough either.

At present, the nonlinear *B-H* property of the magnetic core can be partly considered in TH solutions of some packages e.g. Altair Flux, ANSYS Maxwell, JMAG, and FEMM, by an equivalent curve based on the energetic equivalence method [26]–[28]. By applying this method, accurate scalar values (e.g. currents and torques) can be obtained from the TH solution. For example, the three-phase average line currents (RMS values) given by the TH and TM solutions are 2716 A and 2717 A, respectively, at per-unit slip $s = 0.005$ for a 660 V, 2-pole, 2 MW, 12000 r/min high-speed IM with a solid rotor as reported in [29]. Nevertheless, in steady state the magnetic field distribution given by the TH solution is still far from that given by the TM solution. Fig. 1 shows the flux density distributions of the high-speed IM solved by both TH and TM solvers. It can be seen in this figure that the flux density distributions on the stator side are quite similar in both cases. However, the flux density distributions on the rotor side are very different, even though the equivalent *B-H* curves are used when modelling the machine in the TH solver. This implies that there is sometimes still a very long transient for the TM solution initialized from the TH solution, especially in case of a long rotor electromagnetic time constant.

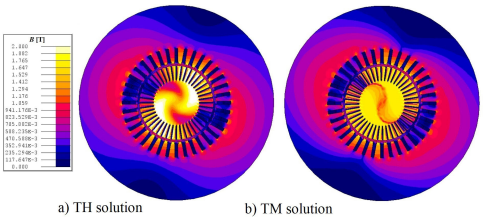

FIGURE 1. Comparison of high-speed IM flux density distributions at per-unit slip $s = 0.005$ plotted by the TH and TM solutions (Altair Flux 2D FEA). (a) Flux density distribution plotted by the TH solution with an equivalent *B-H* curve. (b) Flux density distribution plotted by the TM solution with a nonlinear *B-H* curve. Flux density scale is valid for both models.

In this paper, a new approach is proposed to shorten the time taken by the numerical transient of IMs in time-stepping FEA with the TM solver. Because the long transient for IMs is mainly caused by the stator winding inductance effects

(related to the stator electromagnetic time constant) and rotor eddy-current effects (related to the rotor electromagnetic time constant). The proposed method is implemented by reducing both the stator and rotor electromagnetic time constants in the TM solution. The stator electromagnetic time constant is totally eliminated by using current excitation, and the rotor time constant is significantly reduced by the locked rotor model [18]. The current excitation is switched to a voltage excitation and the machine is also switched from a locked rotor state to a rotating state at appropriate time. The method is discussed in details and tested by solving two IM models (a solid-rotor IM with relatively strong rotor eddy-current effects and a squirrel-cage IM with relatively weak rotor eddy-current effects) in this paper. The error analysis in the last section also shows that the proposed method has a good tolerance of the errors caused by the initial values.

II. DESCRIPTION AND IMPLEMENTATION OF THE PROPOSED APPROACH

A. OVERVIEW OF THE TRADITIONAL TM SOLUTION FOR IMs

For IMs, the numerical transient of a TM solution in time-stepping FEA is highly affected by the time constants of the whole system. There are two main time constants viz. the rotor mechanical time constant and the electromagnetic time constant. The rotor mechanical time constant can be easily eliminated by setting an imposed speed for the rotor, which means that the rotor speed is always a constant during the transient and no mechanical transient is allowed. The mechanical transient is not discussed in detail because it is more related to the mechanical issue and an imposed rotor speed is also used in the simulations.

The electromagnetic time constants can be divided into two components containing the stator electromagnetic time constant and the rotor time constant, which are directly related to the stator and rotor inductances. Table 1 gives the equivalent circuit parameters of the high-speed solid-rotor IM, which is mentioned in the Introduction and will be further discussed as an example when reducing the numerical transient in this paper. According to the table, both the stator and rotor could have long electromagnetic time constants, because the resistances are relatively small. The stator and rotor inductances are $L_{\mathrm{m}} + L_{s\sigma}$ and $L_{\mathrm{m}} + L_{r\sigma}$, respectively. Large inductances and small resistances cause a very long numerical transient. This phenomenon is proven and mitigated by the proposed approach.

TABLE 1. High-speed Solid-rotor IM Equivalent Circuit Parameters.

Parameter	Per-unit value
Magnetizing inductance L_{m}	2.24
Stator resistance R_{s}	0.0016
Stator leakage inductance $L_{s\sigma}$	0.24
Rotor resistance R_{r} ($s = 0.005$)	0.0047
Rotor leakage inductance $L_{r\sigma}$	0.24

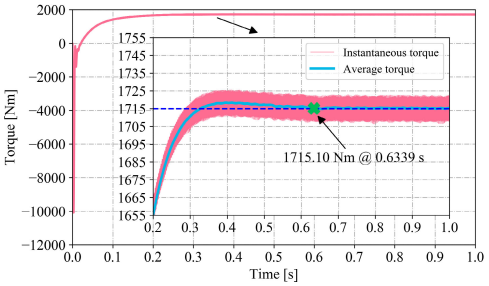

FIGURE 2. Torque as a function of time during the transient at per-unit slip $s = 0.005$ for the high-speed IM (Altair Flux 2D FEA).

Fig. 2 depicts both the instantaneous and average torque curves during a transient of the high-speed IM simulation. The time step used in the FEA is 5×10^{-5} s, which is 1/100th of one electrical period. It can be seen in the figure that the instantaneous torque contains some ripple, and therefore it is difficult to evaluate the steady state accurately based on it. Consequently, a value for the average torque is proposed in the figure. It is defined as the average torque of the last 100 steps (one electrical period) at a certain time. Finally, the machine reaches the steady state at 0.6339 s, which takes 12678 steps and it is about 38 h simulated by Altair Flux on a workstation (Intel Xeon W-2135 CPU @ 3.70 GHz and 256 GB RAM). The simulation time is very long, which is sometimes not acceptable, especially in the multiparameter optimization.

B. IMPLEMENTATION OF THE PROPOSED APPROACH

The main idea of the proposed method to reduce the simulation time of an IM is implemented by reducing the inherent electromagnetic time constants of the machine. Traditionally, the IM torque can be calculated in FEA by using a non-rotating rotor with modified parameters by both TH and TM solutions. The real rotor phase current (described by the classical equivalent circuit, and thus, modelling only the fundamental behavior) and time constant in the following equations are I_{r1} and τ_{r1}, respectively. When the locked rotor calculation is used to analyze a running rotor torque, the rotor resistance R_{r} has to be increased to R_{r}/s with s being the per-unit slip at which the torque is wanted to be calculated. In this case, the rotor phase current and rotor time constant are modified and become I_{r2} and τ_{r2} [18]

$$\begin{cases} I_{\mathrm{r1}} = \dfrac{sE_2}{R_{\mathrm{r}} + js\omega\left(L_{\mathrm{m}} + L_{r\sigma}\right)} \\ I_{\mathrm{r2}} = \dfrac{E_2}{R_{\mathrm{r}}/s + j\omega\left(L_{\mathrm{m}} + L_{r\sigma}\right)} \end{cases} \tag{1}$$

$$\begin{cases} \tau_{\mathrm{r1}} = \dfrac{L_{\mathrm{m}} + L_{r\sigma}}{R_{\mathrm{r}}} \\ \tau_{\mathrm{r2}} = \dfrac{s\left(L_{\mathrm{m}} + L_{r\sigma}\right)}{R_{\mathrm{r}}} \end{cases} \tag{2}$$

where E_2 is the rotor equivalent voltage and $\omega = 2\pi f, f$ is the supply frequency. In the locked rotor rated-torque calculation the ratio of inductive and resistive parts in the rotor impedance can be regarded the same as shown in (2). The main difference is that the rotor frequency has been referred to the stator frequency, e.g. from sE_2 in the real running rotor state to E_2 in the locked rotor state as described in (1). As a result, the rotor electromagnetic time constant is substantially reduced because it is multiplied by s as described in (2). The more specific details has been explained in [18].

According to Table 1, the rotor electromagnetic time constant is rather long. However, (2) indicates that the locked rotor model with modified rotor parameters will significantly reduce the rotor electromagnetic time (to sth share). To apply the same approach to a solid-rotor IM simulation, the rotor speed $n_r = n_0(1-s)$ where n_0 is the synchronous speed, has to be set to zero ($n_r = 0$). In addition, to get a correct torque for a rotor running at slip s (e.g. $s = 0.005$), the rotor conductivity σ has to be reduced to $s\sigma$. Furthermore, if the machine is equipped with an end ring, the end ring resistance R_{ring} has to be increased to R_{ring}/s. A virtual permanent magnet harmonic machine (VPMHM) model described in [29], [30] is used to comfirm the validity of (2). The main idea of the VPMHM model is to replace a stator of the IM with a purely sinusoidal magnetic source in the air gap to excite the machine (the rotor). As a result, the rotor electromagnetic characteristics can be extracted separately and a numerical transient will be caused only by the rotor when the VPMHM model is used.

Fig. 3 illustrates the high-speed IM locked rotor simulation conducted by applying the VPMHM model with only fundamental excitation. In Fig. 3(a), it can be seen that the locked rotor model is capable of creating almost the same flux density distribution in the rotor area compared with Fig. 1(b). Fig. 3(b) shows that the locked rotor model reaches the steady state very fast at 0.0019 s (38 steps). This phenomenon proves that the locked rotor model is valid for reducing the rotor electromagnetic time constant.

Fig. 4 shows the locked-rotor rated-torque simulation results during the transient (correspond to Fig. 1, but the rotor is locked) with voltage source excitation. This figure illustrates that there is still a long transient in the simulation and both the currents and torque reach the steady state at about 0.24 s. This long transient is caused by the stator electromagnetic time constant, because the rotor electromagnetic time constant is almost eliminated by the locked rotor model, which has already been shown by Fig. 3. Moreover, the data in Table 1 also indicate that the stator electromagnetic time constant is quite long.

To further shorten the time taken by the numerical transient, the stator electromagnetic time constant has to be reduced or eliminated by some methods. It can be seen in Fig. 4(a), if voltage source excitation is used (which appears frequently for an IM simulation), a long transient will show in the current curves, which will further affect the torque transient. Therefore, one potential method is to use a current source excitation with the locked rotor model. It is noteworthy, however, that it is not useful to apply current source excitation to the traditional rotating rotor model if the rotor transient is long, because the current source excitation

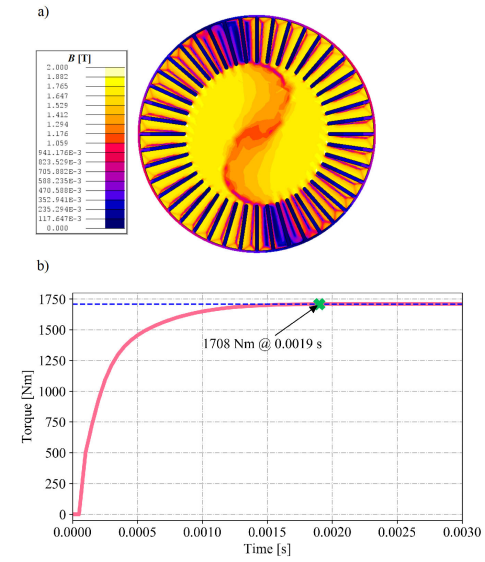

FIGURE 3. High-speed IM locked rotor simulation results using conductivity and resistance modified with a real running per-unit slip $s = 0.005$ by the VPMHM model (Altair Flux 2D FEA). (a) Flux density distribution at steady state. (b) Torque as a function of time during the transient.

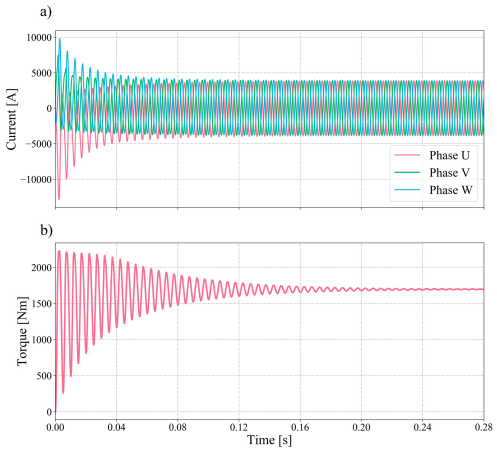

FIGURE 4. High-speed IM locked rotor simulation results using conductivity and resistance modified with a real running per-unit slip $s = 0.005$ with the voltage source excitation (Altair Flux 2D FEA). (a) Three-phase line currents as a function of time. (b) Torque as a function of time. The calculation transient attenuates at about 0.24 s (FEA time).

is only capable of keeping the stator currents as constants and reducing the stator electromagnetic transient (without affecting the rotor electromagnetic transient), not the rotor transient.

According to the analysis in the previous paragraph, it evident that it is essential to use the current source model when accelerating the transient. However, in typical industrial applications, machines are more frequently driven with a voltage source than with a current source. The proposed method is still capable of simulating the voltage-driven cases because the current source in parallel with a resistor is equivalent to the voltage source in series with a corresponding resistor value. The procedure of implementing the proposed approach is described in detail Fig. 5. It can be seen in this figure that at the very beginning, the initial currents can be estimated by the TH solution (as stated above, the currents in the TH are accurate enough for current estimation) or by an analytical method. The main body of the procedure contains three periods. The aim of Period 1 is to reduce the stator and rotor electromagnetic time constants. In Periods 1 and 2, the winding harmonics are considered but the stator and rotor slot effects are not fully considered. Because that in locked rotor status the rotor resistance is modified only based on the fundamental behavior from the classic equivalent circuit. Actually, there are also equivalent circuits in consideration of high frequency harmonics, see [31]. In that case, the rotor resistance has to be modified accordingly. Period 3 is designed to take all the harmonic behaviors into account.

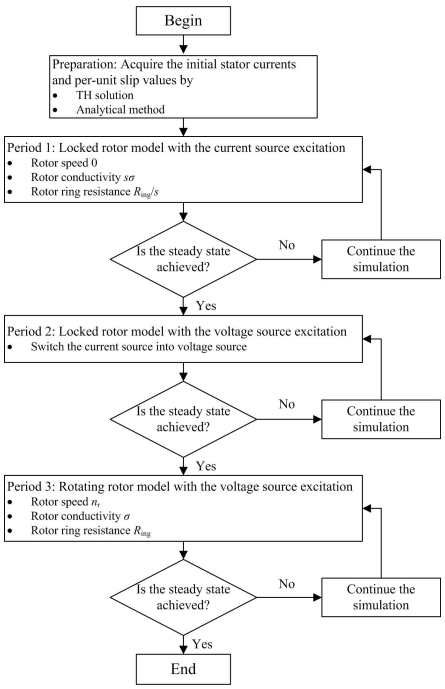

FIGURE 5. Flow chart of the implementation of the proposed approach with the voltage source excitation.

III. APPLICATIONS OF THE PROPOSED APPROACH

Two simulation cases are presented to verify the proposed approach. One is a 660 V, 2-pole, 2 MW, 12000 r/min high-speed solid-rotor IM presented in the Introduction with long electromagnetic time constants. The other one is a 400 V, 4-pole, 5 kW, 1467 r/min squirrel-cage IM with relatively short electromagnetic time constants, which is described in detail in [32]. These two models are regarded as typical cases with different rotor topologies and analyzed in detail because they include situations with relatively strong and weak rotor eddy-current effects. Moreover, all the initial currents are obtained by TH solutions for these two cases as shown in Fig. 5. The error effects of the initial currents are also discussed in this section.

A. SIMULATION OF THE HIGH-SPEED SOLID-ROTOR IM BY THE PROPOSED APPROACH

Fig. 6 shows the torque curve of the high-speed solid-rotor IM (Delta connection) by the proposed approach (initial line currents are 2716 A by the TH solution). In Fig. 6(a), it can be seen that the machine reaches the steady state (1715.10 Nm) at 0.2155 s (4310 steps, 13 h). The simulation time reduces significantly compared with the traditional TM simulation and it is 34% of the original one. The detailed torque curve in Fig. 6(a) indicates that the whole system (after 0.02 s) is a critically damped system, which means that the system is capable of achieving the steady state within the shortest time. Besides, this figure also shows that if some errors are acceptable, the machine reaches the steady state even much faster. The steady states are achieved at 0.0855 s (1710 steps, 5.1 h) with 5 Nm error (0.3% error) and 0.0635 s (1270 steps, 3.8 h) with 10 Nm error (0.6% error). A comparison of the steady-state machine performance between the traditional and proposed approaches is depicted in Table 2. The data in the table demonstrate that the simulation conducted by applying the proposed approach is accurate enough, and the machine performances estimated by the proposed approach are almost the same as those estimated by the traditional fully transient one.

In Fig. 6(b), the current source is switched to the voltage source at 0.00815 s (this switching time is discussed in detail in the following paragraphs) and the locked rotor is switched to the rotating rotor at 0.015 s (any time after switching to the voltage source and here 0.015 s is selected for a better understanding of Period 2 because Period 2 now is long enough). It can be seen that in Periods 1 and 2 from 0 s to 0.015 s the torque curve is very smooth because the rotor is fixed and the slot harmonics are not fully modelled. In Period 3 starting from 0.015 s, the inherent torque ripple appears because of the slotting effects.

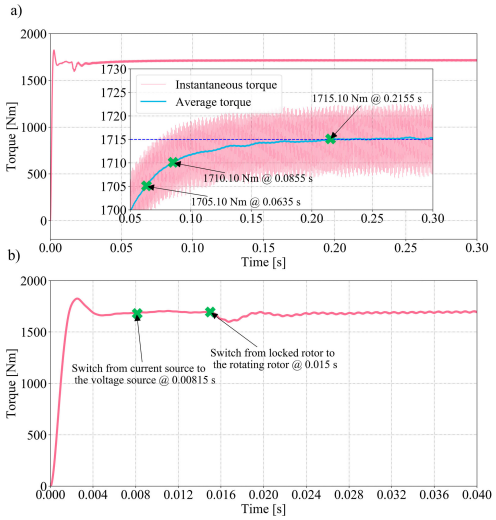

FIGURE 6. High-speed IM simulation at per-unit slip $s = 0.005$ by the proposed approach with initial line currents 2716 A by the TH solution (Altair Flux 2D FEA). (a) Torque as a function of time. (b) Detailed torque curve during the starting process.

TABLE 2. Steady State Performance Comparison Between Different Approaches.

Performance	Traditional approach	Proposed approach
Steady state time (FEA), [s]	0.6339	0.2155
Simulation time, [h]	38	13
Per-unit slip	0.005	0.005
Steady state torque, [Nm]	1710.10	1710.10
Torque ripple (peak-peak value), [Nm]	15.02	14.99
Stator line current, [A]	2717	2717
Stator core losses, [kW]	17.49	17.49
Solid rotor losses, [kW]	13.26	13.26

The three-phase voltage sources are switched simultaneously at 0.00815 s. The time instant 0.00815 s is chosen as the switching time because the phase U voltage is reaching the maximum at 0.00815 s. It is easier to calculate the phase angle for the voltage source of phase U in the next time step, when the voltage reaches the maximum. In addition, because there is always some error, the error is the smallest for phase U when it reaches the maximum (the differential is the minimum). Consequently, the three-phase line voltage equations can be written as

$$\begin{cases} U_{\mathrm{U}}(t) = U_{\mathrm{C,U}}(t)H(t_{\mathrm{s}}-t) + U_{\mathrm{V,U}}(t)H[t-(t_{\mathrm{s}}+\Delta t)] \\ U_{\mathrm{V}}(t) = U_{\mathrm{C,V}}(t)H(t_{\mathrm{s}}-t) + U_{\mathrm{V,V}}(t)H[t-(t_{\mathrm{s}}+\Delta t)] \\ U_{\mathrm{W}}(t) = U_{\mathrm{C,W}}(t)H(t_{\mathrm{s}}-t) + U_{\mathrm{V,W}}(t)H[t-(t_{\mathrm{s}}+\Delta t)] \end{cases} \quad (3)$$

where t is time; t_{s} is the time when the current source is switched to the voltage source; $U_{\mathrm{C,U}}$, $U_{\mathrm{C,V}}$ and $U_{\mathrm{C,W}}$ are the voltages of the three-phase current sources, respectively obtained by FEA; H is the Heaviside step function; Δt is the time step (5×10^{-5} s); $U_{\mathrm{V,U}}$, $U_{\mathrm{V,V}}$ and $U_{\mathrm{V,W}}$ are the voltages of the three-phase voltage sources, and they can be estimated at any time by the analytical method as

$$\begin{cases} U_{\mathrm{V,U}}(t) = V_{\mathrm{V,U}} \cos\left[2\pi f\,(t-t_{\mathrm{s}}) - \varphi_0\right] \\ U_{\mathrm{V,V}}(t) = V_{\mathrm{V,V}} \cos\left[2\pi f\,(t-t_{\mathrm{s}}) - \dfrac{2}{3}\pi - \varphi_0\right] \\ U_{\mathrm{W,V}}(t) = V_{\mathrm{V,W}} \cos\left[2\pi f\,(t-t_{\mathrm{s}}) + \dfrac{2}{3} - \varphi_0\right] \end{cases} \quad (4)$$

where $V_{\mathrm{V,U}}$, $V_{\mathrm{V,V}}$ and $V_{\mathrm{V,W}}$ are the amplitudes of the three-phase voltages; φ_0 is the initial phase and it is 0 when the phase U voltage reaches the maximum at t_{s}.

According to (3) and (4), a special circuit in Altair Flux is built to switch the current sources to voltage sources at t_{s}. The circuit is shown in Fig. 7. It can be seen in this figure that two sets of excitations in parallel containing current sources and voltage sources are used to excite the machine. Switches (resistors are embedded) are utilized to control which circuit is on or off. To be more specific, the current circuit is on before t_{s} and off after t_{s}. Concurrently, the states are the opposite for the voltage circuit. Another critical thing for the excitation switching is to acquire the right time t_{s}. Typically, there are two possible ways for this, the implementation varying from software to software. One method is to make a program for the corresponding logic in (3) to get t_{s} automatically, which is very suitable for open source softwares. However, for some commercial softwares, sometimes it is not very convenient to make a program or script as the codes are embedded in the packages. In that case, it is recommended to run the simulation for a short while (two or three electrical periods) to find the needed t_{s} manually.

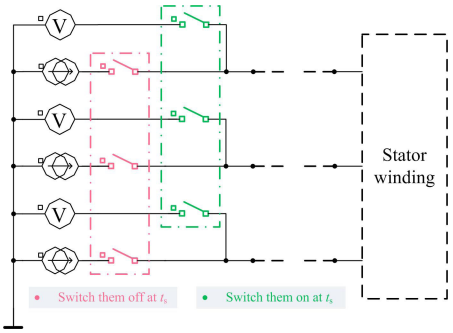

FIGURE 7. The excitation circuit of the proposed method. The switches contain a resistor inside, which can be adjusted accordingly for voltage and current sources.

Fig. 8(a) shows the details about the line voltage curves as a function of time in the neighborhood of 0.00815 s by using the proposed method to switch the excitation sources. In this figure, from 0 to 0.00815 s, the voltage depicts the voltage value of the current source (the current source in Altair Flux

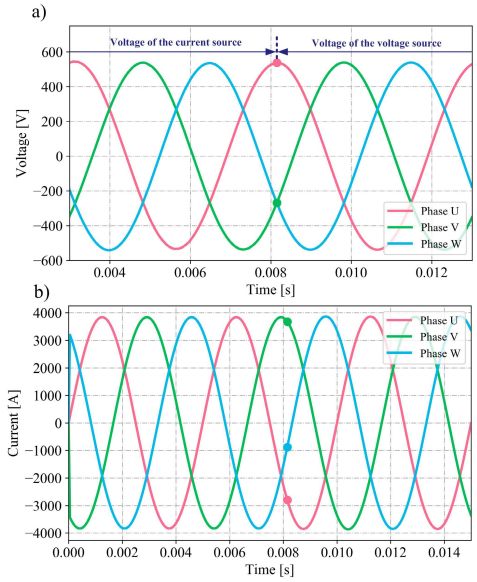

FIGURE 8. Line voltages and currents as a function of time in the neighborhood of 0.00815 s (Delta connection, Altair Flux 2D FEA). (a) Three-phase line voltages as a function of time. (b) Three-phase line currents as a function of time.

is an infinite resistor) and after 0.00815 s, the voltage depicts the voltage value of the voltage source. It can be seen that the current source is switched to voltage source successfully without any obvious ripple, and therefore, there is no extra transient during Period 2 in the torque curve in Fig. 6(b). The three-phase line current curves during the transient from 0 to 0.014 s by the proposed approach are shown in Fig. 8(b). It can be seen in the figure that the line currents reach the steady state at the very beginning and there is no obvious oscillation when the excitation sources are changed at 0.00815 s. All these phenomena indicate that the machine is capable of achieving the steady state in a short time period.

The simulation results show that the proposed approach is very suitable for an IM with very long stator and rotor electromagnetic time constants. The simulation time for reaching accurate steady state decreases from 38 h to 13 h. If some minor error is acceptable, the time can be further reduced (e.g. 3.8 h for 0.6% error, 10% simulation time of the initial solution).

B. SIMULATION OF THE SQUIRREL-CAGE IM BY THE PROPOSED METHOD

A 400 V, 4-pole, 5 kW, 1467 r/min squirrel-cage IM (Star connection) is also simulated in this paper to verify the proposed method. The time step in the simulation is 0.0002 s (1/100th of one electrical period). The excitation is switched

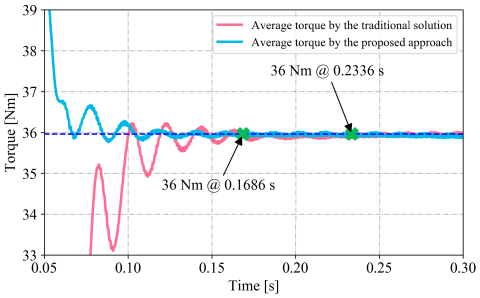

FIGURE 9. Comparison of the average torque of the squirrel-cage IM at the rated speed by the traditional and proposed solutions (Altair Flux 2D FEA).

at 0.0328 s when the phase U line voltage reaches the maximum and the rotor starts to rotate at 0.045 s. Fig. 9 shows the detailed average torque curves acquired by the traditional and proposed approaches. The machine reaches the steady state at 0.2336 s (1168 steps, 2.5 h) and 0.1686 s (843 steps, 1.8 h) for these two cases. Compared to the solid-rotor IM simulation, this squirrel-cage IM simulation is much faster, because the stator winding resistance is relatively large as described in [32], which results in a small stator electromagnetic time constant. The proposed approach is still efficient and the simulation time is reduced by 30% (1.8 h physical time with 0.0002 s time step in FEA).

The same logic of switching the excitations are also utilized in the simulation. The three-phase voltage curves in Fig. 10(a) show that there are some errors, especially for phase U, when the excitations are switched at 0.0328 s. The corresponding currents are illustrated in Fig. 10(b). The current curves show that the voltage errors do not cause any extra significant current oscillations. The reason is that the electrical machine itself contains some resistance and inductance components described from the classic equivalent circuit model, which means that the machine is partly like a filter and capable of filtering the small extra voltage errors. However, some current harmonics appear after 0.045 s because of the slot effects caused by the rotating rotor, as at that time the rotor is switched from the locked state to the rotating state.

All the simulation results indicate that the proposed method is also suitable for squirrel-cage IMs. Even though the simulation by the traditional solution is already very fast, the proposed approach is still capable of further reducing the simulation time.

C. ERROR EFFECTS OF THE INITIAL CURRENTS ON THE SIMULATION TIME

As mentioned in Section III-A, the initial currents for the current sources of the high-speed solid-rotor IM are 2716 A obtained by the TH solution, which is very close to 2717 A

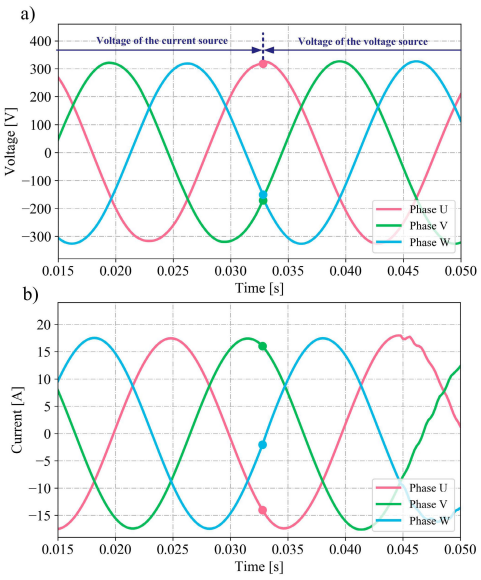

FIGURE 10. Phase voltage and phase current as a function of time in the neighborhood of 0.0328 s (Star connection, Altair Flux 2D FEA). (a) Three-phase phase voltages as a function of time. (b) Three-phase phase currents as a function of time.

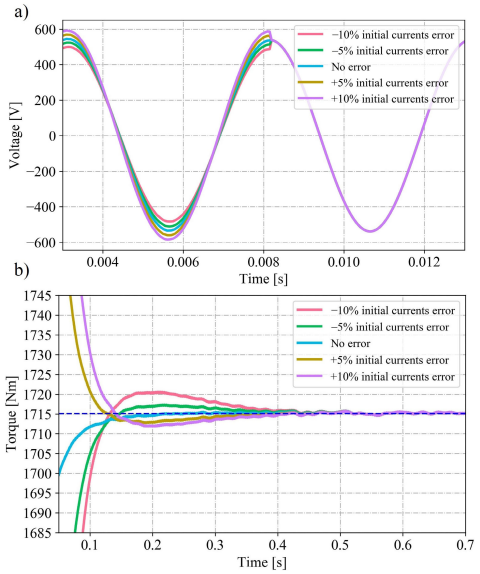

FIGURE 11. Line voltage and torque as a function of time with different initial currents at per-unit slip $s = 0.005$ for the high-speed IM by the proposed approach (Altair Flux 2D FEA). (a) Phase U line voltage as a function of time in the neighborhood of 0.00815 s. (b) Torque as a function of time during the transient process.

given by the TM solution. However, in some cases the TH solution may not provide very accurate initial currents, or analytical methods have to be used to determine the initial currents. In this situation, an error in the initial currents may affect the simulation speed of the proposed approach.

Fig. 11(a) shows the phase U line voltage as a function of time in the neighborhood of 0.00815 s with different initial currents varying from -10% error to $+10\%$ error with respect to the normal value. It can be seen that a large initial current difference can cause a large voltage difference when the excitation is switched at 0.00815 s, which causes a longer numerical transient in the simulation. Moreover, all the rotors start to rotate at 0.015 s, which is exact the same as in the case illustrated in Fig. 6. The torque curves with different initial currents in Fig. 11(b) show that the model reaches the steady state faster with a smaller error. In addition, even though the initial currents have a big error (e.g. $\pm 10\%$), the machine is still capable of reaching the steady state faster (at about 0.48 s) by using the proposed method than the traditional transient solution (0.6339 s). The reason is that an initial condition close to the final steady state has already been created by the initial current excitation regardless of some errors. Consequently, this initial condition makes the transient faster to fully reach the steady state compared with the traditional full transient simulation.

IV. CONCLUSION

To shorten the time taken by the numerical transient during the time-stepping FEA of an IM in the TM solution, a novel approach is proposed based on reducing the stator and rotor electromagnetic time constant, separately. The stator current source excitation is used to eliminate the stator time constant and the locked rotor is used to reduce the rotor time constant at the beginning of the simulation. After that, the current source excitation is switched to a corresponding voltage source excitation and the locked rotor is turned to the rotating state. Consequently, the steady state can be achieved in a short time. Two typical cases (a high-speed solid-rotor IM with long electromagnetic time constants and a squirrel-cage IM with small electromagnetic time constants) are analyzed in detail.

The results show that the proposed approach is useful in both cases. The simulation time of the proposed simulation approach is 34% (the solid-rotor IM) and 70% (the squirrel-cage IM) of the initial simulation time, which indicates that the proposed method is more efficient for the solid-rotor IM with a long rotor electromagnetic time constant. The shorter simulation time also suggests that if some error (e.g. 0.6%) is acceptable in the solid-rotor IM simulation, the transient can be further reduced (e.g. 0.6% error results in 10% simulation time of the initial solution). Finally, error effects of the initial currents on the simulation time are

also investigated. The results show that even with relatively large errors of ±10%, the simulation time by the proposed time is still shorter (about 25% faster) than the traditional full transient simulation. The proposed approach has the potential to be further improved and developed for other applications. For example, it can be modified to simulate the IM with a constant torque load instead of an imposed speed. Moreover, it may also be used to achieve the steady state fast for other cases when eddy-current effects are involved, for instance, in the analysis of magnet eddy-current losses in PMSMs.

ACKNOWLEDGMENT

The authors would like to thank Dr. Hanna Niemelä, Lappeenranta University of Technology, for her linguistic assistance in the preparation of this manuscript.

REFERENCES

[1] Y. Duan and D. M. Ionel, "A review of recent developments in electrical machine design optimization methods with a permanent-magnet synchronous motor benchmark study," *IEEE Trans. Ind. Appl.*, vol. 49, no. 3, pp. 1268–1275, May/Jun. 2013.

[2] Y. Zhang, K. T. Chau, J. Z. Jiang, D. Zhang, and C. Liu, "A finite element–analytical method for electromagnetic field analysis of electric machines with free rotation," *IEEE Trans. Magn.*, vol. 42, no. 10, pp. 3392–3394, Oct. 2006.

[3] H. L. Li, S. L. Ho, and W. N. Fu, "Precise magnetic field modeling techniques of rotary machines using transient finite-element method," *IEEE Trans. Magn.*, vol. 48, no. 11, pp. 4192–4195, Nov. 2012.

[4] X. Sun, C. Hu, G. Lei, Y. Guo, and J. Zhu, "State feedback control for a PM hub motor based on grey wolf optimization algorithm," *IEEE Trans. Power Electron.*, to be published.

[5] X. Sun, B. Su, S. Wang, Z. Yang, G. Lei, J. Zhu, and Y. Guo, "Performance analysis of suspension force and torque in an IBPMSM with V-shaped PMs for flywheel batteries," *IEEE Trans. Magn.*, vol. 54, no. 11, Nov. 2018, Art. no. 8105504.

[6] X. Sun, K. Diao, G. Lei, L. Chen, Y. Guo, and J. Zhu, "Study on segmented-rotor switched reluctance motors with different rotor pole numbers for BSG system of hybrid electric vehicles," *IEEE Trans. Veh. Technol.*, vol. 68, no. 6, pp. 5537–5547, Jun. 2019.

[7] X. Sun, K. Diao, and Z. Yang, "Performance improvement of a switched reluctance machine with segmental rotors for hybrid electric vehicles," *Comput. Elect. Eng.*, vol. 77, pp. 244–259, Jul. 2019.

[8] J. F. Hoburg, "Modeling maglev passenger compartment static magnetic fields from linear Halbach permanent-magnet arrays," *IEEE Trans. Magn.*, vol. 40, no. 1, pp. 59–64, Jan. 2004.

[9] S. Ausserhofer, O. Biro, and K. Preis, "An efficient harmonic balance method for nonlinear eddy-current problems," *IEEE Trans. Magn.*, vol. 43, no. 4, pp. 1229–1232, Apr. 2007.

[10] R. M. Tallam, T. G. Habetler, and R. G. Harley, "Transient model for induction machines with stator winding turn faults," *IEEE Trans. Ind. Appl.*, vol. 38, no. 3, pp. 632–637, May/Jun. 2002.

[11] L. R. Turner, "3-D field computation: The near-triumph of commercial codes," *IEEE Trans. Magn.*, vol. 32, no. 4, pp. 2945–2949, Jul. 1996.

[12] S. N. Makarov, G. M. Noetscher, T. Raij, and A. Nummenmaa, "A quasi-static boundary element approach with fast multipole acceleration for high-resolution bioelectromagnetic models," *IEEE Trans. Biomed. Eng.*, vol. 65, no. 12, pp. 2675–2683, Dec. 2018.

[13] W. Jiang, T. M. Jahns, T. A. Lipo, W. Taylor, and Y. Suzuki, "Machine design optimization based on finite element analysis in a high-throughput computing environment," in *Proc. IEEE Energy Convers. Congr. Expo. (ECCE)*, Sep. 2012, pp. 869–876.

[14] J. Keränen, P. Ponomarev, J. Pippuri, P. Råback, M. Lyly, and J. Westerlund, "Parallel performance of multi-slice finite-element modeling of skewed electrical machines," *IEEE Trans. Magn.*, vol. 53, no. 6, Jun. 2017, Art. no. 7201204.

[15] B. Thierry, A. Vion, S. Tournier, M. El Bouajaji, D. Colignon, N. Marsic, X. Antoine, and C. Geuzaine, "GetDDM: An open framework for testing optimized Schwarz methods for time-harmonic wave problems," *Comput. Phys. Commun.*, vol. 203, pp. 309–330, Jun. 2016.

[16] O. Bíró and K. Preis, "An efficient time domain method for nonlinear periodic eddy current problems," *IEEE Trans. Magn.*, vol. 42, no. 4, pp. 695–698, Apr. 2006.

[17] S. A. Mousavi, C. Carrander, and G. Engdahl, "Comprehensive study on magnetization current harmonics of power transformers due to GICs," in *Proc. Int. Conf. Power Syst. Transients (IPST)*, 2013, p. 20139.

[18] D. Lin, P. Zhou, N. Chen, C. Lu, and M. Christini, "Fast methods for reaching AC steady state in FE transient analysis," in *Proc. IEEE Int. Electr. Mach. Drives Conf. (IEMDC)*, May 2017, pp. 1–6.

[19] D. N. Dyck and P. J. Weicker, "Periodic steady-state solution of voltage-driven magnetic devices," *IEEE Trans. Magn.*, vol. 43, no. 4, pp. 1533–1536, Apr. 2007.

[20] M. Rosu, P. Zhou, D. Lin, D. M. Ionel, M. Popescu, F. Blaabjerg, V. Rallabandi, and D. Staton, *Multiphysics Simulation by Design for Electrical Machines, Power Electronics and Drives*, vol. 66. Hoboken, NJ, USA: Wiley, 2017.

[21] Y. Paquay, O. Brüls, and C. Geuzaine, "Nonlinear interpolation on manifold of reduced-order models in magnetodynamic problems," *IEEE Trans. Magn.*, vol. 52, no. 3, Mar. 2016, Art. no. 7204804.

[22] M. N. Albunni, V. Rischmuller, T. Fritzsche, and B. Lohmann, "Multi-objective optimization of the design of nonlinear electromagnetic systems using parametric reduced order models," *IEEE Trans. Magn.*, vol. 45, no. 3, pp. 1474–1477, Mar. 2009.

[23] Y. Sato and H. Igarashi, "Generation of equivalent circuit from finite-element model using model order reduction," *IEEE Trans. Magn.*, vol. 52, no. 3, Mar. 2016, Art. no. 1100304.

[24] A. Stermecki, I. Ticar, I. Zagradisnik, and P. Kitak, "FEM-based design of an induction motor's part winding to reduce the starting current," *IEEE Trans. Magn.*, vol. 42, no. 4, pp. 1299–1302, Apr. 2006.

[25] S. Wakao, M. Tokuhisa, A. Maeda, and N. Nishioka, "Acceleration of convergence characteristics of time-stepping FE analysis for rotating machines," *IEEE Trans. Magn.*, vol. 37, no. 5, pp. 3558–3561, Sep. 2001.

[26] E. Vassent, G. Meunier, and J. C. Sabonnadière, "Simulation of induction machine operation using complex magnetodynamic finite elements," *IEEE Trans. Magn.*, vol. 25, no. 4, pp. 3064–3066, Jul. 1989.

[27] D. Meeker, "Finite element method magnetics," *Proc. FEMM*, vol. 4, p. 32, Oct. 2010.

[28] A. Stermecki, O. Bíró, K. Preis, S. Rainer, and G. Ofner, "Numerical analysis of steady-state operation of three-phase induction machines by an approximate frequency domain technique," *e i Elektrotechnik Informationstechnik*, vol. 128, no. 3, pp. 81–85, 2011.

[29] C. Di, I. Petrov, and J. J. Pyrhönen, "Extraction of rotor eddy-current harmonic losses in high-speed solid-rotor induction machines by an improved virtual permanent magnet harmonic machine model," *IEEE Access*, vol. 7, pp. 27746–27755, 2019.

[30] C. Di, I. Petrov, and J. J. Pyrhönen, "Modeling and mitigation of rotor eddy-current losses in high-speed solid-rotor induction machines by a virtual permanent magnet harmonic machine," *IEEE Trans. Magn.*, vol. 54, no. 12, Dec. 2018, Art. no. 8111012.

[31] S. J. Lee, J. M. Kim, D. K. An, and J. P. Hong, "Equivalent circuit considering the harmonics of core loss in the squirrel-cage induction motor for electrical power steering application," *IEEE Trans. Magn.*, vol. 50, no. 11, pp. 1–4, Nov. 2014.

[32] P. Lindh, L. Aarniovuori, H. Karkkainen, M. Niemela, and J. Pyrhonen, "IM loss evaluation using FEA and measurements," in *Proc. 13th Int. Conf. Elect. Mach. (ICEM)*, Sep. 2018, pp. 1220–1226.

CHONG DI was born in Wuxi, China, in 1991. He received the B.Eng. and M.Eng. degrees in electrical engineering from the Hefei University of Technology, Hefei, China, in 2014 and 2017, respectively. He is currently pursuing the Ph.D. degree with the Department of Electrical Engineering, Lappeenranta University of Technology, Finland.

His research mainly concerns high-speed electrical machines.

ILYA PETROV received the D.Sc. degree from the Lappeenranta University of Technology (LUT), Finland, in 2015, where he is currently a Research Fellow with the Department of Electrical Engineering.

JUHA J. PYRHÖNEN (M'06–SM'17) was born in Kuusankoski, Finland, in 1957. He received the D.Sc. degree from the Lappeenranta University of Technology (LUT), Finland, in 1991.

He became a Professor of electrical machines and drives with LUT, in 1997. He is involved in the research and development of electric motors and power-electronic-controlled drives. He has wide experience in the research and development of special electric drives for distributed power production, traction, and high-speed applications. Permanent magnet materials and applying them in machines have an important role in his research. He is also currently studying the possibilities of using carbon-based materials in electrical machines.

JIAHAO CHEN (S'17) was born in Wenzhou, China, in 1991. He received the B.Sc. degree in electrical engineering from Zhejiang University, China, in 2014, where he is currently pursuing the Ph.D. degree in electrical engineering with the College of Electrical Engineering.

Since September 2018, he has been with the University of Wisconsin–Madison, USA, where he has been involved in bearingless motors. His research interests include self-sensing techniques and parameter estimation of electric machines, with a special focus on the stable adaptive observer design.

Publication II

Di, C., Petrov, I., and Pyrhönen, J.
Extraction of Rotor Eddy-Current Harmonic Losses in High-Speed Solid-Rotor Induction Machines by an Improved Virtual Permanent Magnet Harmonic Machine Model

Reprinted with permission from
IEEE Access
Vol. 7, pp. 27746-27755, 2019

IEEE Access
Multidisciplinary | Rapid Review | Open Access Journal

Received February 4, 2019, accepted February 25, 2019, date of publication March 1, 2019, date of current version March 13, 2019.

Digital Object Identifier 10.1109/ACCESS.2019.2902240

Extraction of Rotor Eddy-Current Harmonic Losses in High-Speed Solid-Rotor Induction Machines by an Improved Virtual Permanent Magnet Harmonic Machine Model

CHONG DI, ILYA PETROV, AND JUHA J. PYRHÖNEN, (Senior Member, IEEE)
Department of Electrical Engineering, Lappeenranta University of Technology, 53851 Lappeenranta, Finland
Corresponding author: Chong Di (chong.di@lut.fi)

This work was supported in part by the Scholarship from the China Scholarship Council (CSC) under Grant CSC 201706690032.

ABSTRACT High-speed induction machines equipped with a solid steel rotor are capable of achieving a high-rotating speed than other types of machines, because of their simpler and more robust rotor structure. At the same time, however, the eddy-current losses in the solid rotor may be critical, because of the high conductivity of the rotor material, which makes it easy for axial eddy currents to travel in the solid rotor. To efficiently mitigate the rotor eddy-current losses, it is important to accurately determine the rotor eddy-current losses induced by a particular harmonic in advance. In this paper, an improved virtual permanent magnet harmonic machine (VPMHM) model equipped with a sinusoidally magnetized virtual magnet based on the finite element method (FEM) is proposed for determination of the rotor eddy-current harmonic losses. The 2-D fast Fourier transform was used to accurately analyze the time-spatial air-gap flux density harmonics. The VPMHM model was enhanced to ensure that it was able to exactly produce the required flux density harmonics in the air gap. Two algorithms for the improved VPMHM models with different hybrid excitations were proposed to determine the harmonic losses together with the other important harmonic behavior. The model was further investigated to separate the electromagnetic transients from different harmonics. Finally, the simulation time for the harmonic losses required by the enhanced VPMHM model was significantly reduced by separating the harmonic transients. All the results and conclusions presented in this paper are based on the FEM analysis.

INDEX TERMS Solid-rotor high-speed induction machine (IM), finite element method (FEM), 2-D fast Fourier transform, eddy-current losses, improved virtual permanent magnet harmonic machine (VPMHM).

I. INTRODUCTION

High-speed induction machines (IMs) equipped with a solid steel rotor have the advantage of running at a much higher rotational speed than other types of electrical machines, which are also frequently used in high-speed applications, such as permanent magnet synchronous machines (PMSMs) and switched reluctance machines (SRMs) [1]–[4]. It has been reported in [5] that the maximum rotor peripheral speeds that have been achieved in recent years for IMs (a solid rotor coated with a copper layer), PMSMs (rotor surface-mounted permanent magnets with a titanium sleeve), and SRMs (high-strength VCoFe laminations) are 367 m/s, 294 m/s, and 210 m/s, respectively. The solid steel rotor is more robust than other types of rotor structures, and thus, a high power density and torque density can be easily achieved, which makes the solid rotor IMs popular and widely used in many industrial applications, such as air compressors, submersible pumps, and turbos, as reported in [6]–[8].

When considering the mechanical construction, solid rotors are very attractive in high-speed IMs. Nevertheless, solid rotors degrade the electromagnetic performance of the machines because of the extra losses produced by the solid-rotor eddy currents. The high-conductivity rotor material contributes to the induced eddy currents (generated by the air-gap flux density harmonics) traveling in the axial direction

The associate editor coordinating the review of this manuscript and approving it for publication was Kan Liu.

along the rotor shaft. Consequently, high eddy-current losses appear in the solid rotor because of the axial eddy currents. Typically, there are fewer measures available to efficiently cool the solid rotor than for cooling the stator. Therefore, more researchers have been focusing on reducing the solid-rotor eddy-current losses. Much of the present research concentrates on mitigating the rotor eddy-current losses by the design and use of different solid rotor structures, including the smooth solid rotor, slitted solid rotor, coated solid rotor, and caged solid rotor [5], of which the slitted solid rotor is the most popular one. It was stated in [9] that the slitted solid rotor could provide a higher efficiency with lower rotor eddy-current losses at a lower slip than the smooth solid rotor.

Moreover, there are some universal technologies that can be applied to mitigate the rotor eddy-current losses in high-speed IMs, such as rotor skews, semimagnetic wedges, and low-harmonic stator windings [10]–[12]. All these measures aim at minimizing the air-gap flux density harmonics. Correspondingly, to reduce the rotor eddy-current harmonic losses, it is essential to calculate and separate the harmonic losses from the total rotor eddy-current losses. Markovic and Perriard [13] proposed an analytical solution for the calculation of the rotor eddy-current losses in a slotless machine with current sheet excitation. However, because the solution was completely analytical, the iron saturation was neglected and the iron material was treated as linear. Markovic and Perriard [14] proposed an analytical method to determine the eddy-current losses in a configuration with a rotating permanent magnet. The configuration was a simple eddy-current brake based on the analytical method. However, only fundamental related loss was discussed in that paper. To predict the permanent magnet and sleeve eddy-current losses for a permanent magnet brushless machine, Zhu *et al*. [15] proposed an improved analytical method, which was capable of taking the magnetomotive force harmonics into account. However, the slotting effect was completely neglected in that research. All of these analytical methods have something in common; they are fast but not very precise because of different assumptions. Zhang *et al.* [16] and Koo *et al.* [17] utilized the 2-D FEM and 3-D FEM to accurately calculate the permanent magnet eddy-current losses, respectively. However, they were both not capable of extracting the harmonic losses from the total eddy-current losses, which is in highly demand in some real cases.

Recently, Di *et al.* [18] proposed a virtual permanent magnetic harmonic machine (VPMHM) model for solving the rotor eddy-current harmonic losses. The method is capable of generating a particular sinusoidal harmonic required in the air gap by simultaneously taking into account both the saturation and rotor damping effect (the effects of the rotor flux on the air-gap flux). The aim of the VPMHM is to generate a magnetic source, which is realized by setting a special virtual magnet in the FEM software. However, there were two main drawbacks when the VPMHM model was originally presented; one is related to the excitation on the virtual magnet and the other to the rotor permeability. To be more specific, a much lower flux density compared with the required flux density is generated in the air gap when a certain flux density harmonic is produced by the corresponding magnet excitation, as shown in [18, Fig. 2]. It means that the magnet excitation (remanence) has to be adjusted to achieve a correct flux density in the air gap because of the difference in the value of the remanence in the magnet and the actual flux density. Further, a constant rotor permeability with respect to the rotor saturation is used in the calculation of harmonic losses, which means that the rotor saturation is not fully accurately considered. These two problems can easily lead to some calculation errors as the rotor permeability is not evenly distributed on the rotor surface in the load condition.

To further mitigate the solid-rotor eddy-current losses more efficiently in the future, a method to extract the rotor harmonic losses is always in highly demand. When a particular rotor harmonic caused loss is known, effective measures can be taken to suppress the loss correctly. Because different harmonics are generated by different electromagnetic phenomena. The proposed improved VPMHM can provide an exact contribution of each harmonic to the overall rotor losses, that in turn helps to focus on the design aspects that cause the unwanted rotor losses. In this paper, an enhanced VPMHM (for solving the excitation problem) and a new computational algorithm (to solve the rotor permeability problem) are proposed to determine the rotor eddy-current harmonic losses more accurately in a 2-pole, 2 MW, 12000 r/min high-speed IM. The main advantage of the enhanced VPMHM is that it can accurately generate the required flux density and the rotor saturation can be considered in a proper manner, by avoiding possible errors caused by the wrongly assumed rotor damping effect and the saturation condition. First, the 2-D fast Fourier transform is employed to distinguish the air-gap flux density harmonic components. Two algorithms for the improved VPMHM models with different hybrid excitations are proposed to differentiate the harmonic losses together with other important harmonic behavior. Finally, it is shown that the improved VPMHM model is capable of distinguishing the harmonic transients from each other, which makes it possible to accelerate the simulation time with a negligible error.

II. AIR-GAP FLUX DENSITY HARMONIC ANALYSIS BY THE 2-D FAST FOURIER TRANSFORM ALGORITHM

A. INTRODUCTION OF THE HIGH-SPEED IM

In this paper, a 2-pole, 2 MW, 12000 r/min high-speed IM with a solid rotor is investigated. The machine was optimized and reported in detail in [18]. The total solid-rotor eddy-current losses are about 13.3 kW at the nominal load with a per-unit slip of about 0.005, both estimated by the 2-D FEM. For the sake of simplicity, the solid-rotor end effect is not taken into account in detail in this paper. Because the solid-rotor end effect should be accurately modeled by the 3-D FEM in principle. The 3-D FEM for a high-speed IM can

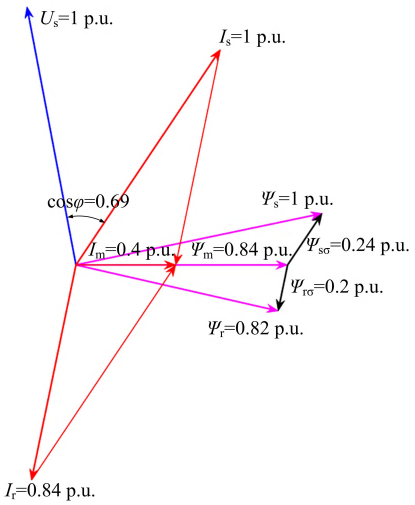

FIGURE 1. Vector diagram of the high-speed IM running at the nominal load with the stator phase voltage $U_s = 1$ p.u., the stator phase current $I_s = 1$ p.u., the rotor phase current $I_r = 0.84$ p.u., the magnetizing current $I_m = 0.4$ p.u., the stator flux linkage $\Psi_s = 1$ p.u., the rotor flux linkage $\Psi_r = 0.82$ p.u., the air-gap flux linkage $\Psi_m = 0.84$ p.u., the stator leakage flux linkage $\Psi_{s\sigma} = 0.24$ p.u., the rotor leakage flux linkage $\Psi_{r\sigma} = 0.2$ p.u., and the power factor cos$\varphi = 0.69$. The stator resistance and the iron loss current are neglected.

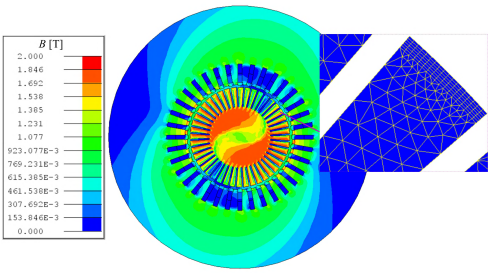

FIGURE 2. Flux density distribution of the high-speed IM at the nominal load in the steady state plotted by the 2-D FEM. It is referred to as "the normal FEM model" to distinguish it from the VPMHM model.

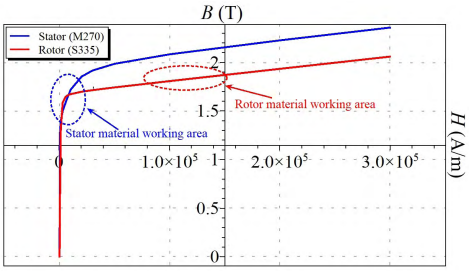

FIGURE 3. *B-H* curves of the stator and rotor materials.

be hardly achieved without an extremely powerful computer, because of the dense mesh and very small time step needed in transient solution. Fig. 1 shows the vector diagram of the machine at the nominal load. It can be seen that the machine has a power factor of 0.69 (it will be lower if the end effect is considered), whereas the leakage fluxes are relatively high. This clearly demonstrates the adverse effects of the methods used to reduce the rotor losses (especially the 7 mm air-gap length, the semimagnetic wedges, and the 4 mm wide rotor slot opening) on the machine performance.

Fig. 2 shows the flux density distribution of the high-speed IM at the nominal load. It can be seen that for accurate computation of the harmonic eddy-current losses, the rotor surface is densely meshed. There are six layers of dense mesh within the depth of 2 mm on the rotor surface. It can be also seen in the figure that the overall flux density in the rotor area is high. However, the overall flux density in the stator area is lower and some high-flux-density areas are only seen in the stator tooth tip areas. The stator material is M270-35A and the rotor material S355.

Fig. 3 shows the *B-H* curves of both the stator and rotor materials. It demonstrates that the stator and rotor are saturated at about 2.0 T and 1.7 T, respectively. Based on the flux density distribution at the nominal load in Fig. 2 and the *B-H* curves of the stator and rotor materials in Fig. 3, it can be concluded that the stator is still operating within the linear area of the material. The solid rotor, however, is highly saturated, which means that a significant proportion of the air-gap saturation harmonic is caused by the solid rotor itself instead of the stator.

B. AIR-GAP HARMONIC ANALYSIS AT THE NOMINAL LOAD

A suitable sampling frequency has to be applied to analyze the air-gap flux density harmonic content and to accurately calculate the rotor eddy-current losses. In this paper, the motor supply frequency is set to 200 Hz and the sampling frequency is 20000 Hz (the time step is 5×10^{-5} s), which means that the simulation can monitor the harmonics within the frequency from −10000 Hz to 10000 Hz based on the Shannon sampling theorem.

The eddy currents in the solid rotor are mainly generated by three different kinds of harmonics, viz. the stator winding harmonics, stator slot harmonics, and saturation harmonics. The source of the stator winding harmonics is the stator winding integer distribution, which for a 3-phase distributed winding can generate for instance the following harmonic orders: +1st, −5th, +7th, and −11th, where the positive sign means the same direction of rotation with the rotor and the negative sign denotes the opposite direction. The source of the stator slot harmonics, again, is the stator slot opening, which for a 36 stator slot machine can generate for instance the following

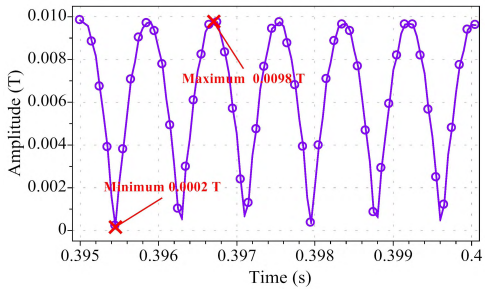

FIGURE 4. Amplitude of the 5th air-gap flux density harmonic at different time instants obtained by the traditional spatial fast Fourier transform at the nominal load.

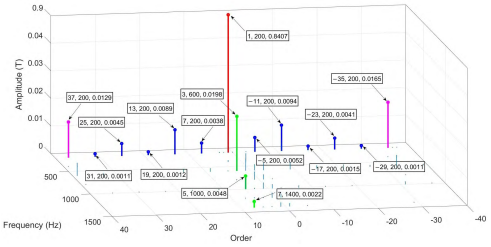

FIGURE 5. Air-gap flux density spectrum obtained by the 2-D fast Fourier transform at the nominal load.

harmonic orders: −35th, +37th, −71st, and +73rd. These two types of harmonics have the same frequency (200 Hz) as the supply frequency and a rotation velocity of Ω_{syn}/ν, where Ω_{syn} is the synchronous speed and ν is the harmonic order. The harmonics caused by saturation are the +3th, +5th, +7th, and so on, and the corresponding stator frequencies are 600 Hz, 1000 Hz, 1400 Hz, and so forth. Because the saturation harmonics are caused by the material properties of the stator and the rotor, they can be divided into stator saturation harmonics and rotor saturation harmonics. They both travel with the same speed of the synchronous speed. Therefore, it is very difficult to distinguish these two kinds of saturation harmonics from each other.

The analysis above reveals that there are some harmonics that have the same order but different frequencies; for example, the −5th winding harmonic operates with the 200 Hz supply frequency but the +5th saturation harmonic travels with the synchronous speed, creating a 1000 Hz phenomenon. This easily results in a calculation error with the traditional spatial fast Fourier transform. Fig. 4 shows the amplitude of the 5th air-gap flux density harmonic at different time instants by the traditional spatial fast Fourier transform at the nominal load. In this figure only the 5th harmonic is shown, since the error caused by the traditional Fourier transform is more obvious for the 5th harmonic than other harmonics. It is emphasized that all the harmonics discussed in this paper are normal components. It can be seen in the figure that at different time steps, different amplitudes of the 5th harmonic can be obtained when the spatial fast Fourier transform is applied. The harmonic can reach the minimum of 0.0002 T and the maximum of 0.0098 T, respectively. Such a variation may cause a mismatch to the actual harmonic component in the machine, which can lead to very different rotor eddy-current losses.

To define the air-gap flux density more accurately, the 2-D fast Fourier transform is applied in this paper. It has been widely used in the vibration analysis of electrical machines [19]. In fact, the air-gap flux density has both time-dependent and spatial properties, which means that they are determined both by frequency and order. For example, the −5th stator harmonic (200 Hz) travels slowly in the air gap in the negative direction, whereas the +5th saturation harmonic (1000 Hz) travels fast in the positive direction. The 2-D fast Fourier transform can provide a fast Fourier transform both in the time and spatial domains at the same time, which makes it possible to correctly determine the harmonics. Fig. 5 illustrates the air-gap flux density spectrum plotted by the 2-D fast Fourier transform at the nominal load. The red, blue, pink, and green bars in Fig. 5 denote the fundamental (which also belongs to the stator winding harmonics and it is emphasized here because of the fundamental property), the stator winding harmonics, the stator slot harmonics, and the saturation harmonics, respectively. It is emphasized that it is still not possible to distinguish the stator and rotor saturation harmonics from Fig. 5 because they are of the same frequencies and orders. However, as shown in Fig. 3, the stator is not saturated yet but the rotor is saturated, which indicates that most of the saturation harmonics belong to the rotor saturation harmonics. The rotor saturation harmonics do not cause any rotor eddy-current losses. The saturation harmonics will be further explained and discussed in Section III-B.

In addition, with the sampling frequency of 20000 Hz, the upper limit of the rotor-eddy current frequency is 10000 Hz. As shown in Fig. 5, the first-order stator slot harmonics (the −35th and +37th harmonics) are considered; they can both cause a 7200 Hz rotor eddy current. It is not possible to calculate the higher order harmonic eddy-current losses with the current sampling frequency. For example, the second-order stator harmonics, the −71st and +73rd ones, can generate a 14400 Hz rotor eddy current. This indicates that all the solid-rotor eddy-current losses can be considered to be caused by the harmonics shown in Fig. 5, especially the stator winding harmonics (containing the fundamental) and the stator slot harmonics.

III. IMPROVED VPMHM MODEL WITH HYBRID EXCITATION

A. IMPROVED VPMHM MODEL

Fig. 6 shows the improved VPMHM model for the separation of the rotor eddy-current harmonic losses. It is mainly aimed at solving the excitation problem, that is, the nonconformity

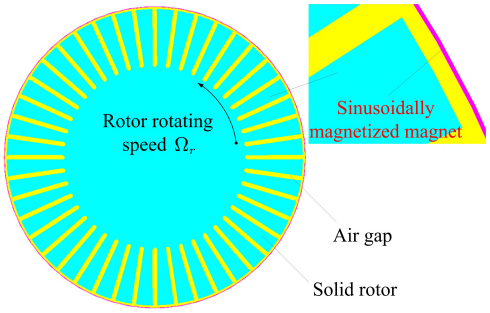

FIGURE 6. Improved VPMHM model for determination of the rotor eddy-current harmonic losses.

between the excitation (remanence) of the magnet and the actual air-gap flux density. It can been seen in Fig. 6 that the improved VPMHM model mainly contains three parts; the whole solid rotor, the air gap, and the sinusoidally magnetized magnet. The rotor has a rotating speed of Ω_r. However, the magnet is fixed, which is different from the rotating magnet presented in [18]. The rotating magnet is used to simulate the rotating property of the air-gap harmonic magnetic fields. Instead of applying a rotating magnet, the rotating property of the harmonics is directly taken into account by the excitation on the magnet with a time-varying signal. The excitation on the magnet can be expressed as

$$b_\nu(\theta, t) = \hat{B}_\nu \cos\left(\nu\theta - \frac{2\pi f_\nu t}{\nu} - \varphi_\nu\right) \tag{1}$$

where θ is the stator position, t is time, and ν is the order of the air-gap flux harmonic. $\hat{B}_\nu, f_\nu$ and φ_ν are the amplitude, stator current frequency, and initial phase angle of the νth harmonic, respectively.

A very thin virtual magnet as shown in Fig. 6 is employed to generate the same value of flux density in the air gap as that of the excitation (remanence) on the magnet. The thickness of the magnet is about 2 mm and the relative permeability of the material is 10^{-30}. The magnet is very thin owing to the algorithm of the software (Altair Flux) used in this paper. When the magnet is magnetized with a constant flux density, the software can only guarantee that the middle of the magnet (the middle of the pink ring in Fig. 6) has a constant value. Therefore, only when the thickness of the magnet is small enough, the flux density traveling from the inner surface of the magnet to the air gap will get close to the excitation on the magnet. The very low relative permeability can ensure a strong enough magnetic voltage in the circuit, which guarantees a robust flux density in the air gap to make the flux density in the magnet almost the same as its remanence.

Table 1 lists the air-gap flux density generated by the improved VPMHM model. The target amplitude denotes the required air-gap flux density, which is obtained by the 2-D fast Fourier transform, as shown in Fig. 5. It is also the excitation (remanence) for the sinusoidally magnetized magnet as shown in Fig. 6. The obtained amplitude in Table 1 denotes the air-gap flux density generated by the improved VPMHM model with the excitation (target amplitude). The table shows that the obtained amplitude is almost the same as the target amplitude, which can ensure an accurate computation of the solid-rotor eddy current losses.

TABLE 1. Air-gap flux density generated by the improved VPMHM model.

Order	Target amplitude, T	Obtained amplitude, T	Error, %
+1	0.8407	0.8425	+0.21
−5	0.0052	0.0052	–
+7	0.0038	0.0038	–
−11	0.0094	0.0094	–
+13	0.0089	0.0089	–
−17	0.0015	0.0015	–
+19	0.0012	0.0012	–
−23	0.0041	0.0041	–
+25	0.0045	0.0045	–
−29	0.0011	0.0011	–
+31	0.0011	0.0011	–
−35	0.0165	0.0164	−0.61
+37	0.0129	0.0128	−0.78

B. HYBRID EXCITED VPMHM MODELS FOR DETERMINATION OF ROTOR EDDY-CURRENT HARMONIC LOSSES

The improved VPMHM can generate a very precise air-gap flux density. To accurately determine the rotor eddy-current harmonic losses, an appropriate rotor relative permeability has to be considered at the nominal load. Because the penetration depth for a rotor eddy-current harmonic is directly affected by the rotor relative permeability, the penetration depth for a particular νth harmonic listed in Table 1 can be expressed as [20] and [21]

$$\delta_\nu = \frac{1}{\sqrt{\pi \mu_0 \mu_r \sigma f\,|1 - \nu\,(1 - s)|}} \tag{2}$$

where μ_0 is the vacuum permeability, μ_r is the relative permeability of the rotor material, σ is the rotor solid-steel conductivity, f is the supply frequency, and s is the per-unit slip. $f\,|1 - \nu\,(1 - s)|$ is the rotor eddy-current harmonic frequency caused by the νth air-gap flux density harmonic.

Fig. 7 shows the distribution of the rotor incremental relative permeability at every node at the nominal load estimated by the 2-D FEM. The rotor incremental relative permeability ($dB/\mu_0 dH$) is described instead of the apparent relative permeability ($B/\mu_0 H$), because it is capable of describing the material property within a small domain, compared with the latter. Because the latter describes the relative permeability with the differences measured from the origin. The incremental relative permeability can more accurately reflect the saturation condition on a certain point of the rotor material. It is clearly shown in Fig. 7 that the incremental relative permeability is not evenly distributed on the solid rotor, which means, according to (2), that the penetration depths for a particular harmonic are different in different rotor positions.

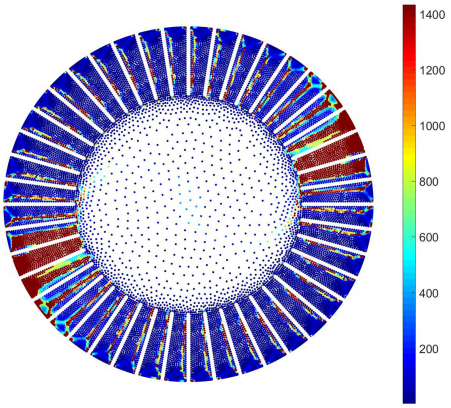

FIGURE 7. Distribution of the rotor incremental relative permeability at every node at the nominal load.

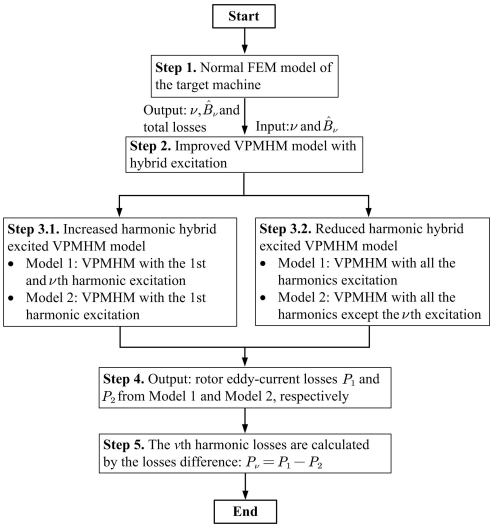

FIGURE 8. Procedure of the determination of solid-rotor eddy-current harmonic losses by the improved VPMHM models with hybrid excitation.

Therefore, accurate modeling of the rotor permeability is of critical importance.

A special computational algorithm based on hybrid excited VPMHM models is proposed to solve the rotor permeability problem. Fig. 8 shows the main procedure of the determination of solid-rotor eddy-current harmonic losses by the improved VPMHM models with hybrid excitation. There are two kinds of hybrid excited models. One is termed "the increased harmonic hybrid excited model" and the other "the reduced harmonic hybrid excited model". The details of the two models are shown in Fig. 8. Common to the two models is that all the hybrid excitations for the models contain the fundamental of the air-gap flux density. The fundamental in the hybrid exictiation is especially used to model the rotor saturation or the non-linear behavior of the material. As the amplitude of the fundamental of the air-gap flux is the largest, the rotor will automatically generate the corresponding rotor main magnetic field, when the fundamental is configured in the air gap by the VPMHM models. This means that the rotor main damping effect is considered automatically and the rotor itself sets the corresponding operating point (the corresponding area in the rotor material *B-H* curve) in the rotor material. Further, when the rotor is operating with the corresponding air-gap flux density harmonics, certain points within the rotor area automatically fit the *B-H* curve. This shows, again, that the rotor saturation has already been considered. Therefore, the permeability distribution in the rotor area and the rotor saturation are both taken into account accurately by the fundamental component excitation. Hence, the harmonic losses can be calculated by the loss difference between Model 1 and Model 2, as shown in Fig. 8. Nevertheless, the stator saturation is completely ignored because the stator does not contribute much to the saturation at the nominal load and it is difficult to get the exact stator saturation harmonic.

The difference between the increased and reduced harmonic hybrid excited VPMHM models is that the former only considers the fundamental effect on the rotor permeability and the latter all the harmonic effects as listed in Table 1 when computing the solid-rotor eddy-current harmonic losses. Because the fundamental effect on the rotor permeability is dominating, the losses calculated by the increased and reduced harmonic hybrid excited VPMHM models should be close to each other. Hence, the losses provided by the two models should verify each other.

IV. DETERMINATION OF ROTOR EDDY-CURRENT HARMONIC LOSSES BY DIFFERENT VPMHM MODELS

A. ROTOR EDDY-CURRENT HARMONIC LOSSES OBTAINED BY THE INCREASED HARMONIC HYBRID EXCITED VPMHM MODEL

By applying the improved VPHMH model with hybrid excitation, the rotor eddy-current harmonic losses can be determined accurately. Fig. 9 shows the harmonic eddy-current losses obtained by the increased harmonic hybrid excited VPMHM model at the nominal load. The fundamental loss (10842 W) is the highest one because the fundamental is very large and the corresponding loss belongs to the slip loss. The -5th and $+7$th harmonic losses are 344 W and 132 W, respectively. They are well suppressed by the short pitch winding ($y_Q = 5/6$). The -11th and $+13$th harmonic losses are 566 W and 430 W, respectively. They are the highest harmonic losses except for the fundamental loss. Further, although the first stator slot harmonics (the -35th and $+37$th harmonics) are significantly mitigated by the semimagnetic

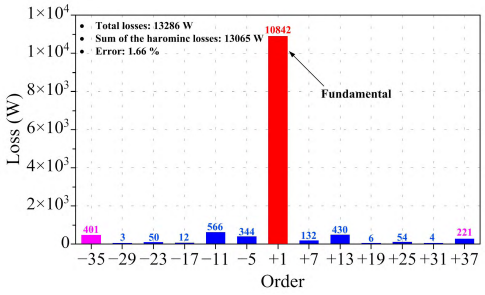

FIGURE 9. Rotor eddy-current harmonic losses obtained by the increased harmonic hybrid excited VPMHM model at the nominal load.

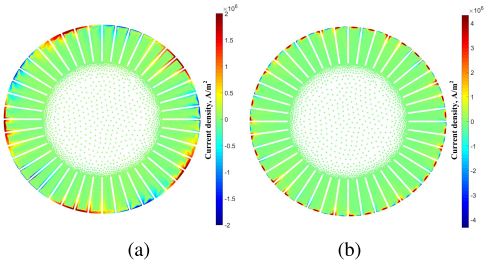

FIGURE 10. (a) Rotor eddy-current density distribution caused by the −5th harmonic at the nominal load estimated by the improved VPMHM model. (b) Rotor eddy-current density distribution caused by the +35th harmonic at the nominal load estimated by the improved VPMHM model.

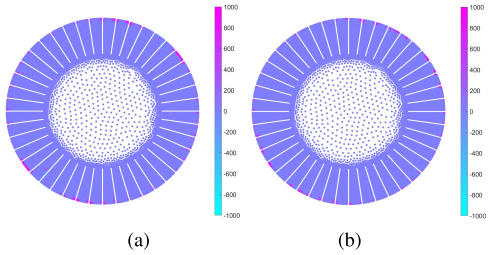

FIGURE 11. (a) Rotor incremental relative permeability distribution caused by the −5th harmonic at the nominal load estimated by the improved VPMHM model. (b) Rotor incremental relative permeability distribution caused by the +35th harmonic at the nominal load estimated by the improved VPMHM model.

wedges, they still cause high eddy-current losses (401 W and 221 W, respectively) in the solid rotor. Because the rest of the harmonics do not cause considerable losses, they are not discussed in detail. The total solid-rotor eddy-current losses are 13286 W calculated by the normal FEM model, as defined and shown in Fig. 2 and Fig. 8. The sum of all the harmonic losses computed by the increased harmonic hybrid excited VPMHM model is 13065 W, which means that the proposed method is accurate enough from the viewpoint of the FEM; the difference between these two models is only 221 W and the error is about 1.66%. This 221 W loss may be generated by the other harmonics including the stator saturation harmonic.

With the improved VPMHM model it is possible to obtain the rotor eddy-current distribution caused by a particular harmonic. Fig. 10 shows the rotor eddy-current density distributions caused by the −5th and +35th harmonics at the nominal load. The rotor eddy-current density distribution is also determined by the algorithm shown in Fig. 8. To be more specific, it is the distribution of the eddy-current density difference between the outputs of Model 1 and Model 2 in Fig. 8. It is clearly shown in Fig. 10 that the eddy current caused by the −5th harmonic penetrates deeper than that of the +35th harmonic, which matches (2) quite well, as the −5th harmonic causes a much lower rotor eddy-current frequency. Fig. 10 also reveals that the rotor eddy-current penetration depth is different in different rotor positions. The rotor eddy current penetrates deeper when the rotor relative permeability is lower. However, the amplitude of the eddy current generated by the +35th harmonic is larger than that of the −5th harmonic, which can be explained by the high eddy-current frequency. Finally, the −5th and +35th harmonics generate 344 W and 401 W rotor eddy-current harmonic losses, respectively.

Following the same logic for obtaining Fig. 10, the distributions of the rotor incremental relative permeability caused by the harmonics can be acquired as shown in Fig. 11. The figure shows that both the −5th and +35th harmonics can hardly change the rotor incremental relative permeability; it only increases in very small regions on the rotor surface within the corresponding penetration depth. The results show that the rotor is highly saturated and the saturation together with the correct relative permeability has already been considered by the fundamental of the hybrid excitation. Further, it indicates that the rotor eddy-current losses computed by the increased and reduced harmonic hybrid excited VPMHM models should have similar results, because the rotor incremental relative permeability cannot be affected much by the high-order harmonics.

B. ROTOR EDDY-CURRENT HARMONIC LOSSES OBTAINED BY THE REDUCED HARMONIC HYBRID EXCITED VPMHM MODEL

The rotor eddy-current harmonic losses determined by the reduced harmonic hybrid excited VPMHM model can be obtained with the algorithm shown in Fig. 8. The computational procedure is similar to that of the increased harmonic hybrid excited VPMHM model. Therefore, it is not discussed in detail here. Table 2 compares the rotor eddy-current harmonic losses determined by these two models, where Loss (inc.) and Loss (red.) denote the losses calculated by the increased harmonic VPMHM model and the reduced

TABLE 2. Comparisons of rotor eddy-current harmonic losses by different VPMHM models.

Order	Rotor induced frequency, Hz	Loss (inc.), W	Loss (red.), W	Error, %
+1	0	10842	10842	–
−5	1200	344	322	−6.4
+7	1200	132	134	+1.5
−11	2400	566	560	−1.1
+13	2400	430	426	−0.9
−17	3600	12	14	–
+19	3600	6	8	–
−23	4800	50	55	–
+25	4800	54	55	–
−29	6000	3	3	–
+31	6000	4	5	–
−35	7200	401	417	+4.0
+37	7200	221	238	+7.7
Total	–	13065	13079	+0.1

harmonic VPMHM model, respectively. Some errors are not listed in the table, either because the error is zero or the losses themselves are very small and can thus be neglected. There is a tendency that the increased harmonic VPMHM model gives more losses for the low-order harmonics. The reduced harmonic VPMHM shows more losses for the high-order harmonics. However, these two methods yield almost the same losses for both the total losses and a particular harmonic loss with very small errors. Moreover, the total losses computed by these VPMHM models (13065 W and 13079 W) are consistent with those (13286 W) obtained from the normal FEM model. Both the results can be considered to validate the accuracy of these two models.

C. DISCUSSION ON THE ACCELERATION OF THE SIMULATION TIME

The improved VPMHM with hybrid excitation proves to be accurate enough for the determination of solid-rotor eddy-current harmonic losses. It is also capable of obtaining the penetration depth on the rotor surface for a particular harmonic. However, the model also has some drawbacks; especially the simulation speed is low. Because of the good mesh quality and a very small time step, the normal FEM model as shown in Fig. 8 takes about 20 h (8000 steps) by a workstation equipped with Intel(R) Xeon(R) W-2135 CPU @ 3.70 GHz and 256 GB RAM before the machine fully reaches its steady state. ''Steady state'' here means that all the electromagnetic characteristics (e.g. torque, rotor speed, and stator current) reach the steady state. One particular improved VPMHM model almost takes the same amount of time as the normal FEM model because of the long transient caused by the fundamental during the simulation. Finally, it takes about 280 h in total including one normal FEM model and thirteen improved VPMHM models. It is not acceptable for some cases, especially certain industrial applications. Therefore, a critical problem is how to accelerate the simulation.

An option is to use the frozen permeability method to accelerate the simulation time. The method applies the rotor permeability distribution from the steady state at the beginning of the simulation so that the the steady state can be reached very quickly. The frozen permeability method has been widely used in PMSMs for instance for reluctance torque analysis and d-q inductance calculation as reported in [22] and [23]. However, this kind of a method is not suitable for the IM, especially the solid-rotor IM. This is explained by the fact that in the solid-rotor IM there are three main types of transient; eddy-current transient, magnetic field transient, and electric field transient. These three transients have to match and follow each other during the simulation, or otherwise, the convergence of the simulation could be lost. The improved VPMHM models with frozen permeability were also simulated in this study, and it was found that the results for the models were divergent.

Another method is based on the possibility of the improved VPMHM model to distinguish the harmonic behaviors (e.g. losses, penetration depth, and permeability) from an actual machine. It is even possible to distinguish the harmonic transients by the improved VPMHM model. Taking the increased harmonic hybrid excited VPMHM model as an example, Fig. 12 shows the rotor eddy-current density distribution caused by the fundamental and −5th harmonic at different time instants during transients from 0.05 s to 0.40 s. Fig. 12(a) reveals that when the time increases, the fundamental eddy current penetrates gradually deeper before it fully reaches the steady state. The eddy current has already penetrated into the rotor yoke area at 0.05 s. For the rest of the simulation time from 0.05 s to 0.40 s, the eddy current on the rotor surface remains almost the same, which means that most of the simulation time is used for the transient of the eddy current in the rotor yoke area caused by the fundamental from 0.25 s to 0.40 s. This is due to the fact that the fundamental has a much higher amplitude and penetrates much deeper at a very low slip. Consequently, the rotor suffers from a strong damping effect, and a much longer time period is needed for the fundamental transient. Fig. 12(b) shows that the rotor eddy current generated by the −5th harmonic remains almost the same after 0.05 s, because the penetration depth is relatively small and it is reached quite fast. The phenomenon indicates that the transients for the fundamental and high-order harmonics are different and the high-order harmonics have much shorter transients. In that case, it is possible to obtain the harmonic losses only during the transient before it fully reaches the steady state.

Fig. 13(a) shows the main high-order harmonic rotor eddy-current losses during the transient. The fundamental is not shown because it fully reaches the steady state only after about 0.40 s. The rest of the harmonic losses are not shown in the figure either because the losses are not high enough. It can be seen that the harmonic losses at 0.05 s are close to those in the steady state. After 0.25 s, all the harmonic losses remain almost the same, which means that all the harmonics complete their transients at around 0.25 s. Fig. 13(b) shows the total rotor eddy-current losses including the fundamental and all the harmonics listed in Table 1 during the transients. The fundamental loss is constant (10842 W) obtained

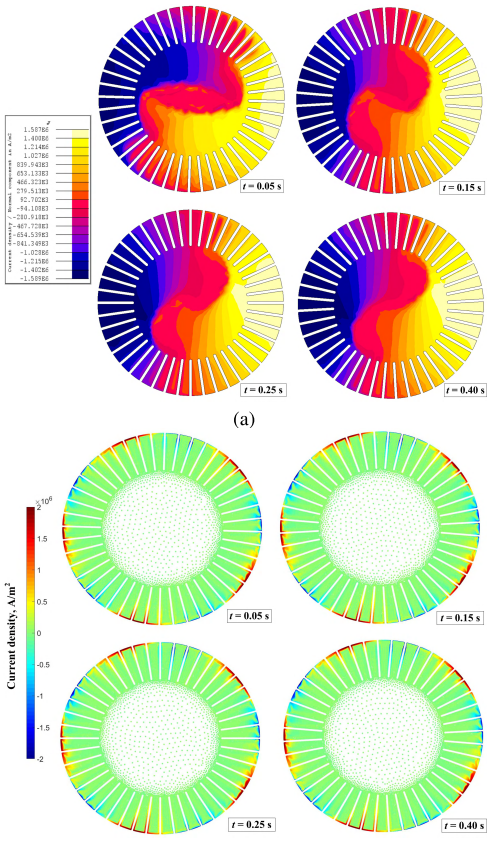

FIGURE 12. (a) Rotor eddy-current density distributions caused by the fundamental during the transient from 0.05 s to 0.40 s estimated by the increased harmonic hybrid excited VPMHM model. (b) Rotor eddy-current density distributions caused by the −5th harmonic during the transient from 0.05 s to 0.40 s estimated by the increased harmonic hybrid excited VPMHM model.

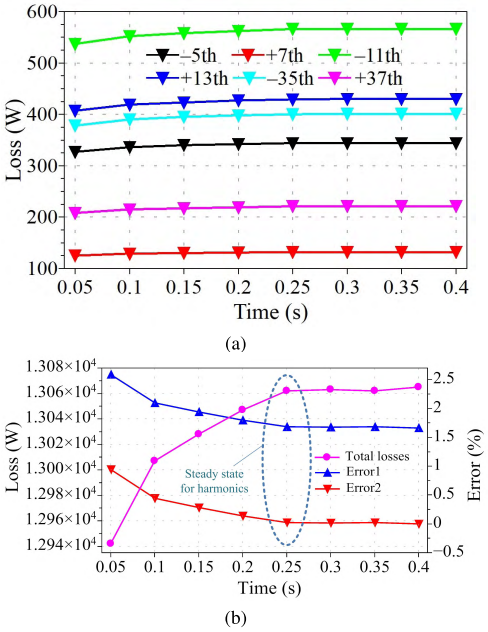

FIGURE 13. (a) Main harmonic rotor eddy-eddy current losses estimated by the improved VPMHM model during the transient. (b) Total rotor eddy-current losses estimated by the improved VPMHM model during the transient.

at 0.40 s. In Fig. 13(b), Error 1 and Error 2 denote the errors with respect to the total losses (13286 W) from the normal FEM model and the total losses (13065 W) in the steady state from the improved VPMHM model. This figure also reveals that the harmonic transients are completed at around 0.25 s, which can help to reduce the simulation time from 280 h to 190 h (40 h in total for the normal FEM model and the fundamental VPMHM model, and 150 h for the harmonic VPMHM models). However, if small errors can be accepted, the simulation time can be reduced to 70 h (40 h in total for the normal FEM model and the fundamental VPMHM model, and 30 h for the harmonic VPMHM models) with Error 1 of 2.59% and Error 2 of 0.94%. The machine studied here is a high-speed IM with a 200 Hz supply frequency, and therefore, the calculation takes time. For a similar 50 Hz machine, the simulation would be much faster (about 18 h in total).

The results and discussion above confirm that the improved VPMHM model is capable of determining the transients for harmonics, and thus, it can be used to significantly accelerate the simulation time with an acceptably small error.

V. CONCLUSION

The solid-rotor eddy-current losses can be mitigated efficiently, after the harmonic losses are correctly analyzed. To accurately separate the solid-rotor eddy-current harmonic losses for a high-speed IM from the total rotor losses, an improved VPHMH model and a computational algorithm were presented in this paper. The 2-D fast Fourier transform was used to distinguish the time-spatial harmonic components in the air-gap flux density. Two different improved VPMHM models were described to calculate the rotor eddy-current losses. The results of the two models proved to be close to each other, and they both provided about 98.5% of the total losses obtained from the normal FEM model. With the improved VPMHM model, it was also possible to obtain the distributions of the rotor eddy current and penetration depth caused by a particular harmonic. Moreover, the simulation time was further optimized for the

VPMHM model, based on the fact the high-order harmonics had shorter transients than the fundamental. Finally, the total simulation time was reduced by 30% (fully completing the harmonic transients) and 75% (with some acceptable errors). With the simulation results, it is possible to mitigate the rotor losses correspondingly. For example, according to the harmonic losses in Fig. 9, it reveals that it is more worthy to suppress the -11th and $+13$th harmonic losses instead of the stator slot harmonic losses. Therefore, the rotor skewed can be utilized and optimized towards the -11th and $+13$th harmonics. The VPMHM model also has the potential to be further developed to estimate other electromagnetic characteristics (e.g. harmonic torques) in electrical machines in the future.

ACKNOWLEDGMENT

The authors would like to thank Dr. Hanna Niemelä, Lappeenranta University of Technology, for her linguistic assistance in the preparation of this manuscript.

REFERENCES

[1] A. Smirnov, N. Uzhegov, T. Sillanpää, J. Pyrhönen, and O. Pyrhönen, "High-speed electrical machine with active magnetic bearing system optimization," *IEEE Trans. Ind. Electron.*, vol. 64, no. 12, pp. 9876–9885, Dec. 2017.

[2] Y. Zhang, S. McLoone, and W. Cao, "Electromagnetic loss modeling and demagnetization analysis for high speed permanent magnet machine," *IEEE Trans. Magn.*, vol. 54, no. 3, Mar. 2018, Art. no. 8200405.

[3] C. Gong and T. Habetler, "A novel rotor design for ultra-high speed switched reluctance machines over 1 million rpm," in *Proc. IEEE Int. Electric Mach. Drives Conf. (IEMDC)*, May 2017, pp. 1–6.

[4] D. H. Lee, T. H. Pham, and J. W. Ahn, "Design and operation characteristics of four-two pole high-speed SRM for torque ripple reduction," *IEEE Trans. Ind. Electron.*, vol. 60, no. 9, pp. 3637–3643, Sep. 2013.

[5] D. Gerada, A. Mebarki, N. L. Brown, C. Gerada, A. Cavagnino, and A. Boglietti, "High-speed electrical machines: Technologies, trends, and developments," *IEEE Trans. Ind. Electron.*, vol. 61, no. 6, pp. 2946–2959, Jun. 2014.

[6] J. Pyrhonen, J. Nerg, P. Kurronen, and U. Lauber, "High-speed, 8 mw, solid-rotor induction motor for gas compression," in *Proc. 18th Int. Conf. Electr. Machines*, Sep. 2008, pp. 1–6.

[7] J. B. Danilevich, V. N. Antipov, I. Y. Kruchinina, and Y. P. Khozikov, "Design considerations of submersible unprotected solid-rotor induction motor," in *Proc. 18th Int. Conf. Electr. Mach.*, Sep. 2008, pp. 1–4.

[8] N. Uzhegov, J. Barta, J. Kurfürst, C. Ondrusek, and J. Pyrhönen, "Comparison of high-speed electrical motors for a turbo circulator application," *IEEE Trans. Ind. Appl.*, vol. 53, no. 5, pp. 4308–4317, Sep. 2017.

[9] J. Pyrhonen, J. Nerg, P. Kurronen, and U. Lauber, "High-speed high-output solid-rotor induction-motor technology for gas compression," *IEEE Trans. Ind. Electron.*, vol. 57, no. 1, pp. 272–280, Jan. 2010.

[10] P. Lazari, J. Wang, and B. Sen, "3-D effects of rotor step-skews in permanent magnet-assisted synchronous reluctance machines," *IEEE Trans. Magn.*, vol. 51, no. 11, pp. 1–4, Nov. 2015.

[11] J. Wang, S. L. Ho, W. N. Fu, and Y. H. Wang, "Design and analysis of a novel traveling wave induction heating system with magnetic slot wedges for heating moving thin strips," *IEEE Trans. Magn.*, vol. 46, no. 6, pp. 2175–2178, Jun. 2010.

[12] O. Misir, S. M. Raziee, N. Hammouche, C. Klaus, R. Kluge, and B. Ponick, "Prediction of losses and efficiency for three-phase induction machines equipped with combined star-delta windings," *IEEE Trans. Ind. Appl.*, vol. 53, no. 4, pp. 3579–3587, Jul./Aug. 2017.

[13] M. Markovic and Y. Perriard, "Analytical solution for rotor eddy-current losses in a slotless permanent-magnet motor: The case of current sheet excitation," *IEEE Trans. Magn.*, vol. 44, no. 3, pp. 386–393, Mar. 2008.

[14] M. Markovic and Y. Perriard, "An analytical determination of eddy-current losses in a configuration with a rotating permanent magnet," *IEEE Trans. Magn.*, vol. 43, no. 8, pp. 3380–3386, Aug. 2007.

[15] Z. Q. Zhu, K. Ng, N. Schofield, and D. Howe, "Improved analytical modelling of rotor eddy current loss in brushless machines equipped with surface-mounted permanent magnets," *IEE Proc. Electr. Power Appl.*, vol. 151, no. 6, pp. 641–650, Nov. 2004.

[16] Y. Zhang, K. Lu, and Y. Ye, "Permanent magnet eddy current loss analysis of a novel motor integrated permanent magnet gear," *IEEE Trans. Magn.*, vol. 48, no. 11, pp. 3005–3008, Nov. 2012.

[17] M. Koo, J. Choi, J. Jeong, J. Kim, and Y. Park, "Comparative analysis of eddy current loss in permanent magnet synchronous generator considering PM shape and skew effect for wind power generation," in *Proc. IEEE Int. Magn. Conf. (INTERMAG)*, May 2015, p. 1.

[18] C. Di, I. Petrov, and J. J. Pyrhönen, "Modeling and mitigation of rotor eddy-current losses in high-speed solid-rotor induction machines by a virtual permanent magnet harmonic machine," *IEEE Trans. Magn.*, vol. 54, no. 12, pp. 1–12, Dec. 2018.

[19] C. Wang, X. Bao, S. Xu, Y. Zhou, W. Xu, and Y. Chen, "Analysis of vibration and noise for different skewed slot-type squirrel-cage induction motors," *IEEE Trans. Magn.*, vol. 53, no. 11, Nov. 2017, Art. no. 8206006.

[20] I. Petrov, M. Niemelä, P. Ponomarev, and J. Pyrhönen, "Rotor surface ferrite permanent magnets in electrical machines: Advantages and limitations," *IEEE Trans. Ind. Electron.*, vol. 64, no. 7, pp. 5314–5322, Jul. 2017.

[21] J. Pyrhonen, T. Jokinen, and V. Hrabovcova, *Design Rotating Electronic Machines*. Hoboken, NJ, USA: Wiley, 2013.

[22] G. T. Paula, J. R. B. A. Monteiro, T. E. P. Almeida, M. P. Santana, W. C. A. Pereira, and M. L. Aguiar, "Investigation of reluctance torque in a BLDC motor using frozen permeability method and equivalent air-gap analysis," *IEEE Latin Amer. Trans.*, vol. 14, no. 8, pp. 3678–3686, Aug. 2016.

[23] G. Li, Z. Q. Zhu, and G. Jewell, "Performance investigation of hybrid excited switched flux permanent magnet machines using frozen permeability method," *IET Electr. Power Appl.*, vol. 9, no. 9, pp. 586–594, Nov. 2015.

CHONG DI was born in Wuxi, China, in 1991. He received the B.Eng. and M.Eng. degrees in electrical engineering from the Hefei University of Technology, Hefei, China, in 2014 and 2017, respectively. He is currently pursuing the D.Sc. degree with the Department of Electrical Engineering, Lappeenranta University of Technology, Finland.

His research interest includes high-speed electrical machines.

ILYA PETROV received the D.Sc. degree from the Lappeenranta University of Technology, Finland, in 2015, where he is currently a Fellow Researcher with the Department of Electrical Engineering.

JUHA J. PYRHÖNEN (M'06–SM'17) born in Kuusankoski, Finland, in 1957. He received the D.Sc. degree from the Lappeenranta University of Technology (LUT), Finland, in 1991.

He was a Professor of electrical machines and drives with LUT, in 1997. He is currently engaged with the research and development of electric motors and power-electronic-controlled drives. He is also studying possibilities of using carbon-based materials in electrical machines. He has wide experience in the research and development of special electric drives for distributed power production, and traction and high-speed applications. Permanent magnet materials and applying them in machines have an important role in his research.

Publication III

Di, C., Petrov, I., and Pyrhönen, J.
Modeling and Mitigation of Rotor Eddy-Current Losses in High-Speed Solid-Rotor Induction Machines by a Virtual Permanent Magnet Harmonic Machine

Reprinted with permission from
IEEE Transactions on Magnetics
Vol. 54, pp. 1-12, 2018

Modeling and Mitigation of Rotor Eddy-Current Losses in High-Speed Solid-Rotor Induction Machines by a Virtual Permanent Magnet Harmonic Machine

Chong Di, Ilya Petrov, and Juha J. Pyrhönen, *Senior Member, IEEE*

Department of Electrical Engineering, LUT School of Energy Systems, Lappeenranta University of Technology, 53851 Lappeenranta, Finland

Being much more rugged than a rotor made of traditional steel sheets, a solid rotor is frequently used in high-power high-speed induction machines (IMs). Furthermore, by a solid-rotor machine, a higher rotating speed can be achieved. However, the solid rotor also has certain disadvantages, the relatively high solid-rotor eddy-current losses being the most serious one. Basically, solid-rotor eddy-current losses are mainly induced by time–spatial air-gap flux density high-order harmonics. The suppression of the high-order harmonics is the key means to mitigate the rotor eddy-current losses. In this paper, a novel computational model is proposed for evaluating the rotor harmonic eddy-current losses of a 2 MW, 12 000 r/min IM. The model was built on a special machine referred to as a virtual permanent magnet harmonic machine (VPMHM). The model was constructed by applying the finite-element method (FEM), and it is based on the time–spatial harmonics produced by a rotating magnet with sinusoidal magnetization. The VPMHM model links the air-gap flux density harmonics directly to the specific rotor eddy-current losses. Furthermore, according to the proposed model, three options, namely, the use of air-gap permeance modifying notches on the stator teeth, semimagnetic wedges, and their combination, were investigated in detail for mitigating the rotor eddy-current losses in the motor nominal operating point. The results and conclusions in this paper are based on the FEM analysis.

Index Terms— **Eddy-current losses, notches on the stator teeth, semimagnetic wedges, solid-rotor high-speed induction machine (IM), virtual permanent magnet harmonic machine (VPMHM).**

I. Introduction

HIGH-SPEED machines are becoming increasingly common in industrial applications because of the rapid development of the power electronics technology, which makes it possible to supply and control a machine with a much higher frequency than the standard network frequency, and, thereby, reach a higher rotational speed. Typically, three types of high-speed machines are applied for different industrial purposes: induction machines (IMs), permanent magnet synchronous machines (PMSMs), and switched reluctance machines (SRMs) [1]– [6]. Compared with the PMSM, the IM has a simpler, low-cost, and rugged rotor structure. The IM also has the advantages of easier control and lower noise over the SRM. The most important advantage of the IM is that the machine can achieve a higher rotor peripheral speed with a solid steel rotor, avoiding the challenges of keeping the rotor constructional elements in place as in PMSMs. Consequently, a solid rotor is very suitable for a high-power high-speed machine application, as recommended in [7].

It has been reported in [8] and [9] that the maximum rotor peripheral speeds for solid- and laminated-rotor IMs are 367 and 290 m/s, respectively. Furthermore, Gerada *et al.* [2] and Lähteenmäki [10] suggest that it is advisable to use a solid rotor for an IM with the highest rotor peripheral speed, higher than 200 m/s. In this paper, a 2 MW, 12 000 r/min high-speed IM with a slitted solid rotor is studied. Its maximum rotor peripheral speed is 209 m/s, which corresponds to the previous recommendation and the similar case reported in [11]. Despite the advantages of the solid rotor, it also has some disadvantages. Among them, the most serious drawback is the relatively high solid-rotor eddy-current loss component. Lateb *et al.* [12] made a comparison of losses between the machines equipped with a slitted solid rotor and a laminated rotor with a squirrel cage. It was found that the former had a higher per-unit slip with 0.7% than the latter (0.46%), which meant that the former machine had higher rotor losses. Typically, the suppression of rotor losses is more important than the reduction of stator losses for high-power high-speed IMs. The reason for this is that it is often more difficult to remove heat generated from the rotor inside the machines and more convenient to cool the stator by different commonly applied methods (e.g., water jacket installed on the stator frame). Therefore, computation and possible reduction of solid-rotor losses are a critical task for high-power high-speed IMs.

Typically, solid-rotor eddy-current losses are induced by time–spatial air-gap flux density harmonics. The fundamental harmonic losses are more related to the slip and output torque. With a certain output torque demand, it is possible to reduce the losses by increasing the fundamental air-gap flux density harmonic, which results in a lower per-unit slip. When it comes to the high-order harmonic losses, the situation is the opposite. Basically, with the higher amplitudes of the high-order harmonics, the higher eddy-current losses appear on the rotor surface. Considering the whole harmonic spectrum of the air-gap flux density distribution, the stator slot harmonics produce most of the harmonics losses, because they typically have

Manuscript received August 16, 2018; revised September 26, 2018; accepted September 26, 2018. Date of publication October 16, 2018; date of current version November 16, 2018. Corresponding author: C. Di (e-mail: chong.di@lut.fi).

Color versions of one or more of the figures in this paper are available online at http://ieeexplore.ieee.org.

Digital Object Identifier 10.1109/TMAG.2018.2873279

higher amplitudes than the other harmonics. There is some literature on the modeling and mitigation of rotor eddy-current losses. Considering the modeling and computation of rotor eddy-current losses, Zhu *et al.* [13] proposed an improved analytical model to predict the rotor eddy-current losses with the consideration of both the time and space magnetomotive force. The predicted results were validated by thermometric measurements. As reported in [13], however, both the stator slotting effect and the eddy-current reaction (brushless machine) were neglected. Räisänen *et al.* [14] developed a method for rapid computation of harmonic eddy-current losses in a high-speed solid rotor, taking the stator slotting effect into account. As described in [14], a limitation was that the rotor saturation was neglected and the rotor material permeability was not corrected. The model introduced in this paper takes both the stator slot harmonic and the rotor saturation into account.

Considering the mitigation of the rotor eddy-current losses, from the rotor side point of view, application of rotor slits is an effective way to reduce the eddy-current losses, as reported in [7] and [15]. Aho [16] recommended that for a slitted rotor, the highest efficiency and power factor can be achieved when the optimum slit depth is about 40%–50% of the rotor radius, when taking the rotor mechanical strength limits into consideration. According to this recommendation, the rotor slit depth was optimized to achieve the lowest rotor eddy-current losses for the model discussed in this paper, and a suitable solution was found to be about 37% of the rotor radius. On the stator side, extra actions can be taken to reduce the losses, most of them being based on suppressing the air-gap flux density harmonics. Special stator windings [17], [18] and magnetic wedges [19], [20] are the most effective means to mitigate the rotor eddy-current losses. This paper focuses on the means to reduce the rotor eddy-current losses on the stator side.

The aim of this paper is to model, predict, and mitigate the rotor eddy-current losses for a 2-pole, 2 MW, 12 000 r/min high-speed IM. Section II introduces an overview of the high-speed IM studied in this paper. Next, modeling of the rotor eddy-current harmonic losses applying the finite-element method (FEM) is described by the virtual permanent magnet harmonic machine (VPMHM) based on the production of time–spatial harmonics by a rotating magnet with sinusoidal magnetization. The effects of stator slotting and rotor damping are considered by the VPMHM model. It also links the specific harmonic amplitudes directly to the rotor eddy-current losses. Section III discusses three actions to mitigate the rotor eddy-current losses from the stator side with the VPMHM. The actions are the use of notches on the stator teeth, semimagnetic wedges, and a combination of them. Finally, an appropriate solution was found, and it was further optimized to achieve the minimum rotor losses.

II. Modeling of the Rotor Harmonic Eddy-Current Losses

A. Overview of the High-Speed IM Model

Some effective measures were taken to further suppress the rotor losses in the previous model of the 2-pole, 2 MW, 12 000 r/min IM, presented in [21]. The air-gap length was increased from 6 to 7 mm, which slightly reduces the fundamental of the air-gap flux density but efficiently suppresses the harmonic components. The stator winding was modified into a two-layer short pitch winding (short pitch $y = 5/6$), which can guarantee smaller phase band harmonics. Because of difficulties in the manufacture, the solid rotor with copper squirrel cage was replaced by a solid rotor with 44 axial slits. This facilitates the manufacture, and the rotor becomes more rugged. The rotor losses are smaller for a rotor with axial slits compared with a rotor with a smooth surface. The effects of magnetic wedges are studied and explained in detail in Section III.

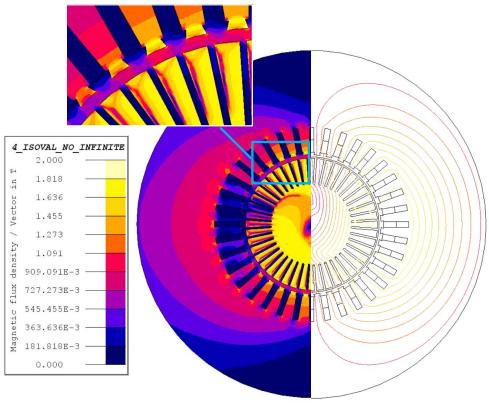

Fig. 1. High-speed IM model with flux density and flux line distributions at the nominal plotted by the 2-D FEM.

The model obtained by Altair Flux 2-D with flux density and flux line distributions in the nominal operating condition is illustrated in Fig. 1. Fig. 1 shows that both the stator tooth tips and the rotor teeth are close to saturation. The machine also suffers from a strong damping effect of the solid rotor running at a certain slip, which is due to the fact that the flux lines are strongly twisted on the solid-rotor core in the rated torque point, as shown in Fig. 1. The air-gap flux density is relatively high, and there are slip-induced eddy currents flowing in the solid rotor. The fundamental-related eddy current penetrates deep into the rotor because of the low per-unit slip. Without any other actions to reduce the rotor losses, the total solid-rotor losses at the nominal load point are about 26.5 kW for this model, containing 23.8 kW in the rotor teeth and 2.7 kW in the rotor yoke estimated by the 2-D FEM.

B. Analysis of the Penetration Depths and Eddy-Current Frequencies

Typically, solid-rotor losses are generated by rotor eddy currents, which are induced by the differentials of the magnetic vector potentials, as reported in [22]. To simplify the analysis, it can be assumed that there are only axial eddy currents traveling in the solid rotor. Thus, all the rotor eddy-current

losses caused by the eddy currents containing all the harmonics can be expressed in the cylindrical coordinates as [23]

$$P_{\text{eddy}} = \sum_{n=1}^{\infty} \left(\int_0^l \int_0^{2\pi} \int_{\text{r}-\delta_n}^{\text{r}} \frac{|J_{Zn}|^2}{2\sigma} d\rho d\theta dz \right) \tag{1}$$

where J_{Zn} is the nth eddy-current harmonic, σ is the conductivity of the solid-rotor steel (2.22×10^6 S/m at temperature $T = 180$ °C), l is the solid-rotor effective length, r is the rotor peripheral radius, and δ_n denotes the penetration depth for the nth eddy-current harmonic. It can be seen from (1) that when the rotor effective length and the rotor peripheral radius are constants, the rotor eddy-current losses mostly depend on two factors, the amplitudes of the eddy currents and the penetration depths. According to the classical theory, the penetration depths for eddy currents with different frequencies can be further expressed as [24]

$$\delta_n = \frac{1}{\sqrt{\mu_0 \mu_{\text{r}} \pi f_n \sigma}} \tag{2}$$

where μ_0 is the vacuum permeability, μ_{r} is the relative permeability of the rotor steel (S355), and f_n is the electrical frequency for the nth rotor eddy current. Using (2) in the case of solid steel is only indicative (not applied in this paper) as the relative permeability of the material changes as a result of saturation. However, as shown in Fig. 1, when the machine is running at its nominal load point, the solid rotor is almost saturated. In other words, the rotor steel is working beyond the liner area of the B–H curve. As a result, the relative permeability of the rotor steel at the nominal load is smaller than the initial relative permeability because of the saturation effect, which is described further in Section II-C.

The rotor eddy currents are generated by all the harmonic spectra of the air-gap flux density. However, different harmonics have different properties; to be more specific, they have different orders, amplitudes, and frequencies. Consequently, they produce eddy currents on the rotor surface with different amplitudes, frequencies, and penetration depths. According to [25], it is possible to analyze the eddy-current frequencies induced by the corresponding air-gap flux density harmonics. In that case, the eddy-current penetration depths can be directly reflected by the frequencies. Table I shows the rotor main eddy-current frequencies caused by the fundamental and stator slot harmonics of the air-gap flux density. Besides the harmonics shown in Table I, the phase-band harmonics, saturation harmonics, and other higher order harmonics also generate eddy-current losses on the rotor surface. These components, which are not listed in Table I, are not discussed in this paper, because all the actions for mitigating the losses are primarily considered from the viewpoint of fundamental and stator slot harmonics.

TABLE I
ROTOR MAIN EDDY-CURRENT FREQUENCIES

Harmonic type	Order	Harmonic velocity (r/min)	Rotor eddy-current frequency (Hz)
Fundamental harmonic	p	n_0	sf_1
Stator slot harmonic	$v=kQ_s+p$	$+n_0/v$	$+f_1[1-v(1-s)]$
	$v=kQ_s-p$	$-n_0/v$	$-f_1[1+v(1-s)]$

where Q_s is the stator slot number, s is the per-unit slip, p is the number of pole pairs, f_1 is the supply frequency, n_0 is the synchronous speed, and k is a positive integer.

C. Implementation of the VPMHM Model

It is relatively easy to compute the total solid-rotor losses directly by the FEM. Nevertheless, it is much more complicated to compute and predict the eddy-current losses caused by the high-order harmonics. Thus, production of the magnetic field is highly critical for the analysis of high-order harmonic losses. One possible way is to model a machine with a certain harmonic rotating in the air gap in such a way that the harmonic effects can be studied separately. Among all the high-order harmonics, the stator slot harmonics are the most critical ones. Therefore, the key aspect of modeling a special machine of this kind is to obtain the time and spatial harmonics based on the fundamental and stator slot harmonics of the air-gap flux density. They can be expressed by the following equation [26]:

$$\begin{cases} b_0(\theta, t) = B_0 \cos(p\theta - \Omega_0 t - \varphi_0) \\ b_v(\theta, t) = B_v \cos(v\theta - \Omega_v t - \varphi_v) \end{cases} \tag{3}$$

where θ is the stator angle, t is the time, and Ω_0 and Ω_v are the mechanical angular velocities of the fundamental and the stator slot harmonics, respectively, which are shown as harmonic velocities in Table I. B_0 and B_v are the amplitudes of the fundamental and stator slot harmonics, respectively, and φ_0 and φ_v are the initial phase angles of the fundamental and stator slot harmonics, respectively.

It can be seen in (3) that the task is to achieve a multiphase rotating magnetic field with different velocities. It is possible to produce this magnetic field with a multiphase stator winding excited with a proper stator current amplitude and frequency. The drawback is, however, that the magnetic field generated by the stator winding is not a pure sinusoidal curve. It can contain several other harmonics, which interfere with each other preventing the computation of the eddy-current losses generated by one particular air-gap flux density harmonic. Hence, the VPMHM model, especially for the harmonic performance analysis, has been developed, as shown in Fig. 2, with a pure sinusoidal magnetic field rotating in the air gap.

The VPMHM model shown in Fig. 2 comprises four parts including the solid rotor, the air gap, a sinusoidal excitation magnet, and an external soft magnetic region. With these four parts, the magnetic flux can travel for instance along the path shown in Fig. 2. The solid rotor rotates with the angular velocity of Ω_{r}. The external soft magnetic region is only used to provide a path for the magnetic flux to travel freely. It can be regarded as any high-permeability material. The air gap consists of three layers with different properties. One layer is set right outside the rotor surface, and it is rotating with the rotor (rotor air layer). Another one is set right inside the magnet surface (magnet air layer), and the last one is fixed in the middle of these two layers (middle air layer). According

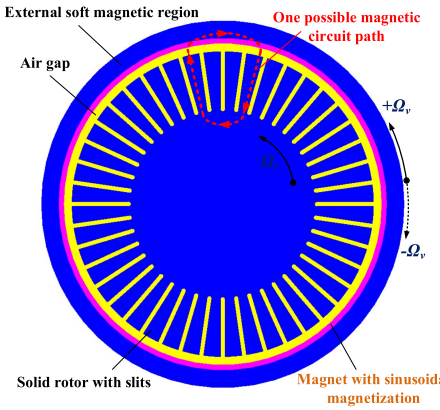

Fig. 2. Proposed VPMHM model for the computation of the rotor eddy-current losses.

to (3), in order to simulate the motion property of the magnetic field, the magnet air layer, the magnet, and the external soft magnetic region should rotate together with a speed of $\pm\Omega_\nu$ (where $+$ denotes the same direction with respect to the rotor velocity and $-$ indicates the opposite direction with respect to the rotor velocity). The magnet is totally sinusoidally magnetized in the normal direction. In that case, no other harmonics are generated on the magnet side. If the origin is located in the rotor geometry center in Fig. 2, the magnetization of the magnet for producing the νth harmonic in the Cartesian coordinate system (x–y coordinate system) can be expressed as

$$\begin{cases} B_x(\theta) = B_{r\nu}\cos(\nu\theta)\cos\theta \\ B_y(\theta) = B_{r\nu}\cos(\nu\theta)\sin\theta \\ \theta = \arctan\dfrac{y}{x} \end{cases} \tag{4}$$

where $B_{r\nu}$ is the amplitude of the remanent flux density of the νth harmonic. In order to generate the flux density B_ν in the air gap in this VPMHM model, the remanent flux density $B_{r\nu}$ in the magnet should be larger. The reason for this is that the flux has to travel through the air and the magnet and also overcome the rotor damping effects, as shown in Fig. 2. Moreover, the relative permeability of the magnet can be set somewhat smaller, which can provide a higher magnetomotive force with the same remanent flux density.

Another key fact is that as shown in Fig. 1, the solid rotor is almost saturated at the nominal load, which means that the rotor material is working far from the initial relative permeability (which is 1443). For this reason, the special rotor permeability has to be applied as follows. At the nominal load, the eddy-current effects in the solid rotor caused by the fundamental and the higher order harmonics of the air-gap flux density can be discussed separately. The fundamental harmonic with much larger amplitude and a lower frequency penetrates considerably deeper into the rotor than do the higher

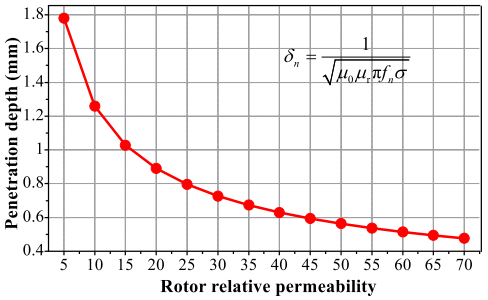

Fig. 3. Penetration depth for the first stator slot harmonic on the rotor surface as a function of rotor relative permeability.

order harmonics at the nominal load. As a result, the solid rotor stays close to the saturation point at the nominal load because of the larger fundamental harmonic. Therefore, when discussing the eddy currents caused by higher order harmonics, the effects of the fundamental harmonic on the rotor permeability have to be taken into account. Thus, when modeling the harmonic losses, the rotor material permeability has to be set at a correct value according to the nominal load. The process for defining the rotor permeability in the calculation of a specific harmonic loss, for example, the first-order stator slot harmonic in the nominal condition, is completed as follows. First, the rotor surface flux density in the nominal condition can be estimated by the FEM, and the average flux density in the specific area (the roughly estimated penetration depth area) is about 1.5 T. Then, based on the B–H curve of the rotor material and the flux density value obtained from the FEM, the rotor relative incremental permeability can be estimated; it is about 50. The first stator slot harmonic frequency f_{35} or f_{37} is about 7200 Hz, and the conductivity is 2.22×10^6 S/m at the temperature $T = 180$ °C. Therefore, according to (2), the corresponding penetration depth for the first-order stator slot harmonic is about 0.56 mm. Fig. 3 shows the penetration depth on the rotor surface for the first stator slot harmonic as a function of rotor relative permeability. The penetration depth reduces with the increment of the rotor relative permeability, and the curve becomes flatter when the permeability gets larger.

With the proposed VPMHM model, it is possible to analyze the solid-rotor eddy-current losses or other characteristics (e.g., harmonic-related torques) caused by different high-order harmonics. However, the VPMHM model cannot be utilized alone. It has to be implemented with the normal FEM model of a machine. Basically, Fig. 4 shows the calculation procedure of the proposed method and the relationship between the normal FEM model and the VPMHM model. Since the solid-rotor eddy-current losses can be estimated separately by the proposed model. The mesh quality and the time step of the VPMHM model can be adjusted and optimized based on the specific harmonics. For example, for the fundamental, a sparse mesh and a longer time step can be used to accelerate the simulation. For the first stator slot harmonic, a dense mesh and a shorter time step have to be used.

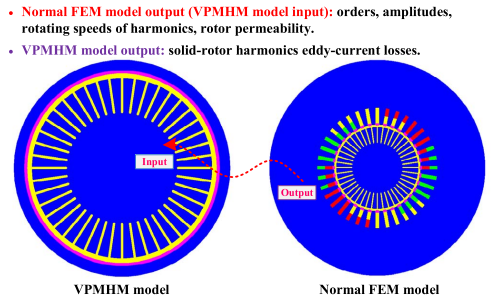

Fig. 4. Calculation procedure of the solid-rotor harmonic eddy-current losses by the proposed method.

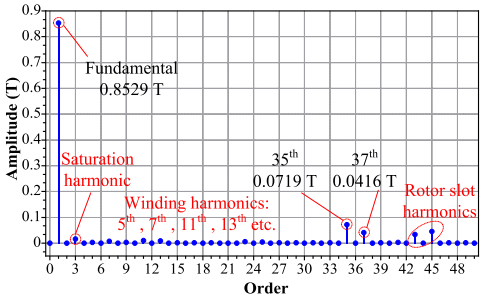

Fig. 5. Harmonics of the air-gap flux density at the nominal load of the normal FEM model estimated by the 2-D FEM.

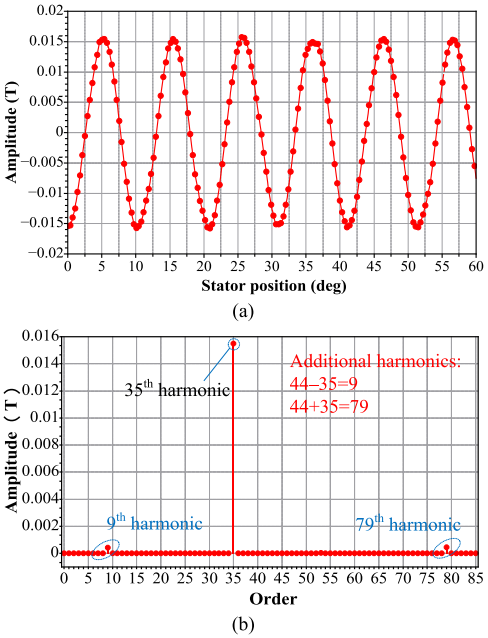

Fig. 6. 35th harmonic of the air-gap flux density generated by the proposed model. (a) Waveform of 35th harmonic. (b) Spectrum of 35th harmonic.

Following the procedure in Fig. 4, Fig. 5 shows the harmonics of the air-gap flux density at the nominal load of the normal FEM model. The 35th and 37th harmonics are the first-order stator slot harmonics (with 36 stator slots); they are much smaller compared with the fundamental harmonic. The 43rd and 45th are the first-order rotor slot harmonics (with 44 rotor slits), but they can be ignored when considering the rotor eddy-current losses. In order to simplify the computation, the saturation and winding harmonics are not discussed in this paper. Please note that all the harmonics in Fig. 5 are air-gap flux density harmonics, which means that they are synthetic results of the stator and rotor harmonics. To be more specific, the solid-rotor damping effect has already been presented in Fig. 5.

By applying the VPMHM model shown in Fig. 2, with proper magnetization and motion settings of the magnet, the losses produced by the harmonics can be computed. Based on the spectrum in Fig. 5, the eddy-current losses generated by the fundamental and the first-order stator harmonics can be studied. When the fundamental-related losses are computed by the VPMHM model, it takes as much time as the normal model (about 30 electrical periods) to reach the steady state for the simulation. As the fundamental air-gap flux density is very high, the rotor damping effect is very strong. If the stator slot harmonic is considered, the simulation is much quicker and only takes some electrical periods.

Fig. 6(a) shows a possible 35th harmonic waveform of the air-gap flux density generated by the proposed VPMHM model. For the sake of clarity and readability, Fig. 6(a) depicts only a part of the waveform instead of the whole 360 electrical degrees. It can be seen in Fig. 6(a) that the waveform is very close to a pure sinusoidal curve, but it still contains some other harmonics. Fig. 6(b) shows the corresponding spectrum of 35th harmonic. The spectrum is obtained from 35th harmonic waveform with 360 electrical degrees. Fig. 6(b) shows that the signal mainly consists of 9th, 35th, and 79th harmonics. Because 9th and 79th harmonics are quite small, they can be ignored and the signal can be regarded as a pure sinusoidal one. The amplitudes are only 3% of the amplitude of 35th harmonic, and they are generated by the interaction of the excitation from the magnet and the first rotor slot permeance harmonic (44 rotor slits). Therefore, Fig. 6 proves that the proposed method can generate a pure stator slot harmonic in the air gap, which is suitable for the analysis of rotor eddy-current losses. As 9th and 79th harmonics are also shown in Fig. 6, it confirms that the rotor damping effects are considered by the VPMHM model.

Based on the proposed method, the fundamental and first-order stator slot harmonic losses can be computed, and the corresponding simulation results are shown in Fig. 7. It is

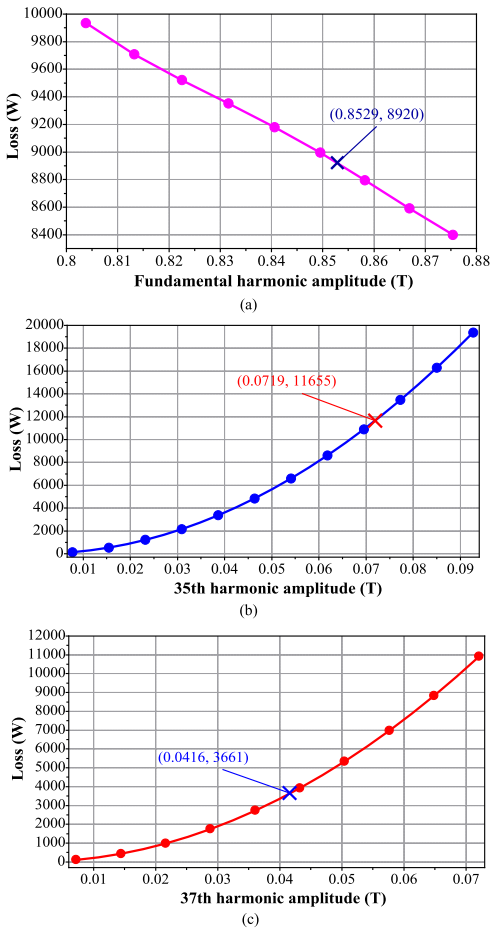

Fig. 7. Fundamental and first-order stator slot harmonic losses as a function of air-gap flux density amplitude estimated by the proposed VPMHM model using the 2-D FEM. (a) Losses varying with the fundamental harmonic. (b) Losses varying with the 35th harmonic. (c) Losses varying with the 37th harmonic.

emphasized that the fundamental losses occur in the whole rotor area, but the stator harmonic losses are only present in the rotor tooth tip areas, which corresponds to the penetration depth described by (2). It should also be clarified that the nonlinear B–H curve is used for the rotor material instead of a constant permeability, when calculating the fundamental-related solid-rotor eddy-current losses. Because the fundamental of the air-gap flux density is very strong, the rotor goes into the saturation automatically. It can be seen in Fig. 7(a) that the fundamental harmonic losses decrease with the increment of the fundamental flux density amplitude. This phenomenon can be explained by the tangential stress [15]. In order to produce the rated electromagnetic torque, once the fundamental flux density amplitude is increased, the linear current density will decrease. As a result, the rotor fundamental losses decrease. In addition, according to Fig. 7(a), it could be concluded that there is a linear relationship between the loss and the fundamental harmonic amplitude, and the fundamental loss can be estimated and predicted by a linear function. However, as shown in Fig. 7(b) and (c), the situation is the opposite. The first-order stator slot harmonic losses increase with the increment of the harmonic amplitude. The higher the harmonic amplitude, the higher are the losses. Furthermore, the curves in Fig. 7(b) and (c) can be fit with quadratic functions. Therefore, the loss generated by a certain harmonic amplitude can be estimated and predicted with a fit quadratic function. In addition, 35th harmonic can generate more losses with the same amplitude compared with 37th harmonic. It is also indicated in Fig. 7 that the fundamental harmonic (0.853 T), 35th harmonic (0.072 T), and 37th harmonic (0.042 T) produce 8.9, 11.7, and 3.7 kW eddy-current losses, respectively, in the solid rotor. The total estimated solid-rotor losses at the nominal load point are 26.6 kW, and thus, the difference between the losses estimated in Fig. 7 and the total solid rotor losses at the nominal load point is 2.3 kW. This difference is mainly caused by some other harmonics, for instance, the saturation harmonic and the winding harmonic.

III. Mitigating of the Rotor Harmonic Eddy-Current Losses

The previous analysis results in this paper showed that the solid-rotor eddy-current losses mainly contain two components: the stator slot harmonics loss and the fundamental harmonic loss. Therefore, there are two main methods to mitigate the rotor losses at the nominal load. One is to increase the fundamental flux density (magnetic component) to reduce the fundamental-related eddy current (electric component), and the other is to reduce the air-gap high-order harmonic flux densities, especially those originating from the stator slots. Hence, the discussion focuses on these two aspects.

A. Mitigation of the Rotor Losses by the Stator Teeth Notches

One of the ways to increase the fundamental air-gap flux density is to reduce the air-gap length. Originally, the machine was designed with the consideration of other issues (e.g., rotor dynamics). Therefore, the air-gap length cannot be changed anymore. Actually, from the magnetic circuit point of view, the air-gap length described as the difference of the stator inner diameter and the rotor outer diameter is not the effective air-gap length. Because of the stator slot opening, the effective air-gap length can be described by the Carter factor, as reported in [27]. Consequently, it is possible to reduce the effective air-gap length by some special means.

In [15], it is shown that in the case of semiclosed stator slots, two special notches can be used on one stator tooth, which compensate for the flux density loss under the stator slot. As a result, the fundamental of the air-gap flux density can be increased. The specific structure is displayed in Fig. 8. It can be seen in Fig. 8 that the notches are located at the

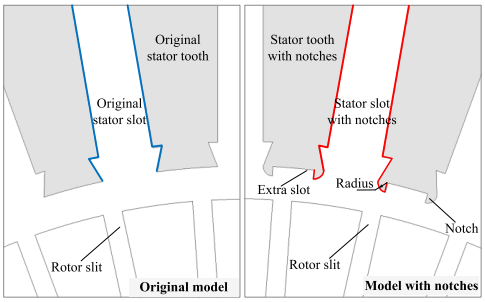

Fig. 8. Model of the notches on the stator teeth.

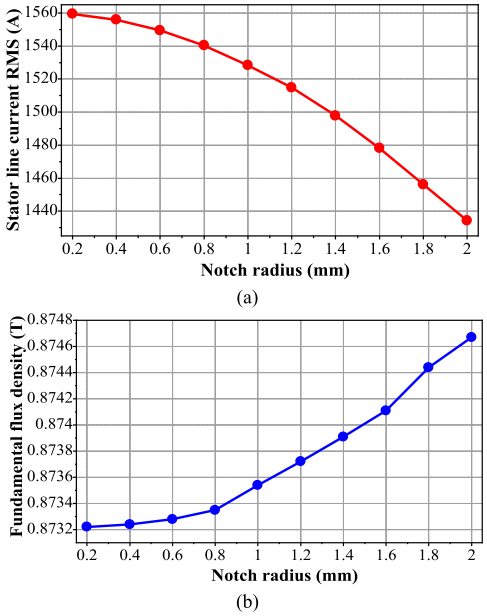

Fig. 9. Stator line currents and fundamentals of the air-gap flux density as a function of notch radius in the no-load condition estimated by the 2-D FEM. (a) Stator line currents varying with the notch radius. (b) Fundamentals of the air-gap flux density varying with the notch radius.

edges of the stator teeth. Every stator tooth has two notches, and each of the notches has a geometry of a quarter of a circle. The radius of the notch is studied in Sections III-A and III-C in the case of open stator slots and a relatively high air-gap length.

In principle, the effective air-gap permeance and the fundamental of the air-gap flux density can be analyzed in the no-load condition. Fig. 9 shows the no-load stator line currents and the fundamentals of the air-gap flux density varying with the notch radius. It reveals that a notch can reduce the no-load

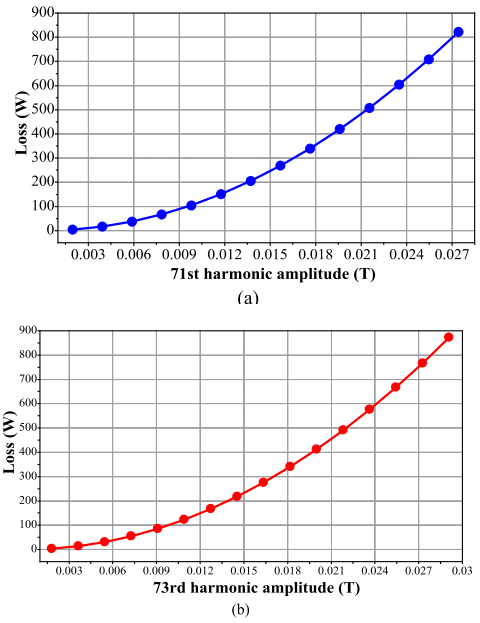

Fig. 10. Second-order stator slot harmonic losses as a function of air-gap flux density amplitude estimated by the proposed VPHMH model using the 2-D FEM. (a) Losses varying with 71st harmonic. (b) Losses varying with 73rd harmonic.

stator line current, which means that the effective air-gap length decreases. As a result, the magnetizing inductance is increased when using notches, and the corresponding power factor gets higher. Another fact is that the fundamental of the air-gap flux density grows with the increment of the notch radius, which makes it possible to mitigate the total solid-rotor eddy-current losses in some cases.

However, the situation is quite different when it comes to the load condition. As shown in Fig. 8, when notches are used, an "extra slot" appears in the stator tooth. Obviously, the effect is stronger with the larger notch radius. Consequently, 71st and 73rd harmonics (the second stator slot harmonic) will become problematic among all the harmonics. Fig. 10 shows the rotor eddy-current losses generated by 71st and 73rd harmonics. The tendencies of the curves in Fig. 10 are quite similar to those in Fig. 7. Thus, the loss generated by a specific harmonic with a different amplitude can also be estimated from the curves in Fig. 10.

Fig. 11 shows the air-gap flux density harmonics in the machine with and without notches at the nominal load. It was decided to take a 2 mm notch radius as a reference value to highlight the effect caused by the notches because the no-load stator line current is smaller and the fundamental flux density is larger in Fig. 9. Because the amplitudes of the harmonics are very small, especially those with a higher order, the decibel

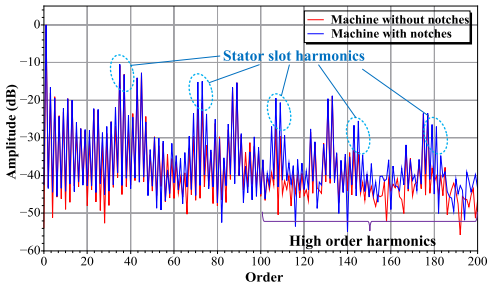

Fig. 11. Comparison of the harmonics of the air-gap flux density in the machines with and without notches at the nominal load. (The notch radius is 2 mm.)

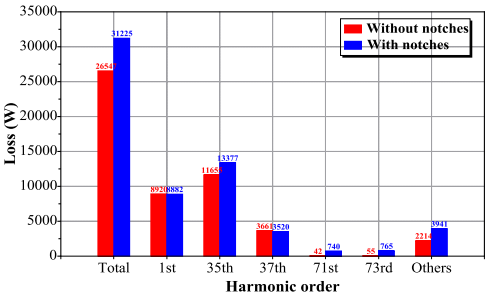

Fig. 12. Comparison of the rotor losses in the machines with and without notches estimated by the 2-D FEM. (The notch radius is 2 mm.)

TABLE II
MAIN AIR-GAP FLUX DENSITY HARMONICS IN THE MACHINES WITH AND WITHOUT NOTCHES AT THE NOMINAL LOAD

Machine type	1st (T)	35th (T)	37th (T)	71st (T)	73rd (T)
Without notches	0.8529	0.0719	0.0416	0.0061	0.0072
With notches	0.8543	0.0770	0.0409	0.0260	0.0271
Increment	0.16%	7.09%	−1.68%	326.23%	276.39%

unit is selected to demonstrate the amplitudes. The base is the amplitude of the fundamental of the machine without notches. The fundamental increases slightly when notches are used, which corresponds to the theoretical analysis and also the curve tendency in Fig. 9(b) in the no-load condition. Nevertheless, the stator slot harmonics appear to be higher compared with the machine without notches. Besides, the higher the order, the larger is the difference. It can be assumed that based on the results shown in Fig. 9, the rotor eddy-current losses should be higher when notches are used, and they become even higher with a higher notch radius. All the corresponding data are listed in Table II. It can be seen that with the strong damping effect at the nominal load point, the fundamental increases slightly when notches are applied. In addition, the air-gap length (7 mm) is relatively large, and the slot opening (11.7 mm) is too wide in this machine. All of these factors make the fundamental increase just a little at the nominal load, when notches are utilized.

The rotor eddy-current losses can be analyzed by the proposed method. In order to simplify the calculation, among all the stator harmonics, only the fundamental, first-order stator slot, and second-order stator slot harmonics are computed. The rest of the harmonics are referred to as "others," and the results are shown in Fig. 12. It should be clarified that the total losses and harmonic losses are estimated by the normal FEM model and VPMHM model, respectively, as defined in Fig. 4. The total rotor losses in the machine with notches are 31.2 kW, and they are higher than with the original design. The total rotor losses increase by 4.7 kW. The fundamental harmonic loss is only 38 W lower in the machine with notches because of the 0.16% increase in the fundamental harmonic amplitude. The first-order stator slot harmonic losses are 1.6 kW higher and the second-order slot harmonic losses are 1.4 kW higher, compared with the origin design. The rest of the increment (1.7 kW) is mainly caused by other high-order harmonics, as shown in Fig. 11.

Typically, the notches on the stator teeth can help to increase the fundamental of the air-gap flux density. Nevertheless, it is not very effective for the machine with a large air-gap length and a wide stator slot opening. Therefore, it is not recommended to use notches in a machine of this kind because of the risk to generate other high-order stator slot harmonics. Furthermore, the solid-rotor machine is very sensitive to stator slot harmonics when the rotor eddy-current losses are considered, which leads to the aimed design topology having smaller high-order harmonics rather than only simply increasing the fundamental.

B. Mitigation of the Rotor Losses by the Semimagnetic Wedges

The slot harmonics are caused by the slot opening. Typically, closed slots can help to mitigate the slot opening effect. However, in this machine, open slots have to be used because prefabricated coils are used. Semimagnetic wedges are a good choice to suppress the stator slot harmonics, especially for the machine with a wider slot opening [28], [29]. Fig. 13 shows the details of the main dimensions of the semimagnetic wedges used in this machine. The initial relative permeability of the wedge is 2.86, and the saturation magnetization point is 0.42 T. Two main parameters, the thickness and the protruding distance, are studied. The thickness can affect the path for the main flux. If the wedge is too thin, the magnetic path can easily get saturated so that only a limited amount of flux can travel through the semimagnetic wedges. The protruding distance can also affect the flux under the slot opening.

Fig. 14 shows the flux line distributions of the machines with and without semimagnetic wedges at the nominal load. It is clear that more flux lines are traveling through the semimagnetic wedges, which means that the semimagnetic wedges can mitigate the effects of the stator slot openings. As a

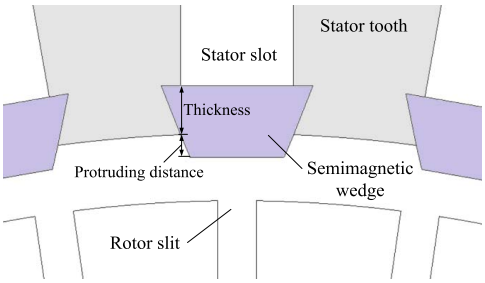

Fig. 13. Schematic view of the semimagnetic wedges.

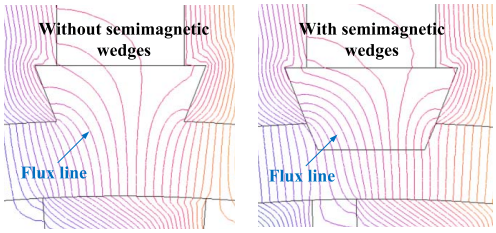

Fig. 14. Comparison of the flux line distribution of the machines with and without semimagnetic wedges at the nominal load.

result, the stator slot harmonics are smaller, and consequently, they produce less eddy-current losses on the rotor side.

Fig. 15 gives the details of the optimization of the rotor eddy-current losses in terms of semimagnetic wedge thickness and protruding distance. Fig. 15(a) shows the rotor eddy-current losses varying with the semimagnetic wedge thickness. The losses decrease significantly from 1 to 4 mm at the beginning of this curve. The curve becomes quite flat from 5 to 6 mm and reaches the minimum at 6 mm with 13.8 kW. (The initial protruding distance is 2 mm.) After that, the losses start to increase. Thus, the optimum thickness for the minimum losses is chosen to be 6 mm. Fig. 15(b) shows the rotor eddy-current losses varying with the semimagnetic wedge protruding distance. The minimum rotor losses are 13.4 kW with the 2.5 mm protruding distance. Therefore, the semimagnetic wedge dimensions are selected with a thickness of 6 mm and a protruding distance of 2.5 mm. It can be noticed from Fig. 15 that after the semimagnetic wedge dimensions reach the best ranges, higher losses will be obtained if the dimensions are further increased. This phenomenon can be explained as follows. Basically, when the semimagnetic wedges are not used, the air-gap harmonics are strong because of the uneven distribution of permeance along the air-gap periphery. The permeance along the air-gap periphery is bigger under the stator teeth than that under the stator slot openings. After the optimization of the semimagnetic thickness and protruding distance, the permeance distribution is even. However, if the wedge thickness and protruding distance are further increased, the permeance distribution becomes uneven again.

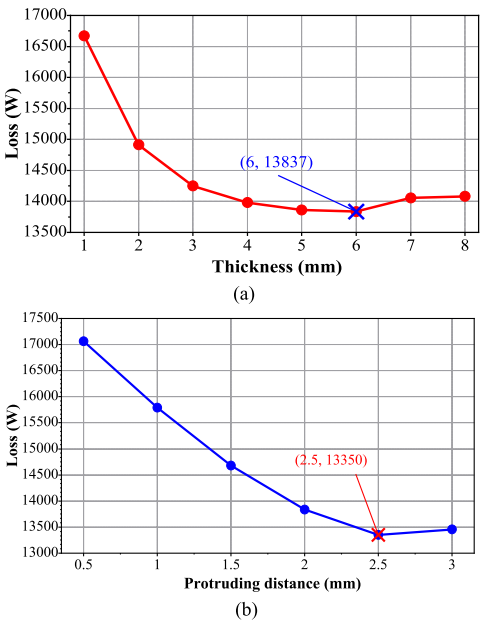

Fig. 15. Optimization of total rotor eddy-current losses with semimagnetic wedges in terms of thickness and protruding distance at the nominal load estimated by the 2-D FEM. (a) Losses varying with the semimagnetic wedge thickness. (Initial protruding distance is 2 mm.) (b) Losses varying with the semimagnetic wedge protruding distance. (Initial thickness is 6 mm.)

TABLE III
MAIN AIR-GAP FLUX DENSITY HARMONICS IN THE MACHINES WITH AND WITHOUT SEMIMAGNETIC WEDGES AT THE NOMINAL LOAD

Machine type	1st (T)	35th (T)	37th (T)
Without wedges	0.8529	0.0719	0.0416
With wedges	0.8436	0.0174	0.0136
Increment	−1.09%	−75.80%	−67.31%

The permeance under the stator slot opening is bigger than that under the stator teeth. The evidence is that the total harmonic distortions are 9.48% (with 6 mm wedge thickness and 2.5 mm protruding distance in the air gap) and 9.56% (with 6 mm wedge thickness and 3 mm protruding distance in the air gap), respectively.

Table III provides a comparison of the main air-gap flux density harmonics in the machine with and without semimagnetic wedges. Table III reveals that in the machine with semimagnetic wedges, the fundamental harmonic decreases slightly but the first stator slot harmonics decrease significantly, which is the main reason for the reduction in rotor losses. Fig. 16 shows a comparison of the corresponding rotor losses. It can be seen that the reduction in losses depends

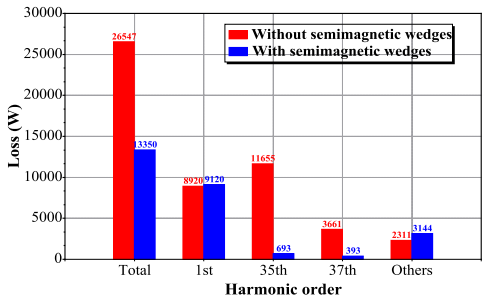

Fig. 16. Comparison of the rotor losses in the machines with and without semimagnetic wedges estimated by the 2-D FEM. (Thickness is 6 mm and protruding distance is 2.5 mm.)

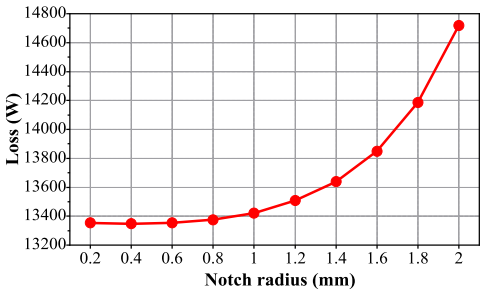

Fig. 17. Rotor eddy-current losses with the combination of notches and semimagnetic wedges (thickness is 6 mm and protruding distance is 2.5 mm) at the nominal load as a function of notch radius estimated by the 2-D FEM.

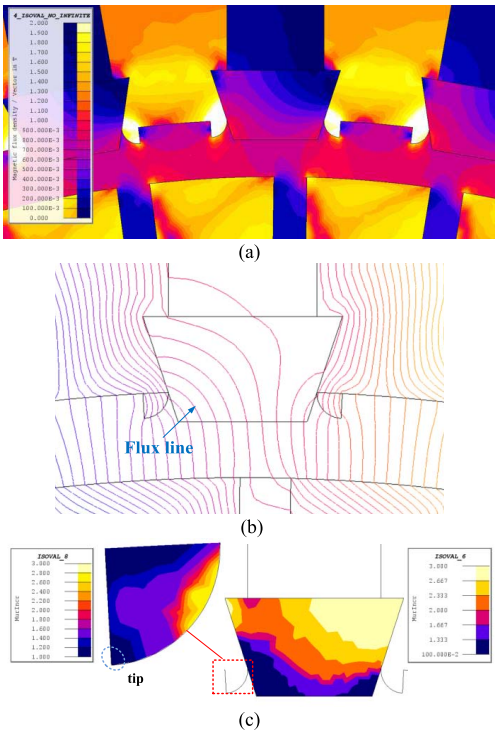

Fig. 18. Flux density, flux line, and relative permeability distributions in the machine with the combination of notches and semimagnetic wedges in the nominal condition. (a) Flux density distribution in the nominal condition. (b) Flux line distribution in the nominal condition. (c) Relative permeability distribution in the nominal condition.

mainly on the reduction in the stator slot harmonics when using the semimagnetic wedges. However, as the fundamental flux density decreases slightly with the semimagnetic wedges, the corresponding fundamental harmonic losses increase by 200 W. In addition, the "Others" bar increases by about 800 W, which is mainly due to the saturation harmonic and some other winding harmonics. Because the fundamental harmonic is slightly smaller, it means that the machine runs in a slightly heavier load point. As a result, all the corresponding saturation harmonics and the winding harmonics increase. All these computation results show that semimagnetic wedges can help to reduce the rotor eddy-current losses because of the suppression of the stator slot harmonics.

C. Mitigation of the Rotor Losses by a Combination of the Notches and Semimagnetic Wedges

As explained in Section III-A, notches cannot help to mitigate the rotor eddy-current losses because of the wide stator slot opening and the effect of the "extra slot." Nevertheless, when semimagnetic wedges are used, it is still possible to also use notches to reduce the losses. When semimagnetic wedges are applied, the stator slot harmonics are greatly reduced, which means that the slot opening effect is mitigated, while magnetically, the stator slot with a magnetic wedge can be considered a semiclosed one. However, the fundamental of the air-gap flux density decreases in the machine with semimagnetic wedges. In that case, it has the potential to use notches together with wedges to further mitigate the losses by raising the fundamental flux density.

Fig. 17 shows the rotor eddy-current losses with a combination of notches and semimagnetic wedges as a function of notch radius in the nominal condition. Fig. 17 shows that at the beginning, when the radius is small (from 0.2 to 1 mm), the losses remain almost unchanged (13 353 W at 0.2 mm, 13 347 W at 0.4 mm, 13 354 W at 0.6 mm, 13 376 W at 0.8 mm, and 13 421 W at 1 mm). However, after 1 mm, the losses start to increase considerably. Meanwhile, the larger the radius, the higher are the losses. This can be explained by the fact that when the radius is small, the "extra slot" effect caused by the notches in Fig. 8 is not strong enough. When the notch radius is larger, the "extra slot" effect becomes more significant.

Another reason why the combination of notches and semimagnetic wedges cannot help to mitigate the rotor losses is that the notches and the semimagnetic wedges have different

material properties, especially permeabilities. The saturated points for the notches (the same as the stator steel sheet) and the semimagnetic wedges are 1.99 and 0.42 T, respectively. Fig. 18 shows the flux density, flux line, and permeability distributions in the nominal condition. In Fig. 18(a), it can be observed that both the notches and the semimagnetic wedges are highly saturated. Because the flux densities in the notches and the semimagnetic wedges are more than 2 and 1 T, respectively, it means that a large proportion of the magnetic flux travels through the notches and the semimagnetic wedges.

Fig. 18(b) shows that there are many flux lines coming out of the notch tips and the wedges. Only a few of these flux lines pass the wedges because the wedges are close to saturation. Fig. 18(c) shows the relative permeability distribution. Fig. 18(c) confirms the previous analysis. The relative permeability in the semimagnetic wedge in the position right beside the notch is below 2. The notch tip has a relative permeability of about 1.5. Consequently, most of the flux lines from the notches can only go through the air gap under the notch tips, which means that the slot effect induced by these "extra slots" becomes clear. As a result, the rotor eddy-current losses inevitably increase because of the "extra slot" effects.

As both the semimagnetic wedges and notches are saturated at the motor nominal load point, the notches cannot help to further suppress the stator slot harmonics and improve the fundamental of the air-gap flux density. They can only cause more rotor eddy-current losses because of the "extra slot" effects when the notch radius increases. Thus, notches are still not recommended for mitigating losses in this solid-rotor high-speed IM, regardless of whether semimagnetic wedges are used or not.

IV. Conclusion

This paper discussed the computation and mitigation of the rotor harmonic eddy-current losses in a 2 MW high-speed IM. All the mitigation actions were studied from the viewpoint of the stator side. First, a special VPMHM model was proposed for the computation and prediction of the rotor harmonic losses related to one particular air-gap flux density harmonic. In order to generate rotating harmonic fields, a magnet with sinusoidal magnetization was developed. Three different approaches based on notches on the stator teeth, semimagnetic wedges, and their combination were investigated for mitigating the rotor eddy-current losses. The proposed VPMHM model was applied to analyze and explain the reasons for changes in the losses and also to predict the specific harmonic losses.

Finally, some conclusions can be drawn from the detailed investigation. The notch itself could help to increase the fundamental of the air-gap flux density and reduce the no-load stator current. However, in this case, it could not suppress the rotor eddy-current losses as the stator opening was wide and the notch effect for improving the fundamental of air-gap flux density at the nominal load was very weak. The "extra slot" effect caused by the notches started to dominate when the notch radius increased. Consequently, the losses became even higher with a larger notch radius. Because of the wide stator slot opening, the semimagnetic wedges were extremely effective. They suppressed the stator slot effect significantly and made the air-gap flux density curve much smoother. The rotor eddy-current losses decreased by 49.4% from 26.5 to 13.4 kW by the optimization of the dimensions of the semimagnetic wedge. After the optimization, the option of using a combination of notches and wedges was also studied in this paper. It was found that both the notches and the wedges were oversaturated, and no more flux coming out of the notches could travel through the wedges. The "extra slot" effect also became stronger when the notch radius was larger. As a result, the combination could not mitigate the solid-rotor eddy-current losses, and only the semimagnetic wedge itself should be used.

Acknowledgment

This work was supported by the scholarship from the China Scholarship Council (CSC) under Grant CSC 201706690032. The authors would like to thank Dr. H. Niemelä, Lappeenranta University of Technology, Lappeenranta, Finland, for her linguistic assistance in the preparation of this manuscript.

References

[1] M. V. Terzic, D. S. Mihic, and S. N. Vukosavić, "Design of high-speed, low-inertia induction machines with drag-cup rotor," *IEEE Trans. Energy Convers.*, vol. 29, no. 1, pp. 169–177, Mar. 2014.

[2] D. Gerada, A. Mebarki, N. L. Brown, K. J. Bardley, and C. Gerada, "Design aspects of high-speed high-power-density laminated-rotor induction machines," *IEEE Trans. Ind. Electron.*, vol. 58, no. 9, pp. 4039–4047, Sep. 2017.

[3] Y. Zhang, S. McLoone, and W. P. Cao, "Electromagnetic loss modeling and demagnetization analysis for high speed permanent magnet machine," *IEEE Trans. Magn.*, vol. 54, no. 3, Mar. 2018, Art. no. 8200405.

[4] D. A. Gonzalez and D. M. Saban, "Study of the copper losses in a high-speed permanent-magnet machine with form-wound windings," *IEEE Trans. Ind. Electron.*, vol. 61, no. 6, pp. 3038–3045, Jun. 2014.

[5] D. H. Lee, T. H. Pham, and J. W. Ahn, "Design and operation characteristics of four-two pole high-speed SRM for torque ripple reduction," *IEEE Trans. Ind. Electron.*, vol. 60, no. 9, pp. 3637–3643, Sep. 2013.

[6] J. Dang, J. R. Mayor, S. A. Semidey, R. G. Harley, T. G. Habetler, and J. A. Restrepo, "Practical considerations for the design and construction of a high-speed SRM with a flux-bridge rotor," *IEEE Trans. Ind. Appl.*, vol. 51, no. 6, pp. 4515–4520, Nov. 2015.

[7] D. Gerada, A. Mebarki, N. L. Brown, C. Gerada, A. Cavagnino, and A. Boglietti, "High-speed electrical machines: Technologies, trends, and developments," *IEEE Trans. Ind. Electron.*, vol. 61, no. 6, pp. 2946–2959, Jun. 2014.

[8] J. Saari and A. Arkkio, "Losses in high speed asynchronous motors," in *Proc. Int. Conf. Electr. Mach. (ICEM)*, vol. 3, Sep. 1994, pp. 704–708.

[9] M. T. Caprio, V. Lelos, J. D. Herbst, and J. Upshaw, "Advanced induction motor endring design features for high speed applications," in *Proc. IEEE Int. Conf. Electr. Mach. Drives*, May 2015, pp. 993–998.

[10] J. Lähteenmäki, "Design and voltage supply of high-speed induction machines," Ph.D. dissertation, Dept. Elect. Commun. Eng., Helsinki Univ. Technol., Espoo, Finland, 2002.

[11] J. Pyrhonen, J. Nerg, P. Kurronen, and U. Lauber, "High-speed high-output solid-rotor induction-motor technology for gas compression," *IEEE Trans. Ind. Electron.*, vol. 57, no. 1, pp. 272–280, Jan. 2010.

[12] R. Lateb, J. Enon, and L. Durantay, "High speed, high power electrical induction motor technologies for integrated compressors," in *Proc. Int. Conf. Elect. Mach. Syst.*, Nov. 2009, pp. 1–5.

[13] Z. Q. Zhu, K. Ng, N. Schofield, and D. Howe, "Improved analytical modelling of rotor eddy current loss in brushless machines equipped with surface-mounted permanent magnets," *IEE Proc. Elect. Power Appl.*, vol. 151, no. 6, pp. 641–650, Nov. 2004.

[14] V. Räisänen, S. Suuriniemi, S. Kurz, and L. Kettunen, "Rapid computation of harmonic eddy-current losses in high-speed solid-rotor induction machines," *IEEE Trans. Energy Convers.*, vol. 28, no. 3, pp. 782–790, Sep. 2013.

[15] J. J. Pyrhönen, T. Jokinen, and V. Hrabovcova, *Design of Rotating Electrical Machines*. Hoboken, NJ, USA: Wiley, 2013.
[16] T. Aho, "Electromagnetic design of a solid steel rotor motor for demanding operation environments," Ph.D. dissertation, Dept. Elect. Eng., Lappeenranta Univ. Technol., Lappeenranta, Finland, 2007.
[17] Y. Lei, Z. Zhao, S. Wang, D. G. Dorrell, and W. Xu, "Design and analysis of star-delta hybrid windings for high-voltage induction motors," *IEEE Trans. Ind. Electron.*, vol. 58, no. 9, pp. 3758–3767, Sep. 2011.
[18] G. Ugalde, Z. Q. Zhu, J. Poza, and A. Gonzalez, "Investigation of rotor eddy current losses in fractional slot PM machines with solid rotor back-iron," in *Proc. Int. Conf. Elect. Mach.*, Aug. 2011, pp. 1–5.
[19] G. D. Donato, F. G. Capponi, and F. Caricchi, "On the use of magnetic wedges in axial flux permanent magnet machines," *IEEE Trans. Ind. Electron.*, vol. 60, no. 11, pp. 4831–4840, Nov. 2013.
[20] P. M. Lindh, J. J. Pyrhönen, P. Ponomarev, and D. Vinnikov, "Influence of wedge material on losses of a traction motor with tooth-coil windings," in *Proc. 39th Annu. Conf. IEEE Ind. Electron. Soc. (IECON)*, Nov. 2013, pp. 2941–2946.
[21] C. Di, I. Petrov, J. J. Pyrhönen, and X. H. Bao, "Unbalanced magnetic pull compensation with active magnetic bearings in a 2 MW high-speed induction machine by FEM," *IEEE Trans. Magn.*, vol. 54, no. 8, Jun. 2018, Art. no. 8202913, doi: 10.1109/TMAG.2018.2837659.
[22] S. Jumayev, M. Merdzan, K. O. Boynov, J. J. H. Paulides, J. J. Pyrhönen, and E. A. Lomonova, "The effect of PWM on rotor eddy-current losses in high-speed permanent magnet machines," *IEEE Trans. Magn.*, vol. 51, no. 11, Nov. 2015, Art. no. 8109204.
[23] Y. H. Hu, S. S. Zhu, and C. Liu, "Magnet eddy-current loss analysis of interior PM machines for electric vehicle application," *IEEE Trans. Magn.*, vol. 53, no. 11, Nov. 2017, Art. no. 7402904.
[24] J. J. Pyrhönen, H. Jussila, Y. Alexandrova, P. Rafajdus, and J. Nerg, "Harmonic loss calculation in rotor surface permanent magnets-new analytic approach," *IEEE Trans. Magn.*, vol. 48, no. 8, pp. 2358–2366, Aug. 2012.
[25] Q. Gu, L. Q. Yuan, Z. M. Zhao, F. Liu, and J. N. Sun, "An accurate stray loss calculation method of squirrel-cage induction motors for efficiency optimization," in *Proc. 18th Int. Conf. Elect. Mach. Syst.*, Oct. 2015, pp. 143–149.
[26] L. Wang, X. H. Bao, C. Di, and Y. Zhou, "Influence on vibration and noise of squirrel-cage induction machine with double skewed rotor for different slot combinations," *IEEE Trans. Magn.*, vol. 52, no. 7, Jul. 2016, Art. no. 8104404.
[27] H. V. Xuan, D. Lahaye, H. Polinder, and J. A. Ferreira, "Influence of stator slotting on the performance of permanent-magnet machines with concentrated windings," *IEEE Trans. Magn.*, vol. 49, no. 2, pp. 929–938, Feb. 2013.
[28] I. Petrov, P. Lindh, W. P. Peng, C. S. Jang, H. P. Yang, and J. J. Pyrhönen, "Improvement of axial flux single-rotor single-stator induction machine performance by applying semi-magnetic wedges," in *Proc. 22nd Int. Conf. Elect. Mach. Syst. (ICEM)*, Sep. 2016, pp. 1795–1800.
[29] J. Montonen, P. Lindh, and J. J. Pyrhönen, "Impact of semi-magnetic slot key on the performance of a tooth-coil traction motor," in *Proc. 17th Eur. Conf. Power Electron. Appl.*, Sep. 2015, pp. 1–8.

Chong Di was born in Wuxi, China, in 1991. He received the B.Eng. and M.Eng. degrees both in electrical engineering from the Hefei University of Technology, Hefei, China, in 2014 and 2017, respectively. He is currently pursuing the Doctoral degree with the Department of Electrical Engineering, Lappeenranta University of Technology, Lappeenranta, Finland.

His current research interests include high-speed electrical machines.

Ilya Petrov received the D.Sc. degree in electrical engineering from the Lappeenranta University of Technology (LUT), Lappeenranta, Finland, in 2015.

He is currently a Fellow Researcher with the Department of Electrical Engineering, LUT.

Juha J. Pyrhönen (M'06–SM'17) was born in Kuusankoski, Finland, in 1957. He received the D.Sc. degree in electrical engineering from the Lappeenranta University of Technology (LUT), Lappeenranta, Finland, in 1991.

He became a Professor of electrical machines and drives at LUT, in 1997. He is involved in the research and development of electric motors and power-electronic-controlled drives. He has wide experience in the research and development of special electric drives for distributed power production, traction, and high-speed applications. His current research interests include permanent magnet materials and applying them in machines, and studying possibilities of using carbon-based materials in electrical machines.

Publication IV

Di, C., Petrov, I., and Pyrhönen, J.
Design of a High-Speed Solid-Rotor Induction Machine with an Asymmetric Winding and Suppression of the Current Unbalance by Special Coil Arrangements

Reprinted with permission from
IEEE Access
Vol. 7, pp. 83175-83186, 2019

IEEE Access
Multidisciplinary ⋮ Rapid Review ⋮ Open Access Journal

Received June 15, 2019, accepted June 21, 2019, date of publication June 26, 2019, date of current version July 11, 2019.

Digital Object Identifier 10.1109/ACCESS.2019.2925131

Design of a High-Speed Solid-Rotor Induction Machine With an Asymmetric Winding and Suppression of the Current Unbalance by Special Coil Arrangements

CHONG DI, ILYA PETROV, AND JUHA J. PYRHÖNEN, (Senior Member, IEEE)
Department of Electrical Engineering, Lappeenranta University of Technology, 53851 Lappeenranta, Finland
Corresponding author: Chong Di (chong.di@lut.fi)

This work was supported in part by the Scholarship from the China Scholarship Council (CSC) under Grant CSC 201706690032.

ABSTRACT High-speed solid-rotor induction machines (IMs) suffer from higher rotor eddy-current losses (as a result of the air-gap flux density harmonics) more than any other type of high-speed machines because of the solid-rotor steel. A double-layer short-pitch asymmetric winding arrangement with prefabricated coils is proposed in this paper to mitigate the solid-rotor losses and enable easier assembly. However, the asymmetric winding also brings some current unbalance because of three-phase asymmetric stator inductances, especially the winding leakage inductances. Current unbalance can cause harmful effects for both the machine and supply, e.g., torque ripples, unbalanced magnetic pulls, and unbalanced thermal loads of the supply network and supply power electronics. Additionally, a three-phase unbalanced current can cause an extra source of electromagnetic emission to the environment, which can be harmful to surrounding electronics and can cause extra eddy-current losses in surrounding solid surfaces (e.g., a metal terminal box). To mitigate the current unbalance, two methods are compared in this paper. The first method is a slight increase of the stator slot height and placing of the coil sides at the top or bottom within the slot height for different phases. The stator slot height is optimized based on the 2-D finite-element method (FEM) to achieve the best solution for mitigation of the current unbalance. The other method is based on the results of the first method, and the coil side position for a specific phase is further adjusted. Unlike conventional methods of mitigating the current unbalance by power electronics, the proposed method suppresses the current unbalance solely by adjusting the machine design, which avoids extra investments for power electronics devices. In addition, the machine control strategy remains unchanged compared with the traditional one.

INDEX TERMS
Solid-rotor high-speed induction machine (IM), 2-D finite element method (FEM), asymmetric winding arrangement, current unbalance suppression, coil arrangement.

NOMENCLATURE

l_{ef}	Effective core length [mm]
$D_{s,in}$	Stator inner diameter [mm]
$D_{s,out}$	Stator outer diamerter [mm]
D_r	Solid rotor diameter [mm]
p	Number of pole pairs
Q_s	Number of stator slots
Q_r	Number of rotor slots
a	Number of parallel branches
N_s	Number of turns in series per phase
y_Q	Coil span in slot pitches
U_N	Line to line rated voltage [V]
f_s	Supply frequency [Hz]
T_N	Rated torque [Nm]
$T_{peak-peak}$	Torque ripple [Nm]
P_N	Rated power [kW]
s	Per-unit slip
$\cos\varphi$	Power factor
$I_{s,N}$	Average supply current at rated load [A]

The associate editor coordinating the review of this manuscript and approving it for publication was Xiaodong Sun.

$I_{p,N}$	Average phase current at rated load [A]
CUR	Current unbalance ratio [%]
I_U	Fundamental of phase U current [A]
I_V	Fundamental of phase V current [A]
I_W	Fundamental of phase W current [A]
CUF_-	Unbalance factor of negative sequence current [%]
CUF_0	Unbalance factor of zero sequence current [%]
$\dot{I}_+$	Positive sequence current [A]
$\dot{I}_-$	Negative sequence current [A]
$\dot{I}_0$	Zero sequence current [A]
$\dot{I}_U$	Phase U current phasor [A]
$\dot{I}_V$	Phase V current phasor [A]
$\dot{I}_W$	Phase W current phasor [A]
$\dot{a}$	Phasor operator
$L_{s,U}$	Phase U stator inductance [H]
$L_{s,V}$	Phase V stator inductance [H]
$L_{s,W}$	Phase W stator inductance [H]
$L_{s\sigma,U}$	Phase U stator leakage inductance [H]
$L_{s\sigma,V}$	Phase V stator leakage inductance [H]
$L_{s\sigma,W}$	Phase W stator leakage inductance [H]

I. INTRODUCTION

High-speed solid-rotor induction machines (IMs) are capable of achieving high rotational speeds and operating in harsh environments, compared with other machines for high speed applications as permanent magnet synchronous machines (PMSMs) and switched reluctance machines (SRMs) [1]–[4]. The PMSM has a higher power density than the IM, but the cost of the machine is higher because of the expensive magnet material and the maximum speed is lower. The SRM has the advantage of the easier manufacturing, but the control becomes more difficult and the noise becomes stronger than in the IM. Therefore, high-speed IMs equipped with a solid rotor are widely used in industrial applications. The rotor of such machines is built of magnetically soft constructional steel, which offers a rugged solution compared to other rotor structures [5], [6]. Although a solid rotor is one of the most robust rotor structures, it also brings some challenges, in particular high solid-rotor losses, which make cooling of the motor challenging and expose the motor to potential machine faults [7]. Typically, there are three types of rotor losses containing the hysteresis, eddy currents, and anomalous losses, which are reported in detail in [8] and can be modeled accurately by the nonlinear lumped parameter equivalent circuit. For solid-rotor IM the majority of the rotor losses are eddy currents related losses. The main reason for the high rotor losses is the relatively low conductivity of the solid-rotor steel compared with the copper, which leads to significant slip related losses at the nominal load. In the case of a pure solid rotor with no extra windings, the high axial conductivity is needed to provide the current flow required in the rotor for torque production. The rotor material has a significant influence on solid-rotor losses, and many different types of rotor materials for high-speed applications have been investigated by researchers. Studied materials include carbon steel alloys, Fe-Si and Fe-Ni alloys, maraging steel, Fe-Co alloys and Fe-Cu alloys, as reported in [9]. Although some of the materials result in much lower rotor losses than others, in all cases the losses are still much higher than those of a machine equipped with a copper cage winding and a laminated rotor. Among the solid rotor core materials studied, Fe-Cu alloy has the lowest resistivity, which is $1.1 \times 10^{-7}\Omega$m at 20°C. This resistivity is still one order higher than the copper resistivity ($1.78 \times 10^{-8}\Omega$m).

Mitigating the solid-rotor losses by modifying the rotor itself has also been studied. For example, slitted rotors are widely used to reduce the slip related losses (caused by the fundamental of the air-gap flux density) [10]–[12]. Rotor sleeves (coatings) are highly recommended to suppress the high-frequency eddy-current losses induced by the air-gap flux density harmonics [13]–[15]. A significant share of the total solid-rotor losses are mainly caused by the air-gap flux density harmonics. Therefore, it is recommended that the stator should be designed to produce the minimal amount of the air-gap flux density harmonics. Typically, semimagnetic wedges are used in the slot openings to suppress the stator slot harmonics and double-layer short-pitch stator windings are used to mitigate the winding harmonics e.g. −5th, +7th, −11th, +13th [16], [17]. Sometimes however, the winding installation and assembly becomes very difficult when double-layer winding is used, especially in the case of prefabricated coils. In a two-pole machine, the manufacturing of a double-layer winding become very difficult as in the worst case half of the coil sides remain hanging in the stator bore leaving almost no space for the practical winding work. Therefore, using alternative techniques to the orthodox two-layer short-pitched winding becomes not just tempting but in some cases a necessity. The asymmetric winding can offer easy manufacturing, as reported in [18], [19]. But this solution comes at the cost of an asymmetric behavior of the main flux and leakage flux.

Using the asymmetric winding causes the machine to suffer some current unbalance. Such unbalance can produce harmful effects, e.g. extra losses, torque ripples, unbalanced magnetic pulls [20], [21]. Therefore, the current unbalance or impedance unbalance of the system should be mitigated as much as possible. Hu *et al.* [20], [22] utilized a compensation unit in both parallel and series to suppress the second harmonic DC-bus voltage pulsation and torque ripple caused by the asymmetric impedance in an asymmetric permanent magnet synchronous generator system. Yepes *et al.* [23] proposed an improved multiple-resonant-controller structure to compensate the current harmonics for a n-phase machine with an asymmetrical winding. Active power filters, as reported in [24], [25], are also very popular for compensating the current unbalance in many applications. However, all of the methods mentioned above require extra power circuit components or power electronics, which increase investment cost for the system. In addition, the control strategy also has to be modified accordingly. Furthermore, not all the proposed solutions are suitable for machines with asymmetric winding,

as some of them are designed for power systems. There is a lack of research that specially investigates current unbalance mitigation strategies for machines with inherently asymmetric windings.

The aim of this paper is to suggest methods to mitigate the current unbalance and other harmful effects (e.g. torque and speed ripples) in a high-speed solid-rotor IM, that result from the usage of an asymmetric double-layer winging arrangement. The proposed methods are based on balancing the stator inductances, as they are the main reason for the current unbalance, when the proposed winding (having much simpler manufacturing routine) is applied. The novel mitigation technique is realized by increasing the stator slot height and then optimizing the positioning of the different phase coils in different stator slots. Based on this approach, two potential methods for current unbalance mitigation are proposed and compared in this paper. The proposed methods are found to be very effective for mitigating unbalance phenomena in the machine and they are easy to implement at low cost. However, a disadvantage is that some of the machine efficiency is sacrificed because of the increment of the overall stator inductance. This efficiency can, however, be taken into account during the design phase and can be easily compensated, e.g. by slightly increasing the supply voltage.

II. HIGH-SPEED SOLIR-ROTOR IM PERFORMANCE ANALYSIS WITH ASYMMETRIC WINDING

A. ASYMMETRIC WINDING DESCRIPTION OF THE HIGH-SPEED SOLID-ROTOR IM

The machine studied is a 660 V, 2 MW, 200 Hz, 12000 r/min high-speed slitted-solid-rotor IM. Its initial design is reported in detail in [26], [27]. The more specific dimensions of the high-speed solid-rotor IM are listed in Table 1. Prefabricated coils are employed in the design, since the machine utilizes direct liquid cooling technology similar to the case reported in [28].

TABLE 1. Main dimensions of the high-speed solid-rotor IM.

Parameter	Value
Effective core length l_{ef}, mm	538
Stator inner diameter $D_{\mathrm{s,in}}$, mm	280
Stator outer diameter $D_{\mathrm{s,out}}$, mm	700
Solid rotor diameter D_{r}, mm	266
Rotor slit depth, mm	50
Number of pole pairs p	1
Number of stator slots Q_{s}	36
Number of rotor slits Q_{r}	44
Number of parallel branches a	2
Number of turns in series per phase N_{s}	6

Prefabricated coils are typically mechanically stiff and it is difficult to bend them further when inserting the coils in the slots. To guarantee the machine performance and solve the manufacturing problem at the same time, a novel asymmetric winding is proposed in this paper. The machine is a low-voltage high-power high-speed machine. Consequently, there are very limited alternatives to realize the motor winding taking the boundaries set by Faraday's law into account. With a traditional two-layer short-pitched winding, it is possible to connect the upper and lower level coil groups in parallel. In a primary asymmetric two-layer winding the parallel paths of the windings become different and, it is therefore impossible to use parallel paths similarly to the orthodox two-layer winding. In this paper, an asymmetric three-phase winding type is introduced in which all individual phase windings have identical parallel paths, enabling manufacturing of a low-voltage machine of this power and speed.

In addition, the winding must still be connected in delta, which is not favorable in the case of an asymmetric winding because it may cause some circulating currents. However, to guarantee the same amount of flux linkage as the winding in delta connection, using star connection should result in about 1200 V (660 V $\times \sqrt{3} = 1143$ V) line-to-line voltage, which makes commercial converters unavailable. Therefore, several compromises have been made to make it possible to realize a high-power high-speed low-voltage machine.

Fig. 1(a) and (b) show a comparison of the traditional and proposed double-layer winding arrangements for the high-speed solid-rotor IM. It can be seen that the asymmetric winding has different arrangements in 24 half-slots with a short pitch $y_{\mathrm{Q}} = 15/18$. The resultant current linkage per

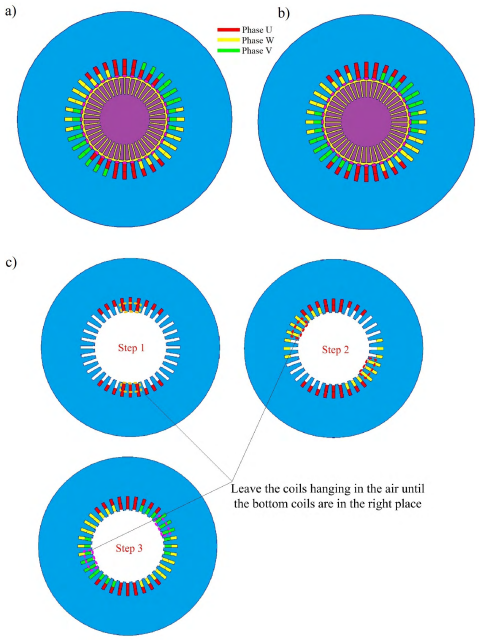

FIGURE 1. (a) The traditional double-layer stator winding arrangement. (b) The proposed asymmetric double-layer stator winding arrangement. (c) Assembly sequence of the proposed asymmetric winding.

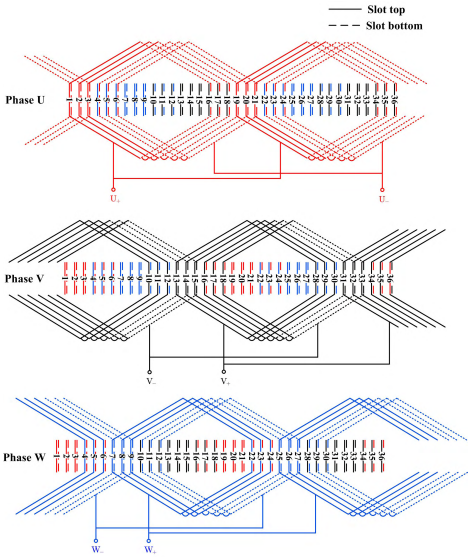

FIGURE 2. The coil arrangements for the proposed asymmetric winding.

phase is exactly the same as in a traditional winding arrangement. From the figure, it can be deduced that the three-phase stator inductances and the stator phase mutual inductances are not fully symmetric. The advantage of the proposed design is that the winding (prefabricated winding) installation becomes much easier when only a few coil sides need to be left hanging in the stator bore before the bottom coil sides are in their right places, as shown in Fig. 1(c). Detailed coil arrangements for this proposed asymmetric winding are described in Fig. 2. There are two parallel branches in the winding, and the winding is in delta connection.

Table 2 lists the main parameters and performances of the machine with the asymmetric winding at the nominal load. All the simulations in this paper are conducted by 2D FEM and the end winding effect is considered by the end winding leakage inductance (7×10^{-5} H by the analytical method) in an external circuit, which is coupled with the finite element model. Meanwhile, the ending winding resistance is added to the total winding resistance. In this table, the three-phase average phase current (phase U, V, and W currents are 1446 A, 1562 A, and 1506 A, respectively) is 1505 A, which means that the machine is suffering some asymmetry because of the proposed winding with three-phase symmetric sinusoidal voltage supply. Additionally, enhanced torque ripple can also be observed at the nominal load. The asymmetry mainly results from the asymmetric stator inductances containing the magnetizing inductance and leakage inductance, because the average position of the coils of each phase within the slot height is different. For example, the number

TABLE 2. Parameters and performances of the IM with the asymmetric winding at the nominal load.

Parameter	Value
Line to line voltage U_{N}, V	660
Connection type	Delta
Supply frequency f_{s}, Hz	200
Torque T_{N}, Nm	1600
Torque ripple $T_{\mathrm{peak-peak}}$, Nm	82
Electric power P_{N}, kW	2000
Per-unit slip s	0.00535
Power factor cosφ	0.68
Average supply current $I_{\mathrm{s,N}}$ (RMS), A	2606
Average phase current $I_{\mathrm{p,N}}$ (RMS), A	1505
Stator copper losses, kW	5
Stator iron losses, kW	15.46
Solid rotor losses, kW	26.23
Mechanical losses, kW	10
Extra losses, kW	10
Total losses, kW	53.580
Efficiency, %	97.321

of windings positioned at the bottom of the slot for phase U is 18 and at the top of the slot is 6. Whereas, for phase V the number of windings positioned at the bottom is 6 and at the top of the slot is 18. Typically, the coil sides placed at the slot bottom generate a higher slot leakage flux and therefore higher leakage inductances compared with those located at the slot top [29]. The leakage flux path for the bottommost coils offers lower reluctance for the leakage magnetic flux than that of the topmost coils. This phenomenon is further explained in more detail in [30].

B. DEFINITIONS OF THE CURRENT UNBALANCE RATIO AND CURRENT UNBALANCE FACTOR

As there are no standardized indices to assess the current unbalance, two measures that include current unbalance ratio (CUR) and current unbalance factor (CUF) are proposed. The factors have similar definitions as the voltage unbalance described in [31], [32]. The CUR is defined as follows

$$CUR = \frac{\max\left(I_{\mathrm{U}}, I_{\mathrm{V}}, I_{\mathrm{W}}\right) - \min\left(I_{\mathrm{U}}, I_{\mathrm{V}}, I_{\mathrm{W}}\right)}{\mathrm{avg}\left(I_{\mathrm{U}}, I_{\mathrm{V}}, I_{\mathrm{W}}\right)} \times 100\% \quad (1)$$

where I_{U}, I_{V}, and I_{W} are the fundamental RMS values of phase or line currents. It can be concluded from (1) that the CUR mainly reflects the maximum current deviation with respect to the average current. Because the machine is in delta connection, the machine has positive, negative and zero sequence phase currents but only positive and negative line currents. The zero sequence phase current only travels inside the delta connection, which is regarded as the circulating current. The CUFs for negative and zero sequence currents can be expressed as

$$CUF_{-} = \frac{\dot{I}_{-}}{\dot{I}_{+}} \times 100\% \quad (2)$$

$$CUF_{0} = \frac{\dot{I}_{0}}{\dot{I}_{+}} \times 100\% \quad (3)$$

where $\dot{I}_+$, $\dot{I}_-$, and $\dot{I}_0$ are the positive, negative and zero sequence components of the phase or line currents (fundamental or harmonic currents). (2) and (3) mainly reveal the corresponding ratios with respect to the positive sequence currents. The positive, negative and zero sequence currents can be calculated as

$$\dot{I}_0 = \frac{\dot{I}_U + \dot{I}_V + \dot{I}_W}{3} \tag{4}$$

$$\dot{I}_+ = \frac{\dot{I}_U + \dot{a} \cdot \dot{I}_V + \dot{a}^2 \cdot \dot{I}_W}{3} \tag{5}$$

$$\dot{I}_- = \frac{\dot{I}_U + \dot{a}^2 \cdot \dot{I}_V + \dot{a} \cdot \dot{I}_W}{3} \tag{6}$$

where $\dot{a} = 1\angle 120°$. $\dot{I}_U$, $\dot{I}_V$, and $\dot{I}_W$ are the phase or line current phasors.

TABLE 3. Asymmetric characteristics of the machine with the asymmetric winding.

Parameter	Value
No-load phase CUR, %	6.409
No-load line CUR, %	2.613
No-load phase CUF$_-$, %	1.536
No-load phase CUF$_0$, %	2.191
No-load phase 3rd order circulating current, A	45.337
No-load line CUF$_-$, %	1.535
Rated-load phase CUR, %	7.683
Rated-load line CUR, %	3.377
Rated-load phase CUF$_-$, %	1.966
Rated-load phase CUF$_0$, %	2.489
Rated-load phase 3rd order circulating current, A	35.331
Rated-load line CUF$_-$, %	1.965
Rated-load torque ripple $T_{\mathrm{peak-peak}}$ (400 Hz), Nm	82.111

Table 3 lists asymmetric characteristics of machine with the proposed winding, without tuning machine properties. Both the phase and line current unbalance indices are shown, because the phase current unbalance is directly related to the machine performance and line current unbalance is important from the supply point of view. In Table 3, only the fundamental and the 3rd order currents are analyzed because they have higher amplitudes than other harmonics. The 3rd order related indices are marked with ''3rd order''. The rest of the indices without a mark are describing the fundamental currents. The 3rd order components only appear in the phase currents and the three-phase 3rd order currents have the exact same phase, which means that they are the circulating currents and they can only travel inside the delta connection. They are not capable of generating any rotating magnetic flux either, instead they create leakage flux.

There is no CUF$_0$ for the line current in Table 3, because the zero sequence line current is negligibly small. The machine has no neutral line (star-delta connection), which means the zero sequence impedance is infinite. It can be seen that the phase current has a higher CUR than the line current at both no load and the rated load. Since the line current has a bigger denominator when CUR is calculated by (1). Similarly, the phase current always has a higher CUF$_-$ and CUF$_0$. Additionally, it can be seen from the table that the zero sequence phase current is higher than the negative sequence phase current. The zero sequence phase current can only create a pulsating magnetic flux, which will cause some extra losses. However, the negative sequence phase current is capable of generating a rotating magnetic flux that travels in the opposite direction with respect to the fundamental magnetic flux. The electromagnetic torque mainly results from the interaction of different magnetic flux harmonics. Therefore, a double supply frequency (400 Hz) torque ripple (82.111 Nm) is shown in the table because of the interaction of the fundamental and the negative sequence magnetic fluxes [20] . The torque ripple can make the control of the machine become more difficult and also increases the noise and vibration level of the machine.

III. SUPPRESSION OF THE CURRENT UNBALANCE AND PERFORMANCE ANALYSIS

The three-phase phase current (fundamental, RMS values) at the nominal load for phases U, V, and W are 1446 A, 1562 A, and 1506 A, respectively, which means that the three-phase stator inductance should be $L_{s,U} > L_{s,W} > L_{s,V}$. The three-phase circuit has exactly the same voltage supply level and winding resistance. Therefore, the current unbalance is caused by the different stator inductances containing the magnetizing inductances and leakage inductances. In Fig. 1(b), there are 18, 6, and 12 conductors located at the slot bottom for phase U, V and W, respectively. As a result, the three-phase stator slot leakage inductance should be $L_{s\sigma,U} > L_{s\sigma,W} > L_{s\sigma,V}$. Because the overall flux linkage (the same voltage supply) for each phase is the same, the different stator leakage inductances further indicate that the three-phase magnetizing inductances are asymmetric, which is directly related to the difference between the overall flux linkage and the flux leakage. Consequently, adjusting the slot leakage inductance for different phases separately may be a potential method to balance the three-phase current.

The method proposed in this paper to mitigate the current unbalance is arranged as follows. The main idea is to balance the three-phase inductance by reducing $L_{s,U}$, and concurrently increasing $L_{s,V}$ and $L_{s,W}$. To be more specific, the phase U stator inductance is reduced by increasing the total magnetic circuit reluctance. For phases V and W, the stator inductances are increased by increasing the stator leakage inductances. The specific implementation is illustrated in Fig. 3. It is shown in Fig. 3(a) that the stator slot height is increased slightly giving an extra area in the slot (marked in blue). The phase U winding is placed at the slot top and phases V and W are placed at the slot bottom. Therefore, the extra slot area is located at the slot bottom for phase U and slot top for phases V and W. The extra slot area can be filled with the non-conducting nonmagnetic material, e.g. a glass-fiber stick. For the phase U, the extra slot area at the slot bottom can reduce the stator inductance because it reduces the stator yoke height which makes the overall magnetizing reluctance of the yoke higher. Phases V and W have extra slot area at the top of the slot and this slot area proposes extra paths for the leakage

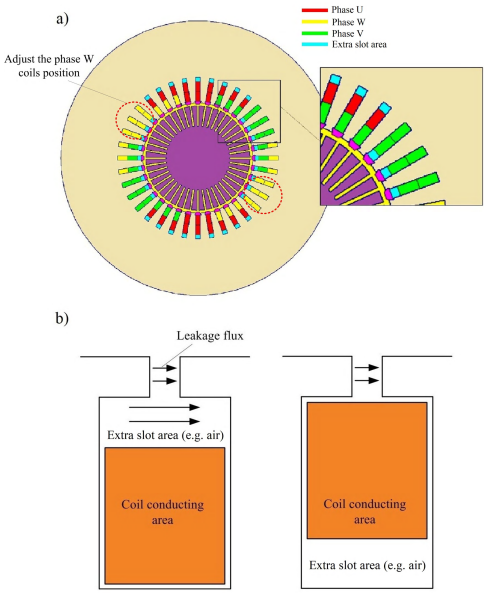

FIGURE 3. (a) Suppression of the current unbalance by modifying the coil arrangement with extra slot height. (b) Main stator slot leakage paths with different coil arrangements.

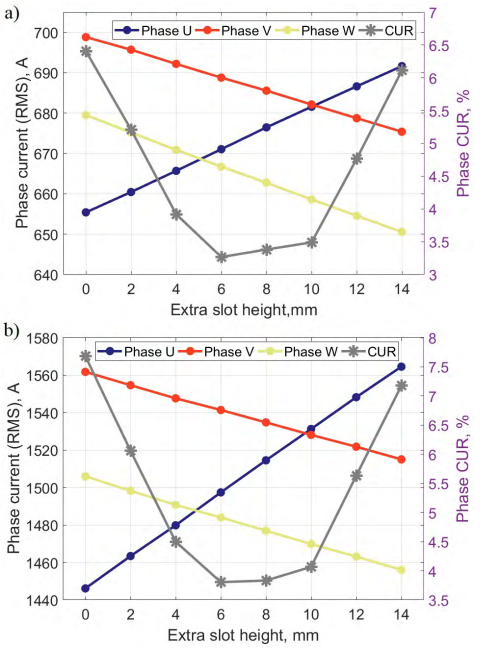

FIGURE 4. (a) No-load phase currents and CURs as a function of the extra slot height (2D FEM). (b) Rated-load phase currents and CURs as a function of the extra slot height (2D FEM).

flux to travel through, as shown in Fig. 3(b). Consequently, the corresponding stator leakage inductances will increase. Although the increased slot height for phases V and W can also reduce the magnetizing inductances (the same situation of phase U), the phases V and W total stator inductances still increase because the leakage inductance increases more. This phenomenon will be further discussed in Section III-A. It should be noted that in the design all the stator slot heights are increased by the same dimension. The stator lamination itself has an isotropic geometry in the cross-section plane, and this isotropic geometry does not complicate the stator lamination during the manufacturing process. The only difference is the winding arrangement in which the specific coils are placed at different positions in different stator slots.

Because all the three-phase stator inductances are different, it is very difficult to fully balance the three-phase stator current with three variables by a single procedure. Therefore, two possible means are studied and compared in the following sections. One possible way of balancing the currents is by placing the phase U winding at the slot top and phases V and W at the slot bottom with the extra slot areas in all the slots. Adjusting the extra slot height makes it possible to acquire the optimized dimension, when all the three-phase currents are close to each other. The other method is that based on the extra slot height adjustment results that are shown in Section III-A, and further balancing the phase W current by adjusting the coil side position in the slots, as shown in Fig. 3(a).

A. CURRENT UNBALANCE MITIGATION BY THE EXTRA STATOR SLOT HEIGHT ADJUSTMENT

To mitigate the current unbalance efficiently, the extra stator slot height can be further optimized. In this study, the extra slot height varies from 0 mm to 14 mm for the optimization. Fig. 4 shows the changes in the phase currents and phase CURs during the optimization of the extra slot height at both no load and the rated load. The figure indicates that the proposed method is very effective, because the phase U current increases with the increment of the slot height, while phase V and W currents decrease. The lowest CURs can be obtained when the extra slot height ranges from 6 mm to 10 mm. The minimum CURs are 3.266% and 3.806%, respectively, at both no load and the rated load, when the extra slot height reaches 6 mm. The situation is similar for the line current unbalance, as shown in Fig. 5. However, the best extra slot height range for smaller CURs is from 4 mm to 8 mm and the minimum CURs are 1.334% and 1.647% at 4 mm, respectively, at no load and the rated load. It can be deduced from Fig. 4 and Fig. 5 that the best range is from 6 mm to 8 mm, which makes both the phase and line CURs small.

Fig. 6 shows the details of the phase currents and CUFs at both no load and the rated load. In Fig. 6(a), the no-load positive sequence current decreases with the increment of the

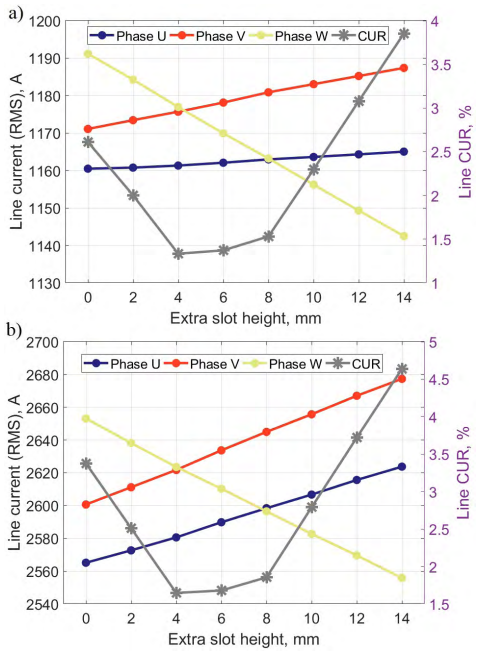

FIGURE 5. (a) No-load line currents and CURs as a function of the extra slot height (2D FEM). (b) Rated-load line currents and CURs as a function of the extra slot height (2D FEM).

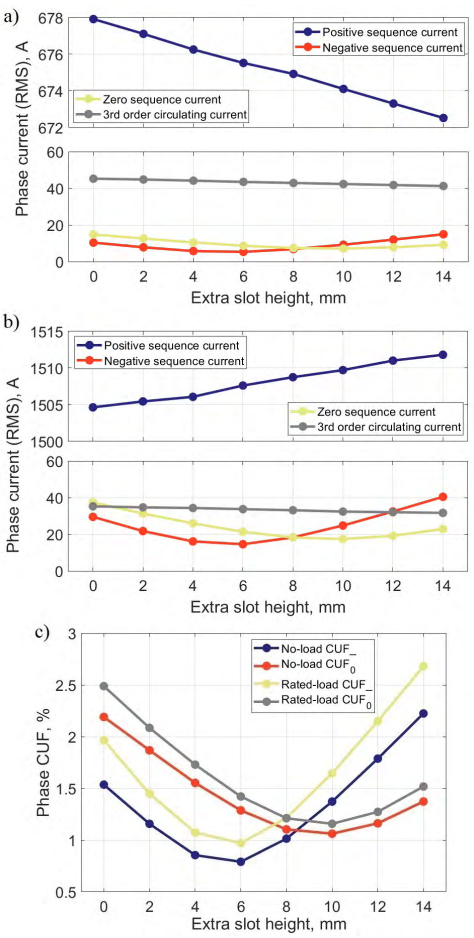

FIGURE 6. (a) No-load phase currents as a function of the extra slot height (2D FEM). (b) Rated-load phase currents as a function of the extra slot height (2D FEM). (c) CUFs as a function of the extra slot height at both no load and the rated load (2D FEM).

extra slot height, because the stator overall leakage inductance increases with larger extra slot height. Concurrently, as shown in Fig. 6(b) the positive sequence phase current increases at the rated load. The larger stator leakage inductance results in a lower air-gap magnetic flux and as a result, the motor slip will increase and a larger stator current will be seen in the stator winding. This outcome further indicates that the proposed method to mitigate the current unbalance is realized by sacrificing some of the machine performance. The proposed technique increases the stator leakage and corresponding reactive voltage drop. The extra leakage (the stator leakage inductance), however, also acts as a current filter smoothening air-gap current linkage time harmonics. The negative and zero sequence currents in both cases decrease at the beginning and increase after reaching the minima. However, the 3rd order circulating currents always decrease with the increment of the extra slot height. In addition, it can be seen in the figure that the negative and zero sequence currents at the rated load are always higher than at no load. This is because the negative and zero sequence currents belong to the fundamental current component. The heavier rated condition can always enhance the fundamental current because of the higher slip. That is to say, the asymmetry is worse under load. However the situation is inverted for the 3rd order circulating current. The 3rd order circulating current is always higher at no load, as shown in Fig. 6.

Fig. 6(c) shows the corresponding CUFs. It can be seen in the figure that the negative sequence current unbalance factor CUF_{-} reaches the minima (0.791% and 0.970%) when the extra slot height is 6 mm and the zero sequence current unbalance factor CUF_0 reaches the minima (1.287% and 1.421%) when the extra slot height is 10 mm. In addition, it also shows that when the extra slot height is small (from 0 mm to 8 mm) the CUF_0 is higher than the CUF_{-}. When the height becomes larger (from 8 mm to 14 mm), the figure shows the opposite result.

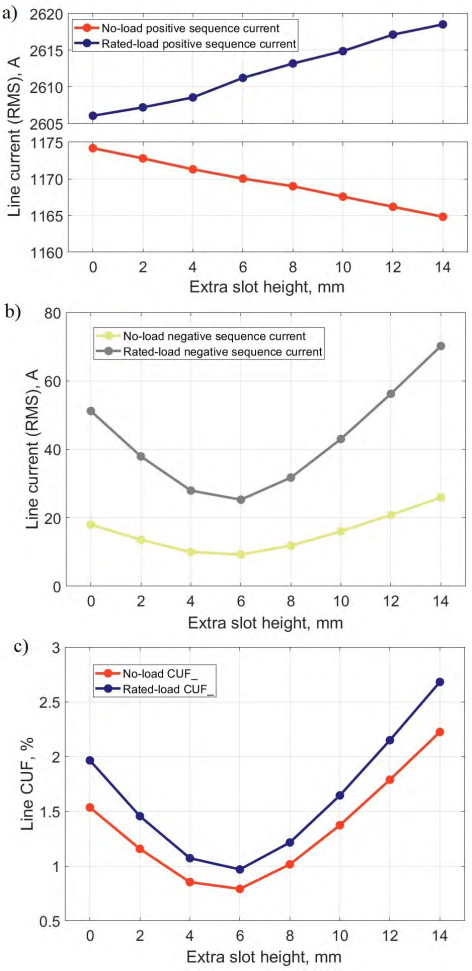

FIGURE 7. (a) Positive sequence line currents as a function of the extra slot height (2D FEM). (b) Negative sequence line currents as a function of the extra slot height (2D FEM). (c) CUFs as a function of the extra slot height at both no load and the rated load (2D FEM).

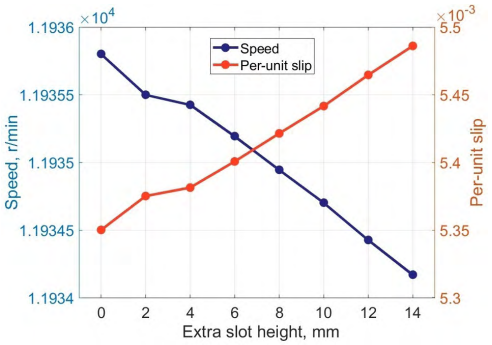

FIGURE 8. Rotating speed and per-unit slip as a function of the extra slot height with the rated torque $T_N = 1600$ Nm (2D FEM).

Fig. 7 shows the line current unbalance at both no load and the rated load. The positive sequence line current has the same tendency as the phase current, when the extra slot height is increased. The negative sequence line current unbalance factor CUF_ curves also show similar patterns as are seen in Fig. 6(c). The minima of the CUF_ are 0.791% and 0.969%, when the extra slot height is 6 mm.

The analysis above shows that the proposed method for mitigating the current unbalance by optimization of the extra slot height is very effective as most of the current unbalance indices can be reduced to almost half of the initial values. The best extra slot height for the different minimum indices varies from 4 mm to 10 mm. The extra dimension can be further determined by the machine performance analysis, which is shown in the next several paragraphs.

Fig. 8 shows the rotating speed and per-unit slip varying as a function of extra slot height. The speed becomes slightly lower and the per-unit slip becomes slightly higher when the slot height is increased. This result indicates that the positive magnetizing flux is smaller with a bigger slot height, since with a smaller magnetizing flux, the machine runs at a lower speed to create the rotor current needed for the same torque. Based on the fundamental behavior of the machine, it can consequently be deduced that the rotor losses may be increased slightly. This feature can however be taken into account and compensated in the machine dimensioning.

The corresponding machine losses as a function of the extra slot height are illustrated in Fig. 9. The solid-rotor losses, stator core losses and copper losses are all estimated by the 2-D FEM. The mechanical losses and extra losses in Table 2 are considered as constants at the rated load and they have been taken into account in the efficiency calculation. In Fig. 9(a), the solid-rotor losses increase because of the higher per-unit slip. The stator core losses and copper losses also increase because more stator leakage is generated in the stator core and a higher slip brings higher copper losses. As a result, the efficiency decreases with the increment of the slot height. This phenomenon exactly shows that the proposed method sacrifices the efficiency to mitigate the current unbalance. This is an interesting result as the original hypothesis was that the negative sequence currents should cause more losses in the machine.

Fig. 10 describes the torque ripple (400 Hz) as a function of the extra slot height at the rated load. It can be seen that it drops at the beginning and reaches a minimum of 41.242 Nm at 6 mm. After that it increases with the increment of the slot height. The double supply frequency torque ripple mostly

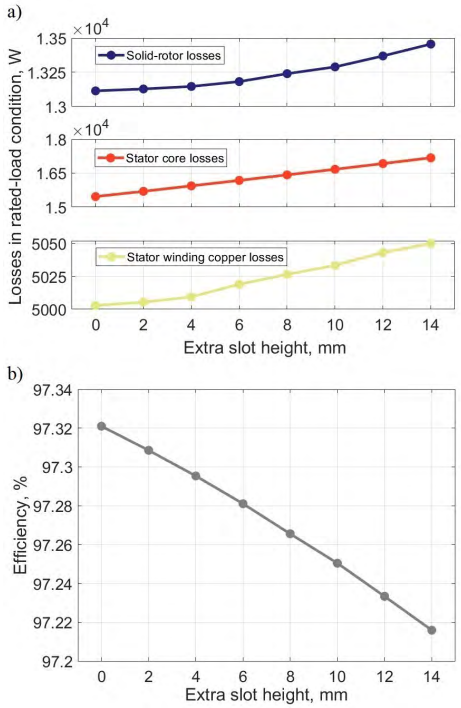

FIGURE 9. (a) Machine main losses as a function of extra slot height with the rated torque $T_N = 1600$ Nm (2D FEM). (b) Machine efficiency as a function of the extra slot height with the rated torque $T_N = 1600$ Nm (2D FEM).

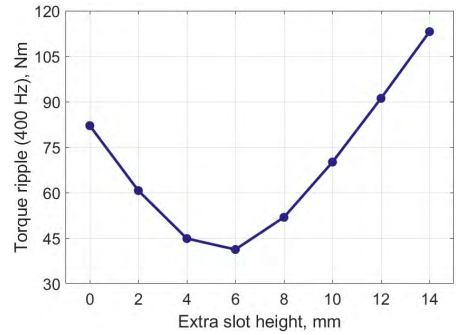

FIGURE 10. Torque ripple as a function of the extra slot height with the rated torque $T_N = 1600$ Nm (2D FEM).

depends on the negative sequence rotating magnetic flux, which is directly related to the negative sequence current as illustrated in Fig. 6. Therefore, it can be seen that the negative sequence current and the torque ripple have the similar curves

TABLE 4. Asymmetric characteristics with the optimized extra slot height.

Parameter	Value	Red. rate
Extra slot height, mm	6	–
No-load phase CUR, %	3.266	0.490
No-load line CUR, %	1.372	0.475
No-load phase CUF$_-$, %	0.791	0.485
No-load phase CUF$_0$, %	1.287	0.413
No-load phase 3rd order circulating current, A	43.566	0.039
No-load line CUF$_-$, %	0.791	0.485
Rated-load phase CUR, %	3.806	0.505
Rated-load line CUR, %	1.679	0.503
Rated-load phase CUF$_-$, %	0.970	0.507
Rated-load phase CUF$_0$, %	1.421	0.429
Rated-load phase 3rd order circulating current, A	33.803	0.043
Rated-load line CUF$_-$, %	0.969	0.507
Rated-load torque ripple $T_{\text{peak}-\text{peak}}$, Nm	42.242	0.486
Efficiency, %	97.250	–

(the same tendency with the increment of the slot height).

Based on the data evaluating the current unbalance and machine performances the shown in the figures a 6 mm extra slot height was selected as the best solution. This value brings very small current unbalance indices (some of them are the minimum) and the minimum torque ripple. The corresponding data are listed in Table 4. The "Red. rate" in this table denotes the reduction rate with respect to the initial case without any extra slot height modification. The values in the table show that the proposed method is effective and most of the current unbalance indices and torque ripple are reduced by about a half. The effect is quite limited for mitigating the phase 3rd order circulating currents at both no load and the rated load, because they are only reduced by around 4%. However the 3rd order circulating currents always exist when a delta connection is used, even in the machine with a fully symmetric winding. All these benefits of smaller the current unbalance and torque ripples are gained by sacrificing the machine efficiency. The machine suffers extra losses of 1.4 kW in total, which reduces the efficiency from 97.321% to 97.250%. This efficiency drop is acceptable because it makes the machine control easier due to the steadier out-put torque and more even converter out-put currents. Additionally, the noise and vibration of the machine is also further suppressed.

B. CURRENT UNBALANCE MITIGATION BY THE COIL SIDE POSITION ADJUSTMENT IN THE STATOR SLOT FOR PHASE W

Based on the phase current curves in Fig. 4, the current unbalance can be further mitigated by adjusting the phase W coil side position. In Fig. 4, there are intersections of the phase currents at both no load and the rated load, when extra slot height is 10 mm. It is possible to get a fully balanced phase current by adjusting the coil side position of phase W, as shown in Fig. 3(a). In the figure the positions of only some coils are recommended to be adjusted, because the coils in other stator slots do not belong to a single phase W. The analysis in Section III-A indicates that most of the indices

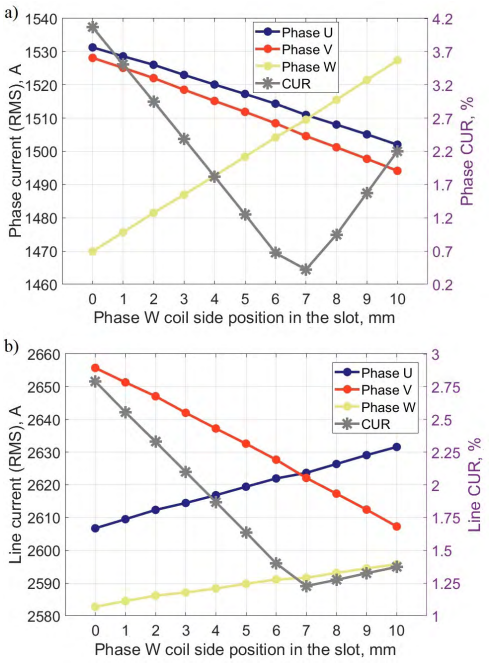

FIGURE 11. (a) Phase currents and CURs as a function of the coil side position of phase W in the stator slot at the rated load with 10 mm extra slot height (2D FEM). (b) Line currents and CURs as a function of the coil side position of phase W in the stator slot at the rated load with 10 mm extra slot height (2D FEM).

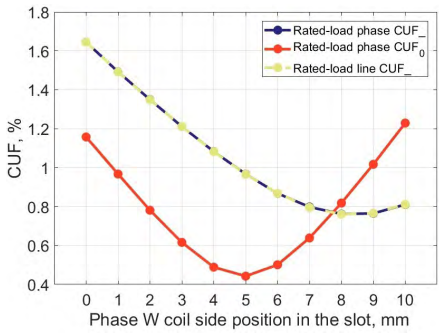

FIGURE 12. Phase and line CUFs as a function of the coil side position of phase W in the stator slot at the rated load with 10 mm extra slot height (2D FEM).

TABLE 5. Asymmetry winding coil side position in the stator slot.

Slot number	34-6	7-9	10-15	16-24	25-27	28-33
Phase	U,V,W	W	V,W	U,V,W	W	V,W
Position, mm	10	7	0	10	7	0

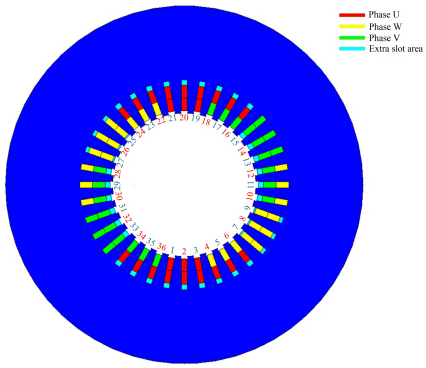

FIGURE 13. Coil arrangements for the three-phase asymmetric winding in different stator slots.

at the rated load have a good agreement with those at no load. Therefore, only the rated current unbalance indices are considered during the optimization of the phase W coil side position.

The adjustment of the coil side position is carried out after choosing a extra slot height of 10 mm, because the three-phase current intersections only show in that situation. Fig. 11 illustrates the three-phase current and CURs as a function of the coil side position of phase W in the stator slot at the rated load. It is assumed that the coil side position is 0 mm when the coil side is placed in the slot bottom, as shown in Fig. 3(a). It can be seen in Fig. 11(a) that the three-phase phase current (fundamental, RMS value, 1511 A, 1505 A, and 1510 A) gets very close to each other when the coil side position is 7 mm and the CUR reaches the minimum of 0.422% at the same time. The same conclusion can be drawn for the three-phase line current and CUR. The currents are 2624 A, 2622 A, and 2592 A, respectively, and the CUR is 1.227% when the coil side position in the stator slot is 7 mm.

Fig. 12 shows phase and line CUFs as a function of the coil side position of phase W in the stator slot at the rated load with 10 mm extra slot height. It can be seen in this figure that the phase and line CUF$_-$ curves coincide with each other. A very small CUF$_-$ can be achieved when coil side position varies from 7 mm to 10 mm. However, the phase CUF$_0$ reaches the minimum when the coil side position is 5 mm. Based on the analysis in Section III-A, it can be concluded that the CUF$_-$ is related to the torque ripple and CUF$_0$ is more related to the losses. The machine is very sensitive to CUF$_-$, which is shown in Fig. 7 and Fig. 10. It was decided to select the 7 mm coil side position as the best solution taking the results in Fig. 11 and Fig. 12 into consideration.

Table 5 lists the specific coil arrangements for the proposed asymmetric winding with 10 mm extra slot height. The slot number is defined in Fig. 2. The more specific

TABLE 6. Asymmetric characteristics with the optimized coil side position.

Parameter	Value	Red. rate
Extra slot height, mm	10	–
Coil side position, mm	7	–
No-load phase CUR, %	0.203	0.968
No-load line CUR, %	1.012	0.613
No-load phase CUF$_-$, %	0.572	0.628
No-load phase CUF$_0$, %	0.670	0.694
No-load phase 3rd order circulating current, A	43.210	0.047
No-load line CUF$_-$, %	0.659	0.571
Rated-load phase CUR, %	0.422	0.945
Rated-load line CUR, %	1.227	0.637
Rated-load phase CUF$_-$, %	0.798	0.594
Rated-load phase CUF$_0$, %	0.639	0.743
Rated-load phase 3rd order circulating current, A	33.397	0.055
Rated-load line CUF$_-$, %	0.796	0.595
Rated-load torque ripple $T_{\mathrm{peak-peak}}$, Nm	34.604	0.579
Efficiency, %	97.255	–

coil arrangements for the three-phase asymmetric winding in different stator slots are illustrated in Fig. 13. Table 6 lists the main current unbalance indices and machine performances with the coil side position of 7 mm for phase W when the extra slot height is 10 mm. In this table, all the current unbalance indices are smaller than those in Table 4, which means that this method gives better results than only adjusting the extra slot height. From the machine point of view, the phase CURs are very small, which means that the phase currents are almost balanced. In addition, the torque ripple is further suppressed and the efficiency (97.255%) is slightly higher than in the previous method (97.250%).

IV. CONCLUSION

An asymmetric double-layer short-pitch winding with prefabricated coils was proposed for a 660 V, 2 MW, 12000 r/min high-speed solid-rotor IM. The purpose of using this winding arrangement was to make the winding manufacture and assembly easier. The proposed asymmetric winding had the disadvantage of generating asymmetric three-phase stator inductances containing magnetizing and leakage inductances, which caused some three-phase current unbalance. The current unbalance brought side effects for the machine and the converter, e.g. control difficulty, torque ripple, and noise and vibration, which should be mitigated as much as possible.

Indices including CUR and CUF were proposed in this paper to evaluate the current unbalance. Two methods were then proposed to mitigate the current unbalance. One was realized by modifying the stator slot height and placing the coils at the slot top or bottom for different phases. The other one was to further adjust the coil side position for phase W, after the slot height was optimized. Consequently, the stator inductances were adjusted successfully as requested by these two methods. As a result, all the corresponding current indices and torque ripple were reduced dramatically. These benefits were realized by at a cost of some extra losses and the machine efficiency dropped from 97.321% to 97.250% and 97.255%, respectively, for these two methods. The second method was capable of acquiring more balanced currents, a smoother torque and a higher efficiency than the first method. The proposed method has the potential to be further utilized for other types of asymmetric windings and machines to guarantee the smaller current unbalance.

ACKNOWLEDGMENT

The authors would like to thank Peter Jones, Lappeenranta University of Technology, for his help with English language of the manuscript.

REFERENCES

[1] D. Gerada, A. Mebarki, N. L. Brown, C. Gerada, A. Cavagnino, and A. Boglietti, "High-speed electrical machines: Technologies, trends, and developments," *IEEE Trans. Ind. Electron.*, vol. 61, no. 6, pp. 2946–2959, Jun. 2014.

[2] Z. Shi, X. Sun, Y. Cai, Z. Yang, G. Lei, Y. Guo, and J. Zhu, "Torque analysis and dynamic performance improvement of a PMSM for EVs by skew angle optimization," *IEEE Trans. Appl. Supercond.*, vol. 29, no. 2, pp. 1–5, Mar. 2019.

[3] X. Sun, K. Diao, G. Lei, Y. Guo, and J. Zhu, "Study on segmented-rotor switched reluctance motors with different rotor pole numbers for BSG system of hybrid electric vehicles," *IEEE Trans. Veh. Technol.*, vol. 68, no. 6, pp. 5537–5547, Jun. 2019.

[4] X. Sun, B. Su, S. Wang, Z. Yang, G. Lei, J. Zhu, and Y. Guo, "Performance analysis of suspension force and torque in an IBPMSM with V-shaped PMs for flywheel batteries," *IEEE Trans. Magn.*, vol. 54, no. 11, Nov. 2018, Art. no. 8105504.

[5] J. F. Gieras and J. Saari, "Performance calculation for a high-speed solid-rotor induction motor," *IEEE Trans. Ind. Electron.*, vol. 59, no. 6, pp. 2689–2700, Jun. 2012.

[6] J. Pyrhonen, J. Nerg, P. Kurronen, and U. Lauber, "High-speed high-output solid-rotor induction-motor technology for gas compression," *IEEE Trans. Ind. Electron.*, vol. 57, no. 1, pp. 272–280, Jan. 2010.

[7] M. Fratila, A. Benabou, A. Tounzi, and M. Dessoude, "Calculation of iron losses in solid rotor induction machine using FEM," *IEEE Trans. Magn.*, vol. 50, no. 2, pp. 825–828, Feb. 2014.

[8] X. Sun, Y. Shen, S. Wang, G. Lei, Z. Yang, and S. Han, "Core losses analysis of a novel 16/10 segmented rotor switched reluctance BSG motor for HEVs using nonlinear lumped parameter equivalent circuit model," *IEEE/ASME Trans. Mechatronics*, vol. 23, no. 2, pp. 747–757, Apr. 2018.

[9] T. Aho, V. Sihvo, J. Nerg, and J. Pyrhonen, "Rotor materials for medium-speed solid-rotor induction motors," in *Proc. IEEE Int. Electr. Mach. Drives Conf.*, vol. 1, May 2007, pp. 525–530.

[10] M. Jagiela and T. Garbiec, "Evaluation of rotor-end factors in solid-rotor induction motors," *IEEE Trans. Magn.*, vol. 48, no. 1, pp. 137–142, Jan. 2012.

[11] S. L. Ho, S. Niu, and W. N. Fu, "A novel solid-rotor induction motor with skewed slits in radial and axial directions and its performance analysis using finite element method," *IEEE Trans. Appl. Supercond.*, vol. 20, no. 3, pp. 1089–1092, Jun. 2010.

[12] M. O. Gulbahce, D. T. Mcguiness, and D. A. Kocabas, "Shielded axially slitted solid rotor design for high-speed solid rotor induction motors," *IET Electr. Power Appl.*, vol. 12, no. 9, pp. 1371–1377, Nov. 2018.

[13] J.-X. Shen, H. Hao, M.-J. Jin, and C. Yuan, "Reduction of rotor eddy current loss in high speed PM brushless machines by grooving retaining sleeve," *IEEE Trans. Magn.*, vol. 49, no. 7, pp. 3973–3976, Jul. 2013.

[14] H.-W. Jun, J. Lee, H.-W. Lee, and W.-H. Kim, "Study on the optimal rotor retaining sleeve structure for the reduction of eddy-current loss in high-speed SPMSM," *IEEE Trans. Magn.*, vol. 51, no. 3, Mar. 2015, Art. no. 8103004.

[15] J.-H. Ahn, C. Han, C.-W. Kim, and J.-Y. Choi, "Rotor design of high-speed permanent magnet synchronous motors considering rotor magnet and sleeve materials," *IEEE Trans. Appl. Supercond.*, vol. 28, no. 3, Apr. 2018, Art. no. 5201504.

[16] M. J. Islam and R. R. Moghaddam, "Loss reduction in a salient pole synchronous machine due to magnetic slot wedge and semiclosed stator slots," in *Proc. 13th Int. Conf. Elect. Mach. (ICEM)*, Sep. 2018, pp. 1267–1272.

[17] L. Huang, Z. Q. Zhu, J. Feng, S. Guo, and J. X. Shi, "Comparative analysis of variable flux reluctance machines with double- and single-layer concentrated armature windings," *IEEE Trans. Ind. Appl.*, vol. 55, no. 2, pp. 1505–1515, Mar./Apr. 2019.
[18] Y. Demir and M. Aydin, "A novel dual three-phase permanent magnet synchronous motor with asymmetric stator winding," *IEEE Trans. Magn.*, vol. 52, no. 7, Jul. 2016, Art. no. 8105005.
[19] Y. Demir and M. Aydin, "A novel asymmetric and unconventional stator winding configuration and placement for a dual three-phase surface PM motor," *IEEE Trans. Magn.*, vol. 53, no. 11, Nov. 2017, Art. no. 8111805.
[20] Y. Hu, Z. Q. Zhu, and M. Odavic, "Compensation of unbalanced impedance of asymmetric wind power PMSG compensated by external circuits in series," *CES Trans. Elect. Mach. Syst.*, vol. 1, no. 2, pp. 180–188, Jun. 2017.
[21] Z. Q. Zhu, M. L. M. Jamil, and L. J. Wu, "Influence of slot and pole number combinations on unbalanced magnetic force in PM machines with diametrically asymmetric windings," *IEEE Trans. Ind. Appl.*, vol. 49, no. 1, pp. 19–30, Jan./Feb. 2013.
[22] Y. Hu, Z. Q. Zhu, and M. Odavic, "An improved method of DC bus voltage pulsation suppression for asymmetric wind power PMSG systems with a compensation unit in parallel," *IEEE Trans. Energy Convers.*, vol. 32, no. 3, pp. 1231–1239, Sep. 2017.
[23] A. G. Yepes, J. Doval-Gandoy, F. Baneira, D. Pérez-Estévez, and O. López, "Current harmonic compensation for n -phase machines with asymmetrical winding arrangement and different neutral configurations," *IEEE Trans. Ind. Appl.*, vol. 53, no. 6, pp. 5426–5439, Nov./Dec. 2017.
[24] P. Verdelho and G. D. Marques, "An active power filter and unbalanced current compensator," *IEEE Trans. Ind. Electron.*, vol. 44, no. 3, pp. 321–328, Jun. 1997.
[25] G. M. Lee, D.-C. Lee, and J.-K. Seok, "Control of series active power filters compensating for source voltage unbalance and current harmonics," *IEEE Trans. Ind. Electron.*, vol. 51, no. 1, pp. 132–139, Feb. 2004.
[26] C. Di, I. Petrov, and J. J. Pyrhönen, "Modeling and mitigation of rotor eddy-current losses in high-speed solid-rotor induction machines by a virtual permanent magnet harmonic machine," *IEEE Trans. Magn.*, vol. 54, no. 12, pp. 1–12, Dec. 2018.
[27] C. Di, I. Petrov, and J. Pyrhönen, "Extraction of rotor eddy-current harmonic losses in high-speed solid-rotor induction machines by an improved virtual permanent magnet harmonic machine model," *IEEE Access*, vol. 7, pp. 27746–27755, 2019.
[28] P. Lindh, I. Petrov, A. Jaatinen-Värri, A. Grönman, M. Martinez-Iturralde, M. Satrústegui, and J. Pyrhönen, "Direct liquid cooling method verified with an axial-flux permanent-magnet traction machine prototype," *IEEE Trans. Ind. Electron.*, vol. 64, no. 8, pp. 6086–6095, Aug. 2017.
[29] M. van der Geest, H. Polinder, J. A. Ferreira, and D. Zeilstra, "Current sharing analysis of parallel strands in low-voltage high-speed machines," *IEEE Trans. Ind. Electron.*, vol. 61, no. 6, pp. 3064–3070, Jun. 2014.
[30] J. Pyrhonen, T. Jokinen, and V. Hrabovcova, *Design of Rotating Electrical Machines*. Hoboken, NJ, USA: Wiley, 2013.
[31] P. Pillay and M. Manyage, "Definitions of voltage unbalance," *IEEE Power Eng. Rev.*, vol. 21, no. 5, pp. 50–51, May 2001.
[32] *IEEE Guide for Self-Commutated Converters*, IEEE Standard 936-1987, 1987, pp. 1–42.

CHONG DI was born in Wuxi, China, in 1991. He received the B.Eng. and M.Eng. degrees in electrical engineering from the Hefei University of Technology, Hefei, China, in 2014 and 2017, respectively. He is currently pursuing the Ph.D. degree with the Department of Electrical Engineering, Lappeenranta University of Technology, Finland.

His research interest includes high-speed electrical machines.

ILYA PETROV received the D.Sc. degree from the Lappeenranta University of Technology (LUT), Finland, in 2015, where he is currently a Fellow Researcher with the Department of Electrical Engineering.

JUHA J. PYRHÖNEN (M'06–SM'17) was born in Kuusankoski, Finland, in 1957. He received the D.Sc. degree from the Lappeenranta University of Technology (LUT), Finland, in 1991.

He became a Professor of electrical machines and drives with LUT, in 1997. He is involved in the research and development of electric motors and power-electronic-controlled drives. He has wide experience in the research and development of special electric drives for distributed power production, traction, and high-speed applications. Permanent magnet materials and applying them in machines have an important role in his research. Currently, he is also studying possibilities of using carbon-based materials in electrical machines.

Publication V

Di, C., Petrov, I., Pyrhönen, J., and Bao, X.
Unbalanced Magnetic Pull Compensation With Active Magnetic Bearings in a 2 MW High-Speed Induction Machine by FEM

Reprinted with permission from
IEEE Transactions on Magnetics
Vol. 54, pp. 1-13, 2018

Unbalanced Magnetic Pull Compensation With Active Magnetic Bearings in a 2 MW High-Speed Induction Machine by FEM

Chong Di[1], Ilya Petrov[1], Juha J. Pyrhönen[1], and Xiaohua Bao[2]

[1]Department of Electrical Engineering LUT Energy, School of Technology, Lappeenranta University of Technology, 53851 Lappeenranta, Finland
[2]School of Electrical Engineering and Automation, Hefei University of Technology, Hefei 230009, China

High-power high-speed induction machines (IMs) are gaining ground in various industrial applications, especially in replacing traditional motors and gearboxes driving compressors or high-pressure pumps, etc. However, the high-speed technology presents extra challenges for the mechanical structure of the machine including bearing systems. Therefore, it is often reasonable to use active magnetic bearings (AMBs) instead of traditional bearings as they provide much smaller friction and allow a not perfectly centered orbit of the rotor without affecting the lifetime of the bearings. Using AMBs in a machine, the nonuniformity of the rotor leads to an inevitable rotor eccentricity; the level of which depends on the control tolerance and dynamic characteristics of the AMB and the maximum force generated by the AMB. This rotor eccentricity results in an unbalanced magnetic pull (UMP) of the rotor, which has to be compensated by the AMB. This paper analyzes the UMPs of a 2 MW, 12 000 r/min IM in the static eccentricity, dynamic eccentricity, and mixed eccentricity conditions. The AMB system was designed and optimized with the consideration of gravity and UMP effects. Furthermore, the required current compensation for the forces in the horizontal and vertical directions was studied during the operation and verified by the finite-element method.

***Index Terms*— Active magnetic bearing (AMB), current compensation, finite-element method (FEM), high-speed induction machine (IM), unbalanced magnetic pull (UMP).**

NOMENCLATURE

Ω_r(rad/s)	Rotor rotating frequency.
f (Hz)	Current signal frequency.
t (s)	Time variable.
θ (rad)	Stator position angle.
θ_{ref} (rad)	Reference stator position angle.
δ_0 (mm)	Air-gap length in a healthy machine.
δ_{se} (mm)	Air-gap length in the SE condition.
δ_{de} (mm)	Air-gap length in the DE condition.
δ_{me} (mm)	Air-gap length in the ME condition.
μ_r	Relative permeability of the magnetic wedge.
l (mm)	Core length.
B_r, B_t (T)	Normal and Tangential components of the air-gap flux density.
w_{d1}, w_{d2} (mm)	Tooth widths of the AMB.
w_{fb} (mm)	Flux barrier width of the AMB.
I_{ac} (A)	Amplitude of the alternating current.
I_{dc} (A)	Value of the direct current.
I_{left}, I_{right} (A)	Compensation currents in the left and right double E-cores.
I_{upper}, I_{lower} (A)	Compensation currents in the upper and lower double E-cores.
F_{UMP} (N)	Force caused by UMP.
F_{left}, F_{right} (N)	Magnetic forces generated by the left and right double E-cores.
F_{upper}, F_{lower}	(N) Magnetic forces generated by the upper and lower double E-cores.
F_{sum}	(N) Sum of the magnetic forces.

Manuscript received January 29, 2018; revised April 4, 2018; accepted May 12, 2018. Date of publication June 7, 2018; date of current version July 18, 2018. Corresponding author: C. Di (e-mail: Chong.Di@lut.fi).

Color versions of one or more of the figures in this paper are available online at http://ieeexplore.ieee.org.

Digital Object Identifier 10.1109/TMAG.2018.2837659

I. INTRODUCTION

THE high-speed technology based on induction machines (IMs), permanent magnet synchronous machines (PMSMs), or switched reluctance machines has been gaining ground as these machine types allow high-speed applications without gearboxes, thereby achieving a high power density and a compact size compared with more conventional-speed machines [1]–[3]. High-speed machines are used in different types of industrial applications including compressors, pump fans, turbines, electric vehicles, flywheel energy storage systems, and high-speed spindles [4]. High-speed IMs with a solid rotor can run at higher speeds than other types of high-speed machines (e.g., PMSM), and they also have a lower material cost. Owing to the limits of the mechanical stresses caused by the centrifugal force, in order to achieve higher rotating speeds, the diameter of the rotor has to be reduced. This leads to a longer rotor length if the torque-producing tangential stress together with the nominal torque is kept constant. Because of mechanical issues and bearing problems, a rotor eccentricity fault often occurs in machines with a long shaft, as reported in [5] and [6]. This problem is even more serious in large-size or high-power electrical machines [7], [8]. The rotor eccentricity can be classified into three types: static eccentricity (SE), dynamic eccentricity (DE), and mixed eccentricity (ME) [9]. It has been reported in many papers that the rotor eccentricity will cause some extra side effects on the performances of the machine, such as noise and vibration, increment in

losses and unbalanced magnetic pull (UMP) [10]–[12]. Rotor eccentricity poses a major challenge for a high-speed machine because of UMP, which occurs during a rotor eccentricity fault, and usually increases the eccentricity more in return. Therefore, prediction of UMP is the machine design and the operation is a critical task.

Because of the high mechanical stresses affecting the bearings at high rotational speeds, conventional bearings may not be suitable for these applications. In recent years, with the rapid development of active magnetic bearing (AMB) systems and relevant control technologies, AMBs are more frequently used to support the rotor shaft in challenging high-speed applications to guarantee a safe operation of the high-speed machines [13], [14]. In many industrial applications, a high-speed machine and the AMBs are often developed as one integrated unit. In this case, the machine should be designed taking the capabilities of the AMB into account, whereas the characteristics of the AMBs should be referred to the machine parameters. Smirnov *et al.* [15] designed a high-speed IM by means of the multi-objective genetic algorithm taking both the machine and bearing designs into consideration. Uzhegov *et al.* [16] designed and made a comparison between a 120 kW, 60 000 r/min high-speed IM and a 225 kW, 50 000 r/min high-speed PMSM with an AMB system for compressor applications.

The rotor eccentricity becomes more complicated, when talking about an electrical machine system with AMB support. When rotor eccentricity occurs, both the electrical machine and the AMB will stay in an asymmetric condition. Typically, maximally 10% eccentricity is acceptable in practice, just from the point of view of the electrical machine. The limit should, however, be smaller for high-speed machine as reported in [17]. However, from the point of view of the AMB, in order to make the AMB run perfectly within the linear area, maximally 50% eccentricity of AMB's air-gap length is suitable [18]. So, actually the practical maximum eccentricity is the smaller one of these two maxima, when the machine and the AMB are regarded as a system. Basically, a big air-gap length can result in rotor eccentricity more easily. The bigger the eccentricity, the more obvious side effects the system will suffer. In this paper, a 2 MW high-speed IM with 280 mm stator bore and 538 mm stack length is studied. Its air-gap length is 6 mm and synchronous speed is 12 000 r/min. From these measures point of view, the max eccentricity for the rotor should not exceed 0.6 mm. However, the safety bearing clearance is 0.25 mm limiting the eccentricity below that value because the AMB actuators air-gap length is 0.5 mm as described in Section III.

The rotor eccentricity brings challenges in the AMB control. It becomes very critical to study how to compensate for the UMP generated by the eccentricity. There are some relevant papers about AMB's control in asymmetric condition. Qiu *et al.* [19] studied the compensation for levitation in a bearingless permanent magnetic synchronous motor (BPMSM) with eccentricity and proved that the proposed control strategy improved the dynamic and static performances of BPMSM. However, the BPMSM itself is a combination of electrical machine and bearing, which is different from the traditional separated system. Mao and Zhu [20] and Tang *et al.* [21] also developed some novel control strategies to suppress the vibration of the rotor due to the rotor mass imbalance. But actually most of the present control strategies are not specially designed for an electrical machine, they can even be applied in other high-speed rotating devices with rotors (e.g., turbine). Because most of them deal with the gravity and mass imbalance of the rotor during the operation, which cause the asymmetry of the AMB itself. However, in an electrical machine system with AMB support, the extra magnetic force, UMP generated from the electrical machine itself during eccentricity should also be compensated by the AMB and this has not been studied in detail yet.

The aim of this paper is to investigate the capability of the proposed AMB design to withstand the UMP generated by a high-speed IM rotating at 12 000 r/min with a nominal power of 2 MW by the finite-element method (FEM). This paper considers the whole system including a high-speed IM and its AMB system. The basic design of the machine is given in Section II. In Section III, the AMB actuators with unequal teeth and flux barriers are designed and optimized based on the sum of gravity and the maximum UMP and the control dynamics requirements, following with verification of the main performance of the AMB actuator by the FEM 2-D. Finally, the current compensation for the total forces is discussed in Section IV.

II. Analysis of UMP in a High-Speed IM

In high-power high-speed IMs, it is often advisable to have longer air-gap length compared with the machines of smaller size and traditional speed because of the target to minimize rotor losses (generated by stator flux density harmonics) and the mechanical issues such as the rotor dynamic problems. Consequently, after long-term operation using traditional bearings, it is possible that the rotor eccentricity incrementally increases. This leads to a non-concentric air gap in the machine, which results in UMP. Fig. 1 shows a schematic view of the possible rotor eccentricity. Typically, SE is a situation when O_s and O_r are not coincident and O_r is the rotating center. The same situation, but with the stator geometric center O_s as the rotating center, is referred to as DE. If the rotating center is O_ω, neither O_s or O_r, it refers to ME.

When only SE occurs, the rotor only rotates around O_r with a speed of Ω_r (Ω_r is the rotor rotating frequency). This indicates that the air-gap length along the stator inner periphery is different and fixed. However, when DE and ME faults occur, the rotating centers are changing from O_r to O_s and O_r to O_ω, respectively. In DE and ME situations the air-gap lengths would be functions of time. The functions of the air-gap lengths in these three situations have been reported in the previous papers. They can be expressed as [22], [23]

$$\begin{cases} \delta_{se}(\theta) = \delta_0 - \varepsilon_{se}\cos\theta \\ \delta_{de}(\theta, t) = \delta_0 - \varepsilon_{de}\cos(\theta - \Omega_r t) \\ \delta_{me}(\theta, t) = \delta_0 - \varepsilon_{se}\cos\theta - \varepsilon_{de}\cos(\theta - \Omega_r t) \end{cases} \tag{1}$$

where δ_0 is the air-gap length in a healthy machine without any eccentricity, ε_{se} and ε_{de} are the eccentricity lengths in

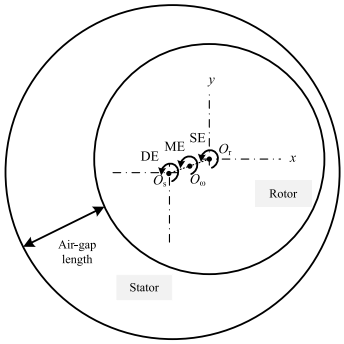

Fig. 1. Schematic of rotor eccentricity faults.

the SE and DE conditions, which are the lengths of $|O_s \cdot O_\omega|$ and $|O_r \cdot O_\omega|$ as shown in Fig. 1, respectively, and θ is the stator position angle counted from a certain reference position. Equation (1) indicates that in the SE condition, the air-gap length is constant in a certain stator position. However, in the DE and ME conditions the air-gap lengths at a certain stator position are changing as functions of time and position.

Following the previous discussions of rotor eccentricity, the high-speed IM model is analyzed in terms of UMPs in different eccentricity conditions, including SE, DE, and ME conditions.

A. High-Speed IM Model

In this paper, a two-pole, 2 MW, a 12 000 r/min IM was analyzed for the calculation of UMP. The air-gap length is set to 6 mm to minimize the rotor Joule losses. The rotor core is made of solid high-permeability construction steel (S355). The rotor contains a copper bar cage winding, which should lead to a small slip, thereby reducing slip-based rotor Joule losses. The stator core is made of the conventional low-loss lamination (M270-35A).

In order to verify the main characteristics of the machine, the FEM was used to conduct the simulation. Fig. 2 shows a detailed FEM model with mesh taking into account both the semi-magnetic wedges and cooling holes below the rotor copper bars. In the simulation, it was found that the semi-magnetic wedge with the relative permeability $\mu_r = 3$ had a significant influence on the solid rotor loss. Because of the high rotational frequency and a large variety of flux density harmonics in the air gap, there are significant Joule losses generated in the solid rotor, which mostly occur on the rotor surface. Therefore, to obtain better simulation results, finer mesh elements were applied on the rotor surface. In Fig. 2, there are about six layers in total in the air gap. The rotor surface also has fine mesh elements, which can help in simulating the skin effect and the rotor surface eddy currents. All these measures should lead to a high precision of the simulation.

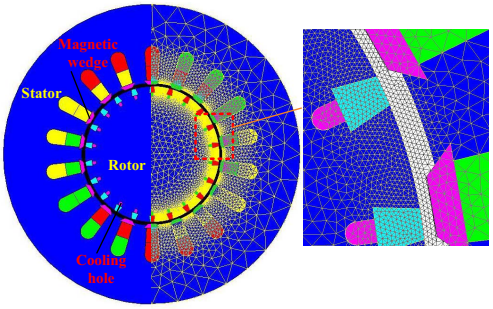

Fig. 2. FEM model of the 2 MW high-speed IM with mesh.

TABLE I
MAIN SIMULATION RESULTS OF THE HIGH-SPEED IM AT NOMINAL LOAD

Parameter	Value
Per unit slip	0.003
Slip frequency (Hz)	0.6
Air-gap flux density peak value (T)	0.96
Copper bar loss with semi-magnetic wedge (kW)	5.91
Solid rotor loss with semi-magnetic wedge (kW)	22.97
Stator copper loss (kW)	7.77
Stator iron loss (kW)	17.50

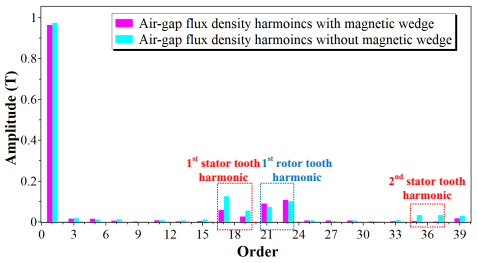

Fig. 3. Air-gap flux density harmonic components of the high-speed IM with and without semi-magnetic wedges.

Table I shows the main simulation results of the high-speed IM with semi-magnetic wedges. The simulation results also show that semi-magnetic wedges have a significant influence on the copper bar loss and solid rotor loss. These losses of the machine with semi-magnetic wedges are only approximately 20% of those in the machine without magnetic wedges. Fig. 3 shows the air-gap flux density harmonic components with and without magnetic wedges, which explains the loss increment on the rotor side. In Fig. 3, 17th and 19th are the harmonics generated by the stator teeth. It can be seen that the amplitudes of these harmonics without wedges are double compared with those with wedges. The situation is even more evident when it comes to the second-order stator tooth harmonics (35th and 37th). However, the stator semi-magnetic wedges do not have a similar effect on the harmonics

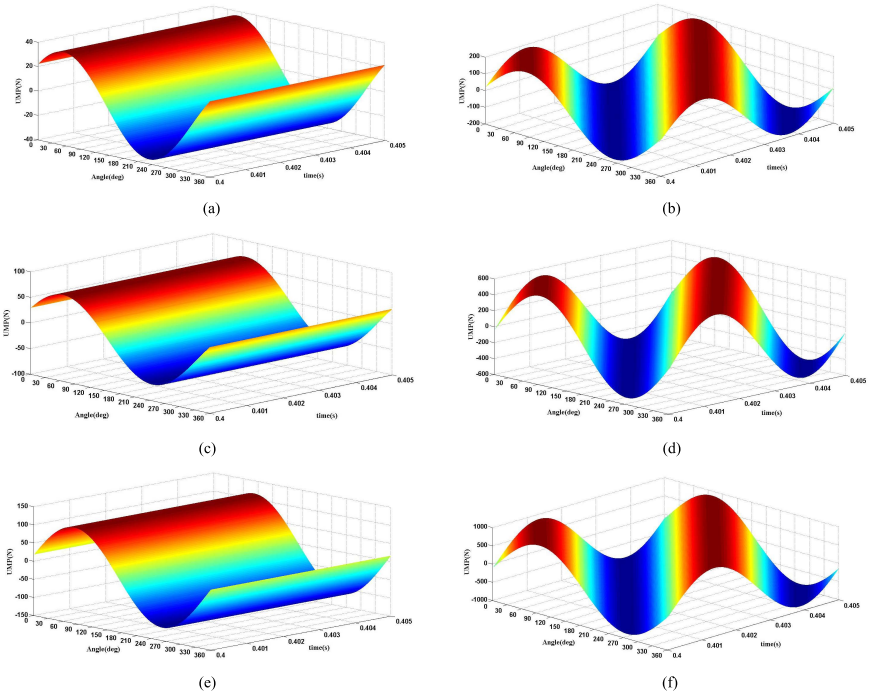

Fig. 4. UMPs in different rotor eccentricity fault conditions. (a) 0.05 mm eccentricity length in the SE condition. (b) 0.05 mm eccentricity length in the DE condition. (c) 0.15 mm eccentricity length in the SE condition. (d) 0.15 mm eccentricity length in the DE condition. (e) 0.25 mm eccentricity length in the SE condition. (f) 0.25 mm eccentricity length in the DE condition. The SE is independent of time while the DE depends on both time and position.

generated by the rotor teeth (21st and 23rd), the amplitudes of which are even slightly larger in the machine with semi-magnetic wedges. However, because they are rotor teeth-based harmonics, they do not generate any eddy currents on the rotor surface, which means that the rotor-based harmonics do not increase the rotor loss.

B. UMP Calculation in the SE, DE, and ME Conditions by FEM

When rotor eccentricity occurs during the operation of the machine, the distribution of air-gap length exhibits an asymmetric pattern. The air-gap permeance is inversely proportional to the air-gap length, and thus, the air-gap flux density also varies in different positions in eccentricity conditions. In principle, when the machine is not saturated, higher flux density occurs in the position with a shorter air-gap length whereas a lower flux density appears at the position with a longer air-gap length. According to Maxwell's tensor method, the UMP that stresses the rotor can be calculated with the following equation [24]:

$$F_{\mathrm{UMP}} = \int_0^{2\pi} \frac{\left(B_r^2 - B_t^2\right)}{2\mu_0} \cos(\Omega_r t - \theta_{\mathrm{ref}}) \cdot l d\theta \qquad (2)$$

where B_r and B_t are the normal and tangential components of the air-gap flux density, l is the core length, and θ_{ref} is the reference stator angle, which also represents the direction of the calculated UMP.

The air-gap length of this AMB is 0.5 mm, which is discussed in Section III. Based on the suggestion of 50% maximum eccentricity in [18], the high-speed IM and the AMB are expected to run within the maximum eccentricity of ± 0.25 mm. Fig. 4 demonstrates the UMPs in different rotor eccentricity fault conditions. It shows that the UMPs increase with the eccentricity length in both SE and DE conditions. However, the UMP in the DE condition is larger than that in the SE condition at the same eccentricity level. It is because in the SE condition, the rotor is fixed in a certain position, and it rotates around itself. The stator current produces a flux, which rotates at the synchronous speed and generates the rotor current, which in turn produces a flux component of its own. The flux produced by the rotor current inherently has a relatively high time constant and cannot change very rapidly, because this flux penetrates through the whole rotor conducting structure and its variation generates a significant amount of eddy currents which try to keep it constant. This phenomenon tries to prevent the flux from alternating and

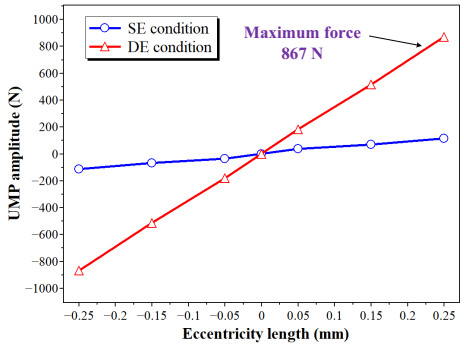

Fig. 5. UMPs as a function of eccentricity displacement in the SE and DE conditions when operating at the rated speed by FEM 2-D.

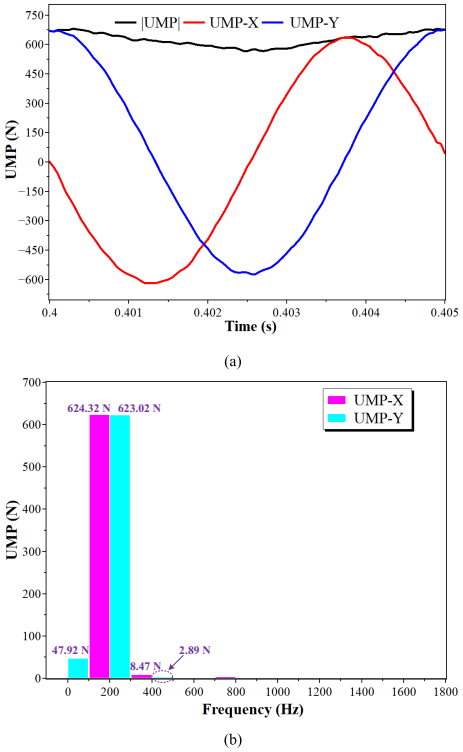

Fig. 6. UMP in the ME (0.05 mm SE + 0.20 mm DE) condition by FEM 2-D. (a) Amplitude of *x*- and *y*-components of the UMP in the ME condition. (b) Spectrums of the *x*- and *y*-components of the UMP in ME condition.

reduces part of certain flux harmonics in the air gap. However, in the DE condition, the rotor rotates together with the eccentricity (neglecting the difference in the speed caused by the slip) and the flux produced by the rotor currents faces the same air-gap length during the whole electrical period. In reality, this flux is varying with the slip frequency of 0.6 Hz but in the worst case the peak flux density occurs in the minimum air-gap area. This condition repeats at every 1.67 s while the rotor makes about 330 revolutions. This leads to a situation where the flux difference produced by the eccentricity does not generate significant eddy currents in the rotor (which would try to keep it constant) as there are very slow flux variations in relation to the rotor. Thus, the flux in the DE condition is alternating much more compared with that in the SE condition. Fig. 5 shows that there may be a linear relationship between the UMP amplitudes and the eccentricity lengths. The reason for this is that machine is not saturated yet, which means that the stator lamination and the rotor steel still work within their linear areas, which is quite typical for high-speed IMs.

The situation becomes more complex when the UMP is discussed in the ME condition. It is better to decompose the amplitude of the UMP into the *x* (horizontal)- and *y* (vertical)-directions. Theoretically, the ME condition contains infinite combinations of different SE and DE conditions. In this paper, only 0.25 mm eccentricity length is analyzed including the combinations of 0.05 mm SE + 0.20 mm DE, 0.10 mm SE + 0.15 mm DE, and 0.15 mm SE + 0.10 mm DE. Fig. 6(a) shows the UMP and the corresponding *x*- and *y*-components in the ME (0.05 mm SE + 0.20 mm DE) conditions. Fig. 6(b) shows the harmonic components of the UMP in the *x*- and *y*-directions. It can be seen that the UMP in the *x*-direction mainly contains 200 and 400 Hz harmonics and UMP in the *y*-direction mainly contains direct component, 200 Hz harmonics and 400 Hz harmonics. The 400 Hz harmonic is very small in the *y*-direction (2.89 N), so it is not very clearly shown in Fig. 6(b). This 400 Hz harmonic is generated by the interaction of the SE and DE. The direct component in the *y*-direction is caused by the SE. When the SE was modeled, the rotor was moved to the *y*-direction by the corresponding length. As a result, the direct component can be observed in the *y*-direction. The 200 Hz harmonics in the *x*- and *y*-directions are 624.32 and 623.02 N, respectively. They are almost the same as shown in Fig. 6(b). It is because this 200 Hz harmonic is generated by the DE. More details about the harmonics in these two directions with different ME conditions are illustrated in Fig. 7. It can be found that if the SE length is increased, the 200 Hz harmonic in both directions will drop. However, the 400 Hz harmonic in both directions and direct component in the *y*-direction will increase. The maxima for the 400 Hz harmonic are about 20 N in the *x*-direction and 12 N in the *y*-direction in the situation of 0.20 mm SE + 0.05 mm DE. The 400 Hz, 20 or 12 N magnetic force cannot affect the rotor dynamic too much. Because the rotor mass is quite large — about 310 kg. The maximum acceleration caused by the force is 20 N/(310 kg/2) = 0.129 m/s^2 and the average one 0.082 m/s^2. Half of the period of 400 Hz is 1.25 ms and the vibration speed amplitude, therefore, 0.16 mm/s = 0.16 μm/ms.

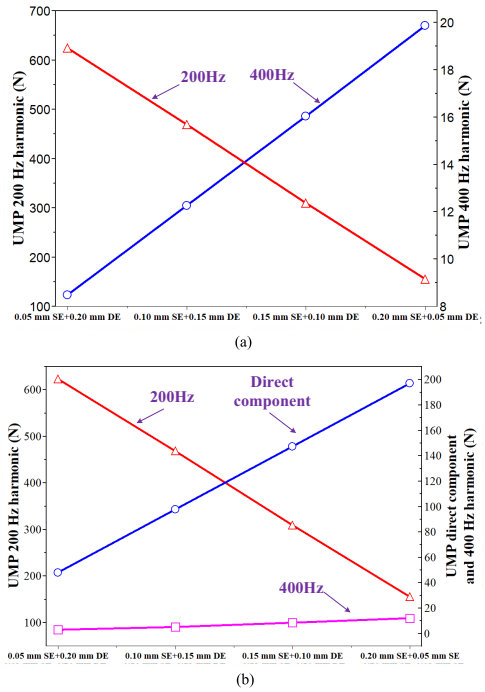

Fig. 7. UMP harmonics in the x- and y-directions in ME conditions. (a) UMP main harmonics in the x-direction. (b) UMP harmonics in the y-direction.

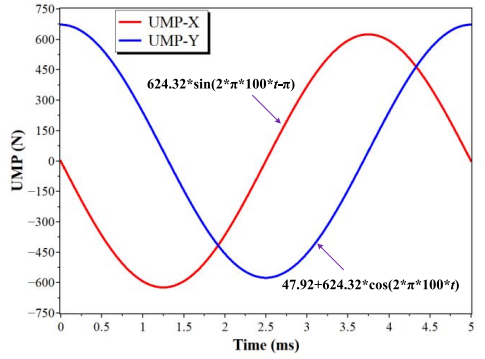

Fig. 8. Ideal UMPs in the x- and y-directions for compensation in the ME (0.05 mm SE + 0.20 mm DE) condition.

Thus, this harmonic can be neglected in the compensation. After getting rid of the high-frequency harmonics, the ideal UMPs in the ME (0.05 mm SE + 0.20 mm DE) condition in the x- and y-directions are shown in Fig. 8.

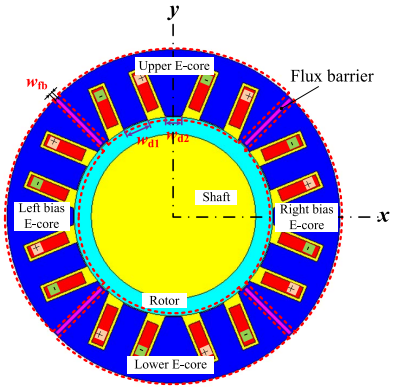

Fig. 9. Parameterized AMB model with optimized parameters.

III. Design and Optimization of the AMB

Because of the relatively high rotating speed of the machine, it is often advisable to use AMBs instead of traditional bearings. Basically, AMBs have a smaller stiffness, which would make the critical speed of the first bending mode larger. This speed can even get very close to the critical speed of the free–free mode so that the machine may run below the first-order critical speed. In the AMB system described here, there are two AMBs in total to lift the whole rotor.

Fig. 9 shows the proposed AMB model with flux barriers. In principle, there are four double E-cores in total; two in the x-direction and two in the y-direction. Double E-cores were selected to enable a smaller outer diameter (because of thinner stator yokes) and a shorter core length of the actuators because of more magnetic poles. The motor is installed in the x-direction, and thus, the maximum magnetic force of the AMB should be in the y-direction including the force for compensation of the rotor weight. The left and right double E-cores are called bias double E-cores. In Fig. 9, w_{d1} and w_{d2} are the tooth widths of the two different teeth, and w_{fb} is the width of the flux barriers. It is found that by applying the flux barriers in the AMB it is possible to achieve a larger magnetic force (having the same current density in the coils) and less mutual inductance between different directions actuators. In other words, the interference between the E-cores is reduced because of a reduction in the mutual inductance between different E-cores. For example, when the upper coils are injected with the currents in an AMB without flux barriers, a magnetic flux appears not only in the top double E-core but also in the bottom double E-core without current. However, the barriers reduce the flux at the bottom to the minimum in the AMB actuator with barriers. As a result, a stronger force is generated in the desired direction and less interference in the control of these coils is observed. Fig. 9 also indicates that the coil currents in each double E-core are $+-+-$, which means that the magnetic pole is in the NSNS arrangement. With the given current supply, the NSNS model can generate

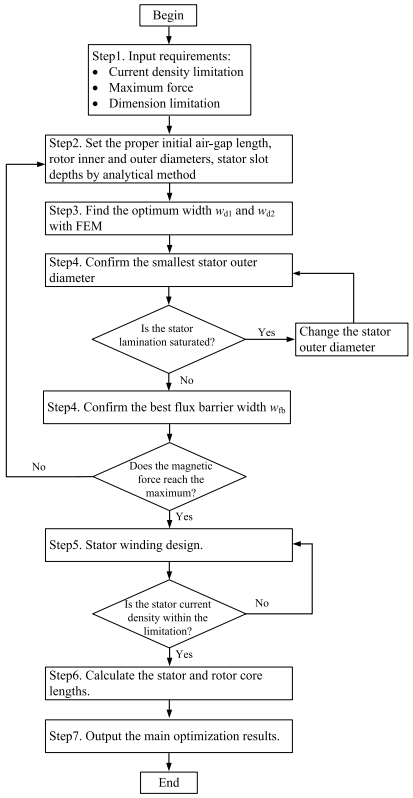

Fig. 10. Optimization design procedure of the AMB.

about 50 kN/m of magnetic force per core length with a 25 W rotor core loss. However, the NSSN model can only generate 40 kN/m of magnetic force per core length with a 33 W rotor core loss, and the NNSS model can generate 32 kN/m of magnetic force per core length with a 40 W rotor core loss. The unit [N/m] denotes the magnetic force per core length; in the design process, it is more convenient to compare the force values before the core length is determined.

The total mass of the rotor including the copper bars is about 310 kg (gravity is 3038 N). The maximum magnetic force caused by the eccentricity (0.25 mm of DE) is 867 N. Thus, the total maximum force that the AMB has to overcome is 3905 N. For each AMB, the maximum force is 1952.5 N. However, this is only the ideal maximum force. Typically, the maximum force of an AMB actuator should be almost tripled compared with the predicted values required for safety reasons. Thus, it was decided that 5500 N is the maximum force that each AMB actuator should achieve. The maximum current density in the upper double E-core is 7.5 A/mm^2 (owning to control requirements, the maximum AMB stator current was originally assumed to be 12 A), which is selected based on the cooling arrangement of the AMB actuators. Consequently, at the same time, the lower double E-core should have no current to reach the maximum lifting force of the AMB. Meanwhile, the bias double E-core continuous current density is 1.94 A/mm^2. In order to achieve the maximum magnetic force by the designed AMB, an optimization procedure shown in Fig. 10 is applied.

TABLE II
DIMENSIONS OF AMB

Specification	Value
Magnetic force direction	Vertical
Maximum force (N)	5500
Number of poles	16
Stator inner diameter (mm)	146
Stator outer diameter (mm)	243
Rotor outer diameter (mm)	145
Core length (mm)	117
Shaft diameter (mm)	120
Air-gap length (mm)	0.5
Tooth width (mm)	12 and 19
Flux barrier width (mm)	3

Strictly following the design and optimization results in Fig. 11, it is possible to obtain the magnetic force with different dimensions. Fig. 11(a) indicates that the magnetic force per core length reaches the maximum value (51 960 N/m), when the teeth widths are $w_{d1} = 19$ mm and $w_{d2} = 12$ mm. Fig. 11(b) shows that the magnetic force per core length continuously increases with larger stator outer diameter (keeping the inner stator diameter the same). However, at some point, the rate of increase in the magnetic force per core length as a function of outer diameter decelerates. Finally, it was decided to set the outer stator diameter to 243 mm to achieve the force per core length (51941 N/m) with a 5 mm initial flux-barrier width. The flux-barrier width has a significant influence on the magnetic force, as shown in Fig. 11(c). The magnetic force increases rapidly when the width is small and reaches the maximum when the width is 3.5 mm. After that, it starts to decrease. Finally, a 3.5 mm was set as the optimum solution. However, owing to manufacturing issues, a 3 mm flux barrier was selected having 52 375 N/m of magnetic force per core length.

Fig. 12 gives a detailed stator winding distribution with a 1.4 mm bare diameter and 161 conductors per slot. The maximum current density is limited to 7.5 A/mm^2, which leads to a total supply current of 11.55 A in the final design. It is slightly less than the initial current of 12 A because of the wire gauge limit. Therefore, the maximum resultant force is 49625 N/m. In order to provide 5500 N, the core length is set to 117 mm. Table II lists the main parameters of the designed AMB.

IV. CURRENT COMPENSATION FOR UMP BY FEM

A. Current Compensation for the UMP Caused by Static Eccentricity

In the SE case, the air-gap length at a certain stator inner periphery point is fixed. It is possible to detect the minimum air-gap length position so that the UMP distribution can be easily found. Thus, it is possible to adjust the currents in the corresponding actuator coils to cancel the force to make the

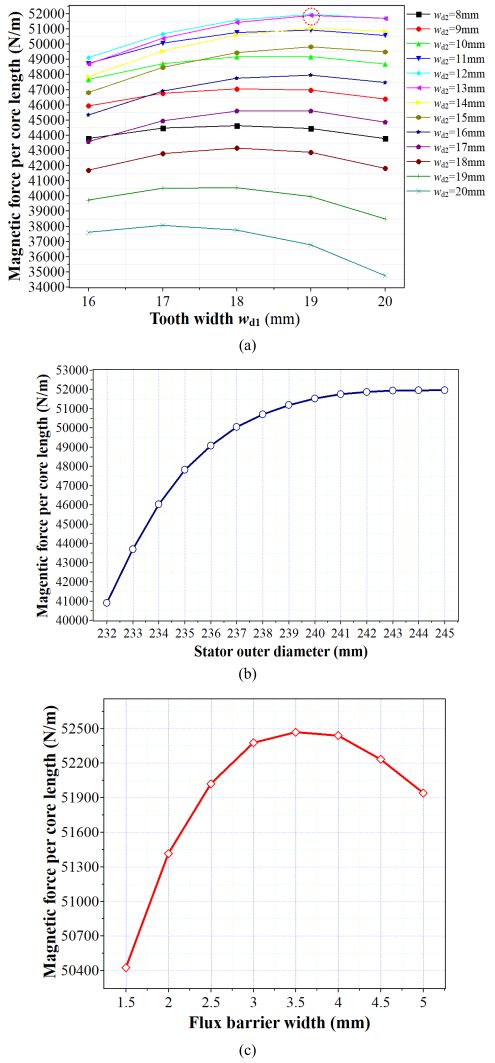

Fig. 11. AMB magnetic force per core length plot as a function of different variable dimensions with a 12 A current in the upper double E-core and 3.11 A current in the bias double E-core. (a) Magnetic force per core length plot as a function of teeth combinations with the initial stator outer diameter (245 mm) and the 5 mm initial flux barrier width. (b) Magnetic force per core length plot as a function of stator outer diameter with the stator teeth widths $w_{d1} = 19$ mm, $w_{d2} = 12$ mm, and the 5 mm initial flux-barrier width. (c) Magnetic force per core length plot as a function of barrier width with a 243 mm stator outer diameter and the stator teeth widths $w_{d1} = 19$ mm and $w_{d2} = 12$ mm.

rotor shaft return concentric. Compared with the DE, this is an easier task. Therefore, the topic is not discussed in detail in this paper, whereas the DE condition is more thoroughly described in the following.

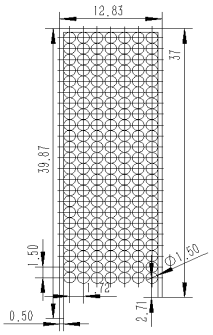

Fig. 12. Stator winding distribution in the slot.

B. Current Compensation for the UMP Caused by Dynamic Eccentricity

The current compensation for UMP in the DE condition is more complicated compared than that in the SE condition, because the direction of the force is always changing. The rotor mechanical rotating speed is 12 000 r/min, and thus, the UMP also rotates at this speed. The described AMB has four double E-cores, which can be divided into two groups. The upper and lower double E-cores are responsible for the force in the y-direction (including gravity and UMP), and the left and right double E-cores are used to adjust the force in the x-direction (only UMP). Thus, the forces should be evaluated separately for the two directions. The current signals for the UMP components and the gravity in the x- and y-directions will be studied first separately. After that the situation will be discussed when the signals are used at the same time.

The UMP compensation in the x-direction is discussed first and there is no current in the double E-cores in the y-direction. When DE is modeled in the FEM software, the AMB shaft is set with the same eccentricity condition as the rotor of the electrical machine. It is assumed that the rotor is initially in the top vertical position with a 0.25 mm eccentricity displacement at the initial time. In order to find the current for the compensation, the frequency of the current can be first estimated by the analytical method. Then, the amplitude can be found by setting different currents in the FEM software. According to the analytical method, the generated magnetic force is proportional to the square of the current. Alternating currents with the same frequency and different phases can be injected in the horizontal coils to compensate for the varying UMP. Thus, the magnetic forces generated by the left double E-core F_{left}, the right double E-core F_{right}, and the sum of the magnetic force F_{sum} described by the magnetizing currents injected in different coils can be expressed as

$$\begin{cases} F_{\text{left}} \propto [I_{\text{ac}} \cos(2\pi f)]^2 = \dfrac{I_{\text{ac}}^2}{2} + \dfrac{I_{\text{ac}}^2}{2} \cos(4\pi f) \\ F_{\text{right}} \propto [I_{\text{ac}} \sin(2\pi f)]^2 = \dfrac{I_{\text{ac}}^2}{2} - \dfrac{I_{\text{ac}}^2}{2} \cos(4\pi f) \\ F_{\text{sum}} \propto F_{\text{left}} - F_{\text{right}} \propto I_{\text{ac}}^2 \cos(4\pi f) \end{cases} \tag{3}$$

where I_{ac} denotes the amplitude of the alternating current, and f is the current signal frequency. Equation (3) indicates that each double E-core can generate one direct component force and one sinusoidal force. However, the sum of the magnetic force is only a sinusoidal force without a direct component, which is needed to compensate for the UMP, and the frequency is double the current supply frequency. Because the UMP frequency is 200 Hz, the current frequency must be 100 Hz. Fig. 13(a) shows the current waveforms in the left and right bias coils for the compensation for the UMP in the x-direction. The compensation currents I_{left} for the left double E-core and $I_{right}$for the right double E-core can be expressed as

$$\begin{cases} I_{left}(t) = [1.79 \cdot \cos(2\pi \cdot 100t + \pi/4)](A) \\ I_{right}(t) = [1.79 \cdot \sin(2\pi \cdot 100t + \pi/4)](A). \end{cases} \tag{4}$$

In Fig. 13(a), it can be seen that when t is 0 ms the currents in the left and right cores are the same and the total force is 0 N. When t is 1.25 ms, the rotor reaches the left position and the left double E-core current gets the minimum value (0 A). However, the right E-core gets the maximum value (1.79 A), so that the magnetic force reaches the maximum in the right direction. When t is 2.5 ms, the sum of the magnetic force is again 0 N. When t is 3.75 ms, the force reaches the maximum in the left direction. All these results correspond to the simulation results, as shown in Fig. 13(b). In Fig. 13(b), the simulated magnetic force generated by the AMB actuator is sufficiently close to the ideal UMP which should be compensated for during the motor operation.

In the y-direction, as a result of gravity, the compensation currents in the upper and lower coils are different from those in the left and right coils. It is assumed that there is no current in the double E-cores in the x-direction when studying the force in the y-direction. According to an analytical analysis, basically there is a direct current injected in the upper coils to compensate for gravity as gravity is a direct component. An alternating current is also injected in the upper coils to compensate for the varying UMP. The same alternating current is applied in the lower coils to eliminate the harmful harmonics of the sum of the magnetic force generated by the upper coils in the y-direction. Thus, the magnetic forces generated by the upper double E-core F_{upper}, the lower double E-core F_{lower}, and the sum of the magnetic force F_{sum} can be described by the magnetizing currents injected in different coils as

$$\begin{cases} F_{upper} \propto [I_{dc} - I_{ac}\cos(2\pi f)]^2 \\ = I_{dc}^2 - 2I_{dc}I_{ac}\cos(2\pi f) + \dfrac{I_{ac}^2}{2} + \dfrac{I_{ac}^2}{2}\cos(4\pi f) \\ F_{lower} \propto [I_{ac}\cos(2\pi f)]^2 \\ = \dfrac{I_{ac}^2}{2} + \dfrac{I_{ac}^2}{2}\cos(4\pi f) \\ F_{sum} \propto F_{upper} - F_{lower} = I_{dc}^2 - 2I_{dc}I_{ac}\cos(2\pi f) \end{cases} \tag{5}$$

where I_{dc} denotes the amplitude of the direct current. It can be seen in the equations that there are four force components generated in the upper double E-core; two direct components and two alternating components. Among all these components, there are three types of harmonics: a direct component (compensates for the gravity), a $2\pi f$ component (compensates for UMP), and a $4\pi f$ component (useless). It is necessary to compensate for the $4\pi f$ component by injecting the same alternating current in the lower double E-core as shown in (5). Consequently, the magnetic force is mainly generated by the upper double E-cores and the lower double E-core is used for eliminating the harmonic components of the force, especially the $4\pi f$ component. Thus, finally there are only the direct component and the $2\pi f$ component remaining. It is found that the compensation currents I_{upper} for the upper double E-core and I_{lower} for the lower double E-core can be written as

$$\begin{cases} I_{upper}(t) = [2.08 - 0.32 \cdot \cos(2\pi \cdot 200t)](A) \\ I_{lower}(t) = [0.32 \cdot \cos(2\pi \cdot 200t)](A). \end{cases} \tag{6}$$

The current frequencies in (6) are quite different from those in the left and right bias coils, especially the current frequency. Based on the analysis of (5), only the upper double E-core generates the force compensating for the UMP and the current frequency is the same with the force frequency (200 Hz). The lower double E-core is only used to reduce the 400 Hz

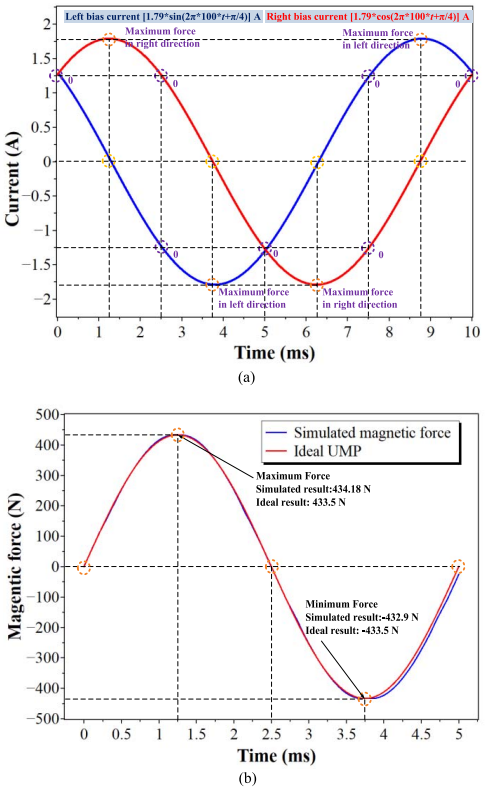

Fig. 13. Compensation for UMP in the x-direction. (a) Left and right bias current waves. (b) Magnetic force compensation for UMP by FEM 2-D.

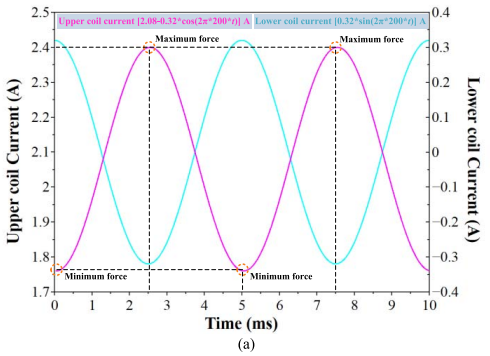

(a)

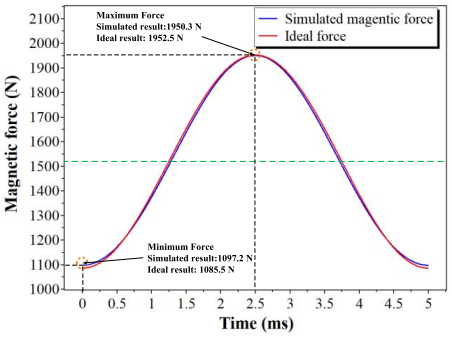

(b)

Fig. 14. Compensation for gravity and UMP in the y-direction. (a) Current waves of the upper and lower coils. (b) Magnetic force compensating for gravity and UMP by FEM 2-D.

harmonic generated by the upper double E-core. The sum of the forces generated by the magnetic AMB actuator is always upward because of gravity. As shown in Fig. 14(a), when t is 0 ms, the rotor is in the top position and the upper coil current is at minimum (1.76 A) so that the sum force is at minimum. When t is 2.5 ms, the upper coil has the maximum current (2.4 A) and the maximum force. At the same time, the rotor reaches the bottom position. All the corresponding results are shown in Fig. 14(b). The simulated curve is quite close to an ideal curve. In order to evaluate this curve, an fast Fourier transform was performed to analyze the quality of the simulated force waveform. Finally, the direct component of the magnetic force is 0 Hz 1511.6 N (which corresponds to gravity), 200 Hz 432.4 N (which corresponds to the rotating UMP), and 400 Hz 4.7 N (which was almost eliminated by the lower double E-core).

The current adjustment characteristics in different coils for the magnetic force are shown in Fig. 15. The alternating currents are used to compensate for the rotating UMP in both the x- and y-directions in all coils (right, left, upper, and lower ones). The direct current has always to be injected into the upper coils to compensate for gravity. Fig. 15(a) shows that the magnetic force generated in the x-direction has a good

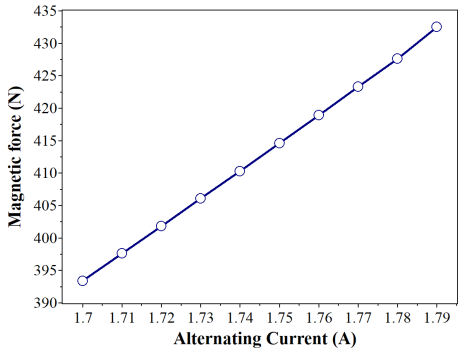

(a)

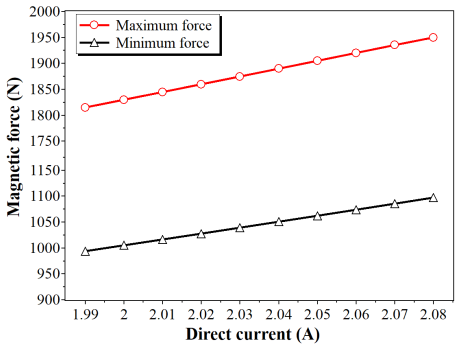

(b)

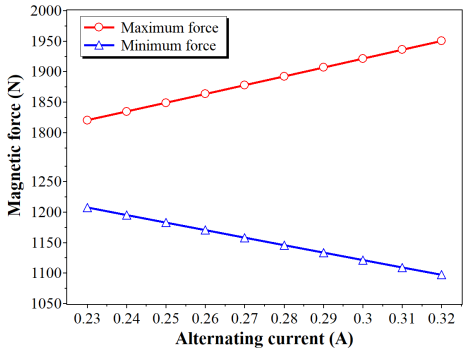

(c)

Fig. 15. Current adjustment characteristics for achieving a particular magnetic force by FEM 2-D. (a) Force in the x-direction as a function of current in the left and right double E-cores. (b) Force in the y-direction as a function of direct current in the upper double E-core with the same alternating current of 0.32 A. (c) Force in the y-direction as a function of alternating current in the upper and lower double E-cores with the unchanged direct current of 2.08 A in the upper E-core.

linear relation with the current amplitude. Fig. 15(b) and (c) also gives the linear curves of the magnetic force generated in the y-direction. Both the maximum force and maximum

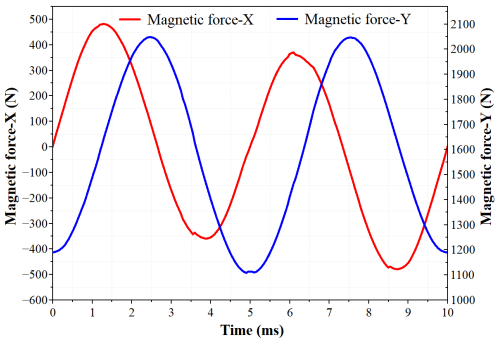

Fig. 16. Magnetic force in the *x*- and *y*-directions with current signals in all double E-cores at the same time by FEM 2-D.

TABLE III
HARMONIC COMPONENTS OF THE MAGNETIC FORCES

Direction	Frequency (Hz)	Amplitude (N)
x	100	82.48
x	200	420.01
y	0	1589.19
y	100	46.42
y	200	448.95

force increase with the direct current increment, as shown in Fig. 15(b). The maximum and minimum forces refer to the maximum and minimum forces generated by the AMB during one mechanical period, which also corresponds to the force definitions in Fig. 14(a). However, in Fig. 15(c), the maximum magnetic force increases and the minimum magnetic force decreases with the increment of the alternating current because of the stronger sinusoidal force component generated by the upper double E-core; this phenomenon also corresponds to the analysis of (5).

The previous analysis shows that the UMP and the gravity in each direction can be compensated, when a separate current signal is used in the double E-cores in the *x*- or *y*-directions. However, when the current signals in the *x*- and *y*-directions are applied at the same time, the situations are quite different because of the mutual inductance effect between the double E-cores in the *x*- and *y*-directions. Fig. 16 shows the magnetic forces in the *x*- and *y*-directions when the current signals in (4) and (6) are used at the same time. It is very clear both of the magnetic forces contain some harmonics.

Table III lists the main harmonic components of the magnetic forces in the *x*- and *y*-directions. It can be found that an extra 100 Hz harmonic component exists in both the *x*-and *y*-directions. The component is generated by the interaction of the 100 Hz current signal in the *x*-direction and the direct current signal in the *y*-direction. According to the algorithm in (5), an extra direct component signal in the *x*-direction and an extra 100 Hz signal in the *y*-direction can be used to mitigate the 100 Hz magnetic force harmonic. In addition, the direct

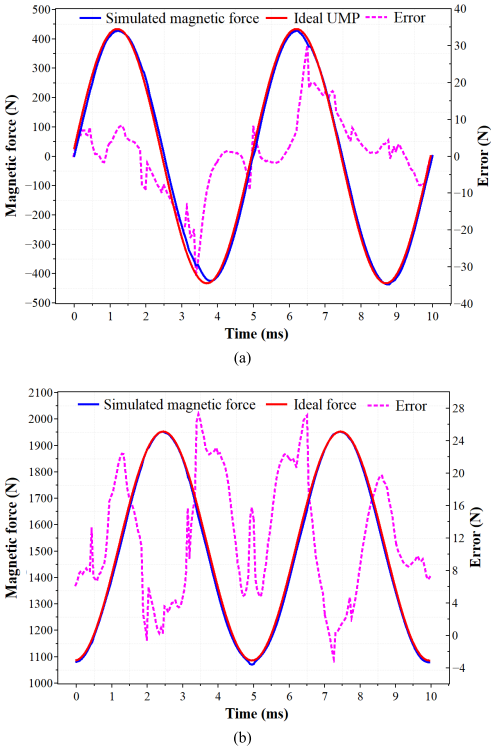

Fig. 17. Magnetic forces in the *x*- and *y*-directions with the modified current signals in all double E-cores at the same time by FEM 2-D. (a) Magnetic force in the *x*-direction. (b) Magnetic force in the *y*-direction.

component in the *y*-direction is higher than expected, so the direct current in the *y*-direction should be reduced by a little. Finally, the modified current signals in all these double E-cores can be expressed as follows:

$$\begin{cases} I_{\text{left}}(t) = [0.11 + 1.79 \cdot \cos(2\pi \cdot 100t + \pi/4)](A) \\ I_{\text{right}}(t) = [0.11 + 1.79 \cdot \sin(2\pi \cdot 100t + \pi/4)](A) \\ I_{\text{upper}}(t) = [2.02 - 0.32 \cdot \cos(2\pi \cdot 200t) \\ \qquad +0.025 \cdot \cos(2\pi \cdot 100t)](A) \\ I_{\text{lower}}(t) = [0.32 \cdot \cos(2\pi \cdot 200t) \\ \qquad +0.025 \cdot \cos(2\pi \cdot 100t)](A). \end{cases} \tag{7}$$

Fig. 17 shows the magnetic force and the corresponding error generated by the AMB with the modified current signals in (7). It reveals that the magnetic forces are very close to the ideal forces in both the *x*- and *y*-directions. Moreover, there are some errors produced by the other harmonics. Although the error peak values are about 30 N, they cannot affect the dynamic state of the rotor too much. Because the error is not a constant, only the instantaneous value at some time will reach 30 N. Another reason is that the rotor runs at a very high

TABLE IV
HARMONIC COMPONENTS OF THE MAGNETIC FORCES WITH MODIFIED CURRENT SIGNALS

Direction	Frequency (Hz)	Amplitude (N)	Error
x	100	8.72	-
x	200	426.61	-1.59%
y	0	1507.14	-0.78%
y	100	2.50	-
y	200	436.10	+0.60%

speed with a big inertia, the rotor dynamic state cannot be changed by a relatively small force unless it coincides with a mechanical resonance of the rotor. Such a case must be carefully analyzed in supercritical cases. However, the rotor in this paper always rotates below the first forward whirling mode of the rotor. Table IV lists the main harmonic components of the magnetic forces and the corresponding errors with respect to the ideal forces. All these corresponding results show that the extra current signals are suitable for mitigating the interaction of the double E-cores in different directions.

C. Current Compensation for the UMP Caused by Mixed Eccentricity

The situation is quite similar for the compensation of the UMP that resulted from ME compared with that in DE condition. Fig. 8 has already shown that the x-direction UMP component is a pure sinusoidal curve and the y-direction UMP component contains a sinusoidal curve and a direct component. In such a case, when the gravity is taken into consideration, the force signals are the same as those in DE condition. So it will not be discussed in this paper further, the force can be compensated by using the same algorithm as in DE condition.

V. CONCLUSION

This paper mainly focused on the AMB actuator design and currents to compensate for the effects of UMP and gravity in a 2 MW high-speed IM. First, the UMPs in SE, DE, and ME conditions were analyzed. Then, the AMB actuator was designed, and the current compensation for UMP and gravity was discussed. The AMB actuator with flux barriers can increase the magnetic force, which can make the system more compact, by reducing the interaction between the double E-cores. Alternating current signals alone can be used for compensation of the UMP in the horizontal direction. However, in the vertical direction, a current signal combining the direct current for gravity and alternating current for UMP has to be applied. Some extra current signals have to be used to mitigate the magnetic force generated by the interaction between the double E-cores in the horizontal and vertical directions. In addition, the AMB system has an acceptable force adjustment performance with a linear current increment.

ACKNOWLEDGMENT

This work was supported in part by the China Scholarship Council under Grant 201706690032.

REFERENCES

[1] D. Gerada, A. Mebarki, N. L. Brown, K. J. Bradley, and C. Gerada, "Design aspects of high-speed high-power-density laminated-rotor induction machines," *IEEE Trans. Ind. Electron.*, vol. 58, no. 9, pp. 4039–4047, Sep. 2017.

[2] S. Xu, X. Liu, and Y. Le, "Electromagnetic design of a high-speed solid cylindrical permanent-magnet motor equipped with active magnetic bearings," *IEEE Trans. Magn.*, vol. 53, no. 8, Apr. 2017, Art. no. 8203715.

[3] S. M. Castano, B. Bilgin, E. Fairall, and A. Emadi, "Acoustic noise analysis of a high-speed high-power switched reluctance machine: Frame effects," *IEEE Trans. Energy Convers.*, vol. 31, no. 31, pp. 69–77, Mar. 2016.

[4] D. Gerada, A. Mebarki, N. L. Brown, C. Gerada, A. Cavagnino, and A. Boglietti, "High-speed electrical machines: Technologies, trends, and developments," *IEEE Trans. Ind. Electron.*, vol. 61, no. 6, pp. 2946–2959, Jun. 2014.

[5] D. G. Dorrell, A. Salah, and Y. G. Guo, "The detection and suppression of unbalanced magnetic pull in wound rotor induction motors using pole-specific search coils and auxiliary windings," *IEEE Trans. Ind. Appl.*, vol. 51, no. 3, pp. 2066–2076, May/Jun. 2017.

[6] D. G. Dorrell, J. Shek, M.-F. Hsieh, and M. A. Mueller, "Unbalanced magnetic pull in cage induction machines for fixed-speed renewable energy generators," *IEEE Trans. Magn.*, vol. 47, no. 10, pp. 4096–4099, Oct. 2011.

[7] D. G. Dorrell, H. Min-Fu, and G. Youguang, "Unbalanced magnet pull in large brushless rare-earth permanent magnet motors with rotor eccentricity," *IEEE Trans. Magn.*, vol. 45, no. 10, pp. 4586–4589, Oct. 2009.

[8] C. Di, X. Bao, H. Wang, Q. Lv, and Y. He, "Modeling and analysis of unbalanced magnetic pull in cage induction motors with curved dynamic eccentricity," *IEEE Trans. Magn.*, vol. 51, no. 8, Aug. 2015, Art. no. 8106507.

[9] Y. Li, Q. Lu, and Z.-Q. Zhu, "Unbalanced magnetic force prediction in permanent magnet machines with rotor eccentricity by improved superposition method," *IET Electr. Power Appl.*, vol. 11, no. 6, pp. 1095–1104, Jul. 2017.

[10] D.-J. Kim, H.-J. Kim, J.-P. Hong, and C.-J. Park, "Estimation of acoustic noise and vibration in an induction machine considering rotor eccentricity," *IEEE Trans. Magn.*, vol. 50, no. 2, pp. 857–860, Feb. 2014.

[11] A. Belahcen and A. Arkkio, "Computation of additional losses due to rotor eccentricity in electrical machines," *IET Electr. Power Appl.*, vol. 4, no. 4, pp. 259–266, 2010.

[12] D. G. Dorrell, M. Popescu, and D. M. Ionel, "Unbalanced magnetic pull due to asymmetry and low-level static rotor eccentricity in fractional-slot brushless permanent-magnet motors with surface-magnet and consequent-pole rotors," *IEEE Trans. Magn.*, vol. 46, no. 7, pp. 2675–2685, Jul. 2010.

[13] S. Xu and J. Fang, "A novel conical active magnetic bearing with claw structure," *IEEE Trans. Magn.*, vol. 50, no. 5, May 2014, Art. no. 8101108.

[14] Z. Huang, J. Fang, X. Liu, and B. Han, "Loss calculation and thermal analysis of rotors supported by active magnetic bearings for high-speed permanent-magnet electrical machines," *IEEE Trans. Ind. Electron.*, vol. 63, no. 4, pp. 2027–2035, Apr. 2016.

[15] A. Smirnov, N. Uzhegov, T. Sillanpää, J. Pyrhönen, and O. Pyrhönen, "High-speed electrical machine with active magnetic bearing system optimization," *IEEE Trans. Ind. Electron.*, vol. 64, no. 12, pp. 9876–9885, Dec. 2017.

[16] N. Uzhegov, A. Smirnov, C. H. Park, J. H. Ahn, J. Heikkinen, and J. Pyrhönen, "Design aspects of high-speed electrical machines with active magnetic bearings for compressor applications," *IEEE Trans. Ind. Electron.*, vol. 64, no. 11, pp. 8427–8436, Nov. 2017.

[17] I. Z. Boguslavskiy, I. Y. Kruchinina, Y. P. Khozikov, and A. S. Liubimtcev, "High-speed synchronous machines: Magnetic pulling tensioning forces calculation approach," in *Proc. IEEE Int. Conf. Electr. Machines (ICEM)*, Sep. 2014, pp. 176–181.

[18] H. Yang, R. X. Zhao, and Q. B. Tang, "Study on inverter-fed three-pole active magnetic bearing," in *Proc. 21st Annu. IEEE Appl. Power Electron. Conf. Expo. (APEC)*, Mar. 2006, p. 6.

[19] Z. J. Qiu, J. Dai, J. Yang, X. Zhou, and Y. Zhang, "Research on rotor eccentricity compensation control for bearingless surface-mounted permanent-magnet motors based on an exact analytical method," *IEEE Trans. Magn.*, vol. 51, no. 11, Nov. 2015, Art. no. 8114004.

[20] M. Chuan and Z. Changsheng, "Unbalance compensation for active magnetic bearing rotor system using a variable step size real-time iterative seeking algorithm," *IEEE Trans. Ind. Electron.*, vol. 65, no. 5, pp. 4177–4186, May 2018, doi: 10.1109/TIE.2017.2772144.
[21] J. Tang, K. Wang, and B. Xiang, "Stable control of high-speed rotor suspended by superconducting magnetic bearings and active magnetic bearings," *IEEE Trans. Ind. Electron.*, vol. 64, no. 4, pp. 3319–3328, Apr. 2017.
[22] J. Y. Song, K. J. Kang, C. H. Kang, and G. H. Jang, "Cogging torque and unbalanced magnetic pull due to simultaneous existence of dynamic and static eccentricities and uneven magnetization in permanent magnet motors," *IEEE Trans. Magn.*, vol. 53, no. 3, Mar. 2017, Art. no. 8200609.
[23] J. Faiz and S. M. M. Moosavi, "Detection of mixed eccentricity fault in doubly-fed induction generator based on reactive power spectrum," *IET Electr. Power Appl.*, vol. 11, no. 6, pp. 1076–1084, Jul. 2017.
[24] J. Pyrhönen, T. Jokinen, and V. Hrabovcova, *Design of Rotating Electrical Machines*. Hoboken, NJ, USA: Wiley, 2013.

Chong Di was born in Wuxi, China, in 1991. He received the B.Eng. and M.Eng. degrees in electrical engineering from the Hefei University of Technology, Hefei, China, in 2014 and 2017, respectively. He is currently pursuing the Ph.D. degree with the Department of Electrical Engineering, Lappeenranta University of Technology, Lappeenranta, Finland.

His current research interests include high-speed electrical machines.

Ilya Petrov received the D.Sc. degree from the Lappeenranta University of Technology (LUT), Lappeenranta, Finland, in 2015.

He is currently a Fellow Researcher with the Department of Electrical Engineering, LUT.

Juha J. Pyrhönen (M'06–SM'17) born in Kuusankoski, Finland, in 1957. He received the D.Sc. degree from the Lappeenranta University of Technology (LUT), Lappeenranta, Finland, in 1991.

In 1997, he joined LUT, as a Professor of electrical machines and drives. He is involved in research and development of electric motors and power-electronic-controlled drives. He has wide experience in the research and development of special electric drives for distributed power production, traction, and high-speed applications. He is currently studying the possibilities of using carbon-based materials in electrical machines. His current research interests include permanent magnet materials and applying them in machines.

Xiaohua Bao (M'14) received the B.Eng., M.Eng., and Ph.D. degrees in electrical engineering from the Hefei University of Technology, Hefei, China, in 1996, 2002, and 2008, respectively.

He joined the School of Electrical Engineering and Automation, Hefei University of Technology, where he was promoted to Professor in 2012. He was a Visiting Scholar with the Virginia Polytechnic Institute and State University, Blacksburg, VA, USA. His current research interests include motor design, magnetic field analysis, and finite-element analysis.

Publication VI

Kurvinen, E., Di, C., Petrov, I., Jastrzebski, R. P., Kepsu, D., and Pyrhönen, J.
Comparison of the Performance of Different Asynchronous Solid-Rotor Constructions in a Megawatt-Range High-Speed Induction Motor

Reprinted with permission from
IEEE International Electric Machines & Drives Conference, IEMDC 2019
pp. 820-825, 2019

Comparison of the Performance of Different Asynchronous Solid-Rotor Constructions in a Megawatt-Range High-Speed Induction Motor

Emil Kurvinen
Department of Mechanical Engineering
LUT School of Energy Systems
Lappeenranta-Lahti University of Technology
Lappeenranta, Finland
emil.kurvinen@lut.fi

Chong Di, Ilya Petrov, Rafal P. Jastrzebski,
Daria Kepsu, Juha Pyrhönen
Department of Electrical Engineering
LUT School of Energy Systems
Lappeenranta-Lahti University of Technology
Lappeenranta, Finland
chong.di@lut.fi, ilya.petrov@lut.fi, rafal.jastrzebski@lut.fi,
daria.kepsu@lut.fi, juha.pyrhonen@lut.fi

***Abstract*—High-speed electrical machines have their advantages, such as higher power density than in traditional electrical machines, and disadvantages, such as very demanding and tailored design and manufacturing process. The manufacturing of the rotor for a high-speed electrical machine is extra complex. In a high-speed electrical machine, the rotor in normal operation experiences various types of loadings, such as centrifugal forces from the rotation, temperature gradients from the operational environment, losses generated in the electrical machine and loads from the process. A failure related to the mechanical integrity of a rotor leads to a halt and very probably to the complete malfunction of the machine. The aim of this study is to compare three different rotor constructions in a high-speed induction electrical machine operating at the megawatt power range. The first one is a full copper squirrel cage rotor that consists of 25 pieces (22 copper bars, two copper end rings and a steel shaft), the second is a slitted solid rotor with copper end rings that consists of three pieces and two materials, and the third is a slitted solid rotor made solely of structural steel consisting of one piece. Further, these rotors are compared in terms of their electromagnetic performance, applying the same stator structure. The manufacturing challenges are directly related to the number of individual parts needed for the construction of the full rotor. The base material for the rotor core of the studied high-speed induction machine is often structural steel that is magnetically soft, has moderate electrical resistivity, and can be combined with copper or aluminum cage winding which is non-magnetic and has high electrical conductivity. From the mechanical perspective, these materials are very different; *e.g.* high-strength copper (CuCrZr) has a 50 % higher thermal expansion coefficient, 13 % higher density, 600 % higher thermal conductivity, and approximately 50 % lower yield strength than common structural steel (S355). This complicates the rotor manufacturing, as the required tolerances for the assembly of the rotor components are very strict and depend on the final manufacturing method of the rotor.**

***Index Terms*—high-speed induction machine (IM), manufacturing, megawatt range, rotor construction**

I. Introduction

High-speed electrical machines have been actively researched for decades, and several different high-speed machine topologies have been developed. [1] The potential positive effect of the increased rotational speed and consequently increased power density leads to an appealing development direction, *i.e.*, physically smaller electrical machines can provide similar or even better performance than currently available traditional machines in bulky size especially when applying them to high-speed applications using a very bulky and lossy step-up gear. The possible improvements compared to standard machines are significant. The awareness of energy utilization has led to increasing usage of frequency converter supplied machines, and further utilizing more tailored machines for a specific purpose, *i.e.*, turbo-machinery applications [2] or natural gas compression applications [3].

High-speed induction machines have proven to be suitable for many applications. [4] The magnetic core of a rotor in induction machine can be constructed from a laminated structure or directly from single solid piece. Laminated rotor could be utilized in induction machines with the surface velocity maximum of 200 m/s. [5]. In this study, the surface velocity of the studied rotor structures is 156 m/s so the laminated structure should in principle be possible. However, as the power of the studied motor is up to megawatt range this brings extra challenges in reliable design and manufacturing of a laminated rotor structure considering its active length, diameter and overall length of the shaft. The active part of a solid-rotor induction electrical machine is often constructed from one of three different types. First, a solid rotor with a squirrel cage made, *e.g.*, from copper or aluminum leads to good electromagnetic performance but to a much more challenging manufacturing process for high-speed purposes, as the rotor contains several different parts with individual tolerances that are assembled together. This leads to a relatively low mechanical rigidity and lower confidence due to noticeable manufacturing variation between different rotors. Second, a slitted solid rotor leads to a slightly lower electromagnetic performance but higher mechanical strength compared to a full squirrel-cage rotor. The slitted rotor can also comprise copper end rings that significantly reduce the total rotor resistance

978-1-5386-9350-6/19/$31.00 ©2019 IEEE

and therefore the slip of the rotor. Slits in the rotor enable better flux flow through the rotor. The copper end rings can be banded with a high strength material to increase the structural strength. The third is a smooth solid rotor, which leads to poor electromagnetic performance but high mechanical strength. [3] The aim of the study is to compare these three different rotor structures and investigate their actual performance in a megawatt range electric motor application.

Designing high-speed machines is in general a complex process due to its highly iterative nature. The design process of an induction machine generally follows similar steps as that of a high-speed two-pole permanent magnet synchronous machine (PMSM) [6]. The design and analysis of a high-speed machine includes bearing, dynamic, electrical, mechanical, structural, seals and thermal designs and analyses and for an application, *e.g.*, compressor it requires the impeller design, too. These individual tasks are highly connected, and to achieve the best possible performance for the machine, certain compromises are needed from all participants.

The design group consists of experts from several fields who all need to be taken into account in the realization of the actual motor design. This is often very challenging, as different machine components are manufactured of different materials such as specific steel, copper and aluminum alloys, which are manufactured with specific tolerances. Further, they require high strength metallic bonding or form-base fixing between them to tolerate the loads caused by a high rotation speed. Due to the floating parameters, such as tolerances, internal material structure and material connection, each component is an individual and the structural strength and dynamic behavior becomes difficult to predict. For example, the generally used ISO 268-2 specifies tolerances for shafts and holes. A shaft with a rated diameter of 250 mm with basic h7 tolerance may be manufactured from 249.48 mm to 250 mm, actually. Also ISO 2768 standard which defines general tolerances for linear and angular dimensions. It is divided into four tolerance classes, of which ”fine” is the most precise. Between 30 mm to 120 mm dimensions this standard allows +/-0.15 mm difference in the actual manufactured parts. This variation leads to challenges when joining separate parts together, *e.g.* in case of squirrel caged rotor. This leads to the fact that the first manufactured high-speed machine contains several factors that increase the risk of failure. The rotor structure is designed so that different parts withstand the mechanical stresses and keep their rigidity even in the worst operational conditions. The design process is fairly well known, but additional challenges arise from demanding manufacturing techniques. There are different techniques to manage the rotor rigidity when different materials are used, such as designing the active part in a way that the copper bars or pipes are embedded in the rotor core or joint to open slots in rotor with brazing [7], hot isostatic pressing (HIP) [8], explosion welding (EXW) [9] or pre-manufactured bimetals.

Lowering the risks that a prototype machine rotor has a manufacturing error is important, especially in the very first revision number. A case study with three different rotor constructions is reported and their electromagnetic performance analyzed. A megawatt sized induction machine supported with active magnetic bearings (AMB) is under focus. Table I depicts the studied structures and the number of individual parts.

TABLE I
STUDIED ROTOR CONSTRUCTIONS AND NUMBER OF INDIVIDUAL PARTS RELATED TO THE STRUCTURES

Case	Description	Number of parts
Case 1	Cu squirrel caged rotor	25 pieces
Case 2	Cu short-circuit rings, slitted core	three pieces
Case 3	Solid slitted rotor with Fe end rings	one piece

The rotor construction can be varied depending on the required mechanical manufacturability and performance of the machine. The number of individual components in a complex structure categorizes the rotor constructions where the copper end rings and copper bars form a squirrel cage induction machine (case 1). The second construction consists of a slitted solid rotor with copper end rings. This construction refers to a medium complexity structure (case 2). The third construction consists of a structural steel slitted rotor that refers to a simple structure (case 3). The purpose of the rotor structure variation is to analyze the rotor made of copper bars integrated into the rotor core and to compare it with a rotor made only of a machined steel slitted active part. The aim of the study is to investigate the selection of different active rotor parts and their consequent effects on the machine performance. High-speed machines and their commissioning involve many risks and potential pitfalls. Naturally, a simpler rotor structure is appealing to decrease the risks, especially in the first prototype.

II. CASES STUDIED

The case study is based on a full squirrel cage induction electrical machine. The machines rated capacity is 2 MW at 12 000 min^{-1} (200 Hz) and it is operated with a 660 V three phase supply. In the case of this high-speed induction rotor, the copper experiences high temperatures and high rotational speeds. Load cycles cause fatigue loading on the copper, and a safety factor needs to be included so that the yield strength is not exceeded. Fig. 1 and Fig. 2 depicts the outlook of the rotor with a full copper squirrel cage (case 1). The end ring is embedded in the construction to make its stresses lower.

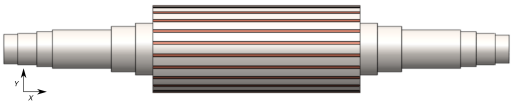

Fig. 1. Layout of the copper squirrel cage rotor (side view). The copper end rings are not seen as they are embedded in the construction (see Fig.2).

Three lowest free-free frequencies of the rotor are 319 Hz, 656 Hz and 1171 Hz. With a 5 MN/m bearing stiffness and 10.5 kg coupling at the drive end, the first bending mode occurs at 18640 min^{-1} (backward whirling mode) and 19 830 min^{-1} (forward whirling mode). The rotors studied have

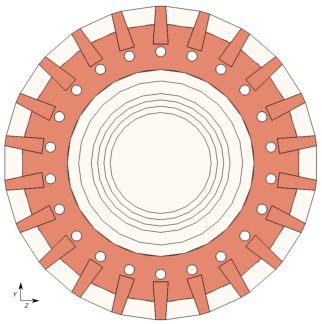

Fig. 2. Layout of the copper squirrel cage rotor (view from axial end) scaled 4:1 compared to Fig. 1.

very similar rotor bending frequencies. However, the torsional stiffness of the slitted rotor is clearly lower compared to the squirrel caged rotor [10]. The inner diameter of the copper end ring is 148 mm, and its outer diameter is 220 mm. At the nominal speed, the copper experiences tangential stress of 155 MPa and radial stress of 8 MPa with a copper density of 8930 kg/m^3 and a Poissons ratio of 0.343. With chromium zirconium copper (CuCrZr), the yield strength is 350 MPa. However, due to the fatigue of loads and uncertainty in joining the copper to steel, approximately half of the yield stress is considered the maximum allowed (175 MPa), thus becoming a limiting factor for utilization. The situation could be improved by adding a high strength band on top of the copper end ring. However, additional materials also affect the performance of the electrical machine and the increase number of connected parts.

When designing a solid-rotor machine one of the most important tasks is to mitigate harmonic losses on the rotor surface. Both stator current linkage harmonics and permeance harmonics caused by slot openings cause rotor losses. Therefore, the means to mitigate harmonic losses include minimization of the harmonic amplitudes in the air gap. This can be done by selecting as high stator slot number as possible which reduces the current linkage harmonics and to try to eliminate the permeance variations caused by the slot openings. Semi-magnetic slot wedges are an efficient means of mitigating the slot harmonics. Also the rotor construction itself may have an impact on the rotor surface losses. Especially, in case of a slitted rotor, skewing may mitigate some of the harmonic losses. In the motor studied the number of stator slots was selected only 18 because of the manufacturing challenges related to the stator winding. However, already this number of stator slots avoids an extensive value of the harmonic losses generated on the rotor surface especially when the stator has a short pitched winding.

Table II depicts the electrical machine parameters and Table III depicts the operational performance for a squirrel-cage rotor (case 1).

TABLE II
HARMONIC COMPONENTS OF THE AIR-GAP FLUX DENSITIES, PER-UNIT SLIP AND ROTOR FREQUENCIES IN THE STUDIED CASES.

Parameter	Value
Stator stack iron length [mm]	538
Stator stack iron outer diameter [mm]	550.5
Stator stack iron inner diameter [mm]	260.5
Rotor outer diameter [mm]	248.5
Rotor tangential tension (at rated torque) [kPa]	31
Number of stator slots	18
Effective coil-turns in the slot	2
Number of stator parallel branches	1
Stator coil-turns per phase in series	6
Single coil copper area (k_{Cu} = 0.45) [mm^2]	335
Winding type: Distributed, $Q_{\mathrm{s/mp}}$	3
Number of pole-pairs	1
Winding connection	Star
Stator core material	M270-35
Rotor core material	S355

TABLE III
OPERATIONAL PERFORMANCE FOR A SQUIRREL CAGED ROTOR (CASE 1).

Parameter	Value
Rated speed n_{N} [min^{-1}]	12000
Rated frequency f_{sN} [Hz]	200
Rated mechanical power P_{N} [kW]	2000
Rated torque T [Nm]	1600
Rated apparent input power S_{N} [kVA]	3100
Rated terminal phase voltage U_{phN} [V_{rms}]	660
Rated stator phase supply current I_{sN} [A_{rms}]	2100
Phase resistance R_{ph} [Ohm]	0.0011
Power factor cosϕ at rated operating point	0.7
Estimated efficiency at the nominal load [%]	96
Current density (with copper space factor 0.45) [A/mm^2]	4.5

Electromagnetic calculations were performed with 2D Finite-element method (FEM). 2D FEM simulation cannot directly take into account lack of copper end ring for case 3. Thus it is appended with the analytical calculation according to [4], which suggests that the rotor resistance should be increased in this case by a factor of 1.73. Fig. 3 depicts the cases studied.

The rotor outer diameter in the electrical machine active part is 284.5 mm and is kept constant for all of the cases studied. The slit depth was varied according to [11], and the minimum rotor losses were experienced at a depth of 55 mm. Thus, 55 mm slits were selected for the cases studied. In cases 2 and 3, the same slit depth is used. In case 1, the copper squirrel cage is formed from 22 copper bars. The copper end rings in cases 1 and 2 are 30 mm thick, with a 120 mm inner diameter and 184.5 mm outer diameter. The end ring is connected to the shaft in order to decrease the stresses that the end ring experiences during operation. The outer diameter is limited in order to decrease the stresses that the copper end ring experiences.

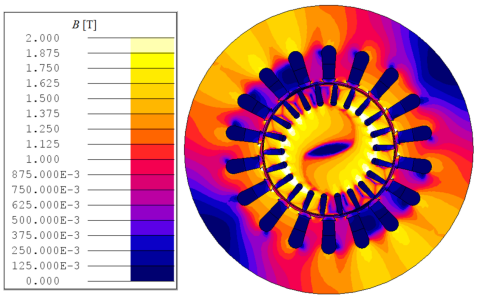

Case 1: Copper squirrel cage

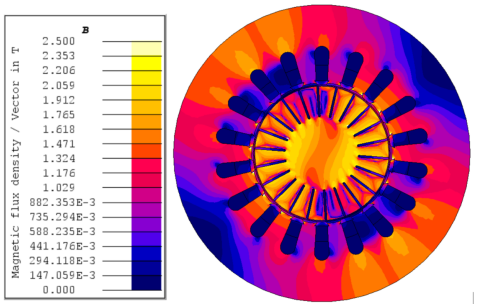

Case 2: Slitted with copper end rings

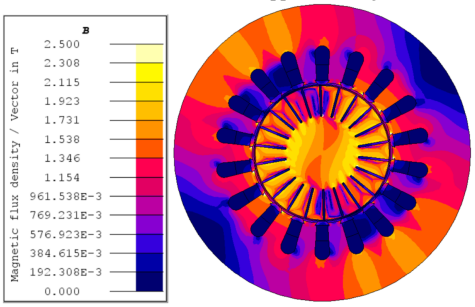

Case 3: Slitted without copper end rings

Fig. 3. Electric machine topologies studied.

III. Results

The power density of the machines are almost constant, as all the machines are operating at 1600 Nm and the volume is almost the same in the machines. The power factor estimated from the 2D analysis for case 1 is 0.697 and for cases 2 and 3 it is 0.675. Comparison of the air-gap flux density harmonic components for different cases is shown in Table IV. Lower stator slot harmonic amplitude is more acceptable as it causes a smaller rotor harmonic eddy-current loss.

Case 1 creates the minimum slip related losses (fundamental harmonic losses) as Case 1 has the lowest per-unit slip, whereas in contrast Case 3 creates the maximum slip related losses. In addition, because Case 3 has the maximum stator slot harmonics (17^{th} harmonic 0.087 and 19^{th} harmonic 0.039), it generates the maximum harmonic losses on the rotor side.

TABLE IV
HARMONIC COMPONENTS OF THE AIR-GAP FLUX DENSITIES, PER-UNIT SLIP AND ROTOR FREQUENCIES IN THE STUDIED CASES.

Parameters	Case 1	Case 2	Case 3
Fundamental, [T]	0.936	0.931	0.932
17^{th} harmonic,* [T]	0.076	0.082	0.087
19^{th} harmonic,* [T]	0.033	0.037	0.039
Per-unit slip s	0.0013	0.0028	0.0049
Rotor frequency s_f, Hz	0.26	0.56	0.98

*17^{th} and 19^{th} harmonics are the 1^{st} order stator slot harmonics.

Table V shows the losses in the copper squirrel-caged rotor (case 1) and the slitted rotor with copper end rings (case 2) and without copper end rings (case 3). A sinusoidal supply was used (converter harmonics are not included) and iron losses were estimated by using the Bertotti method in FEM.

TABLE V
LOSS COMPARISON OF THE STUDIED CASES.

Loss type	Case 1	Case 2	Case 3
Copper losses (stator resistive losses) [kW]	8	8.7	8.7
Iron losses (stator stack) [kW]*	27.2	26.8	26.8
Iron losses (solid rotor) [kW]*	24.7	39.6	40.5
Copper bars losses [kW]*	7	-	-
Extra losses [kW]**	10	10	10
Total electromagnetic losses [kW]	76.9	85.1	86
Electromagnetic efficiency [%]	96.16 %	95.75 %	95.70 %

*Estimated with FEM ** 0.5 % of the nominal load [12]

IV. Discussion

The aim of this study is to compare the performance of different rotor constructions taking the manufacturing complexity and structural rigidity into consideration. The machines physical dimensions were kept the same, with the exception that in Case 3, the copper end rings were removed and rotor was made same length of the same core material as the length with copper end rings are. In a high-speed induction machine with a copper squirrel cage, the machine can have lower slip-related rotor losses and consequently a higher efficiency. However, it is rational to check the electromagnetic performance of the machine also with simpler rotor constructions, as it greatly simplifies the rotor manufacturing procedure, and with certain general machine parameters (*e.g.* number of slots, open slot width, rotational speed, conductivity of the rotor core steel, etc.), it might yield nearly similar machine performance.

Case 3 was the most straightforward, as the rotor could be manufactured from a single solid steel piece with a lathe, milling machine and grinding machine. Case 2 can also be manufactured with the same technique as Case 3 with the addition of making two copper end rings and connecting those to the solid shaft, *e.g.*, with vacuum brazing or electron beam welding. The connection of two different metals, especially copper and steel, requires specific knowledge of metallurgy and additional manufacturing steps prior to commissioning.

In Case 2, the copper ring can be attached in the radial and axial directions, and the dimensions of the copper end rings are fairly small, *i.e.*, the stresses induced by the difference in the thermal expansion coefficient can be withstood without exceeding the materials yield strength. In Case 1, the number of individual pieces increases as 22 copper bars need to be inserted into the structure to manufacture a complete copper squirrel cage. For this structure, the manufacturing becomes more challenging compared to Case 2. The 22 copper bars should be attached mechanically rigidly enough to the rotor core, and galvanic connections with the copper end rings should be achieved to build an intact squirrel cage that carries most of the rotor electric currents. The copper bars can be inserted, *e.g.*, inside the rotor core, and the core steel can hold them in place during operation. This can be achieved by using cannon drilling, designing a suitable shape for the copper bars and rotor slots so that the shape will hold the bars in place, or joining them to the slot for example with vacuum brazing. As can be seen, from the manufacturing perspective Case 3 is the most appealing, Case 2 is the second most appealing, and Case 1 with its full copper squirrel cage rotor is the least appealing.

A. The effect of the rotor construction on active magnetic bearing design

From the AMB design point of view, even small differences in machine topologies can cause different spatial harmonics of flux density in the airgap. Various effects such as harmonics of magnetizing current, saturation of teeth, slot shapes, edge saturation, eddy currents, and winding connections will cause variations of permeability in the stator and rotor and non-symmetrical flux density. These with rotor displacement will result in unbalanced magnetic pull (UMP) that has effect on levitation control.

The control algorithm of AMBs has to take into account the magnetic force caused by the eccentricity. The maximum force produced by an AMB has to overcome the sum of, the gravity force, UMP force, mass unbalance forces, negative stiffness effects of bearings, and other disturbance forces (*e.g.* from the process). At the same time the controller has to ensure that no structural resonances of the rotor and frame are excited. In case of static forces, the typical safety limit is such that the AMB force should be three to four times the maximum total load force in the nominal point. The AMB system by injecting a direct current should compensate for the direct component of the magnetic force and alternating current can be used to compensate for the rotating UMP. The operational range defined by the size of the retainer bearings has to be considered as AMB force capacity will decrease while UMP will increase as a function of the rotor displacement.

With simple modelling, the rotor eccentricity, can be classified as static, dynamic or mixed [13]. The rotor eccentricity introduces UMP, extra noise, vibration, and losses. The squirrel copper cage rotor could result in the biggest value of the UMP. For static eccentricity, UMP can be predicted analytically [14].

B. Electromagnetic performance of studied cases

From the electromagnetic point of view, the copper squirrel cage has the lowest losses because it runs with the lowest slip. However, also this rotor suffers from losses caused by the air gap harmonics in the solid rotor core. Actually, these losses are the dominating ones, and means for mitigating the harmonic losses must be exercised. The losses are greater in the slitted rotor cases (2 and 3). The harmonic losses in the rotor core remain roughly at the same level in these cases. Actually, slitting may even help in reducing the harmonic losses. In the case of the slitted rotors, the copper losses in the stator increase from 8 kW to 8.7 kW because of the weaker rotor power factor, so more stator currents are needed to induce the flux in the rotor. The iron losses in the stator decrease from 27.2 kW to 26.8 kW because of the narrower rotor slot opening, which results in lower stator harmonic core losses. In the actual machine, the stator is liquid cooled and the stator coils are also directly cooled so that the increase of the stator losses can be relatively easily handled with the applied cooling system.

The rotor losses are also increased from 31.2 kW (24.7 kW iron losses and 7 kW copper bar losses) in Case 1 to 39.6 kW (27 % higher) in Case 2 and 40.5 kW (30 % higher) in Case 3. The increased rotor losses are due to the increased rotor resistance as steel electrical conductivity is much lower than that of copper. The higher losses in the rotor may lead to the need to rearrange the rotor cooling or to limit the power output to prevent the rotor from overheating. In Case 3, the rotor without copper enables a much higher rotational speed than in the two other cases, where the limiting factor is the structural strength of the copper end ring. In Case 3, this problem arises only at higher speed when the applied steel material meets its strength limitations. According to preliminary analyses, the machine could be run at 16 000 min^{-1} without any major design revisions of the solid-steel rotor (as the case 1 and case 2 are limited to 12 000 min^{-1}).

V. Conclusions

In the 2 MW case, the electromagnetic efficiency was reduced from 96.16 % by 0.41 % when the copper squirrel cage was replaced with rotor core slits. In the slitted-rotor machines, the efficiency with copper end rings is 95.75 % and without copper end rings 95.70 %, *i.e.*, the copper end rings improve the slitted rotor machine efficiency by 0.05 %. In the case studied, the rotor without copper end rings could be operated at 35 % higher speed and still lead to a well operating machine from the mechanical perspective. When designing new high-speed machines, the one-piece rotor construction is appealing at least in the prototype because the risk of rotor failure is low. The achieved efficiency is lower than what could be achieved with the more complicated constructions. However, those structures need well-proven manufacturing technologies and the manufacturer's specific knowledge in manufacturing complicated solid rotors. In practice, the rotor of a high-speed machine in the megawatt range can be designed in a step-by-step manner starting with a simple solid steel rotor. Later the

rotor can be further developed by adding first the copper end rings and then a squirrel cage in the rotor to minimize the design risks.

REFERENCES

[1] D. Gerada, A. Mebarki, N. L. Brown, C. Gerada, A. Cavagnino, and A. Boglietti. High-speed electrical machines: Technologies, trends, and developments. *IEEE Transactions on Industrial Electronics*, 61(6):2946–2959, June 2014.

[2] H. Bleuler, M. Cole, P. Keogh, R. Larsonneur, E. Maslen, Y. Okada, G. Schweitzer, and A. Traxler. *Magnetic Bearings: Theory, Design, and Application to Rotating Machinery*. Springer Science & Business Media, Berlin Heidelberg, 1st edition, 2009.

[3] J. Pyrhönen, J. Nerg, P. Kurronen, and U. Lauber. High-speed, 8 mw, solid-rotor induction motor for gas compression. In *2008 18th International Conference on Electrical Machines*, pages 1–6, Sept 2008.

[4] J. Pyrhönen, J. Nerg, P. Kurronen, and U. Lauber. High-speed high-output solid-rotor induction-motor technology for gas compression. *IEEE Transactions on Industrial Electronics*, 57(1):272–280, 2010.

[5] D. Gerada, A. Mebarki, N. L. Brown, K. J. Bradley, and C. Gerada. Design aspects of high-speed high-power-density laminated-rotor induction machines. *IEEE Transactions on Industrial Electronics*, 58(9):4039–4047, Sep. 2011.

[6] N. Uzhegov, E. Kurvinen, J. Nerg, J. Pyrhönen, J. Sopanen, and S. Shririnskii. Multidisciplinary design process of a 6-slot 2-pole high-speed permanent-magnet synchronous machine. *IEEE Transactions on Industrial Electronics*, 63(2):784–795, Feb 2016.

[7] J. Barta, N. Uzhegov, P. Losak, C. Ondrusek, Mach M., and J. Pyrhönen. Squirrel cage rotor design and manufacturing for high-speed applications. *IEEE Transactions on Industrial Electronics*, pages 1–10, 2018.

[8] T. Mauffrey, J.-F. Pradurat, L. Durantay, and J Fontini. Comparison of 5 different squirrel cage rotor designs for large high speed induction motors. In *PCIC Europe (PCIC EUROPE), 2013 Conference Record*, pages 1–9. IEEE, 2013.

[9] F. Findik. Recent developments in explosive welding. *Materials & Design*, 32(3):1081 – 1093, 2011.

[10] J. Pyrhönen, J. Nerg, A. Mikkola, J. Sopanen, and T. Aho. Electromagnetic and mechanical design aspects of a high-speed solid-rotor induction machine with no separate copper electric circuit in the megawatt range. *Electrical Engineering*, 91(1):35, Apr 2009.

[11] T. Aho. *Electromagnetic design of a solid steel rotor motor for demanding operation environments*. PhD thesis, Lappeenranta University of Technology, 2007.

[12] J. Pyrhönen, T. Jokinen, and V. Hrabovcová. *Design of Rotating Electrical Machines*. John Wiley & Sons, United Kingdom, 1st edition, 2009.

[13] C. Di, I. Petrov, J. J. Pyrhönen, and X. Bao. Unbalanced magnetic pull compensation with active magnetic bearings in a 2 mw high-speed induction machine by fem. *IEEE Transactions on Magnetics*, 54(8):1–13, Aug 2018.

[14] N. Amati and E. Brusa. Vibration condition monitoring of rotors on amb fed by induction motors. In *2001 IEEE/ASME International Conference on Advanced Intelligent Mechatronics. Proceedings (Cat. No.01TH8556)*, volume 2, pages 750–756 vol.2, July 2001.

ACTA UNIVERSITATIS LAPPEENRANTAENSIS

864. OTRA-AHO, VILLE. A project management office as a project organization's strategizing tool. 2019. Diss.

865. HILTUNEN, SALLA. Hydrothermal stability of microfibrillated cellulose. 2019. Diss.

866. GURUNG, KHUM. Membrane bioreactor for the removal of emerging contaminants from municipal wastewater and its viability of integrating advanced oxidation processes. 2019. Diss.

867. AWAN, USAMA. Inter-firm relationship leading towards social sustainability in export manufacturing firms. 2019. Diss.

868. SAVCHENKO, DMITRII. Testing microservice applications. 2019. Diss.

869. KARHU, MIIKKA. On weldability of thick section austenitic stainless steel using laser processes. 2019. Diss.

870. KUPARINEN, KATJA. Transforming the chemical pulp industry – From an emitter to a source of negative CO2 emissions. 2019. Diss.

871. HUJALA, ELINA. Quantification of large steam bubble oscillations and chugging using image analysis. 2019. Diss.

872. ZHIDCHENKO, VICTOR. Methods for lifecycle support of hydraulically actuated mobile working machines using IoT and digital twin concepts. 2019. Diss.

873. EGOROV, DMITRY. Ferrite permanent magnet hysteresis loss in rotating electrical machinery. 2019. Diss.

874. PALMER, CAROLIN. Psychological aspects of entrepreneurship – How personality and cognitive abilities influence leadership. 2019. Diss.

875. TALÁSEK, TOMÁS. The linguistic approximation of fuzzy models outputs. 2019. Diss.

876. LAHDENPERÄ, ESKO. Mass transfer modeling in slow-release dissolution and in reactive extraction using experimental verification. 2019. Diss.

877. GRÜNENWALD, STEFAN. High power fiber laser welding of thick section materials - Process performance and weld properties. 2019. Diss.

878. NARAYANAN, ARUN. Renewable-energy-based single and community microgrids integrated with electricity markets. 2019. Diss.

879. JAATINEN, PEKKO. Design and control of a permanent magnet bearingless machine. 2019. Diss.

880. HILTUNEN, JANI. Improving the DC-DC power conversion efficiency in a solid oxide fuel cell system. 2019. Diss.

881. RAHIKAINEN, JARKKO. On the dynamic simulation of coupled multibody and hydraulic systems for real-time applications. 2019. Diss.

882. ALAPERÄ, ILARI. Grid support by battery energy storage system secondary applications. 2019. Diss.

883. TYKKYLÄINEN, SAILA. Growth for the common good? Social enterprises' growth process. 2019. Diss.

884. TUOMISALO, TEEMU. Learning and entrepreneurial opportunity development within a Finnish telecommunication International Venture. 2019. Diss.

885. OYEDEJI, SHOLA. Software sustainability by design. 2019. Diss.

886. HUTTUNEN, MANU. Optimizing the specific energy consumption of vacuum filtration. 2019. Diss.

887. LIIKANEN, MIIA. Identifying the influence of an operational environment on environmental impacts of waste management. 2019. Diss.

888. RANTALA, TERO. Operational level performance measurement in university-industry collaboration. 2019. Diss.

889. LAUKKANEN, MINTTU. Sustainable business models for advancing system-level sustainability. 2019. Diss.

890. LOHRMANN, CHRISTOPH. Heuristic similarity- and distance-based supervised feature selection methods. 2019. Diss.

891. ABDULLAH, UMMI. Novel methods for assessing and improving usability of a remote-operated off-road vehicle interface. 2019. Diss.

892. PÖLLÄNEN, ILKKA. The efficiency and damage control of a recovery boiler. 2019. Diss.

893. HEKMATMANESH, AMIN. Investigation of EEG signal processing for rehabilitation robot control. 2019. Diss.

894. HARMOKIVI-SALORANTA, PAULA. Käyttäjät liikuntapalvelujen kehittäjinä - Käyttäjälähtöisessä palveluinnovaatioprosessissa käyttäjien tuottama tieto tutkimuksen kohteena. 2020. Diss.

895. BERGMAN, JUKKA-PEKKA. Managerial cognitive structures, strategy frames, collective strategy frame and their implications for the firms. 2020. Diss.

896. POLUEKTOV, ANTON. Application of software-defined radio for power-line-communication-based monitoring. 2020. Diss.

897. JÄRVISALO, HEIKKI. Applicability of GaN high electron mobility transistors in a high-speed drive system. 2020. Diss.

898. KOPONEN, JOONAS. Energy efficient hydrogen production by water electrolysis. 2020. Diss.

899. MAMELKINA, MARIA. Treatment of mining waters by electrocoagulation. 2020. Diss.

900. AMBAT, INDU. Application of diverse feedstocks for biodiesel production using catalytic technology. 2020. Diss.

901. LAAPIO-RAPI, EMILIA. Sairaanhoitajien rajatun lääkkeenmääräämistoiminnan tuottavuuden, tehokkuuden ja kustannusvaikuttavuuden arviointi perusterveydenhuollon avohoidon palveluprosessissa. 2020. Diss.

LUT University

ISBN 978-952-335-506-4
ISBN 978-952-335-507-1 (PDF)
ISSN-L 1456-4491
ISSN 1456-4491
Lappeenranta 2020